Neoclassical plasma viscosity and transport processes in non-axisymmetric tori

IOP Publishing | International Atomic Energy Agency Nuclear Fusion
Nucl. Fusion 55 (2015) 125001 (104pp) doi:10.1088/0029-5515/55/12/125001

Review Article

Neoclassical plasma viscosity and transport processes in non-axisymmetric tori

K.C. Shaing[1], K. Ida[2] and S.A. Sabbagh[3]

[1] National Cheng Kung University, Tainan 70101, Taiwan, Republic of China
[2] National Institute for Fusion Science, Toki 509-5292, Japan
[3] Columbia University, New York, NY 10027, USA

E-mail: kcs@plasma.pssc.ncku.edu.tw

Received 11 February 2010, revised 3 November 2014
Accepted for publication 11 December 2014
Published 13 November 2015

Abstract

Neoclassical transport processes are important to the understanding of plasma confinement physics in doubly periodic magnetized toroidal plasmas, especially, after the impact of the momentum confinement on the particle and energy confinement is recognized. Real doubly periodic tori in general are non-axisymmetric, with symmetric tori as a special case. An eight-moment approach to transport theory with plasma density N, plasma pressure p, mass flow velocity $\boldsymbol{V}$ and heat flow $\boldsymbol{q}$ as independent variables is adopted. Transport processes are dictated by the solutions of the momentum and heat flux balance equations. For toroidal plasma confinement devices, the first order (in the gyro-radius ordering) plasma flows are on the magnetic surface to guarantee good plasma confinement and are thus two-dimensional. Two linearly independent components of the momentum equation are required to determine the flows completely. Once this two-dimensional flow is relaxed, i.e. the momentum equation reaches a steady state, plasmas become ambipolar, and all the transport fluxes are determined through the flux–force relation. The flux–force relation is derived both from the kinetic definitions for the transport fluxes and from the manipulation of the momentum and heat flux balance equations to illustrate the nature of the transport fluxes by examining their corresponding driven forces and their roles in the momentum and heat flux balance equations. Steady-state plasma flows are determined by the components of the stress and heat stress tensors in the momentum and heat flux balance equations. This approach emphasizes the pivotal role of the momentum equation in the transport processes and is particularly useful in modelling plasma flows in experiments. The methodology for neoclassical transport theory is applied to fluctuation-driven transport fluxes in the quasilinear theory to unify these two theories. Experimental observations in tokamaks and stellarators for the physics discussed are presented.

Keywords: tokamak, non-asymmetric tori, plasma transport

(Some figures may appear in colour only in the online journal)

1. Introduction

The economic feasibility of toroidal thermonuclear fusion reactors such as tokamaks and stellarators critically depends on the understanding and control of plasma particle and energy transport losses in these devices. The strong magnetic fields, forming nested magnetic surfaces, shown in figure 1, are used to confine plasma movements across the magnetic surfaces. Plasma particles and energy are lost from the system through transport processes across the magnetic surface. It was expected that transport losses follow the predictions of classical transport theory [1]. However, it has been known that plasma particle and energy confinement times in tokamaks and stellarators are much shorter than those predicted by classical transport theory. The research neoclassical transport theory began when it was realized that the width of the collisionless particle orbits in the magnetic geometry of tokamaks and stellarators is much wider than that of the classical gyro-orbits [2–5]. This results in much larger transport fluxes than the predicted classical fluxes when coupled to a dissipation mechanism. The dissipative mechanism is Coulomb collisions in neoclassical and classical transport theories of high-temperature plasmas for thermonuclear fusion purposes. Coulomb collisions are present even in turbulent plasmas. Thus, they are the irreducible dissipation mechanism. Neoclassical transport

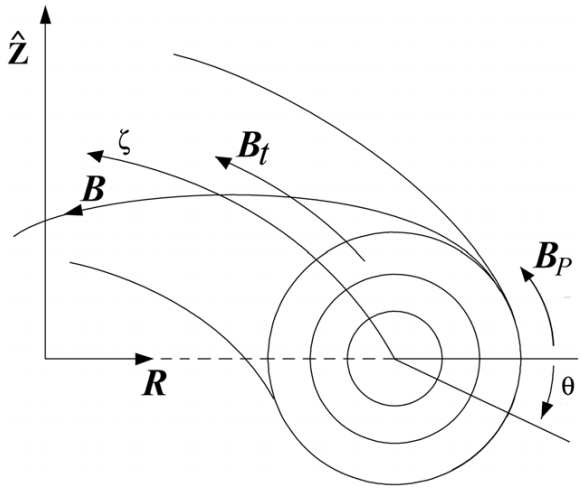

Figure 1. A schematic diagram of the magnetic fields and coordinates for a torus. Here, R is the major radius, ζ is the toroidal angle, θ is the poloidal angle, $\hat{Z}$ is the unit vector perpendicular to the (R, ζ) plane, $\boldsymbol{B}_\mathrm{t}$ is the toroidal magnetic field, $\boldsymbol{B}_\mathrm{p}$ is the poloidal magnetic field, and $\boldsymbol{B} = \boldsymbol{B}_\mathrm{t} + \boldsymbol{B}_\mathrm{p}$ is the magnetic field. The nested circles denote magnetic surfaces.

theory, pioneered by Galeev and Sagdeev [2, 3], is a study of the transport consequences caused by the drift orbits under the influence of Coulomb collisions.

The neoclassical transport processes in tokamaks are fundamentally different from those in stellarators. The magnetic field in ideal tokamaks is toroidally symmetric, or axisymmetric. Toroidal symmetry ties particles to the magnetic surface and limits the radial excursions of the particles. Particles do not drift off the magnetic surface. The magnetic field geometry for stellarators, on the other hand, does not possess any symmetry property. Collisionless particles readily drift off the magnetic surface. Thus, neoclassical transport losses, especially for fusion-born alpha particles, in stellarators are much larger than those in tokamaks. Transport processes in non-axisymmetric tori are further complicated by the limited ability to describe analytically the collisionless particle trajectories in complicated magnetic field configurations.

Even though ideal tokamaks are toroidally symmetric, real tokamaks do not possess such symmetry due to the presence of either the discrete numbers of the toroidal magnetic field coils, or error fields, or low-frequency magnetohydrodynamic (MHD) activity. In this sense, all real magnetically confined toroidal plasmas are non-axisymmetric. Thus, at least in principle, neoclassical transport theory for real tokamaks and stellarators can be formulated with a unified approach. Details are of course much different and depend on the spectrum of the magnetic field strength $B = |\boldsymbol{B}|$, where $\boldsymbol{B}$ is the magnetic field. One of the goals of this review is to address the similarities and differences in the transport properties in these devices.

Neoclassical transport theory for axisymmetric tokamaks is a matured subject. Two excellent review papers on the subject describe the detailed physics, mathematical procedures for solutions of the drift kinetic equation in various asymptotic limits, and transport fluxes of the theory [6, 7]. The approaches described in those two reviews are quite different. In the review by Hinton and Hazeltine [6], a variational approach is adopted. Transport coefficients in the transport matrix are calculated individually by taking the proper moments of the distribution function. To treat approximately the important momentum restoring effects in the Coulomb collision operator, a flow speed, proportional to the radial gradients of the plasma pressure, electrostatic potential, and temperature, that is parallel to the magnetic field $\boldsymbol{B}$ is introduced in the solution of the drift kinetic equation with a variational parameter y to be determined. The parameter y, and thus a relation between the parallel flow and the radial electric field, is determined by minimizing the rate of entropy production, which is equivalent to the ambipolarity condition, for simple electron–ion plasmas [5, 8]. The role of the momentum equation in the theory is not transparent in this approach. In the review by Hirshman and Sigmar [7], a moment approach to the transport theory is employed. In that approach, a parallel flow for each species is introduced, following the insight gleaned from the variational approach, to treat approximately the momentum restoring terms in the Coulomb collision operator. The flux–force relation [9, 10] that relates transport fluxes to forces plays a pivotal role in the theory. Once the components of the viscous forces (or stresses in general) are calculated, all transport fluxes can be obtained by solving for plasma flows that satisfy the momentum and heat balance equations and by substituting the resultant plasma flows into the flux–force relation. Thus, it is not necessary to take the proper moment of the distribution function for each individual transport flux. This approach has several advantages. First, it can be readily generalized to plasmas consisting of multiple ion species, as demonstrated in [7]; second, the components of the viscous tensors can be used for modelling plasma flows in experiments; third, the relation between plasma ambipolarity and momentum relaxation is clearly delineated [11, 12]; and fourth, the crucial role the momentum and heat balance equations played in the theory is transparent. For these advantages, moment approach is adopted in this review to unify the formulation for the transport processes in non-axisymmetric tori for simple electron–ion plasmas. Eight independent fluid variables are employed in the approach. Specifically, the eight moments are plasma density N, plasma pressure p (or temperature T), mass flow velocity $\boldsymbol{V}$ and heat flux $\boldsymbol{q}$. The Braginskii equations [1], by contrast, are based on a five-moment approach where independent variables are N, $\boldsymbol{V}$ and plasma temperature T.

The momentum confinement is not usually emphasized in the neoclassical transport theory for axisymmetric tokamaks presumably because transport fluxes are perceived to be intrinsically ambipolar [6]. The poloidal flow damping process becomes a research subject almost as an after thought [13]. It had been believed that momentum confinement had nothing to do with the particle and energy confinement until the development of the theory for the high confinement mode (H-mode) [14]) to change the paradigm [15–17]. Another paradigm shift concept in the theory is that the turbulence fluctuations can be suppressed by the gradient of the $\boldsymbol{E} \times \boldsymbol{B}$ angular velocity. Here, $\boldsymbol{E}$ is the electrostatic electric field. Turbulence suppression theory and its implications on plasma confinement first appeared in 1988 [17], and were later reviewed in [18]. The electrostatic radial electric

field is determined from the momentum equation, which can have bifurcated solutions resulting from the non-linearity of the plasma viscosity, another paradigm changing idea in tokamak physics. Thus, the momentum confinement intimately affects the particle and energy confinement. These insightful discoveries first demonstrated in [15–17] have led to the intensive theoretical and experimental research efforts on the momentum confinement in all plasma confinement devices. The moment equation approach is particularly suited for investigating the momentum confinement in toroidal plasmas.

Because the variation of the strength of the equilibrium magnetic field on the magnetic surface that causes neoclassical transport fluxes is larger than turbulence fluctuation amplitudes, the components of the viscous forces caused by the equilibrium magnetic field variations can be the dominant forces in the momentum equation. The momentum confinement mechanism is likely to be neoclassical even in turbulent plasmas. It is known that turbulence fluctuations enhance particle and energy transport fluxes but have little effects on the neoclassical bootstrap current and the electric conductivity [19, 20]. This is an indication that neoclassical momentum balance equations are relevant even in turbulent plasmas. Thus, not all transport coefficients are equally anomalous as demonstrated in the neoclassical quasilinear theory [21], and neoclassical theory plays an important role in the understanding of plasma confinement in non-axisymmetric tori with axisymmetric tori as a special case.

1.1. Brief summary of neoclassical transport fluxes for axisymmetric tokamaks

Neoclassical transport fluxes in axisymmetric tokamaks can be summarized in a 3 × 3 matrix [6, 7], schematically:

$$\begin{pmatrix} \Gamma_r \\ q_r/T \\ J_{||}/T \end{pmatrix} = \begin{pmatrix} D_{11} & D_{12} & D_{13} \\ D_{21} & D_{22} & D_{23} \\ D_{31} & D_{32} & D_{33} \end{pmatrix} \begin{pmatrix} X_1 \\ X_2 \\ E_{||}^{(A)} \end{pmatrix}. \qquad (1.1.1)$$

The transport fluxes in equation (1.1.1) are Γ_r, q_r and $J_{||}$, which are the radial (across the magnetic surface) particle flux, radial heat flux and current density parallel to the equilibrium magnetic field, respectively. The thermodynamic forces are X_1, X_2 and $E_{||}^{(A)}$, where $X_1 = X_1\left(p'/p, T'/T\right)$, $X_2 = T'/T$, the prime denotes the radial derivative, and $E_{||}^{(A)}$ is the inductive electric field parallel to the magnetic field. The transport coefficients are D_{ij}, where i and j are positive integers varying from 1 to 3. Because of Onsager symmetry, $D_{ij} = D_{ji}$. The conventional particle and heat diffusion coefficients are D_{11}, D_{22}, and $D_{12} = D_{21}$. The coefficients D_{13} and D_{23} describe the particle and heat fluxes resulting from the Ware pinch [22, 23]. Their conjugate elements D_{31} and D_{32} are coefficients for the bootstrap current driven by the plasma gradients [23, 24]. D_{33} is the electric conductivity with the modification due to the existence of the trapped particles [25].

The fundamental reason that neoclassical transport fluxes deviate from fluxes in the classical theory is because the magnetic field strength B varies on the magnetic surface. In tokamaks, the magnetic field is stronger on the inside of the torus where $\theta = \pi$ and weaker on the outside of the torus where $\theta = 0$. Here, θ is the poloidal angle as shown in figure 1. The right-handed coordinate system is chosen here. In a large aspect ratio tokamak, this variation can be expressed as, when $\varepsilon < 1$, [2–5]

$$B = B_0\left(1 - \varepsilon\cos\theta\right), \qquad (1.1.2)$$

where B is the magnetic field strength on the magnetic surface, B_0 is the magnetic field strength on the magnetic axis, $\varepsilon = r/R$ is the inverse aspect ratio, r is the local minor radius and R is the major radius. The typical distance going from $\theta = 0$ to $\theta = \pi$ along a magnetic field line scales as Rq, where the safety factor $q = rB_t/\left(RB_p\right)$, B_t is the toroidal magnetic field strength, and B_p is the poloidal magnetic field strength.

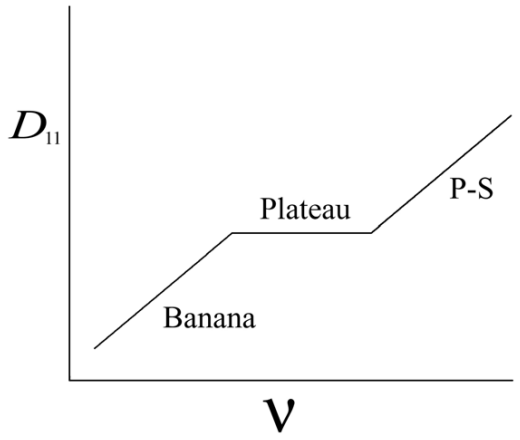

Figure 2. As collision frequency decreases, the diffusion coefficient D_{ij} for i or $j = 1$ or 2 goes from the collisional Pfirsch–Schlüter (P–S) regime, through the intermediate plateau regime and finally to the banana regime. These scalings can be understood in terms of the random walk argument. This is a log–log plot.

Particles drift along the constant B surface as a result of ∇B and curvature drifts due to the non-uniform magnetic field. In a circular tokamak equilibrium, the constant $|B|$ surface is parallel to the $\hat{Z}$-axis. The radial drift speed is, thus, proportional to sin θ, and the poloidal drift speed has cos θ dependence. The radial drift reverses direction across the θ =0 line. On average, particles do not drift off the flux surface in axisymmetric tokamaks. It is this drift motion that enhances the neoclassical transport fluxes over fluxes in the classical theory.

The typical collision frequency dependence for the particle and heat fluxes is shown in figure 2.

Because the magnetic moment $\mu = Mv_\perp^2/(2B)$ is an invariant for physics processes that have characteristic frequencies less than the gyro-frequency $\Omega = eB/(Mc)$, particles are trapped on the outside of the torus where the magnetic field strength is weaker. Here, e is the electric charge of the particle, M is the mass of the particle, $v_\perp$ is the particle speed that is perpendicular to the magnetic field, and c is the speed of light. These trapped particles are called bananas for having a poloidal projection similar to the shape of bananas (see figure 3).

The characteristic width of the trapped particles $(\Delta r)_b$ is of the order of [6, 7]

$$(\Delta r)_b \sim \sqrt{\varepsilon}\rho_p, \qquad (1.1.3)$$

where $\rho_p = v_t/\left|\Omega_p\right|$ is the poloidal gyro-radius, $v_t = \sqrt{2T/M}$ is the thermal speed, $\Omega_p = eB_p/(Mc)$ is the poloidal gyro-frequency. Because $B_p < B$ in tokamaks, the width in

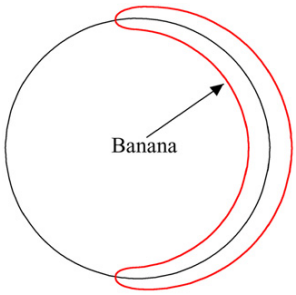

Figure 3. A schematic diagram for a banana orbit.

equation (1.1.3) can be much larger than the gyro-radius $\rho = v_t/|\Omega|$. Typical trapped particles have $v_\parallel/v < \sqrt{\varepsilon}$, where $v_\parallel$ is the particle speed that is parallel to the equilibrium magnetic field. Thus, effective collision frequency for trapped particles to scatter out of the magnetic well is

$$\nu_{\rm eff} \sim \frac{\nu}{\left[\Delta(v_\parallel/v)\right]^2} \sim \frac{\nu}{\varepsilon}, \tag{1.1.4}$$

where ν is the typical collision frequency, $\Delta(v_\parallel/v)$ denotes the width in the pitch angle space that is relevant to the physical process under discussion, and v is the particle speed. Typical diffusion coefficient D can be estimated using a random walk argument, which states that

$$D \sim f_r \frac{(\Delta r)^2}{\Delta\tau}, \tag{1.1.5}$$

where f_r is the fraction of the particles that dominate the transport processes, Δr is the characteristic radial step size in between decorrelations, and $\Delta\tau$ is the typical decorrelation time. Using the argument, when trapped particles dominate the transport processes in tokamaks,

$$D_{\rm b} \sim \nu\sqrt{\varepsilon}\rho_{\rm p}^2, \tag{1.1.6}$$

which is larger than the classical diffusion coefficient $D_{\rm c} \sim \nu\rho^2$ by about two orders of magnitudes when typical $B_{\rm p}$ is about a tenth of B. The scaling in equation (1.1.6) is for the transport coefficients in the banana regime. The banana regime onsets when the collision frequency is infrequent enough so that collisionless orbits of the trapped particles can be formed. Thus, the effective collision frequency in equation (1.1.4) must be less than the bounce frequency of the trapped particles $\omega_{\rm b} \sim v_t\sqrt{\varepsilon}/(Rq)$ which yields $\nu_* = \nu Rq/\left(\varepsilon^{3/2}v_t\right) < 1$.

In the Pfirsch–Schlüter regime, all particles contribute to the transport processes. Thus, $f_r = 1$. The step size is estimated to be the distance a particle can drift within a decorrelation time, thus $\Delta r \sim v_{\rm d}\Delta\tau$, where $v_{\rm d} \sim v_t\rho/R$ is the typical drift speed. The radial drift speed changes direction from the bottom half to the top half of the torus for having $\sin\theta$ dependence. The decorrelation time is determined by the time for this to occur for particles diffusing along a magnetic field line through collisions, and is $\Delta\tau \sim (Rq)^2\left(\nu/v_t^2\right)$. The typical diffusion coefficient is then

$$D_{\rm ps} \sim \nu\rho^2q^2, \tag{1.1.7}$$

which is larger than $D_{\rm c}$ by a factor of q^2 for $q > 1$.

The plateau regime is dominated by the resonant particles that have $v_\parallel \sim 0$ in the sense that they suffer persistent radial drift. This drift is interrupted by the collisions. Thus, $\Delta r \sim v_{\rm d}\Delta\tau$. The fraction of the particles that can participate the transport processes is determined by $v_t\Delta(v_\parallel/v)/Rq < \nu/\left[\Delta(v_\parallel/v)\right]^2$. Physically, this inequality implies that the time for the resonant particles to move from the bottom half to the top half of the torus so that the radial drift reverses the direction must be less than the effective collision frequency to scatter out of the resonance layer [6, 7]. This yields $f_r \sim [\Delta(v_\parallel/v)] \sim \{\nu/[v_t/(Rq)]\}^{1/3}$, and $(\Delta\tau)^{-1} \sim \nu/\left[\Delta(v_\parallel/v)\right]^2$. Thus, the typical diffusion coefficient scales as

$$D_{\rm p} \sim \frac{v_{\rm d}^2}{v_t/(Rq)}. \tag{1.1.8}$$

The plateau regime is limited by $\nu < v_t/(Rq)$, which implies that the particle motion along the magnetic field line is no longer diffusive, but $\nu_* > 1$ to prevent the formation of the trapped particles. It is obvious that the plateau regime can exist only in large aspect ratio tokamaks.

Externally driven electric current parallel to the magnetic field line is carried by particles that are circulating around the torus. In the banana regime, trapped particles cannot circulate around the torus. Thus, electric conductivity is reduced by a fraction proportional to the fraction of the trapped particles in the large aspect ratio limit. When all particles are trapped in the unity aspect ratio tori, electric conductivity must vanish. It should be noted, however, that trapped particles can carry bootstrap current which is diamagnetic in nature.

Bootstrap current is analogous to the diamagnetic current. It is driven by the radial density gradient and is in the direction of the magnetic field. Trapped particles move along the magnetic field line with a speed of the order $\sqrt{\varepsilon}v_t$. Because plasma density is not uniform in the radial direction, there is a parallel fluid flow $V_{||}$ of the order of $V_{||} \sim -\sqrt{\varepsilon}\left(\sqrt{\varepsilon}v_t\right)\sqrt{\varepsilon}\rho_{\rm p}N^{-1}\,{\rm d}N/{\rm d}r$ due to the finite orbit width of the trapped particles. The first $\sqrt{\varepsilon}$ in $V_{||}$ denotes the fraction of the trapped particles. This parallel flow is damped by the bumpiness of the magnetic field strength along the magnetic field line with an effective damping rate $\nu_{\rm eff} \sim \nu/\varepsilon$. So far the argument is independent of the plasma species. For electrons, $\nu \sim \nu_{\rm ei}$, the electron–ion collision frequency. In the electron momentum equation, i.e. Ohmic law, this momentum dissipation must be balanced by the friction force term that scales as $\sim\nu_{\rm ei}J_{||}/Ne$. The parallel current generated is the bootstrap current and is of the order of

$$J_{\rm b} \sim -\sqrt{\varepsilon}\frac{cT}{B_{\rm p}}\frac{{\rm d}N}{{\rm d}r}. \tag{1.1.9}$$

The bootstrap current exists even in the unity aspect ratio tokamaks.

Bootstrap current, Ware pinch, and the modification on the electric conductivity have similar collision frequency dependence. These physics quantities depend strongly on the formation of the collisionless trapped particle trajectories. Thus, they have the largest values in the banana regime where $\nu_* < 1$ and diminish when the collision frequency increases. Schematic collision frequency dependence for these quantities is shown in figure 4.

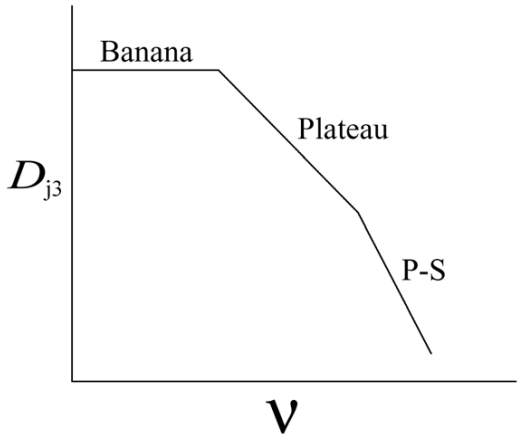

Figure 4. Transport coefficient D_{j3} as a function of collision frequency in a log–log plot is shown.

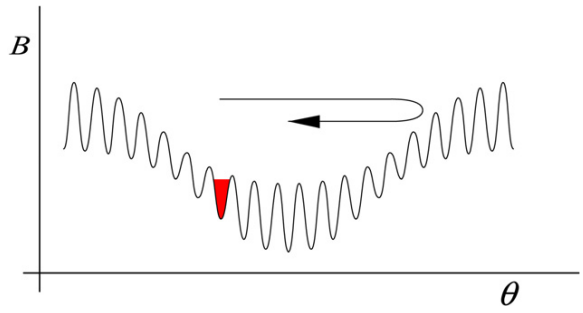

Figure 5. Schematic magnetic field strength B variation along a magnetic field line in a stellarator. The red shaded region indicates particles trapped in a helical well. The arrow indicates particles trapped in a toroidal magnetic field well.

1.2. Brief summary of neoclassical transport fluxes in stellarators

All axisymmetric tokamaks have the same magnetic geometry. However, not all stellarators are equivalent. The simplest model magnetic field for a classic stellarator is [3.4,26]

$$B = B_0 \left(1 - \varepsilon_t \cos\theta - \varepsilon_h \cos\alpha\right), \qquad (1.2.1)$$

where ε_t is the Fourier amplitude for the toroidal harmonic, ε_h is the amplitude of the helical harmonic, $\alpha = m\theta - n\zeta$ is the helical angle, and m and n are integers denoting poloidal and toroidal mode numbers. Usually, in stellarators, $nq > m$. Modern real stellarators have a magnetic field spectrum that is more complicated than that shown in equation (1.2.1) even for real quasi-symmetric stellarators [27]. There is only one class of trapped particles in tokamaks. However, there can be at least two classes of trapped particles in stellarators. Particles can be trapped either in a toroidal magnetic field well or in a helical magnetic field well, as shown in figure 5.

The typical collision frequency dependence of diffusion coefficients for stellarators is shown in figure 6 [3]. This dependence is generic for non-axisymmetric tori.

The transport mechanisms for the Pfirsch–Schlüter regime and the plateau regime in stellarators are the same as those in tokamaks except that there are more than one harmonic in the magnetic field spectrum. The contribution from each harmonic to the diffusion coefficients is additive in these two regimes. This is because plasmas are collisional, the effects of each harmonic on particle motion are decoupled from each other.

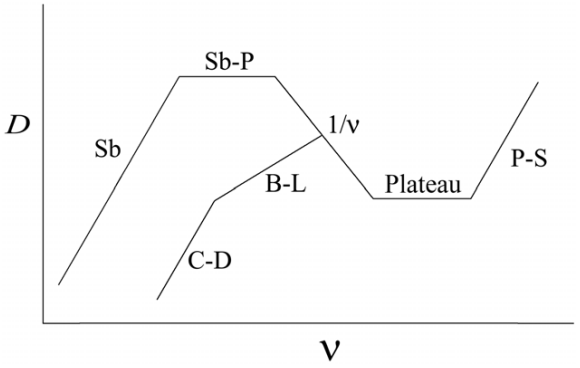

Figure 6. Schematic collision frequency dependence of diffusion coefficients in a stellarator in a log–log plot.

It is important to note that collisionless trapped particles, i.e. bananas, do not drift off the magnetic surface upon averaging over their trajectories in axisymmetric tokamaks because of the toroidal symmetry, as can be seen in figure 3. However, this is no longer the case once the toroidal symmetry is broken as is the case in stellarators and tokamaks with error fields or MHD activities. Typical drift orbits in stellarators, e.g. a superbanana, a circulating banana and an orbit that underwent collisionless detrapping/retrapping, are shown in figure 7. These drift orbits can have a width much larger than the poloidal gyro-radius and cause significant transport losses when normalized magnitudes of the symmetry breaking components in the magnetic field spectrum are fraction of a per cent.

When $\varepsilon_h > \varepsilon_t$, and $nq > m$, as the collision frequency decreases, particles trapped in the helical variation of the magnetic field become collisionless first. These helically trapped particles drift off the magnetic surface under the influence of the toroidal variation of the magnetic field, i.e. the $\varepsilon_t \cos\theta$ variation in equation (1.2.1).

In the $1/\nu$ regime [3, 4], the collision frequency is high enough so that helically trapped particles cannot complete their drift trajectories before being collisionally scattered out of the helical magnetic well. Thus, the step size is $\Delta r \sim v_d \Delta\tau$, and $\Delta\tau \sim (\nu/\varepsilon_h)^{-1}$. An additional $1/\varepsilon_h$ factor in $\Delta\tau$ appears because only a small change in $\Delta(v_\parallel/v) \sim \sqrt{\varepsilon_h}$ is adequate for trapped particles to scatter out of the helical well. The fraction of the particles that participate in the transport process is $f_r \sim \sqrt{\varepsilon_h}$. Recall that $v_d \sim v_t \rho/R$, the diffusion coefficient scales as

$$D \sim \left(\frac{cT}{eBr}\right)^2 \frac{\varepsilon_h^{3/2}\varepsilon_t^2}{\nu}. \qquad (1.2.2)$$

Of course, this $1/\nu$ scaling cannot persist forever.

When the collision frequency decreases even further, the poloidal drift motion cannot be ignored any more. The transport fluxes can be categorized as resonant and non-resonant fluxes depending on whether the poloidal drift speed vanishes or not along the drift trajectories. If poloidal drift

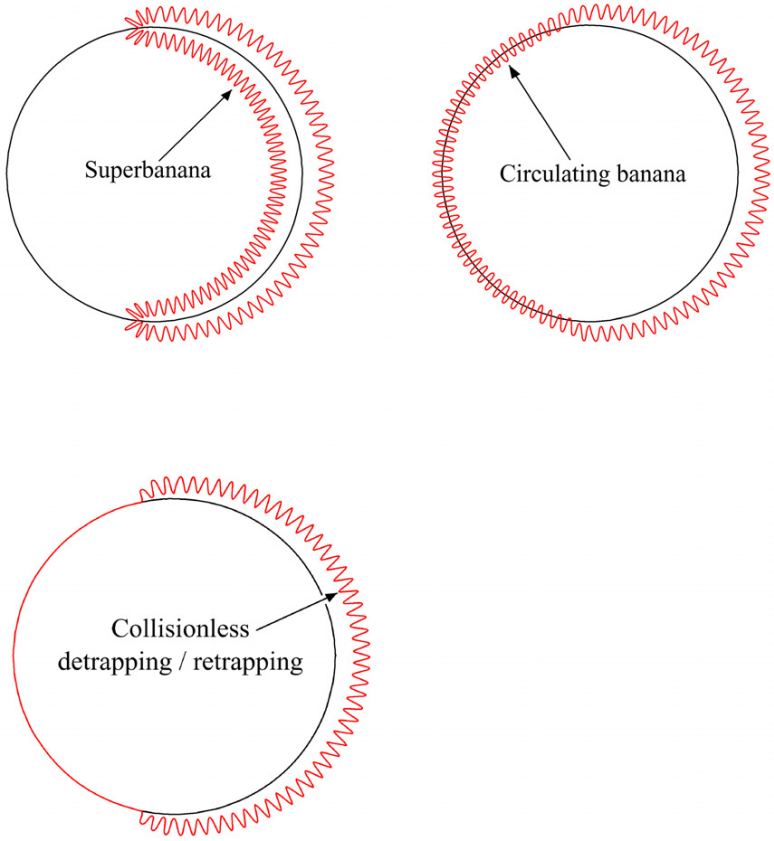

Figure 7. Schematic diagrams for typical orbits in a stellarator. The wriggles indicate the helically trapped particles.

vanishes at some point on the drift trajectories, these are resonant particles because the step size becomes unbounded at the resonance position. Of course, the unbounded step size is unphysical. In the superbanana plateau (Sb-P) regime, the resonance is broadened by collisions analogous to the plateau resonance in axisymmetric tori [6, 7]. In the superbanana (Sb) regime, the resonance is removed by the formation of the non-linear superbananas similar to the banana regime in the axisymmetric tokamaks [6, 7]. The transport coefficients in these two regimes have the same collision frequency dependences as those in the plateau and banana regimes in axisymmetric tokamaks, respectively, but with much larger magnitudes due to larger step sizes. If the poloidal drift does not vanish anywhere along the drift trajectories, particles are not resonant. In that case, it is the particles in the vicinity of the helically trapped and untrapped boundary that dominate the transport processes. These particles can become detrapped or retrapped either through collisions or even without collisions. If the collisional effects dominate, the transport coefficients scales as $\sqrt{\nu}$, a typical scaling resulting from the boundary layer (B-L) analysis [3, 4]. In non-axisymmetric tori, drift orbits can change their topology even without collisions because the second adiabatic invariant J_2 is no longer a good invariant quantity [28]. The diffusion coefficients are still proportional to the collision frequency in this collisionless detrapping (C-D) regime [3].

1.3. Collision operator

The neoclassical theory for non-axisymmetric toroidal plasmas is to solve the drift kinetic equation for the perturbed distribution function to calculate transport coefficients. The equation for each plasma species is [29]

$$\frac{\partial f}{\partial t} + (v_\parallel \boldsymbol{n} + \boldsymbol{v}_\mathrm{d}) \cdot \nabla f + e v_\parallel E_{||}^{(A)} \frac{\partial f}{\partial E} = C\,(f)\,, \qquad (1.3.1)$$

where f is the particle distribution, $\boldsymbol{n}$ is the unit vector in the direction of $\boldsymbol{B}$, $\boldsymbol{v}_\mathrm{d}$ is the drift velocity, $E = Mv^2/2 + e\Phi$ is the energy of the particles, Φ is the electrostatic potential, inductive parallel electric field $E_{||}^{(A)} = -c^{-1}\boldsymbol{n} \cdot \partial A/\partial t$, $\boldsymbol{A}$ is the vector potential, and $C\,(f)$ is the Coulomb collision operator. The independent variables for equation (1.3.1) are $(E, \mu, \boldsymbol{x})$, where $\boldsymbol{x}$ denotes spatial coordinates. The subscripts that indicate plasma species for species-dependent quantities are suppressed for the sake of simplicity. When plasma species in physics quantities needs to be specified, the subscript i is used for ions and e for electrons.

The theory is to solve the linear version of equation (1.3.1) by expressing the particle distribution f as

$$f = f_\mathrm{M} + f_1, \qquad (1.3.2)$$

where

$$f_\mathrm{M} = \frac{N}{\pi^{3/2} v_\mathrm{t}^3} \exp\left(-v^2/v_\mathrm{t}^2\right) \qquad (1.3.3)$$

is the equilibrium Maxwellian distribution function, and f_1 is the perturbed distribution function. Thus, $C(f) = C(f_1)$ because $C(f_M) = 0$ when the temperature equilibration between species is neglected. The operator $C(f_1)$ is an integral–differential operator that makes equation (1.3.1) difficult to solve. An approximate collision operator that can yield accurate transport coefficients is adopted in this review for the illustration purposes, and it is [30]

$$C_{ab}(f_{a1}) = \nu_D^{ab}\frac{Mv_{||}}{B}\frac{\partial}{\partial\mu}v_{||}\mu\frac{\partial f_{a1}}{\partial\mu} + \Delta\nu^{ab}\frac{v_{||}u_{a1}}{v^2}f_{aM} + \nu_s^{ab}\frac{2v_{||}r_{ba}}{v_{ta}^2}f_{aM}, \quad (1.3.4)$$

where the subscript that denotes species is restored, C_{ab} denotes the test particle species a colliding with the field particle species b. The first term on the right side of equation (1.3.4) is the pitch angle scattering operator. The deflection frequency ν_D^{ab} is defined as $\nu_D^{ab} = \nu_{ab}[\Phi(v/v_{tb}) - G(v/v_{tb})]/(v/v_{ta})^3$, where the basic relaxation frequency $\nu_{ab} = 4\pi N_b(e_a e_b)^2 \ln\Lambda/\left(v_{ta}^3 M_a^2\right)$, $\ln\Lambda$ is the Coulomb logarithm, the Chandrasekhar function is $G(x) = \left[\Phi(x) - x\Phi'(x)\right]/\left(2x^2\right)$, and $\Phi(x)$ is the error function. (In this review, when Φ has a dimensionless argument, it denotes error function, and when it has an argument that is the position it is the electrostatic potential.) The second term on the right-hand side of equation (1.3.4) is the momentum restoring term from the test particle operator, where $\Delta\nu^{ab} = \nu_D^{ab} - \nu_s^{ab}$. The slowing down frequency ν_s^{ab} is $\nu_s^{ab} = \nu_{ab}(2T_a/T_b)(1 + M_b/M_a)G(v/v_{tb})/(v/v_{ta})$, and $u_{a1} = \int d(3v_{\|}/2v)v_{\|}f_{a1}/f_{aM}$. The third term is the momentum restoring from the field particle distribution, where $r_{ba} = (3/2)\int d\boldsymbol{v}M_b v_{||}\nu_s^{ba}f_{b1}/\int d\boldsymbol{v}M_a\nu_s^{ab}(v/v_{ta})^2 f_{aM}$.

The eight-moment equation approach to be discussed is not sensitive to the details of the collision operator. The model operator displayed here is to facilitate the illustrations of the theory.

1.4. Summary of moment approach to transport theory

The moment approach to transport theory provides a means to determine plasma flows and as a consequence the transport fluxes. The roles of plasma flows in transport fluxes are explicit. Thus, not only the transport fluxes, but also plasma flows under various physics conditions are of interest in the theory. For large aspect ratio tokamaks, analytic expressions for plasma flows and transport coefficients can be obtained. However, for real stellarators, it is often difficult to have compact analytic expressions for transport fluxes in the low-collisionality regimes for a general magnetic field spectrum. For those cases, plasma flows and transport fluxes for classic stellarators are discussed to illustrate the physics involved.

The moment approach to the transport theory can be summarized in figure 8. The momentum equation is used to determine the plasma flows on the magnetic surface that make plasmas ambipolar. These plasma flows are substituted into the flux–force relation to determine the transport fluxes. The viscous forces in the momentum equation are calculated from the solution of the kinetic equation to close the moment equations.

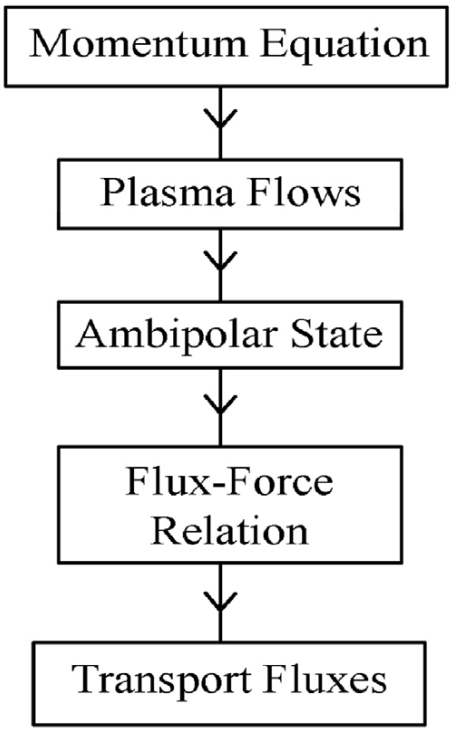

Figure 8. Flow chart for the moment approach.

1.5. Synopsis

The review concerns neoclassical transport processes, including quasilinear theory, formulated using the neoclassical methodology and turbulence suppression theory to provide a theoretical tool to understand plasma transport behaviour in a non-axisymmetric torus with an axisymmetric tokamak as the special case. Because the focus of the theory part of the review is on the analytic neoclassical methodology, only works that are directly related to the development of the moment equation approach are referenced, and numerical works on neoclassical theory are not reviewed here. The subjects and references chosen are biased towards those that are needed in the modelling and understanding of the neoclassical transport phenomena observed in experiments. Thus, they are by no means extensive. The part on the experiments is limited to the review on the experimental tests of neoclassical plasma viscosity and plasma flows in non-axisymmetric tori.

The moment equations are needed for the development of the transport theory. They are employed to construct equilibrium flow patterns and current on the magnetic surface, and the flux–force relation. These equations are displayed in section 2.

Transport theory is to describe the particle, momentum and energy losses in equilibrium plasmas. The standard MHD equilibrium is briefly discussed in section 3. The emphasis is on the flow patterns and the expression for plasmas current in non-axisymmetric tori. These flows and current are to be determined in the transport theory.

The key to the transport theory is the flux–force relation that relates the transport fluxes in the even velocity moment equations to forces in the odd velocity moment equations. Both

moment and kinetic derivations are presented in section 4. The relation together with the momentum equation is used to demonstrate that the ambipolar state is reached when two linearly independent components of momentum equation on the magnetic surface are relaxed. An example of the poloidal flow damping or relaxation in the banana regime is employed to show the relation between flow damping and the so-called intrinsically ambipolar transport in axisymmetric tokamaks. It also demonstrates that the radial electric field is first established on a short time scale of the order of the poloidal flow damping time and further evolves relatively slowly at the transport time scale. Thus, it evolves at two distinct time scales in tokamaks. In addition, it is shown that when neoclassical transport losses are improved so are the anomalous losses by considering the relation between the flow damping rate and improvement of the anomalous losses.

The equivalence between the variational and moment approaches to neoclassical transport theory is illustrated in section 5. The reason for the introduction of the parallel flow into the solution of the kinetic equation is discussed.

The neoclassical transport theory for axisymmetric tokamaks is reviewed in section 6. Analytic expressions for particle trajectories both in the region away from and in the vicinity of the magnetic axis are calculated from conservations of canonical toroidal momentum and energy together with the invariant of the magnetic moment. These expressions are used in a systematic method that calculates the parallel component of the plasma viscous forces in all regimes. Specific physics included are transport theory in unity aspect ratio tokamaks in the Pfirsch–Schlüter regime, effects of orbit squeezing, effects of finite banana width, non-linear plasma viscosity, transport theory in the vicinity of the magnetic axis and shock formation. The application of the theory to low confinement mode (L-mode) to H-mode transition is also presented.

In section 7, the methodology of the neoclassical theory is employed to formulate the quasilinear theory to describe transport losses, including particle, energy and momentum losses, associated with turbulent fluctuations. The turbulent suppression theory is also discussed to complement the neoclassical theory.

Real tokamaks are not axisymmetric. The transport consequences in tokamaks with weak broken symmetry are reviewed in section 8. The theory is relevant to the use of the external coils to control plasma flows and MHD stabilities. All known collisionality regimes are discussed. Approximate analytic expressions that join all asymptotic limits of the solutions of the bounce averaged drift kinetic equation are presented to facilitate modelling of toroidal flow in experiments.

The neoclassical transport theory for stellarators is reviewed in section 9. As the collision frequency decreases, the model for the magnetic field spectrum used in the theory becomes simpler due to the inability to have compact analytic expressions for particle trajectories in real stellarators, and the difficulties to solve the drift kinetic equation. However, more detailed mathematical procedures used to calculate transport fluxes than previous reviews [3, 31] are presented. The key developments after those reviews [3, 31] are the derivation of the flux–force relation, and its use to calculate the plasma flow, radial electric field and transport fluxes. An approximate expression for the bootstrap current for an arbitrary magnetic field spectrum in the low-collisionality regime is also obtained by solving the drift kinetic equation approximately with the aid of the solution of the moment equations.

Neoclassical radial thermal transport does not play an important role in optimized stellarator or heliotron devices as it does in tokamaks. The experimentally evaluated thermal diffusivity is much larger than that predicted by neoclassical theory even in plasmas with electron internal transport barriers, where the turbulence transport is suppressed to some extent [32, 33]. However, neoclassical transport has a significant impact in determining the poloidal and toroidal viscosity in axisymmetric toroidal plasmas and the radial electric field in helical systems. The toroidal viscosity evaluated in experiments is comparable to the neoclassical toroidal viscosity (NTV) in helical plasmas. The transition of the radial electric field from the electron-root to ion-root or vice versa has been found to be consistent with the neoclassical predictions [34–36]. Therefore, it is quite important and interesting to compare the plasma flow observed in experiments with that predicted from neoclassical theory. Experimental results on neoclassical poloidal and toroidal viscosity in stellarators are discussed in section 10.

Neoclassical transport effects due to low-level non-axisymmetric magnetic field perturbations ($\delta B/B \sim \mathrm{O}(10^{-3})$) in otherwise axisymmetric systems (e.g. tokamaks) have been appreciated theoretically since the inception of the theory. However, it was not until the last decade that NTV was appreciated as the cause for plasma rotation alteration by non-resonant field perturbations and other important effects observed in dominantly axisymmetric devices [37–39]. Early theoretical studies discounted NTV as being too weak in theory to reproduce experiment. Eventually, research showed that NTV theory could indeed quantitatively explain experimental observations in tokamaks [40, 41]. A review of the evolution of this appreciation of NTV in tokamaks with corresponding experimental observations is given in section 11.

In section 12, a physics mechanism for the origin of the momentum for intrinsic plasma rotation, which is ubiquitous in theories and experiments discussed, is illustrated. A summary is also given.

2. Moment equations

Transport theory is used to derive the closure relations for quantities in the fluid moment equations. The moment equations are derived by taking the velocity moments of the kinetic equation [6, 7]. In the eight-moment approach, the moment equations for the eight independent variables: plasma density N, plasma pressure p (or plasma temperature T), fluid mass velocity $\boldsymbol{V}$ and heat flux $\boldsymbol{q}$ are required. The theory will not address the effects of sources. Thus, all sources are neglected.

The kinetic equation for the particle distribution function f for each plasma species is

$$\frac{\partial f}{\partial t} + \boldsymbol{v}\cdot\nabla f + \frac{e}{M}\left(\boldsymbol{E} + \frac{1}{c}v\times\boldsymbol{B}\right)\cdot\frac{\partial f}{\partial \boldsymbol{v}} = C\,(f)\,, \qquad (2.1)$$

where $\boldsymbol{v}$ is the particle velocity. Taking the $\boldsymbol{v}^0$, $\boldsymbol{v}$, $Mv^2/2$ and $Mv^2\boldsymbol{v}/2$ moments of equation (2.1) yields the density

conservation equation

$$\frac{\partial N}{\partial t} + \nabla \cdot (N\boldsymbol{V}) = 0, \tag{2.2}$$

the momentum equation

$$NM\frac{\mathrm{d}\boldsymbol{V}}{\mathrm{d}t} = Ne\left(\boldsymbol{E} + \frac{1}{c}\boldsymbol{V}\times\boldsymbol{B}\right) - \nabla p - \nabla\cdot\overleftrightarrow{\pi} + \boldsymbol{F}_1, \tag{2.3}$$

the energy conservation law

$$\frac{\partial}{\partial t}\left(\frac{3}{2}p + \frac{1}{2}NMV^2\right) + \nabla \cdot\left[\boldsymbol{q} + \left(\overleftrightarrow{\pi} + p\,\overleftrightarrow{I}\right)\cdot\boldsymbol{V} + \frac{1}{2}NMV^2\boldsymbol{V} + \frac{3}{2}p\boldsymbol{V}\right] = Q + (Ne\boldsymbol{E} + \boldsymbol{F}_1)\cdot V, \tag{2.4}$$

and the energy flux balance equation

$$\frac{\partial \boldsymbol{Q}}{\partial t} = \frac{e}{M}E\cdot\left[\left(\frac{5}{2}p + \frac{1}{2}NMV^2\right)\overleftrightarrow{I} + \overleftrightarrow{\pi} + NMV\boldsymbol{V}\right] + \frac{1}{c}\frac{e}{M}\boldsymbol{Q}\times\boldsymbol{B} - \nabla\cdot\overleftrightarrow{r} + \frac{\boldsymbol{T}}{M}\left(\frac{5}{2}\boldsymbol{F}_1 + \boldsymbol{F}_2\right), \tag{2.5}$$

where $\mathrm{d}/\mathrm{d}t = \partial/t + \boldsymbol{V}\cdot\nabla$, plasma density $N = \int \mathrm{d}\boldsymbol{v} f$, plasma flow velocity $\boldsymbol{V} = \int \mathrm{d}\boldsymbol{v} f\boldsymbol{v}/N$, plasma pressure $p = \int \mathrm{d}\boldsymbol{v}\left(Mu^2/3\right) f$, $\boldsymbol{u} = \boldsymbol{v} - \boldsymbol{V}$, viscous tensor $\overleftrightarrow{\pi} = \int \mathrm{d}\boldsymbol{v} M\left(\boldsymbol{u}\boldsymbol{u} - u^2\,\overleftrightarrow{I}/3\right) f$, $\overleftrightarrow{I}$ is a unit tensor, friction force $\boldsymbol{F}_1 = \int \mathrm{d}\boldsymbol{v} M\boldsymbol{v} C(f)$, $\boldsymbol{q} = \int \mathrm{d}\boldsymbol{v}\boldsymbol{u}\left(Mu^2/2\right) f$, heat friction force $\boldsymbol{F}_2 = \int \mathrm{d}\boldsymbol{v} M\boldsymbol{v}\left(x^2 - 5/2\right) C(f)$, $x = v/v_{\mathrm{t}}$, collisional energy exchange $Q = \int \mathrm{d}\boldsymbol{v}\left(Mu^2/2\right) C(f)$, the energy flux $\boldsymbol{Q} = \int \mathrm{d}\boldsymbol{v}(Mv^2\boldsymbol{v}/2) f = \boldsymbol{q} + \left(\overleftrightarrow{\pi} + p\,\overleftrightarrow{I}\right)\cdot\boldsymbol{V} + NMV^2\boldsymbol{V}/2 + 3p\boldsymbol{V}/2$, and the energy stress tensor $\overleftrightarrow{r} = \int \mathrm{d}\boldsymbol{v}\left(Mv^2/2\right)\boldsymbol{v}\boldsymbol{v} f$. The density conservation law for the Coulomb collision operator, i.e. $\int \mathrm{d}\boldsymbol{v} C(f) = 0$, has been used in deriving equations (2.2)–(2.5). Note that for energy flux $\boldsymbol{Q}$ and the energy stress tensor $\overleftrightarrow{r}$, the mass flow $\boldsymbol{V}$ has not been subtracted from the particle velocity $\boldsymbol{v}$. Because only the transport theory for the subsonic mass flow, i.e. $|\boldsymbol{V}|/v_{\mathrm{t}} < 1$, will be discussed, whether $\boldsymbol{V}$ has been subtracted from the particle velocity $\boldsymbol{v}$ is not crucial.

An alternative form for the momentum equation, i.e. equation (2.3) is [6]

$$\frac{\partial}{\partial t}(NM\boldsymbol{V}) = Ne\left(\boldsymbol{E} + \frac{1}{c}\boldsymbol{V}\times\boldsymbol{B}\right) - \nabla\cdot\overleftrightarrow{\boldsymbol{P}} + \boldsymbol{F}_1, \tag{2.6}$$

where the stress tensor $\overleftrightarrow{\boldsymbol{P}} = \int \mathrm{d}\boldsymbol{v} M\boldsymbol{v}\boldsymbol{v} f$. The energy flux balance equation can also be cast into a form to emphasize the heat flux balance as

$$\frac{\mathrm{d}\boldsymbol{q}}{\mathrm{d}t} = \frac{e}{Mc}\boldsymbol{q}\times\boldsymbol{B} - \frac{5}{2}\nabla T\cdot\left(\overleftrightarrow{\pi} + p\,\overleftrightarrow{I}\right) - \frac{1}{M}\nabla T\cdot\left(\overleftrightarrow{\Theta} + \vartheta\,\overleftrightarrow{I}\right) - \frac{T}{M}\nabla\cdot\left(\overleftrightarrow{\Theta} + \vartheta\,\overleftrightarrow{I}\right) + \frac{1}{NM}\left(\nabla\cdot\overleftrightarrow{\pi} + \nabla p - \boldsymbol{F}_1\right)\cdot\overleftrightarrow{\pi} - \boldsymbol{q}\cdot\nabla\boldsymbol{V} - \frac{5}{3}\boldsymbol{q}\nabla\cdot\boldsymbol{V} - \overleftrightarrow{\Xi}:\nabla\boldsymbol{V} + \frac{T}{M}\boldsymbol{F}_2, \tag{2.7}$$

where $\overleftrightarrow{\Theta} = \int \mathrm{d}\boldsymbol{u} M\boldsymbol{u}(\boldsymbol{u}\boldsymbol{u} - \overleftrightarrow{I}\,u^2/3) f$, and $\vartheta = \int \mathrm{d}\boldsymbol{u}(Mu^2/2T - 5/2)M\,\overleftrightarrow{I}\,(u^2/3) f$.

For subsonic plasma flow, equations (2.3) and (2.5) can be simplified to

$$NM\frac{\partial \boldsymbol{V}}{\partial t} = Ne\left(\boldsymbol{E} + \frac{1}{c}\boldsymbol{V}\times\boldsymbol{B}\right) - \nabla p - \nabla\cdot\overleftrightarrow{\pi} + \boldsymbol{F}_1 \tag{2.8}$$

and

$$\frac{\partial \boldsymbol{Q}}{\partial t} = \frac{e}{M}\boldsymbol{E}\cdot\left(\frac{5}{2}p\,\overleftrightarrow{I} + \overleftrightarrow{\pi}\right) + \frac{1}{c}\frac{e}{M}\boldsymbol{Q}\times B - \nabla\cdot\overleftrightarrow{r} + \frac{T}{M}\left(\frac{5}{2}\boldsymbol{F}_1 + \boldsymbol{F}_2\right), \tag{2.9}$$

where $\boldsymbol{Q}$ reduces to $\boldsymbol{Q} = \boldsymbol{q} + 5p\boldsymbol{V}/2$.

In the eight-moment approach, quantities $\boldsymbol{F}_1$, $\boldsymbol{F}_2$, $\overleftrightarrow{\pi}$ and $\overleftrightarrow{r}$ as functions of the eight independent variables are derived from the solution of the kinetic equation to close the moment equations. The solutions of the odd velocity moment equations, i.e. the momentum and heat flux balance equations, determine plasma flows and, thus, the transport fluxes, which are employed in the even velocity moment equations of the density and energy conservation laws to determine the plasma density and temperature profiles.

3. Plasma equilibrium

To confine plasmas, all the forces acting on them must be balanced to reach an equilibrium. This involves solving the moment equations, Maxwell's equations, together with the boundary conditions to determine self-consistent magnetic field, electric field, current density, mass flow and heat flow. This is a formidable task for toroidal plasmas. To accomplish this goal, a gyro-radius ordering is commonly employed. The small parameter in the ordering is ρ/L_n where L_n is the typical scale length of the plasma parameters [6, 7]. Note that the gyro-radius here can be replaced by Δr, the generic radial width of the particle orbits. In any plasma confinement device for thermonuclear fusion purpose, Δr must be much smaller than L_n to avoid rapid convective or direct losses. The force balance is maintained at each order in the ordering scheme. In addition, transport ordering is adopted so that equilibrium plasma density and temperature evolve at a rate of the order of $\nu\,(\rho/L_n)^2$ [6, 7].

From equations (2.3) and (2.5), the zeroth-order (in gyro-radius) force balance equations for each plasma species are

$$Ne\left(\boldsymbol{E} + \frac{1}{c}\boldsymbol{V}\times\boldsymbol{B}\right) = \nabla p \tag{3.1}$$

and

$$\frac{e}{Mc}\boldsymbol{q}\times\boldsymbol{B} = \frac{5}{2}\frac{p}{M}\nabla T. \tag{3.2}$$

In the direction of the magnetic field $\boldsymbol{B}$, the solutions for equations (3.1) and (3.2) imply that the equilibrium pressure p, electrostatic potential Φ and the temperature T are flux functions, i.e. $p = p(\chi)$, $\Phi = \Phi(\chi)$ and $T = T(\chi)$, where χ is the poloidal magnetic flux divided by 2π. Thus, equilibrium plasma density N is also a flux function.

Summing equation (3.1) over plasma species yields the force balance equation for plasmas

$$\frac{1}{c}\boldsymbol{J}\times\boldsymbol{B} = \nabla P, \tag{3.3}$$

where $P = \sum_j p_j$ is total plasma pressure, and subscript here j indicates plasma species.

3.1. Magnetic coordinates

Magnetic coordinates in which the magnetic field are straight lines are employed to describe the nested magnetic surfaces. The magnetic field $\boldsymbol{B}$ can be represented as

$$\boldsymbol{B} = q\nabla\chi \times \nabla\theta + \nabla\zeta \times \nabla\chi, \tag{3.1.1}$$

where θ is the poloidal angle, ζ is the toroidal angle, and the safety factor $q(\chi) = \boldsymbol{B}\cdot\nabla\zeta/\boldsymbol{B}\cdot\nabla\theta$ which is the same as the inverse rotational transform $2\pi/\iota$. The Jacobian $\sqrt{g} = (\nabla\chi\times\nabla\theta\cdot\nabla\zeta)^{-1} = 1/\boldsymbol{B}\cdot\nabla\theta$ is arbitrary. For Hamada coordinates [42], $\sqrt{g}$ is a flux function. For Boozer coordinates [43], it is proportional to $1/B^2$. The poloidal flux χ plays the role of the radial coordinate analogous to that in the polar coordinates. The notation θ and ζ denote poloidal and toroidal angles in the coordinates of interest. They are different in different coordinate systems.

The conventional definition for the Jacobian in Hamada coordinates (V,θ,ζ) is $\sqrt{g_{\mathrm{H}}} = (\nabla V\times\nabla\theta\cdot\nabla\zeta)^{-1} = 1$, where V is the volume enclosed inside the magnetic surface divided by $4\pi^2$ [42]. In terms of (V,θ,ζ), the magnetic field in equation (3.1.1) can be expressed as

$$\boldsymbol{B} = \psi'\nabla V\times\nabla\theta - \chi'\nabla V\times\nabla\zeta, \tag{3.1.2}$$

where $\psi' = \boldsymbol{B}\cdot\nabla\zeta$, ψ is the toroidal flux divided by 2π, $\chi' = \boldsymbol{B}\cdot\nabla\theta$, and prime denotes $\mathrm{d}/\mathrm{d}V$. In non-axisymmetric tori, Hamada coordinates are preferred coordinates for transport theory because not only the magnetic field and the current density $\boldsymbol{J}$ are straight lines, but also the incompressible flow velocity $\boldsymbol{V}$ and heat flow $\boldsymbol{q}$. It is easier to express these quantities in Hamada coordinates because there are no complicated angle dependences in these quantities.

The standard axisymmetric tokamak coordinates can be obtained from equation (3.1.1) using the identity

$$\frac{\nabla\chi\times\nabla\theta}{\boldsymbol{B}\cdot\nabla\theta} = R^2\nabla\zeta. \tag{3.1.3}$$

to yield

$$\boldsymbol{B} = I\nabla\zeta + \nabla\zeta\times\nabla\chi, \tag{3.1.4}$$

where $I = R^2\nabla\zeta\cdot\boldsymbol{B}$. The angle ζ is the axisymmetric toroidal angle in the tokamak coordinates.

In this review, the Hamada coordinates are used in the transport theory for non-axisymmetric tori and the tokamak coordinates are used for axisymmetric tokamaks.

The covariant representation $\boldsymbol{B}$ is also useful and is [44, 45]

$$\boldsymbol{B} = G\nabla\theta + F\nabla\zeta - \tau\nabla\chi + \nabla\varphi, \tag{3.1.5}$$

where $F = F(\chi)$ is the poloidal current outside a magnetic surface multiplied by $2\pi c/4\pi$, $G = G(\chi)$ is the toroidal current inside a magnetic surface multiplied by $2\pi c/4\pi$, functions τ and φ satisfy [44]

$$\boldsymbol{B}\cdot\nabla\tau = 4\pi\frac{\mathrm{d}P}{\mathrm{d}\chi}\left(\frac{1}{\sqrt{g}}\frac{1}{\langle 1/\sqrt{g}\rangle} - 1\right), \tag{3.1.6}$$

and

$$\boldsymbol{B}\cdot\nabla\varphi = B^2 - \langle B^2\rangle - (G+Fq)\left(\frac{1}{\sqrt{g}} - \left\langle\frac{1}{\sqrt{g}}\right\rangle\right), \tag{3.1.7}$$

the angular brackets denote the magnetic flux surface average, which is defined as

$$\langle\cdot\rangle = \frac{\iint\sqrt{g}\,\mathrm{d}\theta\,\mathrm{d}\zeta\,(\cdot)}{\iint\sqrt{g}\,\mathrm{d}\theta\,\mathrm{d}\zeta}, \tag{3.1.8}$$

and the integration limits for θ and ζ integrals are from 0 to 2π. There are two identities related to the flux surface average are commonly used [6]; one is

$$\langle\boldsymbol{B}\cdot\nabla\boldsymbol{F}\rangle = 0, \tag{3.1.9}$$

and the other is

$$\langle\nabla\cdot\boldsymbol{F}\rangle = \frac{1}{V'}\frac{\partial}{\partial\chi}\left(V'\langle\boldsymbol{F}\cdot\nabla\chi\rangle\right), \tag{3.1.10}$$

where $V' = \int\mathrm{d}\theta\int\mathrm{d}\zeta\sqrt{g}$.

It is obvious that the symmetry property of a torus does not depend on the specific coordinates chosen because plasmas do not recognize coordinates. This simple concept is used in the development of the transport theory for non-axisymmetric tori [46]. The explicit mathematical proof is first shown in [44].

3.2. Plasma flows

The first-order plasma mass and heat flows that are perpendicular to the magnetic field are [6, 7]

$$\boldsymbol{V}_\perp = c\frac{\boldsymbol{B}\times\nabla\Phi}{B^2} + c\frac{\boldsymbol{B}\times\nabla p}{NeB^2}, \tag{3.2.1}$$

and

$$\boldsymbol{q}_\perp = \frac{5}{2}\frac{cp}{eB^2}\boldsymbol{B}\times\nabla T. \tag{3.2.2}$$

These flows are the standard $\boldsymbol{E}\times\boldsymbol{B}$ flow, diamagnetic flow and diamagnetic heat flow. The general forms for the mass flow $\boldsymbol{V}$ and heat flow $\boldsymbol{q}$ can then be expressed as

$$\boldsymbol{V} = V_{||}\boldsymbol{n} + \boldsymbol{V}_\perp, \tag{3.2.3}$$

and

$$\boldsymbol{q} = q_{||}\boldsymbol{n} + \boldsymbol{q}_\perp. \tag{3.2.4}$$

The first-order (in gyro-radius ordering) parallel flows $V_{||}$ and $q_{||}$ are not yet determined.

Note that both first-order flows $\boldsymbol{V}$ and $\boldsymbol{q}$ are on the magnetic surface, i.e., $\boldsymbol{V}\cdot\nabla\chi = 0$ and $\boldsymbol{q}\cdot\nabla\chi = 0$, and they are two-dimensional vectors. For good plasma confinement concepts, this should be the case so that plasma losses are higher order in the ρ/L_n ordering.

It is also important to realize that there are two unknowns to be determined to specify the first-order flow $\boldsymbol{V}$ completely. One is $V_{||}$, and the other is the radial electric field $-\nabla\Phi = -(\mathrm{d}\Phi/\mathrm{d}\chi)\nabla\chi$. Thus, two linearly independent equations are required. The two equations are two linearly independent components of the momentum equation. These equations and their relation to the ambipolarity will be discussed in section 4.

For subsonic mass flow [6, 7], $\boldsymbol{V}$ is incompressible, i.e.

$$\nabla\cdot\boldsymbol{V} = 0. \tag{3.2.5}$$

and can be expressed as [47]

$$V = V^\zeta\nabla\chi\times\nabla\theta - V^\theta\nabla\chi\times\nabla\zeta + \nabla\chi\times\nabla\eta_V, \tag{3.2.6}$$

where V^ζ and V^θ are functions of χ only, and η_V is a function of (χ, θ, ζ) that satisfies

$$\boldsymbol{B}\cdot\nabla\eta_V = \left(qV^\theta - V^\zeta\right)\left(\frac{1}{\sqrt{g}} - \left\langle\frac{1}{\sqrt{g}}\right\rangle\right). \tag{3.2.7}$$

Using equation (3.1), the standard radial force balance takes the form [47]

$$\left(qV^\theta - V^\zeta\right)\left\langle\frac{1}{\sqrt{g}}\right\rangle = c\Phi' + \frac{c}{Ne}p', \tag{3.2.8}$$

where prime denotes $\mathrm{d}/\mathrm{d}\chi$. In general, $V^\theta = \mathrm{d}V_\chi/\mathrm{d}\chi = V'_\chi$ and $V^\zeta = \mathrm{d}V_\psi/\mathrm{d}\chi = V'_\psi$, where V_χ and V_ψ are respectively the poloidal and toroidal velocity fluxes inside the magnetic surface divided by 2π. Usually, V^ζ and V^θ are not the contravariant components of the flow vector $\boldsymbol{V}$ in non-Hamada coordinates. In Hamada coordinates, using (V, θ, ζ) coordinates, η_V is a function of V only and

$$V = V^\zeta\nabla V\times\nabla\theta - V^\theta\nabla V\times\nabla\zeta, \tag{3.2.9}$$

where $V^\zeta = \mathrm{d}V_\psi/\mathrm{d}V$, and $V^\theta = \mathrm{d}V_\chi/\mathrm{d}V$ are contravariant components of the flow velocity. The velocity $\boldsymbol{V}$ is a straight line in Hamada coordinates.

In helically symmetric tori,

$$\sqrt{g}\boldsymbol{V}\cdot\nabla\alpha = mV^\theta - nV^\zeta, \tag{3.2.10}$$

is a flux function, or, explicitly,

$$\sqrt{g}\boldsymbol{V}\cdot\nabla\alpha = \frac{V_{||}}{B}(m-nq) + \frac{(mF+nG)cT}{eB^2}\left(\frac{p'}{p} + \frac{e\Phi'}{T}\right), \tag{3.2.11}$$

and in particular for $m = 1$ and $n = 0$, i.e. tokamaks,

$$\sqrt{g}\boldsymbol{V}\cdot\nabla\theta = V^\theta = \frac{V_{||}}{B} + \frac{FcT}{eB^2}\left(\frac{p'}{p} + \frac{e\Phi'}{T}\right) \tag{3.2.12}$$

is a flux function. In tokamak coordinates, $F = I$.

Similarly, the incompressible heat flux $\boldsymbol{q}$, i.e.

$$\nabla\cdot\boldsymbol{q} = 0, \tag{3.2.13}$$

can be represented as [47]

$$\boldsymbol{q} = q^\zeta\nabla\chi\times\nabla\theta - q^\theta\nabla\chi\times\nabla\zeta + \nabla\chi\times\nabla\eta_q, \tag{3.2.14}$$

where $q^\zeta(\chi) = \mathrm{d}q_\psi/\mathrm{d}\chi$, $q^\theta(\chi) = \mathrm{d}q_\chi/\mathrm{d}\chi$, q_ψ is the toroidal heat flux inside the magnetic surface divided by 2π, q_χ is the poloidal heat flux inside the magnetic surface divided by 2π, and η_q is a function of (χ, θ, ζ) that satisfies

$$\boldsymbol{B}\cdot\nabla\eta_q = \left(qq^\theta - q^\zeta\right)\left(\frac{1}{\sqrt{g}} - \left\langle\frac{1}{\sqrt{g}}\right\rangle\right). \tag{3.2.15}$$

Note that the scalar q denotes the safety factor. In Hamada coordinates, η_q is a flux function and $\boldsymbol{q}$ is a straight line, i.e.

$$\boldsymbol{q} = q^\zeta\nabla V\times\nabla\theta - q^\theta\nabla V\times\nabla\zeta, \tag{3.2.16}$$

where $q^\zeta = \mathrm{d}q_\psi/\mathrm{d}V$ and $q^\theta = \mathrm{d}q_\chi/\mathrm{d}V$ are, respectively, contravariant toroidal and poloidal components of $\boldsymbol{q}$. There is also a radial heat force balance equation

$$\left(qq^\theta - q^\zeta\right)\left\langle\frac{1}{\sqrt{g}}\right\rangle = \frac{5}{2}\frac{c}{e}pT'. \tag{3.2.17}$$

In helically symmetric tori,

$$\sqrt{g}\boldsymbol{q}\cdot\nabla\alpha = mq^\theta - nq^\zeta \tag{3.2.18}$$

is a flux function, or explicitly,

$$\sqrt{g}\boldsymbol{q}\cdot\nabla\alpha = \frac{q_{||}}{B}(m-nq) + \frac{5}{2}p\frac{(mF+nG)cT}{eB^2}\frac{T'}{T}, \tag{3.2.19}$$

and for tokamaks,

$$\sqrt{g}\boldsymbol{q}\cdot\nabla\theta = q^\theta = \frac{q_{||}}{B} + \frac{5}{2}p\frac{IcT}{eB^2}\frac{T'}{T} \tag{3.2.20}$$

is a flux function.

3.3. Magnetohydrodynamic (MHD) equilibrium

The equilibrium current density perpendicular to the equilibrium magnetic field $\boldsymbol{J}_\perp$, from equation (3.3), is

$$\boldsymbol{J}_\perp = c\frac{\boldsymbol{B}\times\nabla P}{B^2}. \tag{3.3.1}$$

The general form for the current density is then

$$\boldsymbol{J} = J_{||}\boldsymbol{n} + \boldsymbol{J}_\perp, \tag{3.3.2}$$

where the current density parallel to the magnetic field $J_{||}$ in equation (3.3.2) remains undetermined.

Equation (3.3), together with Ampere's law,

$$\nabla\times\boldsymbol{B} = \frac{4\pi}{c}\boldsymbol{J} \tag{3.3.3}$$

and the boundary conditions determine the MHD equilibrium for toroidal plasmas. The typical time scale for establishing MHD equilibrium is $(V_\mathrm{A}/L_\mathrm{A})^{-1}$, where V_A is the Alfvén speed, and L_A is the typical length scale of the torus. The radial force balance relation in equation (3.2.8) is established on this time scale.

In tokamaks because of the toroidal symmetry, the magnetic field lines form nested magnetic surfaces. The equilibrium magnetic surface can be calculated from the Grad–Shafranov equation [48, 49]

$$\Delta^*\chi = -II' - 4\pi R^2P', \tag{3.3.4}$$

for given pressure and current profiles, where $\Delta^*\chi = R^2\nabla\cdot\left(\nabla\chi/R^2\right)$.

In non-axisymmetric tori, in general, the nested magnetic surfaces do not rigorously exist [50]. To facilitate the development of the transport theory, the existence of the nested magnetic surfaces is assumed. There are computer codes that solve for the equilibrium configurations for non-axisymmetric tori. One of such codes is VMEC [51, 52].

From equation (3.3) and Ampere's law in (3.3.3), the current density $\boldsymbol{J}$ is [44]

$$\boldsymbol{J} = \frac{c}{4\pi}\left(\nabla G\times\nabla\theta + \nabla F\times\nabla\zeta - \nabla\tau\times\nabla\chi\right). \tag{3.3.5}$$

In Hamada coordinates, τ is a flux function, and $\boldsymbol{J}$ is a straight line. The current density in equation (3.3.5) satisfies

$$\nabla\cdot\boldsymbol{J} = 0, \tag{3.3.6}$$

as required by the quasi-neutrality of the plasmas.

3.4. Equilibrium parallel current density

The equilibrium current density that is parallel to the magnetic field has not yet been determined. Taking the $\nabla\theta$ component of equation (3.3.3) yields

$$\frac{J_{||}}{B} = -\frac{cF'}{4\pi} - \left[\frac{c}{4\pi}\frac{\langle B^2\partial\tau/\partial\zeta\rangle}{\langle B^2\rangle} + \frac{cP'}{\langle B^2\rangle}(I + \langle\partial\varphi/\partial\zeta\rangle)\right] + \frac{J_{\rm ps}}{B}, \tag{3.4.1}$$

where the Pfirsch–Schlüter current $J_{\rm ps}$ is defined as

$$\frac{J_{\rm ps}}{B} = -\frac{c}{4\pi}\left(\frac{\partial\tau}{\partial\zeta} - \frac{\langle B^2\partial\tau/\partial\zeta\rangle}{\langle B^2\rangle}\right) - cP'\left(\frac{F}{B^2} - \frac{F}{\langle B^2\rangle}\right) - cP'\left(\frac{1}{B^2}\frac{\partial\varphi}{\partial\zeta} - \frac{1}{\langle B^2\rangle}\left\langle\frac{\partial\varphi}{\partial\zeta}\right\rangle\right). \tag{3.4.2}$$

The Pfirsch–Schlüter current has the property that $\langle BJ_{\rm ps}\rangle = 0$. One can also take the $\nabla\zeta$ component of equation (3.3.3) and obtain an equivalent expression for the Pfirsch–Schlüter current. In the case of the toroidally symmetric tokamaks, the Pfirsch–Schlüter current in equation (3.4.2) yields the well-known expression [6, 7]

$$\frac{J_{\rm ps}}{B} = -cP'\left(\frac{I}{B^2} - \frac{I}{\langle B^2\rangle}\right), \tag{3.4.3}$$

in tokamak coordinates.

There is still an undetermined part of the parallel current density that does not vanish upon flux surface averaging, i.e. $\langle BJ_{||}\rangle \neq 0$. This is the bootstrap current [23, 24]. It is determined by the flux-surface-averaged electron momentum equation, i.e. Ohm's law, and the ion momentum equation

$$Ne\langle\boldsymbol{B}\cdot\boldsymbol{E}^{(A)}\rangle - \left\langle\boldsymbol{B}\cdot\nabla\cdot\overleftrightarrow{\pi}\right\rangle + \langle\boldsymbol{B}\cdot\boldsymbol{F}_1\rangle = 0, \tag{3.4.4}$$

in the direction of $\boldsymbol{B}$, where the subscripts that denote the species are omitted for the sake of simplicity [7]. These equations are coupled to the parallel heat flux balance equations through the coupling of the heat flows in the friction and viscous forces. The inductive electric field drives the Ohmic current and the flux-surface-averaged electron parallel viscous forces $\langle\boldsymbol{B}\cdot\nabla\cdot\overleftrightarrow{\pi}\rangle$ and $\langle\boldsymbol{B}\cdot\nabla\cdot\overleftrightarrow{\Theta}\rangle$ drive the bootstrap current [7]. Excluding the ohmic current, the parallel current density can thus be expressed as

$$\frac{J_{||}}{B} = \frac{\langle BJ_{||\rm b}\rangle}{\langle B^2\rangle} + \frac{J_{\rm ps}}{B}, \tag{3.4.5}$$

where $J_{||\rm b}$ is the bootstrap current density. The local bootstrap current is [7]

$$J_{||\rm b} = \frac{\langle BJ_{||\rm b}\rangle}{\langle B^2\rangle}B. \tag{3.4.6}$$

The poloidal magnetic field in stellarators is generated by the electric current in the external magnetic field coils. Thus, there is no need for the inductive plasma current to generate the field. In this sense, stellarators are steady-state plasma confinement devices. This is one of the merits often cited when comparing stellarators and tokamaks as thermonuclear fusion reactors. However, bootstrap current exists in stellarators as well due to finite plasma gradients [53, 54]. It has to be taken into account in MHD equilibrium calculations [55].

Conventional tokamaks are not intrinsically steady-state plasma confinement devices. The plasma current to create poloidal magnetic field in tokamaks is maintained by the inductive electric field induced by the time changing magnetic flux [56]. The discovery of the bootstrap current makes the steady-state operation possible if there is a seed current at the magnetic axis [24]. However, the existence of the potato bootstrap current at the magnetic axis makes the seed current unnecessary [57–59]. The bootstrap current allows tokamaks to become intrinsically steady-state plasma confinement devices as are stellarators [57–59].

4. Flux–force relation, momentum relaxation and ambipolarity

The relation between momentum relaxation (i.e. seeking the steady-state solutions of the momentum equation for plasma flows) and plasma ambipolarity in axisymmetric tokamaks and, in general, non-axisymmetric tori is not well known [60, 61]. However, these two important aspects of the plasma dynamics are intimately related. They need to be treated properly so that the momentum equation is satisfied. The relation that bridges these two important constraints is the flux–force relation. It is first derived for axisymmetric tokamaks in [9, 10] and is employed in the transport theory extensively in [7]. It is generalized for non-axisymmetric tori in [53].

4.1. Flux–force relation

The transport fluxes in the even velocity moment equations, and forces such as perturbed pressure force, viscous forces and friction forces in the odd velocity moment equations that are smaller than the equilibrium quantities by a factor of ρ/L_n have to be expressed in terms of the eight independent variables to close eight moment equations. The flux–force relation relates transport fluxes to these forces. The importance of the relation is that it identifies the transport fluxes calculated from the solution of the kinetic equation with the closure terms in the momentum and heat flux balance equations. This facilitates the determination of the self-consistent plasma flows including parallel flow and the radial electric field that satisfy the momentum equation. This shows that the self-consistent plasma rotation guarantees that the forces acting on the plasmas are balanced. This also indicates that the ambipolar state is related to steady-state solutions of the momentum equation for plasma flows.

There are two methods to derive the relation. One is to manipulate the moment equations [7, 9, 10] and the other is to use the kinetic definition for the transport fluxes [47]. These two approaches are equivalent of course.

4.1.1. Moment approach. Taking the $\boldsymbol{B}\times\nabla\chi$ component of the steady-state momentum equation in equation (2.8) yields the flux surface averaged particle flux, $\Gamma^\chi = \langle N\boldsymbol{V}\cdot\nabla\chi\rangle = \langle\overleftrightarrow{\Gamma}\cdot\nabla\chi\rangle$,

$$\Gamma^\chi = -\left\langle Nc\frac{\boldsymbol{E}\times\boldsymbol{B}\cdot\nabla\chi}{B^2}\right\rangle + \left\langle\frac{c}{eB^2}\boldsymbol{B}\times\nabla\chi\cdot\left(\boldsymbol{F}_1 - \nabla p - \nabla\cdot\overleftrightarrow{\pi}\right)\right\rangle. \tag{4.1.1.1}$$

Using a vector identity [6, 7, 47, 53]:

$$\boldsymbol{B}_{\mathrm{t}} = \frac{(\boldsymbol{B}_{\mathrm{t}}\cdot\boldsymbol{B})\,\boldsymbol{B}}{B^2} - \frac{\boldsymbol{B}\times\nabla\chi}{B^2}, \tag{4.1.1.2}$$

where $\boldsymbol{B}_t = \sqrt{g}\nabla\chi\times\nabla\theta$, to replace $\boldsymbol{B}\times\nabla\chi/B^2$ in equation (4.1.1.1), the particle flux can be further decomposed. With the help of the parallel momentum balance equation

$$Ne\boldsymbol{B}\cdot\boldsymbol{E} - \boldsymbol{B}\cdot\nabla p - \boldsymbol{B}\cdot\nabla\cdot\overleftrightarrow{\pi} + \boldsymbol{B}\cdot\boldsymbol{F}_{\mathrm{I}} = 0, \tag{4.1.1.3}$$

the particle flux is shown to consist of the Pfirsch–Schlüter flux

$$\Gamma^{\mathrm{ps}} = -\frac{c}{e}\left\langle\left(\frac{I_c}{B^2} - \frac{\langle I_c\rangle}{\langle B^2\rangle}\right)\boldsymbol{B}\cdot\boldsymbol{F}_{\mathrm{I}}\right\rangle, \tag{4.1.1.4}$$

the banana–plateau flux

$$\Gamma^{\mathrm{bp}} = -\frac{c}{e}\frac{\langle I_c\rangle}{\langle B^2\rangle}\langle\boldsymbol{B}\cdot\nabla\cdot\overleftrightarrow{\pi}\rangle = -\frac{c}{e}\frac{\langle I_c\rangle}{\langle B^2\rangle}\Big(\langle\boldsymbol{B}\cdot\boldsymbol{F}_{\mathrm{I}}\rangle + \langle Ne\boldsymbol{B}\cdot\boldsymbol{E}^{(A)}\rangle\Big), \tag{4.1.1.5}$$

the non-axisymmetric flux

$$\Gamma^{\mathrm{na}} = \frac{c}{e}\left(\langle\boldsymbol{B}_{\mathrm{t}}\cdot\nabla p\rangle + \langle\boldsymbol{B}_{\mathrm{t}}\cdot\nabla\cdot\overleftrightarrow{\pi}\rangle\right), \tag{4.1.1.6}$$

the classical flux

$$\Gamma^{\mathrm{cl}} = -\frac{c}{e}\langle\boldsymbol{B}_{\mathrm{t}}\cdot\boldsymbol{F}_{\mathrm{I}\perp}\rangle, \tag{4.1.1.7}$$

the flux associated with the moving velocity of the toroidal magnetic flux surface

$$\Gamma^{g} = N\left\langle\boldsymbol{u}_{\psi}\cdot\nabla\chi\right\rangle = Nc\left(\frac{V'\langle\boldsymbol{B}\cdot\boldsymbol{E}\rangle}{4\pi^2 q} - \langle\boldsymbol{E}\cdot\boldsymbol{B}_{\mathrm{t}}\rangle\right) \tag{4.1.1.8}$$

and the residual $\boldsymbol{E}\times\boldsymbol{B}$ flux

$$\Gamma^{E} = Nc\langle\boldsymbol{B}\cdot\boldsymbol{E}\rangle\frac{\langle I_c\rangle}{\langle B^2\rangle}\left(1 - \frac{\langle B^2\rangle}{\langle I_c\rangle}\frac{V'}{4\pi^2 q}\right), \tag{4.1.1.9}$$

where $I_c = \boldsymbol{B}_{\mathrm{t}}\cdot\boldsymbol{B}$, $\boldsymbol{F}_{\mathrm{I}\perp}$ is the component of the friction force perpendicular to the magnetic field, and $\langle\boldsymbol{u}_{\psi}\cdot\nabla\chi\rangle$ is the moving velocity of the toroidal magnetic flux surface [6, 7, 53, 62, 63]. Thus, relative to the moving toroidal magnetic flux surface, $\Gamma^{\chi} - \Gamma^{g}$ consists of the Pfirsch–Schlüter flux, banana–plateau flux, non-axisymmetric flux, classical flux and the residual $\boldsymbol{E}\times\boldsymbol{B}$ flux, which is usually neglected.

It should be noted here that the banana–plateau flux Γ^{bp} not only exists in the banana–plateau regime, but also in the Pfirsch–Schlüter regime. It is subdominant in the Pfirsch–Schlüter regime, however, except when the inverse aspect ratio ε approaches unity.

In the derivation of the flux–force relation using the momentum equation, the viscous tensor is not limited to the Chew–Goldberger–Low (CGL) form [64], which is $\overleftrightarrow{\pi} = (p_{\parallel} - p_{\perp})(\boldsymbol{nn} - \overleftrightarrow{I}/3)$, $p_{\parallel} = \int \mathrm{d}\boldsymbol{v} M u_{\parallel}^2 f$ is the plasma pressure in the direction of the magnetic field, and $p_{\perp} = \int \mathrm{d}\boldsymbol{v}(Mu_{\perp}^2/2)f$ is the pressure in the direction perpendicular to the magnetic field. However, to obtain the neoclassical transport matrix briefly summarized in section 1, the CGL viscous tensor is adequate.

Note that the pressure in equations (4.1.1.1) and (4.1.1.6) is the perturbed pressure driven by the particle drift velocity. In terms of the gyro-radius ordering they are first order. In Hamada coordinates, $\langle\boldsymbol{B}_{\mathrm{t}}\cdot\nabla p\rangle = 0$ for any non-axisymmetric torus, and only $\langle\boldsymbol{B}_{\mathrm{t}}\cdot\nabla\cdot\overleftrightarrow{\pi}\rangle$ contributes to non-axisymmetric particle flux Γ^{na}. Because Γ^{na} is driven by the viscous force and pressure force, it is not intrinsically ambipolar.

A relation between the heat flux and the forces can also be derived. The relevant moment equation is

$$\frac{\partial\boldsymbol{q}}{\partial t} = \frac{e}{cM}\boldsymbol{q}\times\boldsymbol{B} - \nabla\cdot\overleftrightarrow{r} + \frac{5T}{2M}\left(\nabla p + \nabla\cdot\overleftrightarrow{\pi}\right) + \frac{T}{M}\boldsymbol{F}_2, \tag{4.1.1.10}$$

where the higher order terms have been neglected and the heat flux $\boldsymbol{q}$ reduces to

$$\boldsymbol{q} = \boldsymbol{Q} - \frac{5}{2}TN\boldsymbol{V}. \tag{4.1.1.11}$$

Employing the same procedure used to decompose the particle flux, radial heat flux $q^{\chi} = \langle\boldsymbol{q}\cdot\nabla\chi\rangle$ can be decomposed into the non-axisymmetric heat flux q^{na} :

$$\frac{q^{\mathrm{na}}}{T} = \frac{c}{e}\left\langle\boldsymbol{B}_{\mathrm{t}}\cdot\nabla\cdot\overleftrightarrow{\Theta}\right\rangle + \frac{c}{e}\langle\boldsymbol{B}_{\mathrm{t}}\cdot\nabla\vartheta\rangle, \tag{4.1.1.12}$$

the banana–plateau heat flux q^{bp} :

$$\frac{q^{\mathrm{bp}}}{T} = -\frac{c}{e}\frac{\langle I_c\rangle}{\langle B^2\rangle}\left\langle\boldsymbol{B}\cdot\nabla\cdot\overleftrightarrow{\Theta}\right\rangle = -\frac{c}{e}\frac{\langle I_c\rangle}{\langle B^2\rangle}\langle\boldsymbol{B}\cdot\boldsymbol{F}_2\rangle, \tag{4.1.1.13}$$

the Pfirsch–Schlüter heat flux q^{ps}:

$$\frac{q^{\mathrm{ps}}}{T} = -\frac{c}{e}\left\langle\left(\frac{I_c}{B^2} - \frac{\langle I_c\rangle}{\langle B^2\rangle}\right)\left(\boldsymbol{B}\cdot\nabla\vartheta + \boldsymbol{B}\cdot\nabla\cdot\overleftrightarrow{\Theta}\right)\right\rangle = -\frac{c}{e}\left\langle\left(\frac{I_c}{B^2} - \frac{\langle I_c\rangle}{\langle B^2\rangle}\right)\boldsymbol{B}\cdot\boldsymbol{F}_2\right\rangle \tag{4.1.1.14}$$

and the classical heat flux

$$\frac{q^{\mathrm{cl}}}{T} = -\frac{c}{e}\langle\boldsymbol{B}_{\mathrm{t}}\cdot\boldsymbol{F}_{2\perp}\rangle, \tag{4.1.1.15}$$

where $\boldsymbol{F}_{2\perp}$ is the heat friction force that is perpendicular to the magnetic field, the CGL heat viscous tensor $\overleftrightarrow{\Theta} = (\Theta_{\parallel} - \Theta_{\perp})(\boldsymbol{nn} - \overleftrightarrow{I}/3)$, $\vartheta = \Theta_{\parallel}/3 + 2\Theta_{\perp}/3$, $\Theta_{\parallel} = \int \mathrm{d}\boldsymbol{v}(v^2/v_{\mathrm{t}}^2 - 5/2)Mv_{\parallel}^2 f$ and $\Theta_{\perp} = \int \mathrm{d}\boldsymbol{v}(v^2/v_{\mathrm{t}}^2 - 5/2)(Mv_{\perp}^2/2)f$ [6, 7, 53, 62]. For a Maxwellian distribution, $\vartheta = 0$. Again, q^{bp} also exists in the Pfirsch–Schlüter regime.

As can be seen from the flux–force relation, except the Pfirsch–Schlüter fluxes, all transport fluxes are driven by components of the perturbed pressure and viscosity. Once the components of these forces are known, all transport fluxes can be derived by substituting the consistent plasma flows determined from the solutions of the components of the momentum equation. Thus, the key to the development of neoclassical theory in the moment equation approach is to calculate the plasma viscosity in axisymmetric and in general non-axisymmetric tori under a variety of plasma conditions. The main theme of the review is to show the procedures to calculate plasma viscosity, to obtain the consistent plasma flows that satisfy the momentum equation, and to demonstrate the transport consequences.

4.1.2. Kinetic approach The flux–force relation for the neoclassical fluxes can also be derived using the definitions for the neoclassical particle flux

$$\Gamma^{\chi} = \left\langle \int \mathrm{d}\boldsymbol{v} f \boldsymbol{v}_{\mathrm{d}} \cdot \nabla\chi \right\rangle + \left\langle Nc \frac{\boldsymbol{E}^{(A)} \times \boldsymbol{B}}{B^2} \right\rangle, \tag{4.1.2.1}$$

and the heat flux

$$\frac{q^{\chi}}{T} = \left\langle \int \mathrm{d}\boldsymbol{v} \left(\frac{v^2}{v_{\mathrm{t}}^2} - \frac{5}{2} \right) f \boldsymbol{v}_{\mathrm{d}} \cdot \nabla\chi \right\rangle, \tag{4.1.2.2}$$

where f, independent of the gyro-phase, is the solution of the drift kinetic equation [6]. The classical particle and heat fluxes are, thus, excluded.

To proceed, an explicit expression for the drift velocity [6],

$$\boldsymbol{v}_{\mathrm{d}} = -v_{\parallel} \boldsymbol{n} \times \nabla \left(v_{\parallel} / \Omega \right), \tag{4.1.2.3}$$

is needed. Even though the representation for $\boldsymbol{v}_{\mathrm{d}}$ in equation (4.1.2.3) is valid for low-$\bar{\beta}$ plasmas, its radial component, i.e. $\boldsymbol{v}_{\mathrm{d}} \cdot \nabla\chi$, is valid for arbitrary plasma $\bar{\beta}$ [6]. Here, plasma $\bar{\beta}$ is defined as the ratio of plasma pressure to the magnetic field pressure. The radial drift speed $\boldsymbol{v}_{\mathrm{d}} \cdot \nabla\chi$ is

$$\boldsymbol{v}_{\mathrm{d}} \cdot \nabla\chi = \frac{v_{\parallel}}{B} \nabla \cdot \left[\left(\frac{v_{\parallel}}{\Omega} \right) \boldsymbol{B} \times \nabla\chi \right]. \tag{4.1.2.4}$$

Substituting equation (4.1.2.4) into equation (4.1.2.1), and employing the vector identity in equation (4.1.1.2) yields [47, 65]

$$\begin{aligned} \Gamma^{\chi} = & -\left\langle \int \mathrm{d}\boldsymbol{v} f \left(\frac{v_{\parallel}}{B} \right) \nabla \cdot \left(\frac{v_{\parallel} B^2 \boldsymbol{B}_t}{\Omega} \right) \right\rangle \\ & + \left\langle \int \mathrm{d}\boldsymbol{v} f \left(\frac{v_{\parallel}}{B} \right) \nabla \cdot \left[\left(\frac{v_{\parallel} B^2 \boldsymbol{B}}{\Omega} \right) \left(\frac{I_c}{B^2} - \frac{\langle I_c \rangle}{\langle B^2 \rangle} \right) \right] \right\rangle \\ & + \left\langle \int \mathrm{d}\boldsymbol{v} f \left(\frac{v_{\parallel}}{B} \right) \nabla \cdot \left[\left(\frac{v_{\parallel} B^2 \boldsymbol{B}}{\Omega} \right) \frac{\langle I_c \rangle}{\langle B^2 \rangle} \right] \right\rangle \\ & + \left\langle Nc \left(\frac{\boldsymbol{E}^{(A)} \times \boldsymbol{B}}{B^2} \right) \right\rangle. \end{aligned} \tag{4.1.2.5}$$

The non-axisymmetric flux Γ^{na} is

$$\Gamma^{\mathrm{na}} = -\left\langle \int \mathrm{d}\boldsymbol{v} f \left(\frac{v_{\parallel}}{B} \right) \nabla \cdot \left(\frac{v_{\parallel} B^2 \boldsymbol{B}_t}{\Omega} \right) \right\rangle, \tag{4.1.2.6}$$

the banana–plateau flux Γ^{bp} is

$$\Gamma^{\mathrm{bp}} = \left\langle \int \mathrm{d}\boldsymbol{v} f \left(\frac{v_{\parallel}}{B} \right) \nabla \cdot \left[\left(\frac{v_{\parallel} B^2 \boldsymbol{B}}{\Omega} \right) \frac{\langle I_c \rangle}{\langle B^2 \rangle} \right] \right\rangle, \tag{4.1.2.7}$$

and the Pfirsch–Schlüter flux Γ^{ps} together with part of the inductive electric field driven flux Γ^{gp} is

$$\begin{aligned} \Gamma^{\mathrm{ps}} + \Gamma^{\mathrm{gp}} = & \left\langle \int \mathrm{d}\boldsymbol{v} f \left(\frac{v_{\parallel}}{B} \right) \nabla \right. \\ & \left. \cdot \left[\left(\frac{v_{\parallel} B^2 \boldsymbol{B}}{\Omega} \right) \left(\frac{I_c}{B^2} - \frac{\langle I_c \rangle}{\langle B^2 \rangle} \right) \right] \right\rangle. \end{aligned} \tag{4.1.2.8}$$

It is straightforward to show that

$$\begin{aligned} & \int \mathrm{d}\boldsymbol{v} f \left(\frac{v_{\parallel}}{B} \right) \nabla \cdot \left[\left(\frac{v_{\parallel} B^2 \boldsymbol{B}}{\Omega} \right) A \right] \\ & = \frac{c}{e} \nabla \cdot \left(\int \mathrm{d}\boldsymbol{v} f M v_{\parallel}^2 A \boldsymbol{B} \right) - \int \mathrm{d}\boldsymbol{v} v_{\parallel} \left(\boldsymbol{n} \cdot \nabla f \right) \frac{v_{\parallel} A B^2}{\Omega}, \end{aligned} \tag{4.1.2.9}$$

for an arbitrary scalar A. The second term on the right-hand side of equation (4.1.2.9) can be shown to be

$$\begin{aligned} & \int \mathrm{d}\boldsymbol{v} v_{\parallel} \left(\boldsymbol{n} \cdot \nabla f \right) \left(\frac{v_{\parallel} A B^2}{\Omega} \right) \\ & = \frac{c}{e} A \left(\boldsymbol{B} \cdot \nabla p + \boldsymbol{B} \cdot \nabla \cdot \overleftrightarrow{\pi} - Ne \boldsymbol{B} \cdot \boldsymbol{E}^{(S)} \right) \\ & = \frac{c}{e} A \left(\boldsymbol{B} \cdot \boldsymbol{F}_{\mathrm{I}} + Ne \boldsymbol{B} \cdot \boldsymbol{E}^{(A)} \right), \end{aligned} \tag{4.1.2.10}$$

where $\overleftrightarrow{\pi}$ is the CGL viscous tensor, and $\boldsymbol{E}^{(S)} = -\nabla\Phi$ is the electrostatic electric field. The divergence term in equation (4.1.2.9) vanishes upon flux surface averaging. Thus, the neoclassical fluxes are driven fundamentally by the perturbed pressure, perturbed electrostatic potential and viscous forces. Equation (4.1.1.3) has been used to obtain the second equality in equation (4.1.2.10).

Using results given in equations (4.1.2.9) and (4.1.2.10), the banana–plateau, and Pfirsch–Schlüter fluxes can be shown to be the same as those derived in section 4.1.1. The rest of the flux driven by the inductive electric field is the same as those in section 4.1.1. It is important to note here that the Pfirsch–Schlüter flux Γ^{ps} is part of the flux in the definition of the particle flux in equation (4.1.2.1), thus, it exists in all regimes.

The non-axisymmetric particle flux Γ^{na} can be written as

$$\begin{aligned} \Gamma^{\mathrm{na}} = & -\left\langle \int \mathrm{d}\boldsymbol{v} f \frac{\boldsymbol{B}_{\mathrm{t}} \cdot \nabla B}{\Omega} \left(\frac{3}{2} v_{\parallel}^2 - \frac{v^2}{2} \right) \right\rangle \\ & - \left\langle \frac{2}{3} \int \mathrm{d}\boldsymbol{v} f \frac{B \nabla \cdot \boldsymbol{B}_{\mathrm{t}}}{\Omega} \left(\frac{3}{2} v_{\parallel}^2 - \frac{v^2}{2} \right) \right\rangle \\ & - \left\langle \int \mathrm{d}\boldsymbol{v} f \frac{B \nabla \cdot \boldsymbol{B}_{\mathrm{t}}}{\Omega} \frac{v^2}{3} \right\rangle \\ = & \frac{c}{e} \left(\langle \boldsymbol{B}_{\mathrm{t}} \cdot \nabla p \rangle + \left\langle \boldsymbol{B}_{\mathrm{t}} \cdot \nabla \cdot \overleftrightarrow{\pi} \right\rangle \right), \end{aligned} \tag{4.1.2.11}$$

using the following identity:

$$\begin{aligned} \langle \boldsymbol{B}_{\mathrm{t}} \cdot \nabla p \rangle + \left\langle \boldsymbol{B}_{\mathrm{t}} \cdot \nabla \cdot \overleftrightarrow{\pi} \right\rangle = & -\left\langle p_{\parallel} \nabla \cdot \boldsymbol{B}_{\mathrm{t}} \right\rangle \\ & - \left\langle \left(p_{\parallel} - p_{\perp} \right) \frac{\boldsymbol{B}_{\mathrm{t}} \cdot \nabla B}{B} \right\rangle. \end{aligned} \tag{4.1.2.12}$$

The decomposing of the heat flux using the definition in equation (4.1.2.2) follows straightforwardly from that of the particle flux shown here.

4.1.3. Helically symmetric tori. The most general symmetry property in doubly periodic tori is helical symmetry. The flux–force relation in such tori can be obtained from those in sections 4.1.1 and 4.1.2. However, it can be simplified somewhat because the poloidal magnetic field is usually not generated by the inductive plasma current, $\langle \boldsymbol{B} \cdot E_{\parallel}^{(A)} \rangle = 0$, and the motion of the flux surface can be neglected.

When the torus is helically symmetric, the magnetic field strength has the form $B = B(\chi, \alpha)$. There exists a symmetric vector in such tori:

$$\boldsymbol{S} = m\sqrt{g} \nabla\chi \times \nabla\theta - n\sqrt{g} \nabla\chi \times \nabla\zeta, \tag{4.1.3.1}$$

so that $\boldsymbol{S} \cdot \nabla\alpha = 0$. The vector $\boldsymbol{S}$ is also divergence free, i.e. $\nabla \cdot \boldsymbol{S} = 0$. For axisymmetric tokamaks, $m = 1$ and $n = 0$ and $\boldsymbol{S} \cdot \nabla\zeta = 0$. When the symmetry is broken, the vector $\boldsymbol{S}$ can

still be defined although it no longer satisfies $\boldsymbol{S}\cdot\nabla\alpha = 0$. The corresponding flux–force relation, using the identity

$$\boldsymbol{S} = \frac{(\boldsymbol{S}\cdot\boldsymbol{B})\,\boldsymbol{B}}{B^2} - (m-nq)\,\frac{\boldsymbol{B}\times\nabla\chi}{B^2}, \tag{4.1.3.2}$$

can be derived. The relation is the same as the one derived using vector $\boldsymbol{B}_{\rm t}$ in equation (4.1.1.2) except replacing $\boldsymbol{B}_{\rm t}$ by $[\boldsymbol{S}/(m-nq)]$. This replacement forms the basis for the isomorphic transformation that unifies transport fluxes in all symmetric tori to be demonstrated in section 9.

The fundamental reason that the perturbed pressure force also appears in the flux–force relation in magnetic coordinates other than Hamada coordinates is that the vectors $\boldsymbol{B}_{\rm t}$ and $\boldsymbol{S}$ are no longer divergence free in non-axisymmetric tori. However, a divergence free vector $\boldsymbol{S}_1$ can be constructed by adding a term to the vector $\boldsymbol{S}$ so that [66]

$$\boldsymbol{S}_1 = \boldsymbol{S} + R_\parallel B, \tag{4.1.3.3}$$

and $R_\parallel$ satisfies a magnetic differential equation

$$\boldsymbol{B}\cdot\nabla R_\parallel = -\nabla\cdot\boldsymbol{S}. \tag{4.1.3.4}$$

With the choice of the function $R_\parallel$, $\nabla\cdot\boldsymbol{S}_1 = 0$. The solubility constraint for equation (4.1.3.4) is satisfied because $\langle\boldsymbol{B}\cdot\nabla R_\parallel\rangle = -\langle\nabla\cdot\boldsymbol{S}\rangle = 0$. The explicit expression for equation (4.1.3.4) is

$$\boldsymbol{B}\cdot\nabla R_\parallel = -\frac{n}{\sqrt{g}}\frac{\partial\sqrt{g}}{\partial\theta} - \frac{m}{\sqrt{g}}\frac{\partial\sqrt{g}}{\partial\zeta}. \tag{4.1.3.5}$$

The integration constant for the solution to equation (4.1.3.5) is chosen to be zero, because $\boldsymbol{B}\cdot\nabla R_\parallel = 0$ if and only if the torus is helically symmetric. With this choice of the integration constant, $R_\parallel = 0$ in Hamada coordinates, because $\nabla\cdot\boldsymbol{S} = 0$ regardless of the symmetry property in those coordinates. The vector $\boldsymbol{S}_1$ can be projected in the direction of $\boldsymbol{B}$ and in the direction perpendicular to $\boldsymbol{B}$ to obtain

$$\boldsymbol{S}_1 = \frac{(\boldsymbol{S}_1\cdot\boldsymbol{B})\,\boldsymbol{B}}{B^2} - (m-nq)\,\frac{\boldsymbol{B}\times\nabla\chi}{B^2}. \tag{4.1.3.6}$$

The particle and heat fluxes can be decomposed employing equation (4.1.3.6) as before. The results are the same as those obtained previously except for the fact that $\boldsymbol{B}_{\rm t}$ is replaced by $[\boldsymbol{S}_1/(m-nq)]$. However, because $\nabla\cdot\boldsymbol{S}_1 = 0$, $\langle\boldsymbol{S}_1\cdot\nabla p\rangle = 0$, and non-axisymmetric particle flux becomes

$$\Gamma^{\rm na} = \frac{c}{e}\left\langle\boldsymbol{S}_1\cdot\nabla\cdot\overleftrightarrow{\pi}\right\rangle, \tag{4.1.3.7}$$

and non-axisymmetric heat flux reduces to

$$\frac{q^{\rm na}}{T} = \frac{c}{e}\left\langle\boldsymbol{S}_1\cdot\nabla\cdot\overleftrightarrow{\Theta}\right\rangle. \tag{4.1.3.8}$$

The pressure force term in $\Gamma^{\rm na}$ and $\nabla\vartheta$ force term in $q^{\rm na}$ are annihilated rigorously. This also indicates that the decomposition of the flux is not unique for non-axisymmetric tori. However, the total flux through a given magnetic flux surface must be invariant as illustrated in [53].

4.1.4. Useful identities. The explicit expressions for the flux surface averaged components of the CGL viscous forces in terms of the particle distribution function are [67]

$$\left\langle\boldsymbol{B}\cdot\nabla\cdot\overleftrightarrow{\pi}\right\rangle = -\left\langle\left(p_\parallel - p_\perp\right)\frac{\boldsymbol{B}\cdot\nabla B}{B}\right\rangle, \tag{4.1.4.1}$$

$$\left\langle\boldsymbol{B}\cdot\nabla\cdot\overleftrightarrow{\Theta}\right\rangle = -\left\langle\left(\Theta_\parallel - \Theta_\perp\right)\frac{\boldsymbol{B}\cdot\nabla B}{B}\right\rangle, \tag{4.1.4.2}$$

$$\langle\boldsymbol{B}_{\rm t}\cdot\nabla p\rangle + \left\langle\boldsymbol{B}_{\rm t}\cdot\nabla\cdot\overleftrightarrow{\pi}\right\rangle = -\left\langle p_\parallel\nabla\cdot\boldsymbol{B}_{\rm t}\right\rangle - \left\langle\left(p_\parallel - p_\perp\right)\frac{\boldsymbol{B}_{\rm t}\cdot\nabla B}{B}\right\rangle, \tag{4.1.4.3}$$

and

$$\left\langle\boldsymbol{B}_{\rm t}\cdot\nabla\cdot\overleftrightarrow{\Theta}\right\rangle + \langle\boldsymbol{B}_{\rm t}\cdot\nabla\vartheta\rangle = -\left\langle\Theta_\parallel\nabla\cdot\boldsymbol{B}_{\rm t}\right\rangle - \left\langle\left(\Theta_\parallel - \Theta_\perp\right)\frac{\boldsymbol{B}_{\rm t}\cdot\nabla B}{B}\right\rangle. \tag{4.1.4.4}$$

These expressions are used to calculate the components of the viscous forces from the solution of the drift kinetic equation. Sometimes, the components of the viscous forces are calculated directly using the solution of the drift kinetic equation and the transport fluxes are derived using the solutions of the force balance equations. Sometimes, the transport fluxes are calculated directly and the corresponding viscous forces are identified.

4.2. Momentum relaxation and ambipolarity

Summing equation (2.8) over plasma species yields

$$NM\frac{\partial\boldsymbol{V}}{\partial t} = \frac{1}{c}\boldsymbol{J}\times\boldsymbol{B} - \nabla P - \nabla\cdot\overleftrightarrow{\pi}, \tag{4.2.1}$$

where the mass M is approximately ion mass, and $\overleftrightarrow{\pi} = \sum_j\overleftrightarrow{\pi}_j$ is the total viscous tensor. Taking the projection of equation (4.2.1) in the direction of $\boldsymbol{S}$ and flux surface averaging the resultant equation yield the momentum relaxation equation in the direction of symmetry:

$$NM\frac{\partial\langle\boldsymbol{S}\cdot\boldsymbol{V}\rangle}{\partial t} = \frac{m-nq}{c}\langle\boldsymbol{J}\cdot\nabla\chi\rangle - \langle\boldsymbol{S}\cdot\nabla P\rangle - \left\langle\boldsymbol{S}\cdot\nabla\cdot\overleftrightarrow{\pi}\right\rangle. \tag{4.2.2}$$

Using Ampere's law,

$$\langle\boldsymbol{J}\cdot\nabla\chi\rangle = -\frac{1}{4\pi}\frac{\partial\langle\boldsymbol{E}\cdot\nabla\chi\rangle}{\partial t}, \tag{4.2.3}$$

Equation (4.2.2) can be written as

$$NM\frac{\partial\langle\boldsymbol{S}\cdot\boldsymbol{V}\rangle}{\partial t} + \frac{m-nq}{c}\frac{1}{4\pi}\frac{\partial\langle\boldsymbol{E}\cdot\nabla\chi\rangle}{\partial t} = -\langle\boldsymbol{S}\cdot\nabla P\rangle - \left\langle\boldsymbol{S}\cdot\nabla\cdot\overleftrightarrow{\pi}\right\rangle = -\frac{1}{c}\sum\nolimits_j e_j\Gamma_j^{\rm na}. \tag{4.2.4}$$

The left-hand side of equation (4.2.4) represents the plasma momentum and the momentum of the electromagnetic field [6, 60] and the right-hand side of equation (4.2.4) represents the momentum dissipation when symmetry is slightly broken.

If the torus is helically symmetric, the right-hand side of equation (4.2.4) vanishes for CGL viscous tensor. In that case, only the higher order solution in the gyro-radius

ordering for the drift kinetic equation can give rise to a non-vanishing component of the stress tensor in the direction of the symmetry $\boldsymbol{S}$ [68–70]. Setting $m = 1$ and $n = 0$ in $\boldsymbol{S}$ in equation (4.2.4) yields the toroidal momentum relaxation equation for tokamaks with slightly broken toroidal symmetry:

$$NM\frac{\partial\langle\boldsymbol{B}_{\rm t}\cdot\boldsymbol{V}\rangle}{\partial t}+\frac{1}{c}\frac{1}{4\pi}\frac{\partial\langle\boldsymbol{E}\cdot\nabla\chi\rangle}{\partial t}=-\langle\boldsymbol{B}_{\rm t}\cdot\nabla P\rangle$$
$$-\left\langle\boldsymbol{B}_{\rm t}\cdot\nabla\cdot\overleftrightarrow{\pi}\right\rangle=-\frac{1}{c}\sum\nolimits_j e_j\Gamma_j^{\rm na}. \tag{4.2.5}$$

As emphasized previously, the pressure force term vanishes in Hamada coordinates regardless of the symmetry property of the tori. In any other magnetic flux coordinates, it does not vanish when the symmetry is broken unless the momentum equation is projected in the direction of $\boldsymbol{S}_1$ instead of $\boldsymbol{S}$. In that case, in the direction of $\boldsymbol{S}_1$,

$$NM\frac{\partial\langle\boldsymbol{S}_1\cdot\boldsymbol{V}\rangle}{\partial t}+\frac{m-nq}{c}\frac{1}{4\pi}\frac{\partial\langle\boldsymbol{E}\cdot\nabla\chi\rangle}{\partial t}=-\left\langle\boldsymbol{S}_1\cdot\nabla\cdot\overleftrightarrow{\pi}\right\rangle$$
$$=-\frac{1}{c}\sum\nolimits_j e_j\Gamma_j^{\rm na}. \tag{4.2.6}$$

Similarly, the equation for the evolution of the flow component that is perpendicular to the direction of the symmetry is [13, 60, 71]

$$NM\left\langle B^2\right\rangle\left(1-\frac{\langle\boldsymbol{B}\cdot\boldsymbol{S}\rangle^2}{\left\langle B^2\right\rangle\left\langle|\boldsymbol{S}|^2\right\rangle}\right)\frac{\partial K}{\partial t}$$
$$-\frac{m-nq}{c}\frac{1}{4\pi}\frac{\langle\boldsymbol{B}\cdot\boldsymbol{S}\rangle}{\left\langle|\boldsymbol{S}|^2\right\rangle}\frac{\partial\langle\boldsymbol{E}\cdot\nabla\chi\rangle}{\partial t}$$
$$\approx-\left\langle\boldsymbol{B}\cdot\nabla\cdot\overleftrightarrow{\pi}\right\rangle+\frac{\langle\boldsymbol{B}\cdot\boldsymbol{S}\rangle}{\left\langle|\boldsymbol{S}|^2\right\rangle}\left(\langle\boldsymbol{S}\cdot\nabla P\rangle+\left\langle\boldsymbol{S}\cdot\nabla\cdot\overleftrightarrow{\pi}\right\rangle\right)$$
$$=\frac{\left\langle B^2\right\rangle}{c\left\langle I_c\right\rangle}\sum_j e_j\Gamma_j^{\rm bp}+\frac{\langle\boldsymbol{B}\cdot\boldsymbol{S}\rangle}{\left\langle|\boldsymbol{S}|^2\right\rangle}\frac{1}{c}\sum\nolimits_j e_j\Gamma_j^{\rm na}, \tag{4.2.7}$$

where $K(\chi)=\boldsymbol{V}\cdot\nabla\alpha/\boldsymbol{B}\cdot\nabla\alpha=(mV^\theta-nV^\zeta)/(m-nq)$ if symmetry is only slightly broken. For tokamaks, $K(\chi)=V^\theta$. When the torus is either helically symmetric or toroidally symmetric, $(\langle\boldsymbol{S}\cdot\nabla P\rangle+\langle\boldsymbol{S}\cdot\nabla\cdot\overleftrightarrow{\pi}\rangle)=0$. When the symmetry is slightly broken, both the pressure and the viscous forces contribute to the evolution of the flow component K. However, it is most likely that $\langle\boldsymbol{B}\cdot\nabla\cdot\overleftrightarrow{\pi}\rangle$ dominates the dissipative processes in the evolution of K when the symmetry is only slightly broken. It should be noted that even though it is $\Gamma_j^{\rm bp}$ that appears in equation (4.2.7), the same equation is still valid in the Pfirsch–Schlüter regime. In that regime, it is the $\langle\boldsymbol{B}\cdot\nabla\cdot\overleftrightarrow{\pi}\rangle$ not the Pfirsch–Schlüter particle flux in the Pfirsch–Schlüter regime that damps the flow.

It is important to note that in the evolution equations for flows in the direction of the symmetry and in the direction perpendicular to the symmetry, the dissipation mechanisms are directly proportional to the components of the viscous stress and those components are directly proportional to the particle fluxes according to the flux–force relation, as shown in equations (4.2.4)–(4.2.7). In the direction of the symmetry, it is the non-axisymmetric particle flux $\Gamma^{\rm na}$ when the symmetry is slightly broken, and in the direction perpendicular to the symmetry, it is the banana–plateau flux $\Gamma^{\rm bp}$. When these flows are relaxed, plasmas reach the ambipolar state [6, 7], i.e.

$$\sum\nolimits_j e_j\Gamma_j^{\rm na}=0, \tag{4.2.8}$$

and

$$\sum\nolimits_j e_j\Gamma_j^{\rm bp}=0. \tag{4.2.9}$$

These are two linearly independent equations that are required to determine the first-order flow velocity $\boldsymbol{V}$ completely, as discussed in section 3.2. It is important to note that once equations (4.2.8) and (4.2.9) are satisfied, the total particle flux is ambipolar:

$$\sum\nolimits_j e_j\Gamma_j^{\chi}=0. \tag{4.2.10}$$

However, the reverse is not true. Because equation (4.2.10) is only one equation that cannot determine the two unknowns in the flow velocity $\boldsymbol{V}$.

Even though, the toroidal systems with slightly broken symmetry have been employed in the illustrations on the momentum relaxation and ambipolarity, the results and conclusions are also valid for non-axisymmetric tori that cannot be viewed as a perturbation from symmetric tori, as shown in [61].

The momentum relaxation and ambipolarity have been discussed in terms of the neoclassical plasma viscous forces, here, the concept is, however, also applicable when turbulent plasma viscous forces become important. It needs only to replace the neoclassical viscous stress tensor with the turbulence induced viscous stress tensor.

4.2.1. Poloidal flow damping in tokamaks and implications on anomalous transport. As an example, the poloidal flow damping in the banana regime in tokamaks is illustrated here. The magnitude of the parallel viscous force is usually much larger than that of the viscous force in the direction of symmetry, $\boldsymbol{S}$. Thus, the flow component K relaxes much faster than $\langle\boldsymbol{S}\cdot\boldsymbol{V}\rangle$ or the toroidal flow for tokamaks. For axisymmetric tokamaks, the evolution equation for $K(\psi)=V^\theta$ is [60, 71], from equation (4.2.7),

$$NM\left(1+2q^2\right)\left\langle B_{\rm p}^2\right\rangle\frac{\partial K}{\partial t}=-\left\langle\boldsymbol{B}\cdot\nabla\cdot\overleftrightarrow{\pi}\right\rangle, \tag{4.2.1.1}$$

where the term of the order of $V_{\rm A}^2/c^2$ is neglected. Plasma inertia is enhanced by a factor of $(1+2q^2)$ due to the magnetic geometry. Because usually the parallel component of the viscous force for ions is much larger than that for electrons by a factor of $\sqrt{M_{\rm i}/M_{\rm e}}$, only $\langle\boldsymbol{B}\cdot\nabla\cdot\overleftrightarrow{\pi}_{\rm i}\rangle$ is needed in equation (4.2.1.1). To obtain accurate damping rate for V^θ, time dependent $\langle\boldsymbol{B}\cdot\nabla\cdot\overleftrightarrow{\pi}_{\rm i}\rangle$ is required in equation (4.2.1.1) and is approximately [72]

$$\left\langle\boldsymbol{B}\cdot\nabla\cdot\overleftrightarrow{\pi}\right\rangle=NM\left\langle B^2\right\rangle\left[\nu_{\rm ii}\sqrt{\varepsilon}\left(1.1V^\theta-1.28\frac{2}{5}\frac{q^\theta}{p}\right)\right.$$
$$\left.+1.63\varepsilon^{3/2}\frac{\partial V^\theta}{\partial t}\right]. \tag{4.2.1.2}$$

Substituting equation (4.2.1.2) into equation (4.2.1.1) yields a damping rate $\gamma_{\rm p}$ for V^θ to be

$$\gamma_{\rm p}\approx 0.675\nu_{\rm ii}/\varepsilon. \tag{4.2.1.3}$$

The poloidal flow damping rate is much faster than the toroidal flow damping rate in tokamaks, which is of the order of $\nu_{\rm ii}(\Delta r/L_n)^2$. The $\gamma_{\rm p}$ is first obtained in [72] and later confirmed by Hinton and Rosenbluth [73]. For the time

scale longer than γ_p^{-1}, the poloidal flow is damped and $\sum_j e_j \Gamma_j^{bp} = 0$. This is the so-called intrinsically ambipolar state in the neoclassical transport theory for axisymmetric tokamaks because now the banana–plateau flux is driven by the parallel component of the friction force [74, 75]. However, the concept of intrinsic ambipolarity is not really needed to understand neoclassical theory for tokamaks as long as poloidal flow damping is consistently determined from the momentum equation. The toroidal flow is still evolving on a much slower diffusion time scale. When the toroidal flow is relaxed for tokamaks with toroidal symmetry slightly broken, plasmas become ambipolar and $\sum_j e_j \Gamma_j^{na} = 0$. The relaxation of the components of the plasma flow velocity described for tokamaks is applicable for any symmetric tori by replacing the poloidal flow with the flow component perpendicular to the symmetric direction and toroidal flow with the component in the symmetric direction.

After poloidal flow is damped, a combination of the $V_\parallel$ and the radial electric field Φ' is determined, as can be seen from equation (3.2.12). Because the time scale for the toroidal momentum relaxation in axisymmetric tokamaks is of the order of the confinement time, $V_\parallel$, which is approximately the toroidal flow for large aspect ratio tokamaks, evolves at the confinement time scale and has a value approximate to its initial value during the poloidal flow damping process that lasts for a time span of the order of $(\nu_{ii}/\varepsilon)^{-1}$ which is much shorter than the confinement time. Thus, throughout the slow evolution process of the toroidal flow, the radial electric field is determined after the time of the order of $(\nu_{ii}/\varepsilon)^{-1}$, and evolves slowly at the confinement time scale. The same physics processes occur in all quasi-symmetric tori except that the poloidal flow V^θ is replaced by $mV^\theta - nV^\zeta$ in equation (3.2.11). The neoclassical transport theory for axisymmetric tokamaks or for quasi-symmetric tori is much easier to comprehend if the concept of the 'intrinsic' ambipolarity is abandoned and replaced with the concept of the poloidal or helical flow damping instead. Indeed, before the poloidal flow is damped, the transport process is not intrinsically ambipolar in tokamaks.

The Pfirsch–Schlüter particle flux is intrinsically ambipolar because it is driven by the friction force. The time scale for the flux to become intrinsically ambipolar is the time to establish local force balance along the magnetic field line. The classical particle flux is also intrinsically ambipolar at the time when the MHD equilibrium is established.

Here, the simplest model has been used to demonstrate the poloidal flow damping. However, other effects such as orbit squeezing, sonic poloidal $\boldsymbol{E}\times\boldsymbol{B}$ drift speed, non-linear plasma viscosity, orbit loss, etc can also affect the plasma viscosity, transport fluxes and the rate of poloidal flow damping [76, 77]. In addition, because the rate of the poloidal flow damping is important to the zonal flow damping, and thus, anomalous transport fluxes, it has been shown that when neoclassical transport fluxes are reduced due to effects of orbit squeezing, sonic poloidal $\boldsymbol{E}\times\boldsymbol{B}$ drift speed and non-linear plasma viscosity, the rate of the zonal flow damping is also reduced along with the anomalous transport fluxes [78]. Thus, improved neoclassical transport fluxes usually imply the reduced anomalous transport fluxes [78]. This indicates that neoclassical transport processes are important to the understanding of the anomalous transport processes.

In cases where the magnitude of the ion plasma viscous forces is reduced to that of the electron viscous forces, the electron viscous forces can no longer be ignored in the poloidal flow damping equation, i.e. equation (4.2.1.1) and electrons also participate in the poloidal flow damping as demonstrated in [79, 80].

5. Neoclassical methodology

Transport fluxes are calculated by solving the drift kinetic equation given in equation (1.3.1). Usually this is accomplished by simplifying the equation through an ordering scheme to linearize the equation. The transport ordering, assuming $\Delta r/L_n < 1$, is adopted to solve the drift kinetic equation shown in equation (1.3.1) [6, 7]. The time scale for the equilibrium quantities to evolve is of the order of the diffusion time $\nu^{-1}(\Delta r/L_n)^{-2}$. Adopting the maximum ordering to assume that the transit frequency is of the same order as the collision frequency yields

$$v_\parallel \boldsymbol{n}\cdot\nabla f_0 = C(f_0), \tag{5.1}$$

and

$$v_\parallel \boldsymbol{n}\cdot\nabla f_1 + \boldsymbol{v}_d\cdot\nabla f_0 + ev_\parallel E_\parallel^{(A)}\frac{\partial f_0}{\partial E} = C(f_1), \tag{5.2}$$

where the subscripts in f denote the ordering. The time scale for the temperature relaxation is assumed to be the same as that for the radial transport [6, 7].

The solution to equation (5.1) is a Maxwellian distribution, i.e.

$$f_0 = f_M(\chi), \tag{5.3}$$

and equation (5.2) becomes

$$v_\parallel \boldsymbol{n}\cdot\nabla f_1 + \boldsymbol{v}_d\cdot\nabla\chi\frac{\partial f_M}{\partial\chi} + ev_\parallel E_\parallel^{(A)}\frac{\partial f_M}{\partial E} = C(f_1), \tag{5.4}$$

where

$$\frac{\partial f_M}{\partial\chi} = f_M\left[\frac{p'}{p} + \frac{e\Phi'}{T} + \left(\frac{v^2}{v_t^2} - \frac{5}{2}\right)\frac{T'}{T}\right]. \tag{5.5}$$

The prime denotes $\mathrm{d}/\mathrm{d}\chi$. The term $v_\parallel \boldsymbol{n}\cdot\nabla f_1$ in equation (5.4) describes the particle motion along the magnetic field line.

To solve equation (5.4) for f_1, the explicit form for the collision operator is required. Assuming that electrons and ions have a common parallel flow $V_\parallel$, the approximate ion–ion collision operator is, by neglecting the ion–electron collisions due to the common parallel flow assumption,

$$C_{ii}(f_{i1}) = \nu_D^{ii}\frac{M_i v_\parallel}{B}\frac{\partial}{\partial\mu}v_\parallel\mu\frac{\partial f_{i1}}{\partial\mu} + \nu_D^{ii}\frac{2v_\parallel V_\parallel}{v_{ti}^2}f_{iM}. \tag{5.6}$$

The approximate electron collision operator consists of the electron–ion collision operator

$$C_{ei}(f_{e1}) = \nu_D^{ei}\frac{M_e v_\parallel}{B}\frac{\partial}{\partial\mu}v_\parallel\mu\frac{\partial f_{e1}}{\partial\mu} + \nu_D^{ei}\frac{2v_\parallel V_\parallel}{v_{te}^2}f_{eM}, \tag{5.7}$$

and the electron–electron operator

$$C_{ee}\left(f_{e1}\right)=\nu_D^{ee}\frac{M_e v_\parallel}{B}\frac{\partial}{\partial\mu}v_\parallel\mu\frac{\partial f_{e1}}{\partial\mu}+\nu_D^{ee}\frac{2v_\parallel V_\parallel}{v_{te}^2}f_{eM}. \quad (5.8)$$

The terms involving $V_\parallel$ are responsible for restoring the momentum to the test particle pitch angle scattering operator.

The facts that electrons and ions have a common parallel flow $V_\parallel$, and there is no parallel heat flow for both species, i.e. $q_{\parallel e}=q_{\parallel i}=0$, imply that part of the solution, that is responsible for the common flow, is

$$f_{1j}=\frac{2v_\parallel}{v_{tj}^2}V_\parallel f_M, \quad (5.9)$$

which is also the solution for the homogeneous equations

$$C_j\left(f_{1j}\right)=0, \quad (5.10)$$

for each species for the exact collision operator when the relaxation of temperature is neglected, where $j=$ i for ions and e for electrons. The distribution function in equation (5.9) is not localized in the phase space. The pitch angle scattering rate is comparable to the momentum restoring rate for non-localized distribution. Thus, the momentum restoring term is important for this distribution. In the original theory [5], complete $C_{ii}(f_{i1})$, $C_{ee}(f_{e1})$ and $C_{ei}(f_{e1})$ are employed in the treatment of the momentum restoring terms. It should be noted that the solutions that have a common parallel flow do not allow for the driving terms that are proportional to $v_\parallel$ or $P_1(v_\parallel/v)$, the Legendre polynomial.

5.1. Variational method

For the sake of simplicity, the inductive electric field is neglected first, and equation (5.4) reduces to

$$v_\parallel\boldsymbol{n}\cdot\nabla f_1+\boldsymbol{v}_d\cdot\nabla\chi\frac{\partial f_M}{\partial\chi}=C\left(f_1\right). \quad (5.1.1)$$

The perturbed distribution function is now expressed as

$$f_1=\frac{2v_\parallel}{v_t^2}V_\parallel f_M+H, \quad (5.1.2)$$

where

$$V_\parallel=-I\frac{v_{ti}^2}{2\Omega_i}\left[\frac{p_i'}{p_i}+\frac{e_i\Phi'}{T_i}+\left(y-\frac{5}{2}\right)\frac{T_i'}{T_i}\right], \quad (5.1.3)$$

and y is a parameter to be determined. The choice of y, which is not a function of particle energy, is to make sure that the shifted Maxwellian portion of the solution satisfies the homogeneous equation of the collisional operator, i.e. equation (5.10). In the banana–plateau regime, the function H is localized in the phase space resulting from the resonance at $v_\parallel\sim 0$. Note that the $V_\parallel$ in equation (5.1.2) does not contribute to the Pfirsch–Schlüter heat flow, thus, it is incapable of producing the Pfirsch–Schlüter heat flux in the banana–plateau regime. In the Pfirsch–Schlüter regime, H is not localized. The localization is important to the treatment of the momentum restoring effects approximately in the collision operator in the banana–plateau regime when $\varepsilon<1$. The equation resulting from the minimization of the rate of entropy production in the variational procedure to determine y is the same as the ambipolarity constraint, and for $\sqrt{M_e/M_i}<1$, the constraint is that the ion particle flux approximately vanishes [5, 8]. In cases where the ion particle flux is no longer larger than the electron particle flux, the full ambipolarity constraint should be used. It should be noted that the form of $V_\parallel$ in equation (5.1.3) does not satisfy the incompressible flow requirement, i.e. $\nabla\cdot\boldsymbol{V}=0$. For $\varepsilon<1$, however, this is inconsequential.

Substituting equation (5.1.2) into equation (5.1.1) yields, for ions,

$$v_\parallel\boldsymbol{n}\cdot\nabla H_i+\left(\boldsymbol{v}_{di}\cdot\nabla\chi\right)\left(\frac{v^2}{v_{ti}^2}-y\right)\frac{T_i'}{T_i}f_{Mi}=C_i\left(H_i\right), \quad (5.1.4)$$

and, for electrons

$$v_\parallel\boldsymbol{n}\cdot\nabla H_e+\left(\boldsymbol{v}_{de}\cdot\nabla\chi\right)f_{Me}\times\left\{\frac{p_e'}{p_e}+\left(\frac{v^2}{v_{te}^2}-\frac{5}{2}\right)\frac{T_e'}{T_e}+\frac{T_i}{ZT_e}\left[\frac{p_i'}{p_i}+\left(y-\frac{5}{2}\right)\right]\frac{T_i'}{T_i}\right\}=C_e\left(H_e\right), \quad (5.1.5)$$

where Z is the ion charge number. Transport coefficients are evaluated using the localized solution H, and only test particle pitch angle scattering operators for both ions and electrons are employed in the processes. The reason is that for the localized distribution function H, the pitch angle scattering operator dominates the collision operator for being larger than the momentum restoring terms by a factor of ε^{-1}. For this reason, there is no momentum restoring issue for the localized distribution function in the $\varepsilon<1$ limit. This concept is used in the moment equation approach as well.

It is important to note that, as illustrated here, the momentum restoring for the test particle pitch angle scattering operator is treated approximately by introducing a term from the shifted Maxwellian distribution in equation (5.1.2). Once this is done, the momentum non-conservation property for the test particle operator is no longer an issue for the localized distribution H. The parameter y and thus, the parallel flow in equation (5.1.3) is determined from the ambipolarity constraint. It is not necessary to determine y from demanding the momentum conservation of the test particle pitch angle scattering operator for the localized distribution function H in large aspect ratio tokamaks.

When the inductive electric field is taken into account, a Spitzer solution f_{se} for the equation

$$C_e\left(v_\parallel f_{se}\right)=-v_\parallel\frac{e_e}{T_e}f_{Me} \quad (5.1.6)$$

is added in equation (5.1.2) for the electron distribution function f_{e1} [6] so that

$$f_{1e}=\frac{2v_\parallel}{v_{te}^2}V_\parallel f_{Me}+\frac{e_e}{T_e}f_{Me}\int_0^\theta\frac{d\theta}{\boldsymbol{B}\cdot\nabla\theta}\left(BE_\parallel^{(A)}-\frac{B^2}{\langle B^2\rangle}\left\langle BE_\parallel^{(A)}\right\rangle\right)+v_\parallel f_{se}\frac{B}{\langle B^2\rangle}\left\langle BE_\parallel^{(A)}\right\rangle+H_e. \quad (5.1.7)$$

The second term on the right-hand side of equation (5.1.7) is to convert $BE_{\parallel}^{(A)}$ in the driving term in equation (5.4) to $\langle BE_{\parallel}^{(A)}\rangle$ and can be viewed as the perturbed density of the Maxwellian distribution. The term has no explicit neoclassical transport consequences. It is important to note that the Spitzer term in equation (5.1.7) can be viewed as part of the parallel electron flow $V_{\parallel e}$ and heat flow $q_{\parallel e}$, if two-term Laguerre polynomial expansion is used to approximate the Spitzer solution f_{se}. The Spitzer term drives flows that differ from the common parallel flow $V_{\parallel}$ due to the inductive electric field.

In the case of ions, the $\langle BE_{\parallel}^{(A)}\rangle$ term is combined with the ion–electron friction force $F_{\parallel ie}$ from the ion–electron collision operator C_{ie} due to the difference between $V_{\parallel i}$ and $V_{\parallel e}$ to form $\langle BE_*\rangle = \langle B[E_{\parallel}^{(A)} + F_{\parallel ie}/(N_i e_i)]\rangle$ [6]. $\langle BE_*\rangle$ is then replaced by the electron banana–plateau flux using equation (4.1.1.5). Thus, electron and ion fluxes are now coupled through the flux surface averaged parallel momentum balance equation (equation (4.1.1.3)).

5.2. Moment method

In the moment approach, the perturbed distribution function is expressed as [7, 81]

$$f_1 = \frac{2v_{\parallel}}{v_t^2}\left(V_{\parallel}L_0^{(3/2)} - \frac{2}{5}L_1^{(3/2)}\frac{q_{\parallel}}{p}\right)f_M + h \qquad (5.2.1)$$

for each species in large aspect ratio tokamaks, where Laguerre polynomials are $L_0^{(3/2)} = 1$, and $L_1^{(3/2)} = 5/2 - v^2/v_t^2$. In the banana and plateau regimes, h is localized in the phase space, and parallel flows it generates can be neglected in the large aspect ratio limit. As pointed out in section 5.1, the parallel flows in equation (5.2.1) include not only flows required for the momentum restoring in the linear collision operator, but also those from the inductive electric field and, in general, any possible driving terms in the linear drift kinetic equation that is proportional to $P_1(v_{\parallel}/v)f_M$. However, the dependences of these parallel flows on the driving terms remain implicit. For these driving terms, the expansion in equation (5.2.1) implies the two-term Laguerre polynomial approximation to the solution f_{Dj} of the equation

$$C_j\left(v_{\parallel}f_{Dj}\right) = -v_{\parallel}\frac{e_j}{T_j}f_{Mj}. \qquad (5.2.2)$$

It should be noted that the Pfirsch–Schlüter parallel flow and heat flow are included in equation (5.2.1). Thus, it can reproduce Pfirsch–Schlüter fluxes, which exist in all regimes. Substituting equation (5.2.1) into equation (5.1.1) and employing the following relations for incompressible flows

$$V_{\parallel} = BV^{\theta} + \frac{IcT}{eB}\left(\frac{p'}{p} + \frac{e\Phi'}{T}\right), \qquad (5.2.3)$$

and

$$q_{\parallel} = Bq^{\theta} + \frac{5}{2}p\frac{IcT}{eB}\frac{T'}{T}, \qquad (5.2.4)$$

in equations (3.2.12) and (3.2.20) yield

$$v_{\parallel}\boldsymbol{n}\cdot\nabla h + \frac{2v^2}{v_t^2}\left(\frac{3v_{\parallel}^2}{2v^2} - \frac{1}{2}\right)f_M\left[V^{\theta} - \frac{2}{5}L_1^{(3/2)}\frac{q^{\theta}}{p}\right] \times\boldsymbol{n}\cdot\nabla B = C(h), \qquad (5.2.5)$$

for both ions and electrons. The driving term in equation (5.2.5) is basically the parallel viscosity, i.e. η_0 in Brangiskii's classification when the condition that flows are incompressible is imposed and the perpendicular flows are the diamagnetic and $\boldsymbol{E}\times\boldsymbol{B}$ flows [1]. For large aspect ratio tokamaks, the pitch angle scattering operator,

$$C(h) = \nu_D\frac{Mv_{\parallel}}{B}\frac{\partial}{\partial\mu}v_{\parallel}\mu\frac{\partial h}{\partial\mu}, \qquad (5.2.6)$$

where $\nu_D = \nu_D^i = \nu_D^{ii}$ for ions and $\nu_D = \nu_D^e = \nu_D^{ee} + \nu_D^{ei}$ for electrons, is adequate for equation (5.2.5) in the banana and plateau regimes because it is larger than the momentum restoring terms for the localized distribution function h by a factor ε^{-1}. An explicit demonstration for equation (5.2.5) for large aspect ratio tokamaks can be found in [81], where the inductive electric field and the momentum restoring terms using the model collision operator in equation (1.3.4) are included in the derivation. In the Pfirsch–Schlüter regime, h is not localized, and equation (5.2.1) is valid for finite aspect ratio tokamaks as well. In that regime, equation (5.2.5) can be solved using the exact linear collision operator. The plateau regime cannot be clearly defined in finite aspect ratio tokamaks. In the banana regime, equation (5.2.5) can be solved for large aspect ratio tokamaks using the conventional method given in [6]. For finite aspect ratio tokamaks, a different approach is used to obtain flux surface averaged parallel viscous forces [7].

It is important to note that the plasma gradient terms in $\boldsymbol{v}_d\cdot\nabla\chi\partial f_M/\partial\chi$ in equation (5.4) are cancelled by the corresponding gradient terms in equations (5.2.3) and (5.2.4) and are replaced by V^{θ} and q^{θ}. Also the $(v_{\parallel}^2 + v^2)$ dependence in $\boldsymbol{v}_d\cdot\nabla\chi$ is replaced by $P_2(v_{\parallel}/v) = (3v_{\parallel}^2/2v^2 - 1/2)$, the Legendre polynomial. The reason for this replacement is that the B dependence in front of V^{θ} and q^{θ} differs from that in front of the plasma gradient terms in equations (5.2.3) and (5.2.4). The plasma gradient terms contribute to the Pfirsch–Schlüter fluxes. Thus, the cancellation of these terms in equation (5.2.5) imply that the Pfirsch–Schlüter fluxes driven by the friction forces are removed. The V^{θ} and q^{θ} terms do not contribute to the Pfirsch–Schlüter fluxes. In addition, because h is proportional to P_2, it does not contribute to parallel plasma flows in the Pfirsch–Schlüter regime. The information on the parallel flows is included in $f_1 - h$ in equation (5.2.1) in large aspect ratio limits. The Spitzer term in equation (5.1.7) has the same $v_{\parallel}B$ dependence as $V_{\parallel}$ and $q_{\parallel}$ in equations (5.2.3) and (5.2.4). Thus, the Spitzer term does not contribute to the Pfirsch–Schlüter fluxes either.

A more general approach to the moment method is to adopt the drift kinetic equation for large mass flow [82], as demonstrated in [83]. In that approach, the shifted Maxwellian, which describes the plasma mass flow in equations (5.1.2) and (5.2.1), has already been taken into account in the derivation of the drift kinetic equation. The advantages of this approach are that the density, temperature and plasma flows can have arbitrary geometric angle dependences and that plasma flows can be compressible. This allows the resultant drift kinetic equation to be valid for physical situations beyond what the conventional neoclassical theory addressed in [6, 7]. An example is shock formation when the poloidal flow speed is sonic.

5.3. Equivalence of two methods

The treatments of the momentum restoring terms in the variational and moment methods are equivalent in the $\varepsilon < 1$ limit. The parallel flow is introduced into the perturbed distribution function to eliminate the momentum restoring terms resulting from the test particle pitch angle scattering operator for the non-localized distribution function. The difference is that in the variational method, a parameter y is introduced. In the moment method, two independent variables, i.e. V^θ and q^θ, are employed. The relation between V^θ and q^θ is to be determined from

$$\left\langle \boldsymbol{B}\cdot\nabla\cdot\overleftrightarrow{\pi}_{\rm i}\right\rangle = 0, \tag{5.3.1}$$

which is the same as, using the flux–force relation in equation (4.1.1.5),

$$\Gamma_{\rm i}^{\rm bp} = 0. \tag{5.3.2}$$

Equations (5.3.1) and (5.3.2) are also a statement of the relaxation of the poloidal flow to reach the intrinsically ambipolar state, as discussed in section 4. The ambipolarity constraint in equation (5.3.2) is also derived from the variational method to determine the parameter y [5,6].

The pitch angle dependence in equation (5.2.5) differs from that in equations (5.1.4) and (5.1.5). In the moment method, the pitch angle dependence in equation (5.2.5) is $P_2(v_\parallel/v)$. In the variational method, the quantity $\boldsymbol{v}_{\rm d}\cdot\nabla\chi$ has a pitch angle dependence that is $(v_\parallel^2 + v^2)$. This difference in the pitch angle dependence is not important for large aspect ratio tokamaks. The reason is that in the banana–plateau regime it is either the particles that are trapped or are barely circulating or those that have $v_\parallel \sim 0$ that dominate the processes. For these particles either $v_\parallel^2 \sim \varepsilon v^2 < v^2$ in the banana regime or $v_\parallel^2 \sim (\Delta v_\parallel/v)^2 v^2 < v^2$, with $\Delta v_\parallel/v$, the width of the resonance layer in the plateau regime, the difference in the pitch angle dependence is inconsequential. However, this difference becomes important when the resonance is not at $v_\parallel \sim 0$ due to sonic poloidal $\boldsymbol{E}\times\boldsymbol{B}$ drift for the nonlinear plasma viscosity [79, 84].

6. Transport processes in axisymmetric tokamaks

Neoclassical transport theory for axisymmetric tokamaks has been reviewed in [6, 7], where the methods of solutions and the physics involved are illustrated in detail. Transport coefficients have since been calculated using numerical codes [85–87], which indicate that analytic coefficients in [3, 6, 7] have an accuracy of 20%. Some of these numerical results have been incorporated in widely used fitting formulas [86, 88]. The moment approach is also implemented in the NCLASS code to consistently model neoclassical plasma flows and transport for axisymmetric tokamaks with impurities [89]. Here, a few subjects that have been developed after those reviews were published that are relevant to advanced tokamak operations are discussed.

6.1. Orbit trajectory in axisymmetric tokamaks

Particle trajectories are intimately related to the method of the solution to the drift kinetic equation when the collision frequency is infrequent enough so that particles can complete their collisionless trajectories. In axisymmetric tokamaks, particle trajectories are governed by the conservations of the toroidal canonical angular momentum p_ζ, and particle energy $Mv^2/2$ together with the invariant magnetic moment μ. Because p_ζ is conserved, at any two positions on the particle trajectory,

$$p_\zeta = \chi - I\frac{v_\parallel}{\Omega} = \chi_0 - I\frac{v_{\parallel 0}}{\Omega_0}, \tag{6.1.1}$$

where the gyro-phase dependent terms have been averaged out and the subscript 0 indicates that the quantity is evaluated at the reference position (χ_0, θ_0). The equation that determines the orbit trajectories is, then, assuming the poloidal $\boldsymbol{E}\times\boldsymbol{B}$ Mach number $M_{\rm p} = cE_r/(B_{\rm p}v_{\rm t}) < 1$ and neglecting the effects of orbit squeezing,

$$\begin{aligned}(\chi-\chi_0)^2 &+ 2\frac{Iv_{\parallel 0}}{\Omega_0}(\chi-\chi_0)\\ &+2\left(\frac{Iv_{\parallel 0}}{\Omega_0}\right)^2(\varepsilon_0\cos\theta_0 - \varepsilon\cos\theta)\\ &+2\left(\frac{I}{\Omega_0}\right)^2\frac{\mu B_0}{M}(\varepsilon_0\cos\theta_0-\varepsilon\cos\theta) = 0 + O(\varepsilon),\end{aligned} \tag{6.1.2}$$

where E_r is the radial electric field. Both $\varepsilon < 1$ and equation (1.1.2) have been used in deriving equation (6.1.2). The terms that involve $v_{\parallel 0}^2$ and $\mu B_0/M$ in equation (6.1.2) are the curvature and gradient B drifts, respectively.

6.1.1. Banana orbits. If the width of the orbit is much narrower than r, ε can be treated as a constant over the entire orbit trajectory. Because all particles pass through $\theta = 0$, it is convenient to choose $\theta_0 = 0$. In this case, the solution to equation (6.1.2) is

$$\begin{aligned}\chi-\chi_0 = &-\frac{Iv_{\parallel 0}}{\Omega_0} \pm \frac{I}{\Omega_0}\sqrt{2\varepsilon\left(2v_{\parallel 0}^2 + 2\mu B_0/M\right)}\\ &\times\left(k_b^2 - \sin^2\frac{\theta}{2}\right)^{1/2},\end{aligned} \tag{6.1.1.1}$$

where $k_b^2 = v_{\parallel 0}^2/[4\varepsilon(v_{\parallel 0}^2 + \mu B_0/M)]$. For $k_b^2 > 1$, particles are circulating. For $k_b^2 < 1$, particles are trapped in the $(1-\varepsilon\cos\theta)$ well. The typical width $(\Delta\chi)_b$ for trapped particles, i.e. bananas, scales as [6]

$$(\Delta\chi)_b \sim \sqrt{2\varepsilon}\frac{Iv_{\rm t}}{\Omega_0}. \tag{6.1.1.2}$$

6.1.2. Potato orbits. In the vicinity of the magnetic axis, the width of the orbits is comparable to the local minor radius r, ε cannot be treated as a constant [90–96] over orbit trajectories and equation (6.1.2) in general becomes a quartic algebraic equation. In that case, there does not seem to have a simple analytic solution to equation (6.1.2), and the numerical solution yields complicated particle trajectories in the region near the magnetic axis [92, 95]. However, for trajectories passing through the magnetic axis, equation (6.1.2) reduces to a cubic algebraic equation that has relatively compact analytic solutions [94].

The crucial χ dependence enters through $\varepsilon = C_\chi\sqrt{\chi}$, where $C_\chi = \sqrt{2q/(\delta IR)}$, and δ is the elongation parameter of

the magnetic surface. Choosing $\chi_0 = 0$ and neglecting $\mathrm{d}q/\mathrm{d}\chi$, the orbit equation becomes [94]

$$\bar{x}^3 + 2\frac{I v_{\|0}}{\Omega_0}\bar{x} - 2\frac{I^2 C_\chi}{\Omega_0^2}\left(v_{\|0}^2 + \mu B_0/M\right)\cos\theta = 0, \quad (6.1.2.1)$$

where $\bar{x} = \sqrt{\chi}$. Equation (6.1.2.1) describes particle trajectories that go through the magnetic axis. The trajectories can be categorized according to the sign and magnitude of the parameter $\sigma_\mathrm{p} k_\mathrm{p}$, where $\sigma_\mathrm{p} = v_{\|0}/|v_{\|0}|$ is the sign of $v_{\|0}$, and

$$k_\mathrm{p} = \frac{8}{27}\frac{(I\,|v_{\|0}|/\Omega_0)^3}{(I^2 C_\chi/\Omega_0^2)^2 (v_{\|0}^2 + \mu B_0)^2}. \quad (6.1.2.2)$$

When $-\infty < \sigma_\mathrm{p} k_\mathrm{p} < -1$, the poloidal particle speed defined as

$$\omega_\theta = v_\| - v_\| \frac{\partial}{\partial \chi}\left(I\frac{v_\|}{\Omega}\right) \quad (6.1.2.3)$$

does not vanish anywhere on the trajectories. These particles are circulating. There are two classes of circulating particles. One that encircles the magnetic axis is described by

$$\bar{x} = 2\hat{x}(-\sigma_\mathrm{p} k_\mathrm{p})^{1/6} \begin{cases} \cos\left(\dfrac{\beta}{3}\right), & \cos\theta > 0, \\ \sin\left(\dfrac{\pi}{6} + \dfrac{\beta}{3}\right), & \cos\theta < 0, \end{cases} \quad (6.1.2.4)$$

where $\hat{x} = [(I^2 C_\chi/\Omega_0^2)(v_{\|0}^2 + \mu B_0)]^{1/3}$. Angle β is related to the poloidal angle θ through the relation $\cos\beta = \cos\theta/\sqrt{-\sigma_\mathrm{p} k_\mathrm{p}}$ if $\cos\theta > 0$, and the relation $\cos\beta = |\cos\theta|/\sqrt{-\sigma_\mathrm{p} k_\mathrm{p}}$ if $\cos\theta < 0$. The other that intersects the magnetic axis but does not encircle it is described by

$$\bar{x} = 2\hat{x}(-\sigma_\mathrm{p} k_\mathrm{p})^{1/6} \sin\left(\frac{\pi}{6} + \frac{\beta}{3}\right), \cos\theta < 0. \quad (6.1.2.5)$$

This class of circulating particles exist in the second and third quadrants where $\cos\theta < 0$.

Particles with $0 < \sigma_\mathrm{p} k_\mathrm{p} < \infty$ are also circulating. Their trajectories follow the equation

$$\bar{x} = 2\hat{x}(\sigma_\mathrm{p} k_\mathrm{p})^{1/6} \sinh\left(\frac{\beta}{3}\right), \quad (6.1.2.6)$$

where $\sinh\beta = \cos\theta/\sqrt{\sigma_\mathrm{p} k_\mathrm{p}}$ for $\cos\theta > 0$. These particles also intersect and do not encircle the magnetic axis. They only exist in the first and fourth quadrants.

Trapped particles have a poloidal speed that vanishes at turning points on their trajectories, and are characterized by $-1 < \sigma_\mathrm{p} k_\mathrm{p} < 0$. Their trajectories have a complicated functional form. On the outer half of the trajectory,

$$\bar{x} = 2\hat{x}(-\sigma_\mathrm{p} k_\mathrm{p})^{1/6} \begin{cases} \cosh\left(\dfrac{\beta}{3}\right), \text{(i)} \\ \cos\left(\dfrac{\beta}{3}\right), \text{(ii)} \\ \sin\left(\dfrac{\pi}{6} + \dfrac{\beta}{3}\right), \text{(iii)} \end{cases} \quad (6.1.2.7)$$

and on the inner half of the trajectory,

$$\bar{x} = 2\hat{x}(-\sigma_\mathrm{p} k_\mathrm{p})^{1/6} \sin\left(\frac{\pi}{6} - \frac{\beta}{3}\right), \text{(iii)}. \quad (6.1.2.8)$$

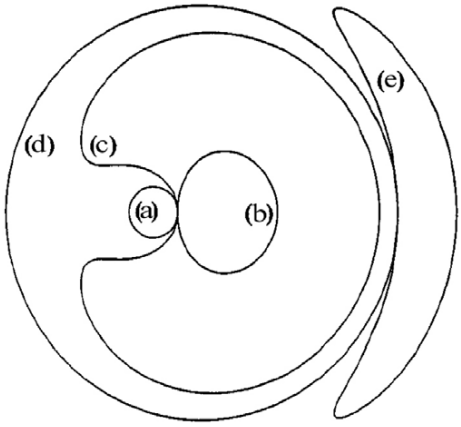

Figure 9. Particle orbits in the vicinity of the magnetic axis and a standard banana orbit are shown. Class (a), (b) and (d) are circulating orbits with $-\infty < \sigma_\mathrm{p} k_\mathrm{p} < -1$ and $0 < \sigma_\mathrm{p} k_\mathrm{p} < \infty$. Class (c) is trapped particles, i.e. potato orbits with $-1 < \sigma_\mathrm{p} k_\mathrm{p} < 0$. Class (e) is a standard banana orbit.

These two halves are separated by the turning points $\pm\theta_\mathrm{t} = \pm(\pi - \theta_c)$, where $\omega_\theta(\pm\theta_\mathrm{t}) = 0$. The angle θ_c satisfies $\sigma_\mathrm{p} k_\mathrm{p} + \cos^2\theta_c = 0$. The region (i) in equation (6.1.2.7) is limited to $-\theta_c < \theta < \theta_c$ and $\cos\theta > 0$. The region (ii) is marked by $\theta_c < \theta < \pi/2$, or $-\pi/2 < \theta < -\theta_c$ and $\cos\theta > 0$. The region (iii) in equations (6.1.2.7) and (6.1.2.8) is characterized either by $(\pi - \theta_c) > \theta > \pi/2$ or by $-(\pi - \theta_c) < \theta < -\pi/2$, and $\cos\theta < 0$. Trapped particles have the shape of potatoes and are thus named [93].

Typical trapped particles and circulating particles in the vicinity of the magnetic axis are shown in figure 9.

The typical width for potato orbits is [90–94]

$$(\Delta\chi)_\mathrm{p} \sim \left(\frac{I^2 C_\chi v_\mathrm{t}^2}{\Omega_0^2}\right)^{2/3}. \quad (6.1.2.9)$$

The ratio of the potato orbit width of ions to that of electrons is $(M_\mathrm{i}/M_\mathrm{e})^{2/3}$ when measured in poloidal flux ψ. The fraction of trapped potato orbits scales as [90–94]

$$f_\mathrm{p} \sim \left(\frac{I C_\chi^2 v_\mathrm{t}}{\Omega_0}\right)^{1/3}, \quad (6.1.2.10)$$

which differs from the fraction of banana orbits. It should be noted that f_p also depends on the mass and temperature of the species. From these estimates, the ion heat conductivity scales as [94], using random walk argument,

$$\chi_\mathrm{i} \sim \nu_\mathrm{i}\left(\frac{I v_\mathrm{t}}{\Omega_0}\right)^{7/3} C_\chi^{2/3}, \quad (6.1.2.11)$$

in the tokamak magnetic coordinates. The potato transport coefficients are valid over a region wider than the potato width.

6.2. Parallel plasma viscosity in axisymmetric tokamaks away from the magnetic axis

In axisymmetric tokamaks, parallel components of the viscous forces (including both viscous and heat viscous forces) play

the key role in the neoclassical transport theory in the banana–plateau regime. Once the closure relations for the parallel viscous forces are known, all the transport coefficients in the banana and plateau regimes are known. In these regimes, the drift kinetic equation (equation (5.2.5)) has a singularity at $v_\parallel = 0$ in the region away from the magnetic axis. There are two ways to resolve this singularity. One is by collisions and this leads to the plateau regime. The other is by the non-linear particle trajectories, which results in the banana regime.

6.2.1. Banana regime This regime is defined by $\nu_* < 1$. The singularity at $v_\parallel = 0$ in the drift kinetic equation (equation (5.2.5)) is resolved by non-linear particle trajectories. Using $\nu_* < 1$ as the auxiliary expansion parameter, equation (5.2.5) can be further expanded and the leading order equation is

$$v_\parallel \boldsymbol{n}\cdot\nabla h_0 + \frac{2v^2}{v_t^2}\left(\frac{3v_\parallel^2}{2v^2}-\frac{1}{2}\right) f_M\left[V^\theta - \frac{2}{5}L_1^{(3/2)}\frac{q^\theta}{p}\right] \times \boldsymbol{n}\cdot\nabla B = 0, \tag{6.2.1.1}$$

and the next order equation is

$$v_\parallel \boldsymbol{n}\cdot\nabla\theta\frac{\partial h_1}{\partial\theta} = C(h_0), \tag{6.2.1.2}$$

where the subscript in h indicates the order in the auxiliary expansion. Note that the non-linear particle dynamics along the magnetic field line described by $v_\parallel$ is kept because the independent variables are E and μ, but the finite width of particle orbits is not because the radial drift motion is neglected in equations (5.2.5) and (6.2.1.1).

Integrating equation (6.2.1.1) yields

$$h_0 = -\frac{2}{v_t^2}v_\parallel B f_M\left[V^\theta - \frac{2}{5}L_1^{(3/2)}\frac{q^\theta}{p}\right] + g_b(\chi, E, \mu), \tag{6.2.1.3}$$

where $g_b(\chi, E, \mu)$ is an integration constant to be determined from the constraint condition of equation (6.2.1.2) and boundary conditions. The constraint condition is to guarantee that h_1 is periodic in θ. The boundary condition for circulating particles is

$$h(\theta = 0) = h(\theta = 2\pi), \tag{6.2.1.4}$$

because the system is periodic in θ. For trapped particles, the reflection boundary condition is satisfied, i.e.

$$h_+(\theta_t) = h_-(\theta_t), \tag{6.2.1.5}$$

and

$$h_+(-\theta_t) = h_-(-\theta_t), \tag{6.2.1.6}$$

where the subscripts $\pm$ indicate the sign of $v_\parallel$ defined as $\sigma = v_\parallel/|v_\parallel|$, and $\pm\theta_t$ are turning points that satisfy $v_\parallel(\chi, \pm\theta_t, E, \mu) = 0$. Integrating equation (6.2.1.2) and using the boundary conditions in equations (6.2.1.4)–(6.2.1.6) yield the constraint condition

$$\langle C(h_0)\rangle_t = 0, \tag{6.2.1.7}$$

where the angular brackets denote the annihilator defined as $\langle\cdot\rangle_t = \int_0^{2\pi}\frac{d\theta}{v_\parallel}B\sqrt{g}(\cdot)$ for circulating particles, $\langle\cdot\rangle_t = \sum_\sigma\int_{-\theta_t}^{\theta_t}\frac{d\theta}{|v_\parallel|}B\sqrt{g}(\cdot)$ for trapped particles, and $\sqrt{g} = 1/\boldsymbol{B}\cdot\nabla\theta$. Equation (6.2.1.7) is an equation for the integration constant g_b. The function g_b must be an odd function of σ by examining equation (6.2.1.7). Thus, $g_b = 0$ for trapped particles after imposing the reflection boundary condition. Substituting h_0 in equation (6.2.1.3) into equation (6.2.1.7) yields [7]

$$g_b = -\sigma\frac{f_M\langle B^2\rangle}{v_t^2 B_M}\int_1^\lambda \frac{d\lambda'}{\langle|v_\parallel|/v\rangle}\left[V^\theta - \frac{2}{5}L_1^{(3/2)}\frac{q^\theta}{p}\right], \tag{6.2.1.8}$$

for circulating particles, where $\lambda = \mu B_M/(Mv^2/2)$, and B_M is the global maximum value of B on the magnetic surface. For axisymmetric tokamaks, B_M is also the maximum value of B on a given magnetic field line. The function h_0 in large aspect ratio tokamaks is determined.

Using the definition for the parallel viscous force and equation (5.2.5) yield a quadratic form for the parallel viscous force

$$\begin{pmatrix}\langle\boldsymbol{B}\cdot\nabla\cdot\overleftrightarrow{\pi}\rangle\\ \langle\boldsymbol{B}\cdot\nabla\cdot\overleftrightarrow{\Theta}\rangle\end{pmatrix} = -\left\langle\int d\boldsymbol{v}\left\{\frac{Mv_t^2}{2}\begin{pmatrix}1\\ x^2-5/2\end{pmatrix} \times\frac{hC(h)}{f_M\left[V^\theta - \frac{2}{5}L_1^{(3/2)}\frac{q^\theta}{p}\right]}\right\}\right\rangle. \tag{6.2.1.9}$$

Flux surface averaged parallel viscous forces are, after substituting h_0 into equation (6.2.1.9),

$$\begin{pmatrix}\langle\boldsymbol{B}\cdot\nabla\cdot\overleftrightarrow{\pi}\rangle\\ \langle\boldsymbol{B}\cdot\nabla\cdot\overleftrightarrow{\Theta}\rangle\end{pmatrix} = NM\langle B^2\rangle\begin{pmatrix}\mu_1 & \mu_2\\ \mu_2 & \mu_3\end{pmatrix}\begin{pmatrix}V^\theta\\ \frac{2}{5}\frac{q^\theta}{p}\end{pmatrix}, \tag{6.2.1.10}$$

where the viscous coefficients are $\mu_j = (8/3\sqrt{\pi})\int_0^\infty dx\times x^4 e^{-x^2}(x^2-5/2)^{j-1}f_t\nu_D$ for $j = 1-3$, which are the large aspect ratio limit of the viscous coefficients for finite aspect ratio tokamaks [7]:

$$\mu_j = \left(8/3\sqrt{\pi}\right)\int_0^\infty dx x^4 e^{-x^2}\left(x^2-5/2\right)^{j-1}(f_t/f_c)\,\nu_D. \tag{6.2.1.11}$$

The coefficients in equation (6.2.1.11) are obtained by solving the conventional drift kinetic equation i.e. equation (5.2) and converting the driving term from the plasma gradients to plasma flows. The fraction of trapped particles is defined as $f_t = 1 - f_c$, and the fraction of circulating particles f_c is defined as [7]

$$f_c = \frac{3}{4}\frac{\langle B^2\rangle}{B_M^2}\int_0^1 d\lambda\frac{\lambda}{\langle|v_\parallel/v|\rangle}. \tag{6.2.1.12}$$

A good approximate expression for f_c, which can be evaluated efficiently by the numerical method presented in [97], is $f_c = 1 - 1.46\sqrt{\varepsilon} + 0.46\varepsilon$. Thus, when $\varepsilon\to 1$, $f_c\to 0$ as expected. It is obvious that viscous forces are Onsager symmetric. As noted previously that the surface averaged parallel viscous forces in equation (6.2.1.10) are valid even when there are external momentum and heat flux inputs as long as those source terms have a pitch angle dependence scales as $v_\parallel f_M$. The inductive electric field $\boldsymbol{n}\cdot\boldsymbol{E}^{(A)}$ in the parallel momentum equation certainly belongs to that class of external

sources. Thus, the viscous forces derived here are applicable to calculate transport consequences resulting from the inductive electric field.

Even though h is no longer localized in the velocity space, h_0 in equation (6.2.1.3) is a valid solution at the unity aspect ratio limit where $g_b = 0$. Indeed, it is straightforward to show that by taking the $v_\parallel$ and $v_\parallel L_1^{(3/2)}$ moments of equation (5.2.1) yields the proper parallel flows at the $\varepsilon = 1$ limit [98]. Furthermore, it can be shown that finite aspect ratio viscous coefficients in equation (6.2.1.11) can also be derived from equation (6.2.1.3) when the method used to determine g_b in terms of poloidal flows developed in [7] is employed by imposing that $v_\parallel$ and $v_\parallel L_1^{(3/2)}$ moments of h_0 vanish. Thus, it is possible that the equation for h is also approximately valid when ε is finite in the banana regime.

In this review, viscous forces in axisymmetric tokamaks are expressed in the form in equation (6.2.1.10) except for the fact that viscous coefficients are different in various asymptotic limits when different physics are involved.

There are four unknowns in the parallel viscous forces in equation (6.2.1.10), i.e. electron and ion parallel flow speed $V_\parallel$ and heat flow $q_\parallel$. The four equations for these unknowns are the flux surface averaged electron and ion parallel momentum and heat flux balance equations

$$\left\langle \boldsymbol{B}\cdot\nabla\cdot\overleftrightarrow{\pi}\right\rangle = \langle \boldsymbol{B}\cdot\boldsymbol{F}_1\rangle\,, \tag{6.2.1.13}$$

$$\left\langle \boldsymbol{B}\cdot\nabla\cdot\overleftrightarrow{\Theta}\right\rangle = \langle \boldsymbol{B}\cdot\boldsymbol{F}_2\rangle\,. \tag{6.2.1.14}$$

The inductive electric field $\langle \boldsymbol{B}\cdot\boldsymbol{E}^{(A)}\rangle$ can also be added to the momentum balance equation in equation (6.2.1.13). However, because coupled equations are linear, unless the electric resistivity needs to be calculated, it is not necessary to include such a term. The explicit expressions for the parallel components of the friction forces are [7] $\boldsymbol{n}\cdot\boldsymbol{F}_{1\mathrm{i}} \equiv F_{1\mathrm{i}} = -\boldsymbol{n}\cdot\boldsymbol{F}_{1\mathrm{e}} \equiv -F_{1\mathrm{e}} = -l^{\mathrm{e}}_{11}(V_{\parallel\mathrm{i}} - V_{\parallel\mathrm{e}}) - (2/5)l^{\mathrm{e}}_{12}q_{\parallel\mathrm{e}}/p_{\mathrm{e}}$, $\boldsymbol{n}\cdot\boldsymbol{F}_{2\mathrm{e}} \equiv F_{2\mathrm{e}} = -l^{\mathrm{e}}_{12}(V_{\parallel\mathrm{i}} - V_{\parallel\mathrm{e}}) - (2/5)l^{\mathrm{e}}_{22}q_{\parallel\mathrm{e}}/p_{\mathrm{e}}$ and $\boldsymbol{n}\cdot\boldsymbol{F}_{2\mathrm{i}} \equiv F_{2\mathrm{i}} = -(2/5)l^{\mathrm{i}}_{22}q_{\parallel\mathrm{i}}/p_{\mathrm{i}}$, where $l^{\mathrm{e}}_{11} = N_{\mathrm{e}}M_{\mathrm{e}}\nu_{\mathrm{ei}}$, $l^{\mathrm{e}}_{12} = 1.5l^{\mathrm{e}}_{11}$, $l^{\mathrm{e}}_{22} = (13/4 + \sqrt{2}/Z)l^{\mathrm{e}}_{11}$ and $l^{\mathrm{i}}_{22} = \sqrt{2}N_{\mathrm{i}}M_{\mathrm{i}}\nu_{\mathrm{ii}}$. Note that $\sum_j \boldsymbol{n}\cdot\boldsymbol{F}_{1j} = 0$, which is a statement of the momentum conservation of the Coulomb collision operator.

In the unity aspect ratio limit where $\varepsilon \to 1$, the fraction of circulating particles $f_{\mathrm{c}} \to 0$, and $\mu_j \to \infty$, i.e. the parallel viscous forces approach infinity. In this limit, the leading order solutions, using the small parameter that is the ratio of the friction forces to the viscous forces, to equations (6.2.1.13) and (6.2.1.14) are

$$V^\theta = 0, \tag{6.2.1.15}$$

and

$$q^\theta = 0, \tag{6.2.1.16}$$

for each species. This implies that the poloidal flow is forbidden when all particles are trapped. However, the parallel flow remains finite and is [7, 98]

$$\frac{V_\parallel}{B} = -\frac{Ic}{B^2}\left(\Phi' + \frac{p'}{Ne}\right), \tag{6.2.1.17}$$

for each species. Thus, even when all particles are trapped, the fluid flow along the magnetic field line is finite. The parallel heat flow is [7, 98]

$$\frac{q_\parallel}{B} = -\frac{5}{2}p\frac{IcT}{eB^2}\frac{T'}{T}, \tag{6.2.1.18}$$

for each species. The parallel flows in equations (6.2.1.17) and (6.2.1.18) include Pfirsch–Schlüter flows as well. Summing the result in equation (6.2.1.17) over plasma species yields a net plasma current along the magnetic field line [7, 98]:

$$\frac{J_\parallel}{B} = -\frac{Ic}{B^2}P', \tag{6.2.1.19}$$

which is diamagnetic in nature. Thus, the plasma current along the magnetic field line remains finite even when all particles are trapped. The current in equation (6.2.1.19) can be decomposed into the bootstrap current $J_{\parallel\mathrm{b}}$ and the Pfirsch–Schlüter current $J_{\parallel\mathrm{ps}}$:

$$\frac{J_{\parallel\mathrm{b}}}{B} = -\frac{IcP'}{\langle B^2\rangle} \tag{6.2.1.20}$$

and

$$\frac{J_{\parallel\mathrm{ps}}}{B} = -IcP'\left(\frac{1}{B^2} - \frac{1}{\langle B^2\rangle}\right). \tag{6.2.1.21}$$

The ion heat flux consists of both the heat viscous driven flux in equation (4.1.1.13) and the heat friction driven flux in equation (4.1.1.14). The ion heat viscous force, in the next order in the ratio of the friction forces to the viscous forces, is

$$\left\langle \boldsymbol{B}\cdot\nabla\cdot\overleftrightarrow{\Theta}_{\mathrm{i}}\right\rangle = l^{\mathrm{i}}_{22}\frac{IcT_{\mathrm{i}}'}{e_{\mathrm{i}}}, \tag{6.2.1.22}$$

by substituting equation (6.2.1.18) into (6.2.1.14). Thus, the ion heat viscous driven flux is, using the expression in equation (4.1.1.13),

$$\frac{q_{\mathrm{i}}^{\mathrm{bp}}}{\mathrm{T_i}} = -l^{\mathrm{i}}_{22}\frac{I^2c^2T_{\mathrm{i}}'}{e_{\mathrm{i}}^2}\frac{1}{\langle B^2\rangle}, \tag{6.2.1.23}$$

and the ion heat friction driven flux is, by substituting equation (6.2.1.18) into equation (4.1.1.14),

$$\frac{q_{\mathrm{i}}^{\mathrm{ps}}}{T_{\mathrm{i}}} = -l^{\mathrm{i}}_{22}\frac{I^2c^2T_{\mathrm{i}}'}{e_{\mathrm{i}}^2}\left(\left\langle\frac{1}{B^2}\right\rangle - \frac{1}{\langle B^2\rangle}\right). \tag{6.2.1.24}$$

Thus, the total ion heat flux $q_{\mathrm{i}}/T_{\mathrm{i}}$, which is the sum of both viscous and friction forces driven flux, is

$$\frac{q_{\mathrm{i}}}{T_{\mathrm{i}}} = -l^{\mathrm{i}}_{22}\frac{I^2c^2T_{\mathrm{i}}'}{e_{\mathrm{i}}^2}\left\langle\frac{1}{B^2}\right\rangle. \tag{6.2.1.25}$$

In the unity aspect ratio limit, the Pfirsch–Schlüter heat flux in equation (6.2.1.24) not only exists but also is important in the banana regime [98].

For finite values of the viscous coefficients μ_js, relatively simple expressions for the ion poloidal flow and ion heat flux can be obtained for arbitrary aspect ratio tokamaks by exploring $\sqrt{M_{\mathrm{i}}/M_{\mathrm{e}}} > 1$. From

$$\sum_{j=\mathrm{i,e}}\left\langle \boldsymbol{B}\cdot\nabla\cdot\overleftrightarrow{\pi}_j\right\rangle = 0 \tag{6.2.1.26}$$

the ion poloidal flow is found to be

$$V_{\rm i}^{\theta} = -\frac{2}{5}\frac{\mu_{2\rm i}}{\mu_{1\rm i}}\frac{q_{\rm i}^{\theta}}{p_{\rm i}}. \tag{6.2.1.27}$$

The poloidal ion heat flow can be calculated, using equation (3.2.20), ion heat flux balance equations (6.2.1.14) and (6.2.1.27), to obtain

$$\frac{2}{5}\frac{q_{\rm i}^{\theta}}{p_{\rm i}} = \frac{-\mu_{2\rm i}V_{\rm i}^{\theta} + \left[l_{22}^{\rm i}/(N_{\rm i}M_{\rm i})\right]\left[IcT_{\rm i}'/\left(e_{\rm i}\left\langle B^2\right\rangle\right)\right]}{\mu_{3\rm i} + l_{22}^{\rm i}/(N_{\rm i}M_{\rm i})}, \tag{6.2.1.28}$$

and

$$V_{\rm i}^{\theta} = -\frac{\mu_{2\rm i}l_{22}^{\rm i}/(N_{\rm i}M_{\rm i})}{|\mu_{\rm i}| + \mu_{1\rm i}l_{22}^{\rm i}/(N_{\rm i}M_{\rm i})}\frac{IcT_{\rm i}'}{e_{\rm i}\left\langle B^2\right\rangle}, \tag{6.2.1.29}$$

where $|\mu_{\rm i}| = \mu_{1\rm i}\mu_{3\rm i} - \mu_{2\rm i}^2$. In the limit of $\varepsilon < 1$, $V_{\rm i}^{\theta}$ reduces to the familiar expression

$$V_{\rm i}^{\theta} = -\frac{\mu_{2\rm i}}{\mu_{1\rm i}}\frac{IcT_{\rm i}'}{e_{\rm i}\left\langle B^2\right\rangle}, \tag{6.2.1.30}$$

where $\mu_{2\rm i}/\mu_{1\rm i} = -1.17$ [6, 7]. The banana–plateau heat flux $q_{\rm i}^{\rm bp}$ driven by $\langle \boldsymbol{B}\cdot\nabla\cdot\overleftrightarrow{\Theta}_{\rm i}\rangle$ is

$$\frac{q_{\rm i}^{\rm bp}}{T_{\rm i}} = -NM\left\langle B^2\right\rangle\left(\frac{Ic}{e_{\rm i}\left\langle B^2\right\rangle}\right)^2\frac{\left(|\mu_{\rm i}|/\mu_{1\rm i}\right)\left[l_{22}^{\rm i}/(N_{\rm i}M_{\rm i})\right]}{|\mu_{\rm i}|/\mu_{1\rm i} + l_{22}^{\rm i}/(N_{\rm i}M_{\rm i})}T_{\rm i}'. \tag{6.2.1.31}$$

The heat flux can be expressed as the combination of two parts [99]

$$\left(\frac{q_{\rm i}^{\rm bp}}{T_{\rm i}}\right)^{-1} = \left(\frac{q_{\rm i}^{\rm bp}}{T_{\rm i}}\right)_{\rm f}^{-1} + \left(\frac{q_{\rm i}^{\rm bp}}{T_{\rm i}}\right)_{\mu}^{-1}, \tag{6.2.1.32}$$

where the part that depends on friction force, valid when $\varepsilon \to 1$, is

$$\left(\frac{q_{\rm i}^{\rm bp}}{T_{\rm i}}\right)_{\rm f}^{-1} = -N_{\rm i}M_{\rm i}\left\langle B^2\right\rangle\left(\frac{Ic}{e_{\rm i}\left\langle B^2\right\rangle}\right)^2\frac{l_{22}^{\rm i}}{N_{\rm i}M_{\rm i}}T_{\rm i}', \tag{6.2.1.33}$$

and the heat viscous part, appropriate when $\varepsilon \to 0$, is

$$\left(\frac{q_{\rm i}^{\rm bp}}{T_{\rm i}}\right)_{\mu}^{-1} = -N_{\rm i}M_{\rm i}\left\langle B^2\right\rangle\left(\frac{Ic}{e_{\rm i}\left\langle B^2\right\rangle}\right)^2\frac{|\mu_{\rm i}|}{\mu_{1\rm i}}T_{\rm i}'. \tag{6.2.1.34}$$

The proper way to combine these two limits is the well-known inverse law as shown in equation (6.2.1.32). The total heat flux is the sum of $q_{\rm i}^{\rm bp}$ and $q_{\rm i}^{\rm ps}$.

The bootstrap current can be obtained by solving equations (6.2.1.13) and (6.2.1.14) for electrons for plasma current. The result is [7]

$$\begin{aligned}\left\langle J_{\parallel \rm b}B\right\rangle = -\sigma_{\rm eff}\frac{M_{\rm e}\mu_{1\rm e}}{N_{\rm e}e_{\rm e}^2}Ic\Bigg[&\left(1 + \frac{l_{12}^{\rm eb}}{l_{22}^{\rm eb}}\frac{\mu_{2\rm e}}{\mu_{1\rm e}}\right)\\ &\times\left(P' + \frac{\mu_{2\rm i}l_{22}^{\rm i}/N_{\rm i}M_{\rm i}}{|\mu_{\rm i}| + \mu_{1\rm i}l_{22}^{\rm i}/N_{\rm i}M_{\rm i}}\frac{1}{Z}N_{\rm e}T_{\rm i}'\right)\\ &+N_{\rm e}T_{\rm e}'\left(\frac{\mu_{2\rm e}}{\mu_{1\rm e}} + \frac{l_{12}^{\rm eb}}{l_{22}^{\rm eb}}\frac{\mu_{3\rm e}}{\mu_{1\rm e}}\right)\Bigg],\end{aligned} \tag{6.2.1.35}$$

where $l_{11}^{\rm eb} = l_{11}^{\rm e} + N_{\rm e}M_{\rm e}\mu_{1\rm e}$, $l_{12}^{\rm eb} = l_{12}^{\rm e} - N_{\rm e}M_{\rm e}\mu_{2\rm e}$, $l_{22}^{\rm eb} = l_{22}^{\rm e} + N_{\rm e}M_{\rm e}\mu_{3\rm e}$, and neoclassical plasma conductivity is [6, 7]

$$\sigma_{\rm eff} = \left(N_{\rm e}e_{\rm e}\right)^2\frac{l_{22}^{\rm eb}}{l_{11}^{\rm eb}l_{22}^{\rm eb} - \left(l_{12}^{\rm eb}\right)^2}. \tag{6.2.1.36}$$

In the case of $\varepsilon \to 1$, all particles are trapped, and $\sigma_{\rm eff} \to 0$. It is straightforward to show that when $\varepsilon \to 1$, equation (6.2.1.35) reproduces equation (6.2.1.20).

It should be noted that the transport fluxes in the banana regime obtained using the eight-moment approach are not as accurate as those in [100] because only P_1 dependence in the momentum restoring terms is kept. Indeed, by including the P_3 moment in the collision operator, the accuracy of the viscous coefficients in the banana regime can be greatly improved, as demonstrated in [101, 102]. Here, P_3 is the Legendre polynomial. These modified coefficients can be used to improve the accuracy of NCLASS.

6.2.2. Plateau regime. When collisions are frequent enough so that $\nu_* > 1$, but infrequent enough so that $\nu/\omega_{\rm t} < 1$, plasmas are in the plateau regime. Here, $\omega_{\rm t} = v_{\rm t}/Rq$ is the transit frequency. The condition $\nu_* > 1$ is used to neglect the mirror force that is responsible for the non-linear motion of the trapped particles. The condition $\nu/\omega_{\rm t} < 1$ is used to obtain the localized solution in the vicinity of the resonance. It is obvious that only when $\varepsilon < 1$, the asymptotic limit of the plateau regime can exist. In this regime, the singularity at $v_{\parallel} = 0$ is removed by collisions.

By changing independent variables from (χ, θ, E, μ) to $(\chi, \theta, v_{\parallel}, v)$ in the linear drift kinetic equation, equation (5.2.5) becomes

$$\begin{aligned}&v_{\parallel}\boldsymbol{n}\cdot\nabla h - \frac{1}{2}\left(v^2 - v_{\parallel}^2\right)\boldsymbol{n}\cdot\nabla\left(\ln B\right)\frac{\partial h}{\partial v_{\parallel}}\\ &\quad+\frac{2v^2}{v_{\rm t}^2}\left(\frac{3v_{\parallel}^2}{2v^2} - \frac{1}{2}\right)f_{\rm M}\left[V^{\theta} - \frac{2}{5}L_1^{(3/2)}\frac{q^{\theta}}{p}\right]\boldsymbol{n}\cdot\nabla B\\ &\quad= \frac{\nu_{\rm D}}{2}\frac{\partial}{\partial\left(v_{\parallel}/v\right)}\left(1 - \frac{v_{\parallel}^2}{v^2}\right)\frac{\partial h}{\partial\left(v_{\parallel}/v\right)}.\end{aligned} \tag{6.2.2.3}$$

The second term on the left-hand side of equation (6.2.2.3) is the mirror force term that is responsible for pulling trapped particles back from the turning points and can be neglected when $\nu_* > 1$. It is trivial to realize that it is not because particles are highly circulating but because $v_{\parallel}$ is an independent variable that $v_{\parallel}$ is not a function of the poloidal angle θ [103]. By contrast, in the banana regime, $v_{\parallel}$ is not an independent variable but rather a function of E, μ, χ and θ. Thus, in the plateau regime, the equation to be solved is [81]

$$\begin{aligned}&v_{\parallel}\boldsymbol{n}\cdot\nabla h + \frac{2v^2}{v_{\rm t}^2}\left(\frac{3v_{\parallel}^2}{2v^2} - \frac{1}{2}\right)f_{\rm M}\left[V^{\theta} - \frac{2}{5}L_1^{(3/2)}\frac{q^{\theta}}{p}\right]\boldsymbol{n}\cdot\nabla B\\ &\quad= \frac{\nu_{\rm D}}{2}\frac{\partial}{\partial\left(v_{\parallel}/v\right)}\left(1 - \frac{v_{\parallel}^2}{v^2}\right)\frac{\partial h}{\partial\left(v_{\parallel}/v\right)}.\end{aligned} \tag{6.2.2.4}$$

Equation (6.2.2.4) can be solved either using a Krook model to approximate the pitch angle scattering operator on the right-hand side of equation (6.2.2.4) or approximating the pitch angle scattering operator as

$$\frac{\nu_{\rm D}}{2}\frac{\partial}{\partial\left(v_{\parallel}/v\right)}\left(1 - \frac{v_{\parallel}^2}{v^2}\right)\frac{\partial h}{\partial\left(v_{\parallel}/v\right)} \approx \frac{\nu_{\rm D}}{2}\frac{\partial^2 h}{\partial\left(v_{\parallel}/v\right)^2} \tag{6.2.2.5}$$

because the localized distribution function is centred around $(v_\parallel/v) \approx 0$. The width of the singular layer can be estimated by balancing the pitch angle scattering operator with the collisional broadening of the singularity at $v_\parallel = 0$, i.e. the first term on the left-hand side of equation (6.2.2.4). Indeed, the proper interpretation for that term is that it represents the collisional broadening of the resonance at $v_\parallel = 0$. Expanding $v_\parallel$ in terms of Taylor series at $v_\parallel = 0$ yields

$$v_\parallel = 0 + \frac{\mathrm{d}v_\parallel}{\mathrm{d}v_\parallel}\Big)_{v_\parallel=0} v_\parallel, \tag{6.2.2.6}$$

where the 0 on the right-hand side of equation (6.2.2.6) indicates the singularity or resonance, and the second term denotes the collisional broadening. Thus, the collisional broadening yields a singular layer width $\Delta(v_\parallel/v) \sim (\nu/\omega_\mathrm{t})^{1/3} < 1$. Using the Krook model for the collision operator, i.e. $C(h) = -\nu h$, and expanding h as

$$h = h_s \sin\theta + h_c \cos\theta \tag{6.2.2.7}$$

yield the resonant part of the solution

$$h_s = \frac{\nu}{\left(v_\parallel \boldsymbol{n}\cdot\nabla\theta\right)^2 + \nu^2}\frac{v^2}{v_\mathrm{t}^2}\left(\boldsymbol{B}\cdot\nabla\theta\right)\varepsilon f_\mathrm{M} \times\left[V^\theta - \frac{2}{5}L_1^{(3/2)}\frac{q^\theta}{p}\right], \tag{6.2.2.8}$$

and the non-resonant part of the solution

$$h_c = -\frac{v_\parallel \boldsymbol{n}\cdot\nabla\theta}{\left(v_\parallel \boldsymbol{n}\cdot\nabla\theta\right)^2 + \nu^2}\frac{v^2}{v_\mathrm{t}^2}\left(\boldsymbol{B}\cdot\nabla\theta\right)\varepsilon f_\mathrm{M} \times\left[V^\theta - \frac{2}{5}L_1^{(3/2)}\frac{q^\theta}{p}\right]. \tag{6.2.2.9}$$

Equation (1.1.2) has been employed in obtaining equations (6.2.2.8) and (6.2.2.9). The plateau asymptotic limit is reached when $\nu/\omega_\mathrm{t} < 1$, and in that limit the resonance function

$$\frac{\nu}{\left(v_\parallel \boldsymbol{n}\cdot\nabla\theta\right)^2 + \nu^2} \to \pi\delta\left(v_\parallel \boldsymbol{n}\cdot\nabla\theta\right), \tag{6.2.2.10}$$

where $\delta(s)$ is a delta function in the resonant part of the solution. The resonance occurs at the singular point $v_\parallel = 0$. Thus, fundamentally, the solution in the plateau regime results from the resonance at which the kinetic part of the drift kinetic equation vanishes. Indeed, this is a generic behaviour in the kinetic theory. One can view the resonance as Landau resonance [104] for a zero frequency mode. The non-resonant solution does not contribute to the flux surface averaged parallel viscous forces because it is out of phase with $\boldsymbol{n}\cdot\nabla B$ in the expressions of the parallel viscous forces.

The parallel viscous forces are obtained by substituting h_s in equation (6.2.2.8) into the expressions for the parallel viscous forces in equations (4.1.4.1) and (4.1.4.2). The viscous coefficient μ_j is then [81]

$$\mu_j = \frac{\sqrt{\pi}}{4}\omega_\mathrm{t}\varepsilon^2 2\int_0^\infty \mathrm{d}x x^5\left(x^2 - \frac{5}{2}\right)^{j-1}\mathrm{e}^{-x^2}, \tag{6.2.2.11}$$

for $j = 1-3$. The energy integrals in equation (6.2.1.11) can be evaluated and they are, respectively, $C_1 = \Gamma(3)$, $C_2 = \Gamma(4) - (5/2)\Gamma(3)$ and $C_3 = \Gamma(5) - 5\Gamma(4) + (25/4)\Gamma(3)$. Here, $\Gamma(s)$ is the gamma function.

6.2.3. Pfirsch–Schlüter regime When $\nu/\omega_\mathrm{t} > 1$, plasmas are in the Pfirsch–Schlüter regime. In this regime because the collisional effects dominate, the linear drift kinetic equation in equation (5.2.5) reduces to

$$2\frac{v^2}{v_\mathrm{t}^2}\left(\frac{3}{2}\frac{v_\parallel^2}{v^2} - \frac{1}{2}\right) f_\mathrm{M}\boldsymbol{n}\cdot\nabla B\left(V^\theta - \frac{2}{5}L_1^{3/2}\frac{q^\theta}{p}\right) = C(h). \tag{6.2.3.1}$$

It can be solved by expanding the distribution function h in terms of Legendre polynomial P_2 and Laguerre polynomials of order (5/2), i.e. $L_j^{(5/2)}$ [7]. However, a simple Krook model $C(h) = -\nu_T h$ with a judiciously chosen collision frequency $\nu_T = 3\nu_\mathrm{D} + \nu_E$ for the collision operator yields viscous coefficients that are accurate to about 20% [7]. Here, ν_E is the energy exchange frequency and is defined as $\nu_E^{ab} = 2\nu_s^{ab} - 2\nu_\mathrm{D}^{ab} - \nu_\parallel^{ab}$, where $\nu_\parallel^{ab} = 2\nu_{ab}G(v/v_{\mathrm{t}b})/(v/v_{\mathrm{t}a})^3$ [30]. It is also easier to join results from various asymptotic limits using a Krook model in the Pfirsch–Schlüter [7, 105]. Thus,

$$h = -\nu_T^{-1}2\frac{v^2}{v_\mathrm{t}^2}\left(\frac{3}{2}\frac{v_\parallel^2}{v^2} - \frac{1}{2}\right) f_\mathrm{M}\boldsymbol{n}\cdot\nabla B\left[V^\theta - \frac{2}{5}L_1^{(3/2)}\frac{q^\theta}{p}\right], \tag{6.2.3.2}$$

when a Krook model for the collision operator is employed.

The viscous coefficients μ_js for $j = 1-3$ in the Pfirsch–Schlüter regime are, thus,

$$\mu_j = \frac{8}{5\sqrt{\pi}}\frac{v_\mathrm{t}^2\left\langle(\boldsymbol{n}\cdot\nabla B)^2\right\rangle}{\left\langle B^2\right\rangle}\int_0^\infty \mathrm{d}x x^6\mathrm{e}^{-x^2}\left(x^2 - \frac{5}{2}\right)^{j-1}\frac{1}{\nu_T}. \tag{6.2.3.3}$$

The parallel viscosity obtained here is mainly employed to calculate the poloidal flow damping in the Pfirsch–Schlüter regime and yields the well-known relation between the parallel flow and the radial electric field. It is known that because the viscous forces decrease with increasing collision frequency, bootstrap current in the Pfirsch–Schlüter regime is small because it scales as $(\nu/\omega_\mathrm{t})^{-2}$ and is usually neglected. However, because the factor $\langle(\boldsymbol{n}\cdot\nabla B)^2\rangle$ approaches infinity which compensates the $1/\nu$ dependence in the viscous forces, the viscous forces also drive a bootstrap current and contribute to the ion thermal conductivity when the aspect ratio A of tokamaks approaches unity. For a circular equilibrium with $B = [B_0/(1+\varepsilon\cos\theta)][(\varepsilon/q)\hat{\theta} + \hat{\zeta}]$,

$$\left\langle(\boldsymbol{n}\cdot\nabla B)^2\right\rangle = \left[\frac{\varepsilon^2}{2\left(1-\varepsilon^2\right)^{3/2}}\right]\left(\frac{B_0\varepsilon}{rq}\right)^2, \tag{6.2.3.4}$$

where $\hat{\theta}$ and $\hat{\zeta}$ are unit vectors in the poloidal and toroidal directions respectively [105]. Thus, when $\varepsilon = 1/A \to 1$, $\langle(\boldsymbol{n}\cdot\nabla B)^2\rangle \to \infty$. The factor $\langle(\boldsymbol{n}\cdot\nabla B)^2\rangle$ has been calculated numerically using an equilibrium code, and is shown in figure10 [106].

Thus, both $\langle\boldsymbol{B}\cdot\nabla\cdot\overleftrightarrow{\pi}\rangle$ and $\langle\boldsymbol{B}\cdot\nabla\cdot\overleftrightarrow{\Theta}\rangle$ diverge in unity aspect ratio tokamaks for any finite value of collision frequency. The consequences for the bootstrap current and plasma flows are that these quantities are exactly the same as those in the banana regime when $\varepsilon \to 1$. Furthermore, the heat viscous force driven ion heat flux also becomes comparable to the friction force driven ion heat flux. The total ion heat flux in the Pfirsch–Schlüter regime is the same as that in the banana

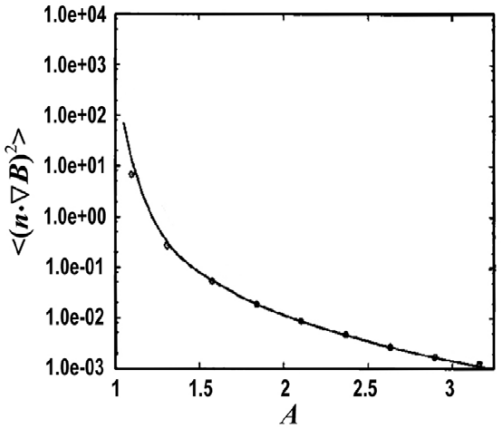

Figure 10. The geometric factor $\langle(\boldsymbol{n}\cdot\nabla B)^2\rangle$ as a function of the aspect ratio A for a fixed q profile and toroidal magnetic field strength on the axis. The circles are calculated from numerical equilibrium and the solid line is from equation (6.2.3.4).

regime in the $\varepsilon \to 1$ limit [98, 105]. This collisionless-like behaviour in the collisional Pfirsch–Schlüter regime appears when $\nu_t < v_t[\langle(\boldsymbol{n}\cdot\nabla B)^2\rangle/\langle B^2\rangle]^{1/2}$ by balancing the friction forces with the viscous forces in the collisional regime and neglecting the numerical coefficients of the order of unity.

6.2.4. Approximate analytic expressions for parallel viscous forces. To model tokamak plasmas, it is convenient to use a formula that joins analytic expressions of the parallel viscous forces in the asymptotic limits of the banana, plateau and Pfirsch–Schlüter regimes. This is accomplished by using the rational approximation. The approximate expression for the parallel viscous forces, after extending the analytic expressions for the parallel viscous forces to multiple poloidal modes in the $|\boldsymbol{B}|$ spectrum to allow for arbitrary magnetic surface shape, is [105]

$$\mu_j = \frac{8}{3\sqrt{\pi}}\int_0^\infty \mathrm{d}x x^4 \mathrm{e}^{-x^2}\frac{K_\mathrm{B}K_\mathrm{PS}}{K_\mathrm{B}+K_\mathrm{PS}}\left(x^2-\frac{5}{2}\right)^{j-1}, \tag{6.2.4.1}$$

for $j = 1-3$, where

$$K_\mathrm{B} = \frac{f_\mathrm{t}}{f_\mathrm{c}}\nu_\mathrm{D}, \tag{6.2.4.2}$$

$$K_\mathrm{PS} = \frac{3}{2}v_\mathrm{t}^2x^2\sum_{m=1}^{\infty}F_m\frac{\nu_T I_R^m}{\nu_T}, \tag{6.2.4.3}$$

$$F_m = \frac{2}{\langle B^2\rangle\langle\boldsymbol{B}\cdot\nabla\theta\rangle}\Big[\langle(\sin m\theta)\boldsymbol{n}\cdot\nabla B\rangle \times\langle(\sin m\theta)(B\cdot\nabla\theta)\boldsymbol{n}\cdot\nabla B\rangle +\langle(\cos m\theta)\boldsymbol{n}\cdot\nabla B\rangle\langle(\cos m\theta)(B\cdot\nabla\theta)\boldsymbol{n}\cdot\nabla B\rangle\Big], \tag{6.2.4.4}$$

$$\nu_T I_R^m = -\frac{3}{2}\left(\frac{\nu_T}{\omega_m}\right)^2-\frac{9}{2}\left(\frac{\nu_T}{\omega_m}\right)^4 +\left\{\frac{1}{4}+\left[\frac{3}{2}+\frac{9}{4}\left(\frac{\nu_T}{\omega_m}\right)^2\right]\left(\frac{\nu_T}{\omega_m}\right)^2\right\}\frac{2\nu_T}{\omega_m}\tan^{-1}\left(\frac{\omega_m}{\nu_T}\right), \tag{6.2.4.5}$$

and $\omega_m = v_\mathrm{t}xm\boldsymbol{n}\cdot\nabla\theta$. A similar expression for the viscosity coefficients that connects all regimes is also constructed in [107].

The expression in equation (6.2.4.1) has been benchmarked [105] using the Drift Kinetic Equation Solver (DKES) code [108]. A boundary layer analysis has been carried out to make the slope of the perturbed distribution function continuous across the trapped-circulating boundary that leads to the modification scales as $\sqrt{\nu}$ to transport fluxes in the banana regime [8]. This $\sqrt{\nu}$ scaling has been incorporated into the connection formulas for the transport coefficients that join all asymptotic limits in [6]. However, as can been seen in the figures in [105] that show the viscous coefficient versus the collision frequency for several values of the aspect ratio, the μ_j evaluated using equation (6.2.4.1) fits the DKES results quite well without the $\sqrt{\nu}$ scaling. Indeed, the connection formula that joins all asymptotic limits usually gives a fairly good description of the viscous coefficients or transport fluxes without the need of the results obtained from the boundary layer analysis. The μ_j shown in equation (6.2.4.1) has also been implemented in the NCLASS code to model neoclassical transport processes in axisymmetric tokamaks [89].

6.2.5. Effects of orbit squeezing and finite banana width. The orbit trajectories discussed in section 6.1 are based on the assumption that the width of a banana $\sqrt{\varepsilon}\rho_\mathrm{p}$ is much less than L_n. However, in the edge region of H-mode, L_n is comparable to ρ_p. In that case, the width of the banana orbits is squeezed from the standard scaling $\sqrt{\varepsilon}\rho_\mathrm{p}$ [109]. Thus, in the edge region of the H-mode plasmas, anomalous transport losses are improved as a result of the turbulence suppression [16, 17], and the neoclassical ion transport losses are also reduced due to the effects of orbit squeezing [110].

In the conventional neoclassical theory, the finite width of the banana orbits is neglected. The bounce motion is the zeroth order and the radial drift is the first order in gyroradius ordering. Thus, the bounce motion with zero banana width is the 'unperturbed' orbit. The information of the width of the banana orbits is obtained by integrating along the unperturbed orbits. The method employed in solving the kinetic equation for the theory for the effects of orbit squeezing has to include the finite width in the unperturbed orbits because in the (χ,θ,E,μ) space $v_\parallel$ only describes bounce motion and contains no orbit squeezing information. Here, $E = Mv^2/2+e\Phi$. Thus, the theory that describes effects of orbit squeezing intrinsically is a finite orbit width theory in the context of the local transport. In the limit when the orbit squeezing is insignificant, the theory becomes a theory for the finite banana width of large aspect ratio tokamaks.

6.2.5.1. Squeezed banana orbits. The squeezed banana orbit trajectories can be calculated from the constants of motion p_ζ and total particle energy $E = Mv^2/2 + e\Phi$, together with invariant magnetic moment μ. The energy conservation implies

$$\frac{v_\parallel^2}{2}+\frac{\mu B}{M}+\frac{e\Phi}{M} = \frac{v_{\parallel 0}^2}{2}+\frac{\mu B_0}{M}+\frac{e\Phi_0}{M}, \tag{6.2.5.1}$$

where the subscript 0 indicates that quantities are evaluated at the reference point (χ_0,θ_0). Expanding the equilibrium

potential yields

$$\Phi = \Phi_0 + \Phi_0'(\chi - \chi_0) + \frac{1}{2}\Phi_0''(\chi - \chi_0)^2 + \cdots. \quad (6.2.5.2)$$

The width of the orbits is obtained by solving equations (6.1.1), (6.2.5.1) and (6.2.5.2) for $(\chi - \chi_0)$ to yield [79, 110]

$$(\chi - \chi_0) = -\frac{I}{S\Omega_0}\left(v_{\|0} + \frac{I}{\Omega}\frac{e\Phi_0'}{M}\right) \pm \frac{I\omega_s}{S\Omega_0}, \quad (6.2.5.3)$$

where

$$\omega_s = \sigma_s\hat{\omega}_s\left(1 - k_s\sin^2\frac{\theta}{2}\right)^{1/2}, \quad (6.2.5.4)$$

$$\hat{\omega}_s = \left|v_{\|0} + \frac{I}{\Omega}\frac{e\Phi_0'}{M}\right|, \quad (6.2.5.5)$$

σ_s denotes the sign of ω_s, the orbit squeezing factor S is defined as [109]

$$S = 1 + \frac{I^2}{\Omega^2}\frac{e\Phi_0''}{M}, \quad (6.2.5.6)$$

and the pitch angle parameter k_s is

$$\frac{1}{k_s} = \frac{\left[v_{\|0} + Ie\Phi_0'/(\Omega M)\right]^2}{4|S|\varepsilon\left(v_{\|0}^2 + \mu B_0/M\right)}. \quad (6.2.5.7)$$

For trapped particles, $k_s > 1$ and for circulating particles, $k_s < 1$. Note that k_s is a constant of motion. For $S > 0$ particles are trapped on the weak field side of the torus, and θ_0 is chosen to be 0. When $S < 0$ particles are trapped on the strong field side of the torus, and $\theta_0 = \pi$. For $|S| > 1$, the transport fluxes do not depend on the sign of S. Without loss of generality S is chosen to be positive. It can be inferred from the expression of ω_s that the fraction of the trapped particles is increased by a factor of $\sqrt{S}$ to $\sqrt{\varepsilon S}$.

Using equation (6.2.5.3), equation (6.1.1) can be recast into [79]

$$\chi - p_\zeta = -\frac{I}{S\Omega_0}\left[(S-1)v_{\|0} + \frac{I}{\Omega_0}\frac{e\Phi_0'}{M}\right] + \frac{I\omega_s}{S\Omega_0} = \frac{Iv_\|}{\Omega}. \quad (6.2.5.8)$$

Because Φ_0''' is neglected, S is constant on particle trajectories, the difference between $\chi - p_\zeta$ and $I\omega_s/(S\Omega_0)$ is a constant of motion as can be seen from equation (6.2.5.8). Thus, $I\omega_s/(S\Omega_0)$ plays the role of $Iv_\|/\Omega$ in the conventional theory. It should also be noted that squeezed orbits only exist in $(E, \mu, p_\zeta, \theta)$ space and not in (E, μ, χ, θ) space from single particle point of view. Indeed, in (E, μ, χ, θ), the only sinusoidal variation in ω_s, which can be shown to be $(v_\| + Ic\Phi'/B)$, is associated with the equilibrium magnetic field in $v_\|$; and both the electrostatic potential Φ in $v_\|$, and the radial electric field Φ' are constant.

Examining the definition for S, it is obvious that the effects of squeezing are significant when $\rho_p|\mathrm{d}\ln E_r/\mathrm{d}r|$ is of the order of unity or larger. It is easier for ions to meet this requirement for having larger poloidal gyro-radii. This requirement is usually satisfied in the edge region of the H-mode plasmas and inside the internal transport barriers. The typical width of the trapped particles is, inferred from equation (6.2.5.3),

$$(\Delta\chi)_{\mathrm{Sb}} \sim \sqrt{2\varepsilon}\frac{Iv_t}{\Omega_0\sqrt{S}}. \quad (6.2.5.9)$$

Thus, the width of the bananas is reduced by a factor of $\sqrt{S}$ when $S > 1$ [79, 109, 110]. The corresponding ion heat flux is reduced by a factor of $S^{3/2}$ [110].

6.2.5.2. Linear drift kinetic equation and its solution. Because the width of the trapped particles is squeezed when $S > 1$, the transport fluxes must be modified. The squeezed orbit is a result of the finite width of the particle orbits. When particles drift to a neighbouring magnetic surface, they see a different value of the radial electric field, and thus experience a different value of the poloidal $\boldsymbol{E}\times\boldsymbol{B}$ drift if the radial electric field has a sharp radial gradient. Larger poloidal $\boldsymbol{E}\times\boldsymbol{B}$ drift leads to smaller radial width of the orbits. Thus, to describe the physics of the effects of the orbit squeezing, the radial drift motion must be included in the linear drift kinetic equation. The linear drift kinetic equation equation (5.4) becomes

$$v_\|\boldsymbol{n}\cdot\nabla f_1 + \boldsymbol{v}_d\cdot\nabla\theta\frac{\partial f_1}{\partial\theta} + \boldsymbol{v}_d\cdot\nabla\chi\frac{\partial f_1}{\partial\chi} = C(f_1) - \boldsymbol{v}_d\cdot\nabla\chi\frac{\partial f_M}{\partial\chi} - ev_\|E_\|^{(A)}\frac{\partial f_M}{\partial E}. \quad (6.2.5.2.1)$$

The linear terms of the left-hand side of equation (6.2.5.2.1) describe the particle motions. In this case, the drift motions, especially the radial drift motion, are included to describe orbits with finite radial width because even though $|f_1| < f_M$ but $|\partial f_1/\partial\chi| \sim |\partial f_M/\partial\chi|$ [111] Again, to treat the momentum restoring terms, and the driving terms that are proportional to $P_1(v_\|/v)f_M$, f_1 is expanded as

$$f_1 = \frac{2v_\|}{v_t^2}\left[V_\| - \frac{2}{5}L_1^{(3/2)}\frac{q_\|}{p}\right]f_M + h, \quad (6.2.5.2.2)$$

and the localized function h satisfies

$$v_\|\boldsymbol{n}\cdot\nabla h + \mathbf{v}_d\cdot\nabla\theta\frac{\partial h}{\partial\theta} + \mathbf{v}_d\cdot\nabla\chi\frac{\partial h}{\partial\chi} - C(h) \times 2\frac{v^2}{v_t^2}\left(\frac{1}{2} - \frac{3}{2}\frac{v_\|^2}{v_t^2}\right)f_M\left[V^\theta - \frac{2}{5}L_1^{(3/2)}\frac{q^\theta}{p}\right]\boldsymbol{n}\cdot\nabla B. \quad (6.2.5.2.3)$$

Terms that are smaller by a factor of ρ/L_n are neglected to obtain equation (6.2.5.2.3). Note that the $\boldsymbol{v}_d\cdot\nabla\theta\partial h/\partial\theta$, and $\boldsymbol{v}_d\cdot\nabla\chi\partial h/\partial\chi$ terms must be kept when parallel plasma flows are introduced to keep the small but finite poloidal $\boldsymbol{E}\times\boldsymbol{B}$ drift. The collision operator in equation (6.2.5.2.3) is the test particle pitch angle scattering operator because $\varepsilon < 1$ is assumed. The poloidal $\boldsymbol{E}\times\boldsymbol{B}$ drift Mach number M_p, and $V_\|/v_t$ are both assumed to be less than unity. With these assumptions, only the effects of the orbit squeezing are included in equation (6.2.5.2.3). Because $\varepsilon < 1$, $\boldsymbol{v}_d\cdot\nabla\theta \approx Ic\Phi'\boldsymbol{B}\cdot\nabla\theta/B^2$. The equation to be solved is then

$$\left(v_\| + \frac{Ic\Phi'}{B}\right)\boldsymbol{n}\cdot\nabla\theta\frac{\partial h}{\partial\theta} + \mathbf{v}_d\cdot\nabla\chi\frac{\partial h}{\partial\chi} - C(h) = 2\frac{v^2}{v_t^2}\left(\frac{1}{2} - \frac{3}{2}\frac{v_\|^2}{v_t^2}\right)f_M\left[V^\theta - \frac{2}{5}L_1^{(3/2)}\frac{q^\theta}{p}\right]\boldsymbol{n}\cdot\nabla B. \quad (6.2.5.2.4)$$

Changing the independent variables from (χ, θ, E, μ) to $(p_\zeta, \theta, E, \mu)$, the terms for the orbit dynamics reduce to

$$\left(v_\| + \frac{Ic\Phi'}{B}\right)\boldsymbol{n}\cdot\nabla\theta\frac{\partial h}{\partial\theta} + \mathbf{v}_d\cdot\nabla\chi\frac{\partial h}{\partial\chi} = \left(v_\| + \frac{Ic\Phi'}{B}\right)\boldsymbol{n}\cdot\nabla\theta\left.\frac{\partial h}{\partial\theta}\right|_{p_\zeta,E,\mu},$$

and equation (6.2.5.2.4) becomes

$$\left(v_\parallel + \frac{Ic\Phi'}{B}\right)\boldsymbol{n}\cdot\nabla\theta\left.\frac{\partial h}{\partial\theta}\right|_{p_\zeta,E,\mu} - C(h) = 2\frac{v^2}{v_t^2}\left(\frac{1}{2} - \frac{3}{2}\frac{v_\parallel^2}{v_t^2}\right) f_M\left[V^\theta - \frac{2}{5}L_1^{(3/2)}\frac{q^\theta}{p}\right]\boldsymbol{n}\cdot\nabla B. \quad (6.2.5.2.5)$$

Expanding $\Phi' = \Phi'_0 + \Phi''_0(\chi - \chi_0)$, and using results in section 6.2.5.1, yield

$$v_\parallel + \frac{Ic\Phi'}{B} = \omega_s. \quad (6.2.5.2.6)$$

Equation (6.2.5.2.5) can be solved by the standard subsidiary expansion appropriate for the banana regime. The small parameter is $\nu_{*s} = \nu_* S^{-3/2} < 1$, where the additional S factor reflects the increased fraction of trapped particles. The leading order equation is

$$\left(v_\parallel + \frac{Ic\Phi'}{B}\right)\boldsymbol{n}\cdot\nabla\theta\left.\frac{\partial h_0}{\partial\theta}\right|_{p_\zeta,E,\mu} = 2\frac{v^2}{v_t^2}\left(\frac{1}{2} - \frac{3}{2}\frac{v_\parallel^2}{v_t^2}\right) f_M\left[V^\theta - \frac{2}{5}L_1^{(3/2)}\frac{q^\theta}{p}\right]\boldsymbol{n}\cdot\nabla B, \quad (6.2.5.2.7)$$

and the next order equation is

$$\left(v_\parallel + \frac{Ic\Phi'}{B}\right)\boldsymbol{n}\cdot\nabla\theta\left.\frac{\partial h_1}{\partial\theta}\right|_{p_\zeta,E,\mu} = C\left(h_0\right), \quad (6.2.5.2.8)$$

where the subscript in h denotes the subsidiary ordering.

When $\varepsilon < 1$ and $M_p < 1$, the tips of the squeezed bananas are still centred around $v_\parallel \approx 0$, and the $v_\parallel^2/v^2$ term on the right-hand side of equation (6.2.5.2.7) can be neglected for being small by a factor of $\varepsilon S < 1$. Equation (6.2.5.2.7) can then be integrated straightforwardly to yield

$$h_0 = -4\frac{D_s B_0 \varepsilon}{\hat{\omega}_s^2 k_s}\omega_s f_M + g_s, \quad (6.2.5.2.9)$$

where g_s is an integration constant, and $D_s = (v^2/v_t^2)[V^\theta + (v^2/v_t^2 - 5/2)2q^\theta/(5p)]$. Note that g_s is also a constant of motion. To determine g_s, the constraint condition for equation (6.2.5.2.8)

$$\langle C\left(h_0\right)\rangle_t = 0, \quad (6.2.5.2.10)$$

is solved. The operator $\langle\cdot\rangle_t$ annihilates the left-hand side of equation (6.2.5.2.8) to guarantee that h_1 is periodic. This is accomplished by using the periodic boundary condition for circulating particles and reflection boundary condition for trapped particles (see equations (6.2.1.4)–(6.2.1.6)). The operator $\langle\cdot\rangle_t$ is thus defined as $\langle\cdot\rangle_t = (2\pi)^{-1}\int_0^{2\pi} d\theta(\cdot)/\omega_s$ for circulating particles, and $\langle\cdot\rangle_t = (2\pi)^{-1}\sum_{\sigma_s}\int_{-\theta_t}^{\theta_t} d\theta(\cdot)/|\omega_s|$, for trapped particles. Here, the turning points are defined as $\omega_s(\pm\theta_t) = 0$. Of course, the integral in $\langle\cdot\rangle_t$ is performed holding (p_ζ, E, μ) fixed. However, it is not necessary to express the integrand in terms of (p_ζ, E, μ) explicitly. All that is required is that all the quantities in the integrand are constants on the particle trajectory. The pitch angle scattering operator dominates the test particle operator and is approximately $C(f) = (\nu_D/2)\partial^2 f/\partial(v_\parallel/v)^2$, when the independent variables are $(\boldsymbol{x}, v, v_\parallel/v)$. This simple operator can reproduce all standard transport coefficients in the $\varepsilon < 1$ limit for axisymmetric tokamaks [79], because for a localized distribution the highest derivative dominates. Physically, the second derivative corresponds to estimating the de-correlation time in random walk argument using $\tau \sim \nu_{\rm eff}^{-1} \sim f_r^2/\nu$. Changing variables to $(\boldsymbol{x}, v, \omega_s)$ yields

$$C(f) = \frac{\nu_D}{2}v^2\frac{\partial^2 f}{\partial\omega_s^2}. \quad (6.2.5.2.11)$$

To perform bounce averaging along the particle trajectory, the independent variables are changed to (χ_0, θ, v, k_s). Neglecting terms smaller by a factor of $\sqrt{\varepsilon S} < 1$, equation (6.2.5.2.10) can be made explicit to become

$$k_s\frac{\partial}{\partial k}\left(\frac{k_s}{\hat{\omega}_s^2}\langle\omega_s\rangle_\theta\frac{\partial g_s}{\partial k_s}\right) = 0, \quad (6.2.5.2.12)$$

where $\langle\omega_s\rangle_\theta = (2\pi)^{-1}\int_0^{2\pi} d\theta\omega_s$ for circulating particles, and $\langle\omega_s\rangle_\theta = (2\pi)^{-1}\int_{-\theta_t}^{\theta_t} d\theta|\omega_s|$ for trapped particles. The relation $\partial\omega_s/\partial k_s = -\hat{\omega}_s^2/(2k_s\omega_s)$ has been used to obtain equation (6.2.5.2.12). Because g_s is odd in ω_s, and $\partial g_s/\partial\theta = 0$,

$$g_s = 0, \quad (6.2.5.2.13)$$

for trapped particles. For circulating particles, the solution to equation (6.2.5.2.12) is

$$\frac{\partial g_s}{\partial k_s} = \frac{C_s\hat{\omega}_s^2}{k_s\langle\omega_s\rangle_\theta}, \quad (6.2.5.2.14)$$

where C_s is a constant. To determine C_s, imposing the boundary condition that $\partial h_0/\partial\omega_s$ is localized in the velocity space yields $C_s = -2[DB_0\varepsilon/(\hat{\omega}_s^2 k_s)]f_M$, and

$$\frac{\partial g_s}{\partial\omega_s} = 4\frac{DB_0\varepsilon}{\hat{\omega}_s^2 k_s}\frac{\omega_s}{\langle\omega_s\rangle_\theta}f_M, \quad (6.2.5.2.15)$$

for circulating particles. Combining the solutions for g_s for both trapped and circulating particles yields

$$\frac{\partial h_0}{\partial\omega_s} = -4\frac{DB_0\varepsilon}{\hat{\omega}_s^2 k_s}f_M\left[1 - H(1-k_s)\frac{\omega_s}{\langle\omega_s\rangle_\theta}\right], \quad (6.2.5.2.16)$$

where H is step function. Knowing $\partial h_0/\partial\omega_s$ is adequate for the calculations of the parallel plasma viscosity.

6.2.5.3. Parallel viscous forces. Because effects of orbit squeezing resulting from the finite width of the particle orbits are described in equation (6.2.5.2.4), local transport theory exists only in the radial averaged sense [110, 111]. Physically, local radial transport fluxes are meaningful on a scale larger than the typical radial width of the particle orbits but smaller than L_n. Thus, the kinetic definition for the flux surface and radially averaged parallel viscous force is

$$\begin{pmatrix}\langle\boldsymbol{B}\cdot\nabla\cdot\overleftrightarrow{\pi}\rangle\\ \langle\boldsymbol{B}\cdot\nabla\cdot\overleftrightarrow{\Theta}\rangle\end{pmatrix} = \left\langle\int d\boldsymbol{v}fMv^2\begin{pmatrix}1\\ v^2/v_t^2 - 5/2\end{pmatrix}\times\left(\frac{1}{2} - \frac{3}{2}\frac{v^2}{v_\parallel^2}\right)\frac{\boldsymbol{B}\cdot\nabla B}{B}\right\rangle_r, \quad (6.2.5.3.1)$$

where the angular brackets with the subscript r denote both flux surface and radial averages

$$\langle\cdot\rangle_r = \int \frac{\mathrm{d}\chi}{\Delta\chi}\int \mathrm{d}\theta\sqrt{g}\,(\cdot)\Big/\int\int \mathrm{d}\theta\sqrt{g}, \qquad (6.2.5.3.2)$$

and $\Delta\chi$ is an interval in χ that is larger than the squeezed banana width but smaller than L_n. Using equation (6.2.5.2.5), $\langle \boldsymbol{B}\cdot\nabla\cdot\overleftrightarrow{\pi}\rangle$ can be expressed in terms of the collision operator to obtain

$$\left\langle \boldsymbol{B}\cdot\nabla\cdot\overleftrightarrow{\pi}\right\rangle = -\left\langle \int 2\pi v\,\mathrm{d}v\int \mathrm{d}k_s\frac{\hat{\omega}^2}{2k\omega}\frac{Mv_\mathrm{t}^2}{2} \times\frac{hC(h)}{\left[V^\theta-\frac{2}{5}L_1^{(3/2)}\frac{q^\theta}{p}\right]f_\mathrm{M}}\right\rangle_r. \qquad (6.2.5.3.3)$$

Integration over poloidal angle to annihilate $\omega_s\partial h_0/\partial\theta|_{E,\mu,p_\zeta}$ has been made to obtain equation (6.2.5.3.3), which is quadratic in h that is related to the local rate of entropy production. This is made possible by the radial average. Without the radial average, the quadratic form in equation (6.2.5.3.3) cannot be obtained. In the case of the conventional neoclassical transport theory, a similar quadratic form is derived without the radial average because particle drifts that describe the finite width of the orbits in equation (6.2.5.2.3) are not required in the theory. However, for squeezed orbits, those drifts are indispensable in the theory. The radial average allows the average to be performed in (E,μ,p_ζ,θ) space. The averaging process illustrated here is valid for the finite orbit width induced transport theory. Note that the quadratic in h in equation (6.2.5.3.3) corresponds to the $(\Delta x)^2$ in the random walk argument. Integrating by parts in k_s and substituting $\partial h_0/\partial\omega_s$ in equation (6.2.5.2.16) in the resultant expression yield the viscous coefficient μ_j, for $j=1-3$ [110]:

$$\mu_j = 2\sqrt{\frac{2}{\pi}}I_\mathrm{ps}\frac{\sqrt{\varepsilon}}{S^{3/2}}\int_0^\infty \mathrm{d}x\,\nu_\mathrm{D}x^4\left(x^2-\frac{5}{2}\right)^{j-1}\mathrm{e}^{-x^2}, \qquad (6.2.5.3.4)$$

where I_ps is a pitch angle integral defined as

$$I_\mathrm{ps} = \int_0^\infty \frac{\mathrm{d}k_s}{k_s^{3/2}}\left(\left\langle\frac{\hat{\omega}_s}{|\omega_s|}\right\rangle_\theta - H\,(1-k_s)\,\frac{\hat{\omega}_s}{\langle|\omega_s|\rangle_\theta}\right)\approx 1.38. \qquad (6.2.5.3.5)$$

The viscous coefficients are reduced by a factor of $S^{3/2}$, however, with the same numerical number, when compared with the large aspect ratio limit of μ_j in equation (6.2.1.11). The integration in k_s corresponds to the fraction of the trapped particles in the random walk argument. In the process of calculating the viscous coefficients for the effects of orbit squeezing, the one to one correspondence between the analytic calculations and random walk argument is demonstrated. The same correspondence can be made for most of the particle and heat flux calculations.

6.2.5.4. Transport fluxes. Once parallel viscous forces are known, transport fluxes follow naturally from the solutions of the parallel components of the momentum and heat flux balance equations, as shown in section 6.2.1, using the flux–force relation.

The four linearly independent equations to be solved are

$$\left\langle \boldsymbol{B}\cdot\nabla\cdot\overleftrightarrow{\pi}_\mathrm{i}\right\rangle - N_\mathrm{i}e_\mathrm{i}\left\langle BE_\parallel^{(A)}\right\rangle = \langle BF_{1\mathrm{i}}\rangle\,, \qquad (6.2.5.4.1)$$

$$\left\langle \boldsymbol{B}\cdot\nabla\cdot\overleftrightarrow{\pi}_\mathrm{e}\right\rangle - N_\mathrm{e}e_\mathrm{e}\left\langle BE_\parallel^{(A)}\right\rangle = \langle BF_{1\mathrm{e}}\rangle\,, \qquad (6.2.5.4.2)$$

$$\left\langle \boldsymbol{B}\cdot\nabla\cdot\overleftrightarrow{\Theta}_\mathrm{i}\right\rangle = \langle BF_{2\mathrm{i}}\rangle\,, \qquad (6.2.5.4.3)$$

and

$$\left\langle \boldsymbol{B}\cdot\nabla\cdot\overleftrightarrow{\Theta}_\mathrm{e}\right\rangle = \langle BF_{2\mathrm{e}}\rangle\,. \qquad (6.2.5.4.4)$$

The subscripts i and e are restored to indicate ion and electron quantities, and the subscript r that indicates the radial average is suppressed for simplicity.

6.2.5.4.1 Moderate squeezing. When the value of the orbit squeezing factor S is moderate so that ion viscous forces are still larger than electron viscous forces, the coupled equations (6.2.5.4.1)–(6.2.5.4.4) can be solved approximately by exploring differences in the magnitudes of these viscous forces.

Examining equations (6.2.5.4.2)–(6.2.5.4.4) it is noted that, when $\varepsilon<1$, friction forces are larger than the viscous forces by at least a factor of $\sqrt{\varepsilon}$. Thus, the leading order solutions to equations (6.2.5.4.2) and (6.2.5.4.4) are

$$q_{\parallel\mathrm{i}}\approx 0, \qquad (6.2.5.4.1.1)$$

$$q_{\parallel\mathrm{e}}\approx 0, \qquad (6.2.5.4.1.2)$$

and

$$V_{\parallel\mathrm{i}}\approx V_{\parallel\mathrm{e}}. \qquad (6.2.5.4.1.3)$$

The result in equation (6.2.5.4.1.3) is well known [6, 7]. It implies that electrons and ions have common parallel flow in large aspect ratio tokamaks, as discussed in section 5.

To determine ion parallel flow or common flow, summing equations (6.2.5.4.1) and (6.2.5.4.2) yields equation (6.2.1.26), i.e. $\langle \boldsymbol{B}\cdot\nabla\cdot\overleftrightarrow{\pi}_\mathrm{i}\rangle+\langle \boldsymbol{B}\cdot\nabla\cdot\overleftrightarrow{\pi}_\mathrm{e}\rangle=0$. For simplicity, it is assumed that even though the magnitudes of the ion viscous coefficients are reduced as a result of orbit squeezing, they are still much larger than those of the electron viscous coefficients. With this assumption, the ion parallel flow is determined by solving $\langle \boldsymbol{B}\cdot\nabla\cdot\overleftrightarrow{\pi}_\mathrm{i}\rangle\approx 0$, and the result is,

$$V_\mathrm{i}^\theta = -\frac{\mu_{2\mathrm{i}}}{\mu_{1\mathrm{i}}}\frac{2}{5}\frac{q_\mathrm{i}^\theta}{p_\mathrm{i}}, \qquad (6.2.5.4.1.4)$$

or explicitly, after using equations (3.2.12) and (3.2.20),

$$\frac{\langle V_\parallel B\rangle}{\langle B^2\rangle}+\frac{IcT_\mathrm{i}}{e_\mathrm{i}\langle B^2\rangle}\frac{e_\mathrm{i}\Phi'}{T_\mathrm{i}} = -\frac{IcT_\mathrm{i}}{e_\mathrm{i}\langle B^2\rangle}\left(\frac{p_\mathrm{i}'}{p_\mathrm{i}}+\frac{\mu_{2\mathrm{i}}}{\mu_{1\mathrm{i}}}\frac{T_\mathrm{i}'}{T_\mathrm{i}}\right), \qquad (6.2.5.4.1.5)$$

where $\mu_{2\mathrm{i}}/\mu_{1\mathrm{i}}=-1.17$. The relation between the parallel mass flow and the radial electric field in equation (6.2.5.4.1.5) is the same as that in the conventional theory [112]. Even though the individual viscous coefficient is modified by the orbit squeezing factor S, the ratio of $\mu_{2\mathrm{i}}/\mu_{1\mathrm{i}}$ is not modified. Thus, the orbit squeezing does not modify the relation between the ion parallel flow and the radial electric field when the squeezing is moderate in large aspect ratio tokamaks [112].

For the approximation that leads to results in equations (6.2.5.4.1.1)–(6.2.5.4.1.3) and (6.2.5.4.1.5), it is convenient to evaluate the heat flux using the heat viscous force in equation (4.1.1.13). Substituting results in equations (6.2.5.4.1.1) and (6.2.5.4.1.4) into heat viscous force yields

$$\frac{q_{\rm i}^{\rm bp}}{T_{\rm i}} = -N_{\rm i}M_{\rm i}\frac{c^2}{e_{\rm i}^2}\frac{I^2}{\langle B^2\rangle}\mu_{3{\rm i}}\left(1-\frac{\mu_{2{\rm i}}^2}{\mu_{1{\rm i}}\mu_{3{\rm i}}}\right)\frac{{\rm d}T_{\rm i}}{{\rm d}\chi}. \quad (6.2.5.4.1.6)$$

When $S = 1$, the ion heat flux in the conventional theory is reproduced. Note that the ratio $\mu_{2{\rm i}}^2/(\mu_{1{\rm i}}\mu_{3{\rm i}})$ is not affected by S. The orbit squeezing effects on the ion heat flux and ion heat conductivity appear in the coefficient $\mu_{3{\rm i}}$, which is reduced by a factor of $S^{3/2}$ when $S > 1$ [110]. The scaling can be understood in terms of the random walk argument using the facts that the orbit width is reduced by a factor of $\sqrt{S}$ in χ and the fraction of trapped particles increases by a factor of $\sqrt{S}$ [110]. The $S^{-3/2}$ scaling in the ion heat conductivity is also observed in a Monte Carlo simulation [113].

Electron transport fluxes are not modified because the ratios of the ion viscous coefficients remain the same as those in the conventional theory. The bootstrap current is driven by the parallel viscous forces and is [7], by solving equations (6.2.5.4.2) and (6.2.5.4.4),

$$\langle J_{\|{\rm b}}B\rangle = \frac{\sigma_s}{N_{\rm e}e}\left(\left\langle \boldsymbol{B}\cdot\nabla\cdot\overleftrightarrow{\pi}_{\rm e}\right\rangle + \frac{l_{12}^{\rm e}}{l_{22}^{\rm e}}\left\langle \boldsymbol{B}\cdot\nabla\cdot\overleftrightarrow{\Theta}_{\rm e}\right\rangle\right), \quad (6.2.5.4.1.7)$$

where Spitzer conductivity $\sigma_s = (N_{\rm e}e)^2 l_{22}^{\rm e}/[l_{11}^{\rm e}l_{22}^{\rm e} - (l_{12}^{\rm e})^2]$, and $e = |e_{\rm e}|$. The ion contribution to $\langle J_{\|{\rm b}}B\rangle$ appears in $V_{\rm e}^{\theta}$ by expressing it as

$$V_{\rm e}^{\theta} = \left(V_{\rm e}^{\theta} - V_{\rm i}^{\theta}\right) + V_{\rm i}^{\theta}. \quad (6.2.5.4.1.8)$$

The $\langle B(V_{\|{\rm i}} - V_{\|{\rm e}})\rangle$ term in $(V_{\rm e}^{\theta} - V_{\rm i}^{\theta})$ represents the modification on the electric conductivity in tokamaks resulting from the existence of trapped particles. Because ion dynamics do not modify it in the approximation adopted here, the effects of orbit squeezing do not modify the electric conductivity in the conventional neoclassical theory. Evaluating the viscous forces in equation (6.2.5.4.1.7) yields the bootstrap current

$$\langle J_{\|{\rm b}}B\rangle = -\sigma_s\frac{M_{\rm e}\mu_{1e}}{N_{\rm e}e^2}Ic\left[\left(1+\frac{l_{12}^{\rm e}}{l_{22}^{\rm e}}\frac{\mu_{2{\rm e}}}{\mu_{1{\rm e}}}\right)\left(P' + \frac{\mu_{2{\rm i}}}{\mu_{1{\rm i}}}\frac{1}{Z}N_{\rm e}T_{\rm i}'\right) + N_{\rm e}T_{\rm e}'\left(\frac{\mu_{2{\rm e}}}{\mu_{1{\rm e}}} + \frac{l_{12}^{\rm e}}{l_{22}^{\rm e}}\frac{\mu_{3{\rm e}}}{\mu_{1{\rm e}}}\right)\right], \quad (6.2.5.4.1.9)$$

where $P' = P_{\rm e}' + P_{\rm i}'$, and $\mu_{j{\rm e}}$ for j =1–3 is the same as the standard viscous coefficients because orbit squeezing is ineffective for electrons. From equation (6.2.5.4.1.9), it is clear that the bootstrap current is not affected by the orbit squeezing because the ratio $\mu_{2{\rm i}}/\mu_{1{\rm i}}$ remains unchanged in the approximation adopted here. Thus, the Ware pinch flux is not modified either.

The ambipolar electron particle flux and the electron heat flux can also be calculated by evaluating the viscous force in the flux–force relation. Because the ion parallel flow is determined by neglecting the electron viscous force, the electron particle flux in equation (4.1.1.5) is the ambipolar particle flux, i.e. $e_{\rm e}\langle\Gamma_{\rm e}\cdot\nabla\chi\rangle = -e_{\rm i}\langle\Gamma_{\rm i}\cdot\nabla\chi\rangle$ within the approximation adopted here. The $\langle B(V_{\|{\rm i}} - V_{\|{\rm e}})\rangle$ term in $(V_{\rm e}^{\theta} - V_{\rm i}^{\theta})$ now represents the Ware pinch particle flux. The ambipolar particle flux is then

$$\Gamma_{\rm e}^{\rm bp} = -N_{\rm e}M_{\rm e}\frac{c^2}{e^2}\frac{I^2}{\langle B^2\rangle}\mu_{1{\rm e}}\left(\frac{P'}{N_{\rm e}} + \frac{\mu_{2{\rm e}}}{\mu_{1{\rm e}}}T_{\rm e}' + \frac{\mu_{2{\rm i}}}{\mu_{1{\rm i}}}\frac{1}{Z}T_{\rm i}'\right). \quad (6.2.5.4.1.10)$$

Using the results for plasma flows, the electron heat flux can be evaluated to obtain

$$\frac{q_{\rm e}^{\rm bp}}{T_{\rm e}} = -N_{\rm e}M_{\rm e}\frac{c^2}{e_{\rm i}^2}\frac{I^2}{\langle B^2\rangle}\mu_{2{\rm e}}\left(\frac{P'}{N_{\rm e}} + \frac{\mu_{3{\rm e}}}{\mu_{2{\rm e}}}T_{\rm e}' + \frac{\mu_{2{\rm i}}}{\mu_{1{\rm i}}}\frac{1}{Z}T_{\rm i}'\right). \quad (6.2.5.4.1.11)$$

Both the ambipolar electron particle flux and the electron heat flux are not affected by the orbit squeezing because the ratio $\mu_{2{\rm i}}/\mu_{1{\rm i}}$ remains unchanged.

Thus, in the moderate squeezing limit, only the ion heat flux is modified by squeezed ion orbits. The rest of the transport fluxes are not modified [110, 112].

It is important to note that in evaluating bootstrap current, the ion poloidal flow is used in evaluating the electron viscous forces because equation (6.2.5.4.1.8) is employed in the process. Since the bootstrap current is neoclassical in tokamaks, this implies that the ion poloidal flow must be neoclassical or very close to neoclassical. This important relation between the ion poloidal flow and the bootstrap current is transparent in the moment approach.

6.2.5.4.2. Strong squeezing. When the squeezing factor S is large enough so that the ion and electron viscous coefficients are comparable, the electron viscous force also contributes to the momentum relaxation [114]. In this case, all transport coefficients are modified except the effect of the trapped electrons on the electric conductivity [114].

Because $|\mu_{j{\rm e}}| < \nu_{\rm e}$, and $|\mu_{j{\rm i}}| < \nu_{\rm i}$, the conclusions that $V_{\|{\rm i}} \approx V_{\|{\rm e}}$, $q_{\|{\rm e}} \approx 0$, and $q_{\|{\rm i}} \approx 0$ are still valid. However, since $N_{\rm i}M_{\rm i}|\mu_{j{\rm i}}| \sim N_{\rm e}M_{\rm e}|\mu_{j{\rm e}}|$, the electron viscous force cannot be neglected in solving equation (6.2.5.4.1) for $V_{\rm i}^{\theta}$. In this case, $V_{\rm i}^{\theta}$ becomes

$$V_{\rm i}^{\theta} = -\frac{\mu_{2{\rm i}}}{\mu_{1{\rm i}} + \frac{N_{\rm e}M_{\rm e}}{N_{\rm i}M_{\rm i}}\mu_{1{\rm e}}}\frac{IcT_{\rm i}'}{e_{\rm i}\langle B^2\rangle} + \frac{\mu_{2{\rm e}}}{\mu_{1{\rm e}} + \frac{N_{\rm i}M_{\rm i}}{N_{\rm e}M_{\rm e}}\mu_{1{\rm i}}}\frac{IcT_{\rm e}'}{e\langle B^2\rangle} + \frac{\mu_{1{\rm e}}}{\mu_{1{\rm e}} + \frac{N_{\rm i}M_{\rm i}}{N_{\rm e}M_{\rm e}}\mu_{1{\rm i}}}\left[\frac{IcP'}{N_{\rm e}e\langle B^2\rangle} + \left(1+\frac{l_{12}^{\rm e}}{l_{22}^{\rm e}}\frac{\mu_{2{\rm e}}}{\mu_{1{\rm e}}}\right)\frac{\sigma_s\left\langle E_{\|}^{(A)}B\right\rangle}{N_{\rm e}e\langle B^2\rangle}\right]. \quad (6.2.5.4.2.1)$$

The $\langle E_{\|}^{(A)}B\rangle$ term is obtained by approximating $\langle J_{\|}B\rangle = \sigma_s\langle E_{\|}^{(A)}B\rangle$ and $(2/5)\langle q_{\|{\rm e}}B\rangle/p_{\rm e} = -(l_{12}^{\rm e}/l_{22}^{\rm e})\sigma_s\langle E_{\|}^{(A)}B\rangle/(N_{\rm e}e)$, which are the solutions to equations (6.2.5.4.2) and (6.2.5.4.4) when the electron viscous forces are suppressed. Thus, besides the ion temperature gradient, electron temperature gradient, and total pressure gradient, the inductive electric field contributes to the ion poloidal flow. These additional contributions become important only when ion and electron viscous forces become comparable. The $V_{\rm i}^{\theta}$ in equation (6.2.5.4.2.1) is a simplified version of that shown in [114] by neglecting higher order viscous terms.

The bootstrap current becomes

$$\langle J_{\|b} B\rangle = -\sigma_s \frac{M_e \mu_{1e}}{N_e e^2} Ic\left[\left(1+\frac{l^e_{12}}{l^e_{22}}\frac{\mu_{2e}}{\mu_{1e}}\right)\left(P' - \frac{N_e e\langle B^2\rangle}{Ic} V_i^\theta\right) + N_e T_e'\left(\frac{\mu_{2e}}{\mu_{1e}} + \frac{l^e_{12}}{l^e_{22}}\frac{\mu_{3e}}{\mu_{1e}}\right)\right], \quad (6.2.5.4.2.2)$$

where V_i^θ is made explicit to emphasize the role it plays. It is also clear that the neoclassical bootstrap current implies the neoclassical poloidal flow as discussed in section 6.2.5.4.1. In the limit where $N_i M_i |\mu_{ji}| < N_e M_e |\mu_{je}|$, the P' in V_i^θ tends to cancel the explicit P' dependence in equation (6.2.5.4.2.2), and the magnitude of the bootstrap current can be reduced as a result. This phenomenon was first discussed in [114] and can be used to control the bootstrap current in the pedestal region in H-mode plasmas and, thus, edge localized modes (ELMs) [115]. Note that the inductive electric field also contributes to the bootstrap current through ion poloidal flow when $N_i M_i \mu_{ji} \sim N_e M_e \mu_{je}$. Thus, in the strong squeezing limit, the bootstrap current is fundamentally different from that in the conventional theory.

The ambipolar particle flux is

$$\Gamma_e^{bp} = -M_e \frac{I^2 c^2}{e^2\langle B^2\rangle}\mu_{1e}\left[P' - \frac{N_e e\langle B^2\rangle}{Ic} V_i^\theta + \frac{\mu_{2e}}{\mu_{1e}} N_e T_e' + \left(1+\frac{l^e_{12}}{l^e_{22}}\frac{\mu_{2e}}{\mu_{1e}}\right)\frac{\sigma_s\langle B E_\|^{(A)}\rangle}{Ic}\right], \quad (6.2.5.4.2.3)$$

and the electron heat flux is

$$\frac{q_e^{bp}}{T_e} = -M_e \frac{I^2 c^2}{e^2\langle B^2\rangle}\mu_{2e}\left[P' - \frac{N_e e\langle B^2\rangle}{Ic} V_i^\theta + \frac{\mu_{3e}}{\mu_{2e}} N_e T_e' + \left(1+\frac{l^e_{12}}{l^e_{22}}\frac{\mu_{3e}}{\mu_{2e}}\right)\frac{\sigma_s\langle B E_\|^{(A)}\rangle}{Ic}\right], \quad (6.2.5.4.2.4)$$

where Ware pinch fluxes are also displayed. The Onsager symmetry between the bootstrap current and the Ware pinch is obvious by examining coefficients in front of the thermodynamic forces.

The effect of trapped particles on the electric conductivity is not modified by the strong squeezing as long as the electrons are not squeezed significantly. However, if the bootstrap current driven by the inductive electric field is viewed as part of the ohmic current, the electric conductivity is also modified through the ion poloidal flow even though electrons are not squeezed. In that case, the inductive electric field driven current should be removed from the bootstrap current expression to avoid double counting.

The ion heat flux is, using the flux force relation in equation (4.1.1.13),

$$\frac{q_i^{bp}}{T_i} = -N_i M_i T_i \frac{c^2}{e_i^2}\frac{I^2}{\langle B^2\rangle}\left(\mu_{2i}\frac{e_i\langle B^2\rangle}{IcT_i} V_i^\theta + \mu_{3i}\frac{T_i'}{T_i}\right). \quad (6.2.5.4.2.5)$$

6.2.5.5. Effects of finite width of banana orbits. When the orbit squeezing factor $S = 1$, the theory for orbit squeezing becomes a theory for the effects of finite banana width. The results of the theory indicate that the finite banana width has no effect on the transport fluxes in large aspect ratio tokamaks [116]. The effects have been studied using numerical codes [117, 118]. The same conclusion is reached in the numerical calculations [117].

6.3. Potato orbit induced transport fluxes in the vicinity of the magnetic axis

In the vicinity of the magnetic axis, the potato width scales differently from the banana width. The transport fluxes must be different from those away from the magnetic axis discussed in section 6.2.1. The analysis of the drift kinetic equation for potato orbits is similar to that for the squeezed banana orbits because both the poloidal and radial drifts must be included to describe the potato orbits in the near axis region.

6.3.1. Perturbed distribution for potato orbits. The linear drift kinetic equation to be solved for potato orbits near the magnetic axis is the same as that for squeezed banana orbits, i.e. equation (6.2.5.2.3). Finite width of the orbits must be taken into account in the transport theory. However, the width of the orbits must be smaller than L_n to facilitate a local transport analysis.

Similar to the method used for calculating the effects of orbit squeezing, the poloidal angle dependence in the poloidal particle speed ω_θ in equation (6.1.2.3) needs to be made explicit to facilitate the solution to equation (6.2.5.2.3). Assuming $\varepsilon < 1$ and using $\varepsilon = C_\chi\sqrt{\chi}$, ω_θ becomes [94], using equations (6.1.2.1), (6.1.2.2), and $\chi_0 = 0$,

$$\omega_\theta = \hat{\omega}_\theta\left(4T_p^2 + \sigma_p\right), \quad (6.3.1.1)$$

where $\hat{\omega}_\theta = (3/4)(\Omega_0/I)\hat{x}^2 k_p^{1/3}$, and T_p is one of the following functions: $\cos(\beta/3)$, $\sin(\pi/6 \pm \beta/3)$, $\sinh(\beta/3)$ and $\cosh(\beta/3)$. A typical potato has the poloidal speed of the order of $\omega_\theta \sim v_t f_p$ by estimating $k_p \sim 1$, where the fraction of potatoes f_p is given in equation (6.2.1.10).

In the potato regime, where $\nu_{*p} = \nu[v_t f_p^3/(Rq)]^{-1} < 1$, equation (6.2.5.2.3) is solved by a subsidiary expansion procedure, i.e. $h = h_0 + h_1 + \ldots$, using the small parameter ν_{*p}. Employing the same procedure that solves the linear drift kinetic equation for the squeezed orbits yields

$$\frac{\partial h_0}{\partial \omega_\theta} = -\frac{3}{4}\frac{I}{\Omega_0} D_p\left(1 - \frac{|\omega_\theta|}{\langle|\omega_\theta|\rangle_\theta} H_p\right), \quad (6.3.1.2)$$

where $D_p = (2/v_t^2)(\Omega_0 B_0/I) f_M[V^\theta + (v^2/v_t^2 - 5/2)2q^\theta/(5p)]$, $H_p = 1$ for circulating particles, and $H_p = 0$ for trapped particles. To calculate parallel viscous forces, knowing $\partial h_0/\partial\omega_\theta$ is adequate.

6.3.2. Parallel viscous forces. The parallel viscous forces accounting for the physics of potato orbits are calculated from the definitions in equations (4.1.4.1) and (4.1.4.2). Because potato orbits have finite width, the radial average in addition to the flux surface average must be performed over parallel viscous forces to obtain the local transport fluxes valid over a region larger than the width of potatoes.

The viscous coefficients μ_j for $j = 1$–3 are calculated to be [119], using equation (6.3.1.2),

$$\mu_j = 1.12\frac{I_{pp}}{\sqrt{\pi}}\left(\frac{I v_t C_\chi^2}{\Omega_0}\right)^{1/3} 2\int_0^\infty dx x^{13/3}\left(x^2 - \frac{5}{2}\right)^{j-1} \times \nu_D e^{-x^2}, \quad (6.3.2.1)$$

where the constant $I_{pp} = 2.77$ is a result of the pitch angle integral over the k_p space [94]. It should be noted that μ_j scales as the fraction of trapped potatoes f_p.

6.3.3. Effects of orbit squeezing on potato orbits. When the potato width is comparable to L_n, the effects of orbit squeezing become important. The squeezing makes the real squeezed potato width smaller than the L_n, and facilitates a local transport analysis [116].

The analysis for squeezed potato orbits is the same as that for squeezed banana orbits. The orbit equation for the squeezed potato orbits that pass through the magnetic axis is [119]

$$S\bar{x}^3 + 2\left(\frac{Iv_{\parallel 0}}{\Omega_0} + \frac{I^2 e\Phi_0'}{M\Omega_0^2}\right)\bar{x} - \frac{2I^2C_1}{\Omega_0^2}\left(v_{\parallel 0}^2 + \mu B_0\right)\cos\theta = 0, \tag{6.3.3.1}$$

where the squeezing factor S is the same as that for squeezed banana orbits defined in equation (6.2.5.6). The orbit trajectories for potato orbits in equations (6.1.2.4)–(6.1.2.8) can be used for squeezed potato orbits when the quantities σ_p, k_p and $\hat{x}$ in those equations are redefined as

$$\sigma_p = \mathrm{sgn}\left(\frac{v_{\parallel 0} + Ic\Phi_0'/B}{S\Omega_0}\right), \tag{6.3.3.2}$$

$$k_p = \frac{8}{27}\left(\frac{I}{|S|\,\Omega_0}\right)^3 \frac{\left|v_{\parallel 0} + Ic\Phi_0'/B_0\right|^3}{\left(I^2C_\chi/|S|\,\Omega_0^2\right)^2\left(v_{\parallel 0}^2 + \mu B_0\right)^2}, \tag{6.3.3.3}$$

and

$$\hat{x} = \left[\left(I^2C_\chi/|S|\,\Omega_0^2\right)\left(v_{\parallel 0}^2 + \mu B_0\right)\right]^{1/3}. \tag{6.3.3.4}$$

From equation (6.3.3.4), it is obvious that the width of the potato orbits is reduced by a factor of $|S|^{-2/3}$ in χ. For $|S| > 1$, the local transport analysis is valid even when the width of unsqueezed potato orbits is comparable to L_n. The fraction of trapped potatoes increases by a factor of $|S|^{1/3}$, which can be inferred from the modified parameter k_p in equation (6.3.3.3). The viscous coefficients are reduced by a factor of $|S|^{-5/3}$, and become [120]

$$\mu_j = 1.12\frac{2I_{pp}}{\sqrt{\pi}\,|S|^{5/3}}\left(\frac{Iv_t C_\chi^2}{\Omega_0}\right)^{1/3} \times \int_0^\infty dx\, x^{13/3}\left(x^2 - \frac{5}{2}\right)^{j-1}\nu_D e^{-x^2}. \tag{6.3.3.5}$$

As in the case for squeezed bananas, orbit squeezing does not affect the electron potato orbits significantly.

It should be noted that for a parabolic profile for the radial electric field in local radius r, it has a linear profile in poloidal flux χ. For this profile, Φ'' in the squeezing factor S is finite. Thus, orbit squeezing is an important mechanism to make local transport analysis valid in the vicinity of the magnetic axis. As pointed out in [116], whenever the width of the orbit is comparable to L_n, the effects of orbit squeezing become important to make the real width of the orbits smaller than L_n.

6.3.4. Transport fluxes in the vicinity of the magnetic axis The transport fluxes can again be obtained by solving the parallel force balance equations and utilizing the flux–force relation. In the large aspect ratio limit, the formal expressions for transport fluxes in terms of the viscous coefficients are the same as those in section 6.2.5.4. Only the detailed expressions for the viscous coefficients differ.

For the moderate squeezing case, the ion poloidal flow in the near magnetic axis region is

$$\frac{\langle V_\parallel B\rangle}{\langle B^2\rangle} + \frac{IcT_i}{e_i\langle B^2\rangle}\frac{e_i\Phi'}{T_i} = -\frac{IcT_i}{e_i\langle B^2\rangle}\left(\frac{p_i'}{p_i} + \frac{\mu_{2i}}{\mu_{1i}}\frac{T_i'}{T_i}\right), \tag{6.3.4.1}$$

where $\mu_{2i}/\mu_{1i} = -1.021$ for the potato regime instead of -1.17 for the banana regime. The ion heat flux is

$$\frac{q_i^{bp}}{T_i} = -0.8\nu_{ii}\left(\frac{Iv_{ti}}{\Omega_i}\right)^{7/3}\left(\frac{q}{\delta IR}\right)^{1/3} S^{-5/3}N_i\frac{T_i'}{T_i}, \tag{6.3.4.2}$$

which can be understood in terms of the random walk argument in χ using the fraction of trapped potatoes, the width of potato orbits, and $\nu_{eff} \sim \nu/f_p^2$. For typical tokamaks, the width of an ion potato is about 15% of the minor radius. Thus, local ion transport theory is meaningful on a length scale longer than this width, and ion transport fluxes are averaged over this length scale as well. The equilibrium profiles must be relatively flat on this length scale because ion potato orbits smooth out the profiles. When converting q_i^{bp} in equation (6.3.4.2) into cylindrical coordinates, the radius r is only meaningful in the radially averaged sense. Thus, r cannot be set to 0.

The transport fluxes for potato orbits of alpha particles have also been calculated in [57]. The results are to replace the fraction of bananas in the transport theory for alpha particles away from the axis [121] by the fraction of potatoes just as discussed here.

The electric conductivity is also modified by the finite value of f_p. The formal expression for σ_{eff} in equation (6.2.1.36) is still valid when the viscous coefficients for potato orbits are used. The potato bootstrap current is proportional to f_p of electrons as can be seen from equation (6.2.5.4.1.9), and does not vanish on the magnetic axis. The same scaling for the potato bootstrap current is also obtained in [122]. The existence of the bootstrap current on the magnetic axis provides a possibility to have steady-state 100% bootstrap current tokamak equilibria without the need to have external current drive [58, 59]. The potato orbits of alpha particles can also drive a bootstrap current on the magnetic axis [57, 58]. The transport fluxes for electron potatoes are more local in radius than those for ion potatoes. Thus, electron potato transport fluxes easily satisfy the requirement for the local transport theory.

6.3.5. Intrinsic steady-state tokamak: 100% bootstrap current equilibria. Conventionally, tokamaks are not intrinsically steady state devices because the poloidal magnetic field is created by the plasma current, which, in turn, is driven by the inductive electric field $\boldsymbol{E}^{(A)}$. This is one of the main criticisms for tokamak fusion power plants. To maintain a steady-state tokamak discharge, plasma current must be driven externally using either neutral particle beams or radio frequency waves to deliver momentum to electrons or utilizing a self-generated bootstrap current. However, because bootstrap current in the standard theory vanishes on the magnetic axis, a seed current is needed to maintain plasma equilibrium [24, 123]. Because the bootstrap current driven by potatoes does not vanish on the magnetic axis as shown in section 6.3.4, the steady-state tokamak equilibrium can be sustained with bootstrap current alone. Thus, tokamaks are intrinsically steady-state devices

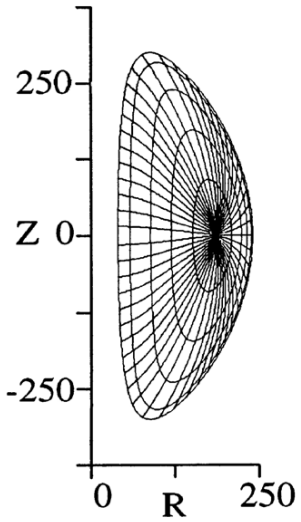

Figure 11. Flux surface grid of a steady-state tokamak equilibrium for $A = 1.4$, $\delta = 3.0$ and $\kappa = 0.522$.

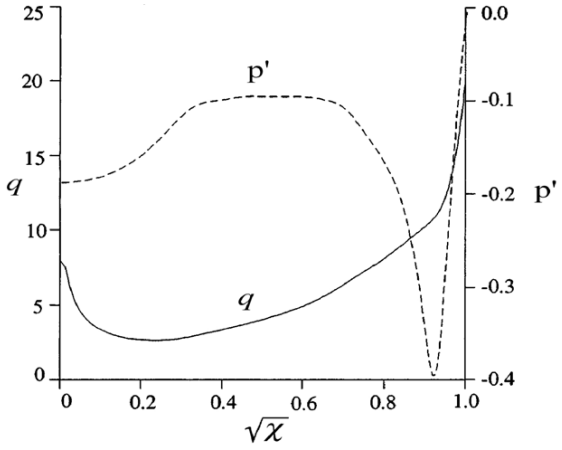

Figure 12. Safety factor q, and pressure gradient P' profiles as a function of normalized radius $\sqrt{\chi}$.

without the need of the external current drive. The steady-state tokamak equilibrium can also be maintained by the potato bootstrap current from fusion-born alpha particles [58].

Tokamak equilibria with 100% bootstrap current are obtained by solving the Grad–Shafranov equation [48, 49] including the bootstrap current induced from the potato orbits [59]. The function I and I' in the Grad–Shafranov equation can be calculated from [124]

$$\langle J_{\|b} B \rangle = -Ic P' - \frac{c \langle B^2 \rangle}{4\pi} I'. \qquad (6.3.5.1)$$

An example for the 100% bootstrap current equilibrium which is stable against ballooning modes is shown in figures 11–13 for a tokamak with $A = 1.4$, $\delta = 3.0$, and triangularity $\kappa = 0.522$ [59].

The equilibrium has a reversed q profile as shown in figure 12, which may have better plasma confinement than

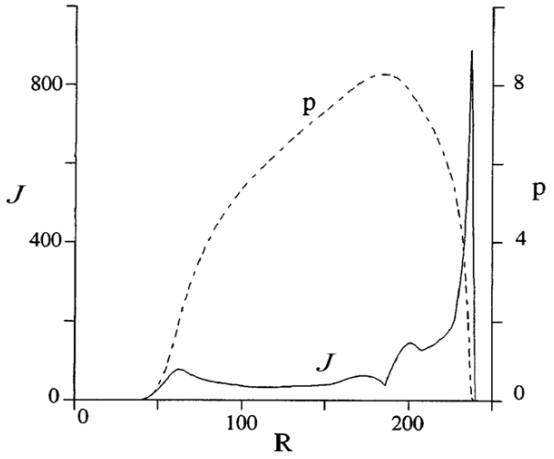

Figure 13. Pressure and toroidal current density profiles as a function of the major radius R.

the monotonically increasing q profile. Thus, a tokamak with 100% bootstrap current may have more than one beneficial trait.

From the economic point of view, it is attractive to operate thermonuclear fusion power plants in a steady state. This will relax the requirements for the plasma facing materials. Issues related to steady-state tokamak fusion reactors have been reviewed in [125].

6.3.6. Potato plateau regime. The resonance in the plateau regime in the vicinity of the magnetic axis does not occur at $v_\| = 0$ anymore; instead it occurs at $\omega_\theta = 0$, as can be seen from equation (6.2.5.2.3), which are also the turning points of the potato orbits. However, this shift in the resonance position in the phase space does not change the transport fluxes in the plateau regime because $f_p < 1$. The reason is that $v_\|^2 < v^2$ in the driving terms of equation (6.2.5.2.3) by a factor of $f_p^2 < 1$. Thus, the parallel viscous forces in the plateau regime away from the magnetic axis are still valid in the near axis region [126].

However, for the sake of practical applications, because in the potato regime the viscous forces are both flux surface and radially averaged, it might be convenient to radially average the potato plateau viscous forces. This has been done in [127] using the orbit trajectories in section 6.1.2.

6.4. Non-linear plasma viscosity

In the edge region of H-mode plasmas and in the core region inside transport barriers, the poloidal $\boldsymbol{E} \times \boldsymbol{B}$ Mach number M_p can be of the order of unity or higher. The plasma viscous forces become a non-linear function of M_p [128]. The poloidal momentum equation can have bifurcated solution for the radial electric field that leads to turbulence suppression and thus improved plasma confinement [15, 129]. Here, it should be emphasized that $M_p \sim 1$ does not necessarily imply that the toroidal rotation speed is sonic. The more relevant physics to the edge region of H-mode plasmas is that the poloidal flow is sonic if the diamagnetic flow speed is not adequate to cancel

the poloidal $\boldsymbol{E}\times\boldsymbol{B}$ flow. In that case, a poloidal shock can form [130–132]. However, usually the poloidal diamagnetic flow almost cancels the poloidal $\boldsymbol{E}\times\boldsymbol{B}$ flow to make the real poloidal speed subsonic.

As can be seen from the method developed to solve the drift kinetic equation, the way to treat the momentum restoring terms in Coulomb collision operator, and the driving terms that are proportional to P_1 is to introduce parallel flows. This goal can also be accomplished by using the drift kinetic equation derived with the assumption of the large mass flow [82]. However, the flow velocity is interpreted to be the velocity for each species [83]. One of the advantages of using the drift kinetic equation with the large mass flow is that the parallel flow with arbitrary geometric angle dependence is treated rigorously in the kinematic part of the drift kinetic equation. Compressible plasma flow, i.e. $\nabla\cdot\boldsymbol{V}\neq 0$, can also be treated using this approach [83]. This feature for compressible flow is not needed for sonic M_p but the real mass flow is subsonic. This condition can be satisfied when the poloidal $\boldsymbol{E}\times\boldsymbol{B}$ flow cancels approximately the poloidal diamagnetic flow, a phenomenon often observed in tokamak experiments. Thus, even though the drift kinetic equation with large mass flow is adopted here, the gyro-radius ordering is also used so that the equation is valid for sonic M_p but subsonic mass flow.

The drift kinetic equation with a large mass flow is [82]

$$\frac{\partial f}{\partial t}+\left(v_\parallel\boldsymbol{n}+\boldsymbol{v}_\mathrm{d}+\boldsymbol{V}\right)\cdot\nabla f+\dot{\bar{w}}\frac{\partial f}{\partial\bar{w}}=C(f). \tag{6.4.1}$$

The independent variables in equation (6.4.1) are $(\boldsymbol{x}, t, \mu, \bar{w})$, where $\bar{w}=v^2/2$. Components of particle velocity $v_\parallel$, and $v_\perp$ together with v are all defined relative to the mass flow velocity $\boldsymbol{V}$ for each species. The drift velocity $\boldsymbol{v}_\mathrm{d}$ is defined as [82]

$$\boldsymbol{v}_\mathrm{d}=\frac{\boldsymbol{F}_\mathrm{HW}\times\boldsymbol{n}}{\Omega}+\frac{\mu B\boldsymbol{n}}{M\Omega}\left(\frac{J_\parallel}{B}\right)+\frac{\boldsymbol{n}}{\Omega}\times\left[\mu\nabla B/M+v_\parallel\boldsymbol{n}\cdot\nabla\boldsymbol{V}+\boldsymbol{V}\cdot\nabla\left(v_\parallel\boldsymbol{n}\right)+v_\parallel^2\boldsymbol{n}\cdot\nabla\boldsymbol{n}\right], \tag{6.4.2}$$

where the force $\boldsymbol{F}_\mathrm{HW}$ is

$$\boldsymbol{F}_\mathrm{HW}=\frac{e}{M}\left(\boldsymbol{E}+\frac{1}{c}\boldsymbol{V}\times\boldsymbol{B}\right)-\frac{\partial\boldsymbol{V}}{\partial t}-\boldsymbol{V}\cdot\nabla\boldsymbol{V}. \tag{6.4.3}$$

The approximate expression for $\dot{\bar{w}}$ is [82]

$$\dot{\bar{w}}=\boldsymbol{F}_\mathrm{HW}\cdot v_\parallel\boldsymbol{n}-\frac{\mu B}{M}\nabla\cdot\boldsymbol{V}-\left(v_\parallel^2-\frac{\mu B}{M}\right)\left(v_\parallel^2-\mu B\right)\boldsymbol{n}\cdot\boldsymbol{n}\cdot\nabla\boldsymbol{V}+\boldsymbol{v}_\mathrm{d}\cdot\boldsymbol{F}_\mathrm{HW}. \tag{6.4.4}$$

The full expression for $\dot{\bar{w}}$ is tedious and only first-order (in gyro-radius ordering) terms are displayed. For the case where the flow velocity $\boldsymbol{V}$ is first order, the neglected terms are second order.

To solve equation (6.4.1), the solution is expressed as [128]

$$f=f_\mathrm{M}-\frac{2v_\parallel}{v_\mathrm{t}^2}\frac{2}{5}\frac{q_\parallel}{p}L_1^{(3/2)}f_\mathrm{M}+h, \tag{6.4.5}$$

where f_M is the shifted Maxwellian distribution because particle velocity $\boldsymbol{v}$ is defined relative to the flow velocity $\boldsymbol{V}$. Note that the $(2v_\parallel V_\parallel/v_\mathrm{t}^2)f_\mathrm{M}$ term used in treating the momentum restoring terms and the driving terms proportional to P_1 in the standard drift kinetic equation is already included in f through the shifted Maxwellian f_M. The role of the $q_\parallel$ term is the same as before. The $q_\parallel$ term is assumed to be the first order in the gyro-radius ordering in equation (6.4.5).

Substituting equation (6.4.5) into equation (6.4.1) yields an equation for h, for incompressible flows,

$$\left[(v_\parallel+V_\parallel)\boldsymbol{n}+\boldsymbol{V}_E+\boldsymbol{v}_\mathrm{d}\right]\cdot\nabla h-C(h)=2\frac{v^2}{v_\mathrm{t}^2}\left(\frac{1}{2}-\frac{3}{2}\frac{v_\parallel^2}{v_\mathrm{t}^2}\right)f_\mathrm{M}\times\left[\frac{\boldsymbol{V}\cdot\nabla B}{B}+\left(\frac{v^2}{v_\mathrm{t}^2}-\frac{5}{2}\right)\frac{\boldsymbol{q}\cdot\nabla B}{B}\right], \tag{6.4.6}$$

where $\boldsymbol{V}_E=c\boldsymbol{E}\times\boldsymbol{B}/B^2$ is the $\boldsymbol{E}\times\boldsymbol{B}$ drift velocity. To obtain equation (6.4.6), the steady-state density and temperature evolution equations, i.e. $\boldsymbol{V}\cdot\nabla N=0$, and $\boldsymbol{V}\cdot\nabla T=0$, in addition to an approximate expression $\boldsymbol{F}_\mathrm{HW}\approx\nabla p/(NM)$, have been used. Equation (6.4.6) is valid for subsonic incompressible flow. For compressible flows, both $\nabla\cdot\boldsymbol{V}$ and $\nabla\cdot\boldsymbol{q}$ also contribute to the right-hand side of equation (6.4.6). These compressible terms dominate when shocks form in sonic rotating plasmas [130–133].

The time-dependent $\partial h/\partial t$ term can also be added to the left-hand side of equation (6.4.6). In that case, time-dependent density and temperature evolution equations must be used. However, this does not change the right-hand side of equation (6.4.6). The $\partial h/\partial t$ term has been used in the drift kinetic equation to develop the theory for the time-dependent plasma viscosity to calculate the poloidal flow damping rate [13, 72, 133].

The key difference between equations (6.4.6) and (6.2.5.2.3) is the appearance of the $V_\parallel\boldsymbol{n}\cdot\nabla h$ term in the kinetic part. Thus, only the combination of $\boldsymbol{V}_E$ and $V_\parallel\boldsymbol{n}$ appears in equation (6.4.6) and in the solution for tori that possess symmetry. The flux surface averaged viscous forces determine this combined quantity and, subsequently, all the transport fluxes as a consequence. Without the $V_\parallel\boldsymbol{n}\cdot\nabla h$ term in equation (6.4.6), the parallel flow speed and the component of $\boldsymbol{V}_E$ appear as two independent entities even in tori that possess symmetry. The averaged parallel force balance equations alone are not adequate to determine plasma flows and transport fluxes if that is the case. In addition, when $V_\parallel\boldsymbol{n}+\boldsymbol{V}_E$ is in the toroidal direction in axisymmetric tokamaks, the resonant shift of the tips of the banana particles does not occur, as evidenced in [134]. Thus, to have proper physics when $\boldsymbol{V}_E$ is important, the parallel flow velocity must be included in the drift kinetic equation. This important physics is often ignored, however.

6.4.1. Plateau–Pfirsch–Schlüter regime. In the $\varepsilon<1$ limit, the ∇B and curvature drifts can be neglected and equation (6.4.6) reduces to

$$\left[(v_\parallel+V_\parallel)\boldsymbol{n}+\boldsymbol{V}_E\right]\cdot\nabla h-C(h)=2\frac{v^2}{v_\mathrm{t}^2}\left(\frac{1}{2}-\frac{3}{2}\frac{v_\parallel^2}{v^2}\right)f_\mathrm{M}\times\left[\frac{\boldsymbol{V}\cdot\nabla B}{B}+\frac{2}{5}\left(\frac{v^2}{v_\mathrm{t}^2}-\frac{5}{2}\right)\frac{\boldsymbol{q}\cdot\nabla B}{pB}\right]. \tag{6.4.1.1}$$

In the plateau–Pfirsch–Schlüter regime, equation (6.4.1.1) can be solved using a Krook model to approximate the collision

operator, i.e., $C(h) = -\nu_T h$. The viscous coefficients are [135]

$$\mu_j = \frac{v_t}{Rq}\frac{\varepsilon^2}{2\sqrt{\pi}}\int_0^\infty \mathrm{d}x x^5 \mathrm{e}^{-x^2}\left(x^2-\frac{5}{2}\right)^{j-1} \times \int_{-1}^{1}\mathrm{d}y\left(1-3y^2\right)^2\left(\frac{v\boldsymbol{B}\cdot\nabla\theta}{B}\right)R_{10}, \quad (6.4.1.2)$$

where $R_{10} = \nu_T/(\omega_{\theta a}^2+\nu_T^2)$ and $\omega_{\theta a} = (v_\parallel + V_\parallel)B\cdot\nabla\theta/B + \boldsymbol{V}_E\cdot\nabla\theta$.

In the plateau regime where ν_T approaches 0, the resonant function R_{10} reduces to a delta function. The resonant singularity, however, is no longer at $v_\parallel = 0$ as in the conventional theory. Instead, it is at

$$v_\parallel = -V_\parallel - B\frac{\boldsymbol{V}_E\cdot\nabla\theta}{\boldsymbol{B}\cdot\nabla\theta} = -V_\parallel - \frac{Ic\Phi'}{B}. \quad (6.4.1.3)$$

Because $|v_\parallel/v| < 1$, the resonance condition in equation (6.4.1.3) can be satisfied only when

$$\frac{v}{v_t} > \left|\frac{V_\parallel}{v_t}+\frac{Ic\Phi'}{Bv_t}\right| = \left|\frac{V_\parallel}{v_t}-\frac{cE_r}{B_p v_t}\right|. \quad (6.4.1.4)$$

Since the equilibrium distribution function is a Maxwellian, the number of particles that can satisfy the resonance condition diminishes exponentially, and the viscous coefficients in equation (6.4.1.2) decrease exponentially as $|U_{p,m}| = |V_\parallel/v_t - cE_r/(B_p v_t)|$ increases. This exponentially decay dependence is the characteristic behaviour for the resonant transport when the radial electric field becomes important to the particle dynamics. The viscous coefficients scale linearly with $U_{p,m}$ when $|U_{p,m}| < 1$, reach an extreme when $|U_{p,m}|$ is of the order of unity, and decrease exponentially when $|U_{p,m}| > 1$.

In the Pfirsch–Schlüter regime, the resonant function can have two distinct scalings. One is when $\nu_T > |\omega_{\theta a}|$ and $R_{10} \sim \nu_T^{-1}$. This reproduces the standard viscous forces in the Pfirsch–Schlüter regime shown in section 6.2.3. The other limit is when $|\omega_{\theta a}| > \nu_T$, and $R_{10} \sim \nu_T/\omega_{\theta a}^2$. The viscous forces in equation (6.4.1.2) decrease as $1/|U_{p,m}|$ in this limit. This algebraic decay dependence is the characteristic behaviour for the non-resonant transport.

The integrals in the viscous coefficients μ_j properly describe the transitions from various limits in the plateau–Pfirsch–Schlüter regime. It is important to note that plasma viscous forces are a non-linear function of $U_{p,m}$. When $|U_{p,m}|$ increases, plasma viscous forces decrease either exponentially for the resonant transport mechanism or algebraically for the non-resonant transport mechanism.

6.4.2. Banana regime. The non-linear dependence of the viscous forces on $U_{p,m}$ also exists in the banana regime [136]. In the edge region of H-mode plasmas, the effects of orbit squeezing are also important. Thus, it is better to combine these two pieces of physics in the theory for the non-linear plasma viscosity in the banana regime.

To have the non-linear plasma viscosity dependence on $U_{p,m}$ for axisymmetric tokamaks, the theory for squeezed orbits must also include the parallel mass flow $V_\parallel$ in addition to the customarily included poloidal $\boldsymbol{E}\times\boldsymbol{B}$ drift, as shown in [136]. Using this generalized theory for the squeezed orbits and the method in solving the drift kinetic equation developed for the effects of orbit squeezing yield the viscous coefficients for the non-linear plasma viscosity in the banana regime for large aspect ratio tokamaks, for $j = 1$–3, [79, 136]

$$\mu_j = \frac{8\sqrt{2}}{\sqrt{\pi}}I_{pn}\frac{\sqrt{\varepsilon}}{S^{3/2}}\int_{U_{p,m}}^\infty \mathrm{d}x\nu_D F_f x^4\left(x^2-\frac{5}{2}\right)^{j-1} \times \mathrm{e}^{-x^2}\left(\frac{1}{2}-\frac{3}{2}\frac{U_{p,m}^2}{x^2}\right)^2\left(1+\frac{U_{p,m}^2}{x^2}\right)^{-3/2}, \quad (6.4.2.1)$$

where $I_{pn} = 1.38$, and

$$F_f = \left(1-\frac{U_{p,m}^2}{x^2}\right)+\frac{\nu_\parallel}{\nu_D}\frac{U_{p,m}^2}{x^2}. \quad (6.4.2.2)$$

The factor F_f results from the energy dependence in the resonant condition that makes the energy scattering operator important in the de-correlation of the squeezed banana orbits. The viscous coefficients in the banana regime have a similar dependence on $U_{p,m}$ as those in the plateau regime. They decrease exponentially as $\mathrm{e}^{-U_{p,m}^2}$ when $|U_{p,m}|$ is larger than unity.

6.4.3. Approximate analytic expressions for non-linear viscous coefficients and electrode-induced bifurcation. To facilitate modelling of the bootstrap current and the neoclassical transport processes in the pedestal region it is convenient to have approximate analytic expressions for viscous coefficients that join asymptotic limits in the banana and plateau–Pfirsch–Schlüter regimes that include effects of orbit squeezing and finite values of $|U_{p,m}|$. This can be accomplished by using rational approximation [6, 7] that reproduces asymptotic limits, and the results are [115]

$$\mu_j = \frac{8}{3\sqrt{\pi}}\int_{|U_{p,m}|}^\infty \mathrm{d}x x^4\mathrm{e}^{-x^2}\left(x^2-\frac{5}{2}\right)^{j-1}\frac{\mu_b\mu_{pps}}{\mu_b+\mu_{pps}} + \frac{8}{3\sqrt{\pi}}\int_0^{|U_{p,m}|}\mathrm{d}x x^4\mathrm{e}^{-x^2}\left(x^2-\frac{5}{2}\right)^{j-1}\mu_{pps}, \quad (6.4.3.1)$$

for $j = 1$–3, where

$$\mu_b = 3\sqrt{2}I_{pm}\frac{\sqrt{\varepsilon}}{S^{3/2}}\nu_D F_f\left(\frac{1}{2}-\frac{3}{2}\frac{U_{p,m}^2}{x^2}\right)^2\left(1+\frac{U_{p,m}^2}{x^2}\right)^{-3/2}, \quad (6.4.3.2)$$

$$\mu_{pps} = \frac{3}{16}\frac{v_t}{Rq}\varepsilon^2\int_{-1}^{1}\mathrm{d}y\left(1-3y^2\right)^2 \times \frac{\nu_T/\omega_t}{\left(y+U_{p,m}/x\right)^2+\left[\nu_T/(x\omega_t)\right]^2}. \quad (6.4.3.3)$$

and $\omega_t = v_t\boldsymbol{B}\cdot\nabla\theta/B$. The first term on the right-hand side of equation (6.4.3.1) represents the resonant contribution in the banana–plateau regime and the non-resonant part from the Pfirsch–Schlüter regime. The second term is the non-resonant contribution in the Pfirsch–Schlüter regime.

A schematic dependence of the non-linear plasma viscosity in the plateau–Pfirsch–Schlüter regime on $U_{p,m}$ [15] is shown in figure 14.

The dynamics of the L–H transition theory based on the non-linear plasma viscosity [15] has been observed in electrode-induced L–H transition experiments [137]. The

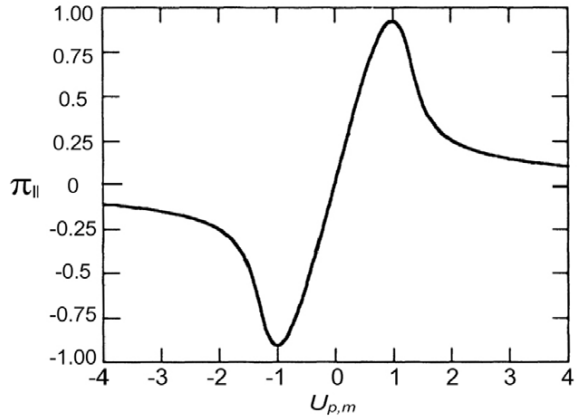

Figure 14. Typical non-linear plasma viscosity in the plateau–Pfirsch–Schlüter regime as a function of $U_{\mathrm{p},m}$ in a tokamak. The extrema occur at $|U_{\mathrm{p},m}|$ of the order of unity. It decays exponentially when $|U_{\mathrm{p},m}|$ is greater than unity. When $|U_{\mathrm{p},m}|$ is much larger than unity, it decays algebraically.

radial current driven by the orbit loss in the banana regime in the theory is replaced by the electrode current. When the electrode current vanishes, the standard neoclassical poloidal flow is reproduced in the theory as expected because it is $U_{\mathrm{p},m}$ not poloidal $\boldsymbol{E}\times\boldsymbol{B}$ drift that is employed in the formulation of the theory. As the current in the biased electrode increases, $U_{\mathrm{p},m}$, and, thus the radial electric field, deviates from the neoclassical value. When the electrode current is further increased, $U_{\mathrm{p},m}$ bifurcates as predicted by the non-linear plasma viscosity [15]. The bifurcation in experiments provides a direct test of the non-linearity in the viscous forces. Because the compressibility is not included in the theory, the shock formation is prevented. This implies that the real poloidal flow speed is assumed to be subsonic. Physically, this assumption implies that improved plasma confinement due to turbulence suppression results in a steep pressure gradient that almost cancels the increased $\boldsymbol{E}\times\boldsymbol{B}$ drift [132, 133]. If the real poloidal flow is sonic, the plasma flow velocity becomes compressible, and shock formation will occur. In that case, the shock viscosity becomes the relevant force for the electrode-induced bifurcation [132, 133].

The concept of the perpendicular conductivity or resistivity in toroidal plasmas [138] has often been used to describe the electrode-induced bifurcation. The conductivity or resistivity has been calculated by following the pioneering work in [139, 140]. The work in [139, 140] is also extended to describe the L–H transition in [141].

6.4.4. Transport fluxes The neoclassical transport fluxes associated with the non-linear plasma viscosity are different from those in the standard neoclassical theory when $U_{\mathrm{p},m}$ is of the order of unity or higher and when $S > 1$. The transport fluxes are smaller than those in the conventional theory. Thus, neoclassical plasma confinement is improved in the edge region of tokamaks after L–H transitions.

The specific transport fluxes can be obtained by substituting the viscous coefficients in the expressions for the fluxes in equations (6.2.5.4.2.1)–(6.2.5.4.2.5). Unlike when only the effects of the orbit squeezing are included, all transport fluxes are now modified except the neoclassical electric conductivity when $U_{\mathrm{p},m}$ is finite because the ratios of ion viscous coefficients are no longer the same as those in the conventional theory.

The equation for ion poloidal flow is a non-linear equation for $U_{\mathrm{p},m}$ by casting V_{i}^{θ} as

$$V_{\mathrm{i}}^{\theta} = \frac{U_{\mathrm{p},m}}{\langle B^2\rangle^{1/2}} v_{\mathrm{t}} + \frac{IcT_{\mathrm{i}}}{e_{\mathrm{i}}\langle B^2\rangle}\frac{p_{\mathrm{i}}'}{p_{\mathrm{i}}}, \tag{6.4.4.1}$$

in large aspect ratio tokamaks. When $N_{\mathrm{i}}M_{\mathrm{i}}|\mu_{ji}| \sim N_{\mathrm{e}}M_{\mathrm{e}}|\mu_{je}|$, the equation for V_{i}^{θ} in equation (6.2.5.4.2.1) can be expressed explicitly as a non-linear equation for $U_{\mathrm{p},m}$:

$$\begin{aligned}\frac{U_{\mathrm{p},m}}{\langle B^2\rangle^{1/2}} v_{\mathrm{t}} = &-\frac{IcT_{\mathrm{i}}}{e_{\mathrm{i}}\langle B^2\rangle}\frac{p_{\mathrm{i}}'}{p_{\mathrm{i}}} - \frac{\mu_{2\mathrm{i}}}{\mu_{1\mathrm{i}} + \frac{N_{\mathrm{e}}M_{\mathrm{e}}}{N_{\mathrm{i}}M_{\mathrm{i}}}\mu_{1\mathrm{e}}}\frac{IcT_{\mathrm{i}}'}{e_{\mathrm{i}}\langle B^2\rangle} \\ &+ \frac{\mu_{2\mathrm{e}}}{\mu_{1\mathrm{e}} + \frac{N_{\mathrm{i}}M_{\mathrm{i}}}{N_{\mathrm{e}}M_{\mathrm{e}}}\mu_{1\mathrm{i}}}\frac{IcT_{\mathrm{e}}'}{e\langle B^2\rangle} + \frac{\mu_{1\mathrm{e}}}{\mu_{1\mathrm{e}} + \frac{N_{\mathrm{i}}M_{\mathrm{i}}}{N_{\mathrm{e}}M_{\mathrm{e}}}\mu_{1\mathrm{i}}} \\ &\times\left[\frac{IcP'}{N_{\mathrm{e}}e\langle B^2\rangle} + \left(1 + \frac{l_{12}^{\mathrm{e}}}{l_{22}^{\mathrm{e}}}\frac{\mu_{2\mathrm{e}}}{\mu_{1\mathrm{e}}}\right)\frac{\sigma_s\left\langle E_{\parallel}^{(A)}B\right\rangle}{N_{\mathrm{e}}e\langle B^2\rangle}\right].\end{aligned} \tag{6.4.4.2}$$

This non-linear equation is similar to the bifurcation equation in the L–H transition theory in [15, 129] to determine $U_{\mathrm{p},m}$ in H-mode plasmas.

Ion heat flux $q_{\mathrm{i}}^{\mathrm{bp}}/T_{\mathrm{i}}$ decreases exponentially as $\mathrm{e}^{-U_{\mathrm{p},m}^2}$ in addition to the reduction as $S^{-3/2}$ resulting from effects of orbit squeezing in the banana regime [110]. In the plateau regime, it decreases as $\mathrm{e}^{-U_{\mathrm{p},m}^2}$ [142]. In both regimes, there are additional dependences on the complicated rational functions of $U_{\mathrm{p},m}$.

The bootstrap current and Ware pinch flux are also modified through ion poloidal flow V_{i}^{θ} or $U_{\mathrm{p},m}$. When the magnitudes of the ion and electron viscous forces are comparable, the bootstrap current can be reduced and can be used to control ELMs in the pedestal region.

6.5. Orbit loss

In the edge region of a tokamak, parallel plasma viscosity in the banana regime in the conventional neoclassical theory is no longer valid because collisionless particle orbits intersect the plasma boundary, which is either determined by a limiter or a divertor. There exists a loss region in the velocity space, analogous to the loss cone in a mirror machine [143–145]. When particles collisionally scatter into the loss region, they move out of the confinement zone. However, the loss process in tokamaks differs from that in mirror machines. In mirror machines, particles scatter into the loss region locally. In tokamaks, particles first transport radially to the edge region and then collisionally scatter into the loss region [146]. The process involves both spatial transport and velocity space scattering. It transports particle, momentum and energy from the core region to the edge region. Physically, this is to set a gradient scale length in the edge region so that the radial transport rate is the same as the orbit loss rate. This modifies the parallel plasma viscosity in the edge region, and thus, the parallel momentum balance equation.

The loss cone is not isotropic in the velocity space. It results in a toroidal flow even without obvious dissipation processes [147, 148]. This is another important aspect of the orbit loss process for the physics of plasma flows in the H-mode plasmas.

6.5.1. Estimated orbit loss rate. The detailed orbit loss rate depends on the position and the configuration of the limiter or the divertor. Thus, it varies from configuration to configuration. However, the gross scaling of the loss rate should be robust and only depend on the fundamental physics processes involved. Because the width of the ion orbits is greater than that of electrons, ions dominate the orbit loss process. In rare occasions when the electron temperature is much higher than the ion temperature, electrons can dominate the orbit loss process.

Particle, momentum and energy losses in the banana regime are all modified by the presence of the orbit loss region in the edge of tokamaks. The theory for energy loss was first developed in [146] using model orbits in a divertor configuration. By balancing the radial ion energy transport rate to the edge energy loss rate to determine a temperature gradient scale length, the corresponding ion energy flux at the separatrix is [146]

$$Q_{\rm i}^{\chi} = \frac{\pi}{2\Omega_2}\frac{I_{\rm G}}{W}\int {\rm d}v\nu_{\rm D}v^3\frac{M_{\rm i}v^2}{2}f_0, \qquad (6.5.1.1)$$

where Ω_2 is the ion gyro-frequency evaluated at the outer radius in a square well magnetic field model, $I_{\rm G} = 3\varepsilon^{1/2} - 2\varepsilon^{3/2}$, $W = 0.8\varepsilon$, and f_0 is the equilibrium ion distribution function which is non-Maxwellian [149] because the radial transport rate is comparable to the collisional energy scattering rate of the Coulomb collision operator. The rate of the energy loss does not depend explicitly on the plasma gradients. The effects of orbit squeezing are not included in equation (6.5.1.1). It is argued that because particle transport is intrinsically ambipolar in tokamaks, ion orbit loss does not affect the radial electric field [146].

However, from the flux–force relation and the theory for the poloidal flow damping discussed in section 4, the particle flux prior to the damping of the poloidal flow is proportional to the flux surface averaged parallel plasma viscosity, which is not governed by the intrinsic ambipolarity. When parallel flow is neglected, the poloidal flow is driven by the radial gradients of the plasma potential and pressure. In the edge region, the orbit loss process dictates that the gradient scale length is of the order of the squeezed orbit width [150]

$$\Delta\chi \sim \sqrt{\varepsilon}\frac{Iv_{\rm ti}}{\Omega_{\rm i}\sqrt{S}}, \qquad (6.5.1.2)$$

in equation (6.2.5.9). This is also the scaling of the width of the orbit loss region and effectively the scaling for the pedestal width in H-mode plasmas [150]. In the banana regime, the parallel plasma viscosity driven particle flux prior to the poloidal flow damping must be balanced by the collisional orbit loss rate. Thus, the parallel plasma viscosity scales as

$$\left\langle \boldsymbol{B}\cdot\nabla\cdot\overleftrightarrow{\pi}_{\rm i}\right\rangle \sim -N_{\rm i}M_{\rm i}Bv_{\rm ti}\frac{\nu_{\rm ii}}{S}. \qquad (6.5.1.3)$$

This yields an estimated orbit loss rate in the banana regime [151]

$$\left(\frac{\partial\langle N\rangle}{\partial t}\right)_{\rm orbit} = -\frac{1}{\Delta\chi}\int {\rm d}\left(\frac{v^2}{2}\right)\pi\nu_{\rm D}\frac{Iv^2}{\Omega_{\rm i}S}4.4f_0, \qquad (6.5.1.4)$$

including the effects of orbit squeezing.

The radial electric field is negative when the parallel viscous force due to orbit loss in the banana regime is coupled to the viscous force in the plateau and Pfirsch–Schlüter regimes [15, 129]. The radial electric field is to make ion particle loss vanish approximately to satisfy the ambipolarity constraint. This process also corresponds to the poloidal flow damping in the presence of the orbit loss region. When electron dominates the orbit loss process, the sign of the radial electric field becomes positive in the edge region.

It should be noted that the existence of the separatrix does not change the collision frequency scaling of the orbit loss rate because it merely changes the shape of the loss region in the phase space but not the fundamental physics of the coupling of the core transport with the collisional scattering into the loss region to determine the gradient scale length in the edge region [152].

Ion orbit loss flux when coupled to the electron anomalous particle flux leads to a non-linear equation for the radial electric field, first obtained in [153]. It has bifurcated solutions. It is the first theory to explain the L–H transition in tokamaks.

6.5.2. Non-linear momentum equation and L–H transition. The parallel momentum balance equation in the core region of axisymmetric tokamaks is a linear function of $U_{{\rm p},m}$. In tokamaks, only this combined quantity is determined from the parallel momentum balance equation. In the edge region, however, $U_{{\rm p},m}$ is of the order of unity, i.e., sonic because the radial gradient scale length of the radial electric field is of the order of the ion poloidal gyro-radius in the pedestal of H-mode plasmas. This makes the non-linear plasma viscosity relevant to the parallel momentum balance equation. Coupling the non-linear plasma viscosity to the ion orbit loss in the parallel momentum equation leads to a non-linear equation for $U_{{\rm p},m}$ and it has bifurcated solutions [15, 129].

A model for the non-linear equation based on the orbit loss for a bi-Maxwellian distribution function

$$f = \frac{N_{\rm c}}{\pi^{3/2}v_{\rm tc}^3}{\rm e}^{-v^2/v_{\rm tc}^2} + \frac{N_{\rm H}}{\pi^{3/2}v_{\rm tH}^3}{\rm e}^{-v^2/v_{\rm tH}^2}, \qquad (6.5.2.1)$$

is [129]

$$\frac{\nu_{*si}^{\rm c}}{\sqrt{2S\varepsilon}}\left(\frac{N_{\rm H}}{N_{\rm c}}\right)\left(\frac{T_{\rm c}}{T_{\rm H}}\right)^{3/2} \times\exp\left(-\left\{\nu_{*si}^{\rm c}\left(\frac{T_{\rm c}}{T_{\rm H}}\right)^2+\left[\frac{1}{2}\left(\frac{T_{\rm c}}{T_{\rm H}}\right)^2\frac{U_{{\rm p},m}}{\sqrt{2S\varepsilon}}\right]^4\right\}^{1/2}\right) = \frac{\pi}{9}\left(\frac{\sqrt{\varepsilon}\rho_{\rm pi}^{\rm c}}{\Delta r}\right)I_{ps}\left(\frac{V_{\rm p}B}{v_{\rm ti}^{\rm c}B_{\rm p}}\right), \qquad (6.5.2.2)$$

where the subscript c indicates that the quantities are for the cold component of the distribution, the subscript H is for the hot component, the left-hand side is the ion orbit loss associated with the parallel plasma viscosity for the hot component that is in the banana regime, the right-hand side is the parallel plasma viscosity for the cold component, $\nu_{*si}^{\rm c}$ is the ν_{*s} for cold ions, $V_{\rm p} = V^{\theta}B/v_{\rm ti}$, and Δr is $\Delta\chi$ in cylindrical r coordinate. The $I_{\rm bps}$ is defined as

$$I_{\rm bps} = \frac{2}{\pi}\int_0^{\infty}{\rm d}x x^5{\rm e}^{-x^2}\frac{K_{\rm bs}K_{\rm psn}}{K_{\rm bs}+K_{\rm psn}}, \qquad (6.5.2.3)$$

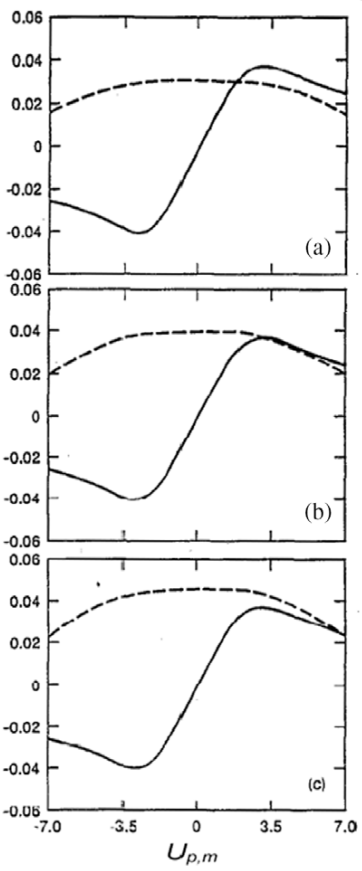

Figure 15. Bifurcated solution for $U_{\mathrm{p},m}$ as the ion orbit loss rate increases by increasing the ratio of $N_{\mathrm{H}}/N_{\mathrm{c}}$ from 0.1 (a) to 0.13 (b) and to 0.15 (c). The dashed line is the orbit loss rate, and the solid line is the non-linear plasma viscosity.

where $K_{\mathrm{psn}} = \int_{-1}^{1} \mathrm{d}y(1-3y^2)^2 \nu_{*si}\varepsilon^{3/2}(\nu_T/\nu x)\times \{(y+U_{\mathrm{p},m}/x)^2 + [\nu_{*si}\varepsilon^{3/2}(\nu_T/\nu x)]^2\}^{-1}$, $K_{\mathrm{bs}} = 2.5\nu^{\mathrm{c}}_{*si}\times (x^4|S|^{3/2})$. It is a formula that joins the non-linear plasma viscosity in the plateau–Pfirsch–Schlüter regime and the orbit squeezing viscosity in the banana regime. The poloidal heat flow in the plasma viscosity for the cold component and the electron viscosity are neglected in equation (6.5.2.2). The non-linear equation (6.5.2.2) has bifurcated solutions for $U_{\mathrm{p},m}$ over a wide range value of ν^{c}_{*si}. An example is shown in figure 15. When the orbit loss rate from the hot component is small, $U_{\mathrm{p},m}$ is the standard neoclassical value when the ion heat flow term is restored in the plasma viscosity for the cold component. This is the L-mode solution (figure 15(a)). As the orbit loss rate increases, there can be three solutions for $U_{\mathrm{p},m}$. Besides the L-mode solution, two more solutions appear; only one of them is stable. The new stable solution is the H-mode solution (figure 15(b)). As the orbit loss rate further increases, only H-mode solution for $U_{\mathrm{p},m}$ exists (figure 15(c)). The L-mode solution and H-mode solution are separated by the extremum of the viscous force, which occurs at a critical value of $U_{\mathrm{p},m}$, defined as $U^{C}_{\mathrm{p},m}$. This critical value of $U^{\mathrm{c}}_{\mathrm{p},m}$ as a function of ν_{*si} that separates L-mode from H-mode is shown in figure 16 for $\varepsilon = 1/4$ and $S = 1$.

The orbit loss also drives a poloidal flow as can be seen from equation (6.5.2.2). The direction of the flow is in the direction of the poloidal flow in the plateau–Pfirsch–Schlüter regime in the standard neoclassical theory [6, 7]. Thus, as far as the poloidal flow is concerned, the orbit loss mechanism is to increase the nominal value of ν_* effectively. In the L-mode case, the magnitude of this flow is insignificant. In H-mode, because of the large value of $U_{\mathrm{p},m}$ and S, it should not modify the neoclassical poloidal flow in (6.2.5.4.2.1) significantly either. In both cases, the poloidal flow should be determined by the neoclassical processes.

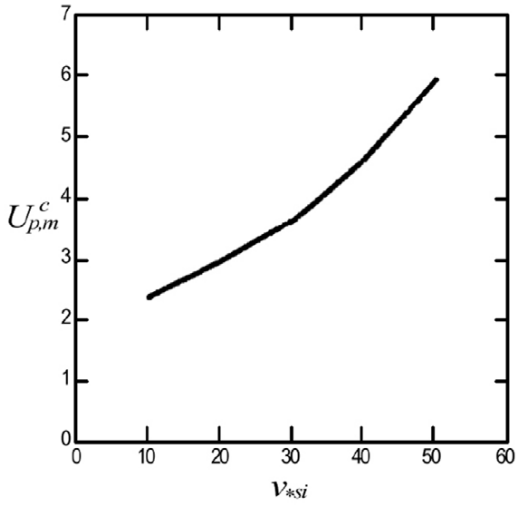

Figure 16. Critical value of $U^{\mathrm{c}}_{\mathrm{p},m}$ that separates L-mode from H-mode discharges as a function of ν_{*si} for $\varepsilon = 1/4$ and $S = 1$.

There are other observed L–H transition phenomena that can also be understood in terms of the theory presented here. The ion orbit loss mechanism provides a natural explanation for the dependence of the H-mode power threshold on the direction of the ion gradient B drift [154]. Neutral particles also affect the L–H transition. Through the charge exchange momentum loss mechanism, the extremum of the effective viscous force disappears when the density of the neutral particles exceeds a critical value [155]. This prevents the bifurcation, and thus the L–H transition. The effects of the guiding center shift also affect the radial electric field and, thus, L–H transition [156].

Neoclassical theory is usually employed to calculate the radial electric field. However, using the physics of the Pfirsch–Schlüter flow, the electrostatic potential variation in the edge region of the H-mode plasmas is also predicted in [157–159], which is in agreement with the experimental observations.

6.5.3. Shock formation. When the poloidal flow speed becomes sonic, i.e. the poloidal Mach number $M_{ps} = V_\theta B/(B_{\mathrm{p}} v_{\mathrm{t}})$ is of the order of unity, a poloidal shock can form as a result of the resonance between the parallel components of the inertia $NV\cdot\nabla V$ and plasma pressure ∇P [130–133]. A Bernoulli equation along the magnetic line can be derived. Because the magnetic field is not uniform on the magnetic surface, the poloidal flow along the field line is similar to a nozzle flow in gas dynamics. However, because the magnetic field is periodic in θ, the Bernoulli equation satisfies the periodic boundary condition, which differs from

the boundary condition for the nozzle flow. The plasma density and temperature vary on the magnetic surface resulting from plasma rotation. When $M_{ps} \ll 1$, the density and temperature variations are negligible. However, when $|1 - M_{ps}| < \sqrt{\varepsilon}$, a shock forms that is characterized by sharp variations of density and temperature with a width that depends on the dissipation of the system. This sharp variations of the density and temperature lead to a large viscous stress in the region where $|1 - M_{ps}| < \sqrt{\varepsilon}$ [130–133,160,161].

The viscosity is still calculated from the kinetic equation, but with an important difference. The equilibrium Maxwellian distribution is no longer a flux function. The density and temperature are allowed to have angle dependences. The drift kinetic equation is derived using the full density and temperature evolution equations including compressibility terms as illustrated in [132, 133].

7. Neoclassical quasilinear theory and turbulence suppression

Toroidal plasmas are plagued with turbulent fluctuations. The quasilinear theory can be adopted to give qualitative explanations to the observed anomalous particle, energy and momentum transport fluxes [162–171]. The effects of turbulence fluctuations on the bootstrap current, Ware pinch flux and modification on plasma resistivity are not usually addressed in the theory. In this regard, the conventional quasilinear theory is not as sophisticated as the neoclassical theory. However, the methodology of the neoclassical theory is well developed and should be used to describe transport related phenomena in toroidal plasmas. The purpose of the neoclassical quasilinear theory is to apply the methodology of the neoclassical theory to the quasilinear theory to unify both theories. The emphasis here is on the methodology and not on the magnetic geometry. Indeed, the methodology of the neoclassical theory can be applied even to unmagnetized plasmas.

The unification of neoclassical theory and quasilinear theory is first accomplished in [19, 21]. The methodology of the neoclassical theory is applied to solve the drift kinetic equation in the presence of turbulent fluctuations. The quasilinear transport fluxes including not only particle and energy fluxes but also bootstrap current [19, 21, 172], Ware pinch flux, and modification of plasma resistivity [19, 21, 167] are obtained in the theory.

There are several important implications and consequences as a result of the unification. It is first noted that the turbulence fluctuation spectrum can be affected by the radial electric field [21, 173]. This eventually leads to the development of the turbulence suppression theory [17]. The fluctuation driven bootstrap current, Ware pinch flux, and modification of the electric resistivity are shown to be relatively small compared with the corresponding transport coefficients in the neoclassical theory. This provides a natural explanation as to why even in turbulent tokamak and stellarator plasmas these transport fluxes are close to the values of the neoclassical theory. When the neoclassical methodology is applied to calculate the toroidal component of the stress in tokamaks, the toroidal momentum convective flux and the residual stress emerge naturally [174–178] besides the conventional toroidal momentum diffusion flux [179] similar to the constituents of the axisymmetric neoclassical toroidal plasma viscosity [68–70, 134, 180–188].

7.1. Particle, energy and current transport

Particle and energy transport fluxes are routinely calculated in quasilinear theory for toroidal plasmas [162–171]; the bootstrap current and its conjugate, i.e. Ware pinch, are not. The bootstrap current density parallel to the equilibrium magnetic field can be calculated in the theory using the neoclassical methodology. This puts the quasilinear theory on the same level of sophistication as the neoclassical theory.

7.1.1. Flux–force relation. As in the neoclassical theory, the flux–force relation is important to identify the forces that drive transport fluxes. For the sake of simplicity, only electrostatic fluctuations are discussed. When the electrostatic potential and, subsequently, the plasma density and temperature are allowed to have spatial and temporal random fluctuations, plasma transport losses are enhanced due to perturbed radial $\boldsymbol{E} \times \boldsymbol{B}$ drift.

Using the procedure that leads to the flux–force relation in the neoclassical theory, the electrostatic potential fluctuation-induced radial particle flux $\Gamma^{\rm an}$ and heat flux $q^{\rm an}$ are, in Hamada coordinates, [21]

$$\Gamma^{\rm an} = \frac{c}{\chi'\psi' e}\left\langle eN\boldsymbol{B}_{\rm t}\cdot\nabla\tilde{\Phi}\right\rangle - \frac{c}{\chi'\psi' e}\left\langle (\boldsymbol{B}_{\rm t}\cdot\boldsymbol{n})\, Ne\boldsymbol{n}\cdot\nabla\tilde{\Phi}\right\rangle, \tag{7.1.1.1}$$

and

$$q^{\rm an} = \frac{c}{\chi'\psi' e}\left\langle e\left(\frac{3}{2}\bar{N}\tilde{T} - \tilde{N}\tilde{T}\right)\boldsymbol{B}_{\rm t}\cdot\nabla\tilde{\Phi}\right\rangle - \frac{c}{\chi'\psi' e}\left\langle \frac{\boldsymbol{B}_{\rm t}\cdot\boldsymbol{B}}{B^2}e\left(\frac{3}{2}\bar{N}\tilde{T} - \tilde{N}\tilde{T}\right)\boldsymbol{B}\cdot\nabla\tilde{\Phi}\right\rangle, \tag{7.1.1.2}$$

where the angular brackets denote both flux surface average and ensemble average in this section, the tilde denotes fluctuation quantities, the overbar denotes equilibrium quantities and prime denotes $\mathrm{d}/\mathrm{d}V$. The definition for heat flux is $\langle \boldsymbol{q}\cdot\nabla V\rangle = \langle \boldsymbol{Q}\cdot\nabla V\rangle - (5/2)\langle N\boldsymbol{V}\cdot\nabla V\rangle\bar{T}$. From the expressions for $\Gamma^{\rm an}$ and $q^{\rm an}$, it is obvious that these fluxes are driven by the coupling between the perturbed potential and the perturbed density and temperature. To calculate these fluxes, the forces on the right-hand sides of equations (7.1.1.1) and (7.1.1.2) must be evaluated from the solution of the kinetic equation.

7.1.2. Linear drift kinetic equation. Low frequency fluctuations, with frequency $\omega < |\Omega|$, usually cause larger step size. Therefore transport fluxes are larger than higher frequency modes, and the drift kinetic equation is appropriate to use, in neoclassical quasilinear theory. The gyro-kinetic equation can also be used [189]. However, the important qualitative results do not depend on which kinetic equation is employed in the theory.

The drift kinetic equation is [29]

$$\frac{\partial f}{\partial t} + v_{\parallel}\boldsymbol{n}\cdot\nabla f + v_{\rm d}\cdot\nabla f + \left(e\frac{\partial\Phi}{\partial t} + ev_{\parallel}E_{\parallel}^{(A)}\right)\frac{\partial f}{\partial E} = C\,(f)\,. \tag{7.1.2.1}$$

Assuming $|e|\tilde{\Phi}/T \sim \varepsilon < 1$, and $\omega \sim \omega_d < \omega_t = v_t/(Rq) \sim \nu$, equation (7.1.2.1) can be linearized. Here, ω_d is the typical drift frequency, which is of the order of mv_d/L_n. The lowest order equation is

$$v_{||} n \cdot \nabla f_0 = C(f_0), \tag{7.1.2.2}$$

which has a solution

$$f_0 = f_M = \frac{\bar{N}}{\pi^{3/2} v_t^3} \exp\left(-\frac{v^2}{v_t^2} - \frac{2e\tilde{\Phi}}{Mv_t^2}\right). \tag{7.1.2.3}$$

The next order equation is

$$\frac{\partial f_1}{\partial t} + v_{\|} \boldsymbol{n} \cdot \nabla f_1 + \boldsymbol{v}_d \cdot \nabla f_1 + \boldsymbol{v}_d \cdot \nabla f_M + \left(e\frac{\partial \tilde{\Phi}}{\partial t} + ev_{\|} E_{||}^{(A)}\right) \frac{\partial f_M}{\partial E} = C(f_1), \tag{7.1.2.4}$$

where both neoclassical and quasilinear effects are included. Again to treat the momentum restoring terms in the collision operator, and the driving terms that are proportional to P_1, the solution is expanded as [19, 21]

$$f_1 = h + \frac{2v_{||}}{v_t^2}\left(V_{||} - \frac{2}{5} L_1^{(3/2)} \frac{q_{||}}{\bar{p}} + \cdots\right) f_M. \tag{7.1.2.5}$$

Substituting equation (7.1.2.5) into equation (7.1.2.4), keeping only the perturbed $\boldsymbol{E}\times\boldsymbol{B}$ drift terms that are first order in ρ/L_n ordering, and neglecting neoclassical ∇B and curvature drift terms yield

$$\frac{\partial h}{\partial t} + v_{\|} \boldsymbol{n} \cdot \nabla h + \boldsymbol{v}_d \cdot \nabla h - C(h) = \frac{e}{\bar{T}} \frac{\partial \tilde{\Phi}}{\partial t} f_M + \left(V_p - \frac{2}{5} L_1^{(3/2)} \frac{q_p}{\bar{p}}\right)\left(\frac{e}{\bar{T}} \frac{\partial \tilde{\Phi}}{\partial \theta}\right) f_M + \left(V_t - \frac{2}{5} L_1^{(3/2)} \frac{q_t}{\bar{p}}\right)\left(\frac{e}{\bar{T}} \frac{\partial \tilde{\Phi}}{\partial \zeta}\right) f_M, \tag{7.1.2.6}$$

where equilibrium flows are

$$V_p = (\boldsymbol{n} \cdot \nabla\theta) V_{||} + \frac{\bar{T}}{M} \frac{\boldsymbol{B} \times \nabla V \cdot \nabla\theta}{B\Omega}\left(\frac{\bar{p}'}{\bar{p}} + \frac{e\bar{\Phi}'}{\bar{T}}\right), \tag{7.1.2.7}$$

$$V_t = (\boldsymbol{n} \cdot \nabla\zeta) V_{||} + \frac{\bar{T}}{M} \frac{\boldsymbol{B} \times \nabla V \cdot \nabla\zeta}{B\Omega}\left(\frac{\bar{p}'}{\bar{p}} + \frac{e\bar{\Phi}'}{\bar{T}}\right), \tag{7.1.2.8}$$

$$\frac{q_p}{\bar{p}} = (\boldsymbol{n} \cdot \nabla\theta) \frac{q_{||}}{\bar{p}} + \frac{5\bar{T}}{2M} \frac{\boldsymbol{B} \times \nabla V \cdot \nabla\theta}{B\Omega} \frac{\bar{T}'}{\bar{T}}, \tag{7.1.2.9}$$

and

$$\frac{q_t}{\bar{p}} = (\boldsymbol{n} \cdot \nabla\zeta) \frac{q_{||}}{\bar{p}} + \frac{5\bar{T}}{2M} \frac{\boldsymbol{B} \times \nabla V \cdot \nabla\zeta}{B\Omega} \frac{\bar{T}'}{\bar{T}}. \tag{7.1.2.10}$$

It is important to note that if the neoclassical ∇B and curvature drift terms are kept in equation (7.1.2.6), neoclassical viscous forces and, subsequently, all neoclassical fluxes can be obtained as demonstrated in [21]. Thus, the unification is accomplished.

The standard quasilinear theory corresponds to the 'plateau' regime in the neoclassical theory. In the 'plateau' regime, where $\omega_{tmn}|e\tilde{\Phi}_{mn}/T|^{3/2} < \nu < |\omega_{mn}^E| \sim \omega_{tmn}$, the dissipation mechanism is the resonance between the transit frequency $\omega_{tmn} = [v_t/(Rq)]|m - nq|$ and the Doppler shifted mode frequency $\omega_{mn}^E = \omega + \omega_E$. Here, $\tilde{\Phi}_{mn}$ is the amplitude of the fluctuating electrostatic potential with mode number (m, n), and $\omega_E = (c\bar{\Phi}'/B^2)(mB \times \nabla V \cdot \nabla\theta - nB \times \nabla V \cdot \nabla\zeta)$. The lower limit of this regime prevents electrostatic particle trapping from occurring. The upper limit is the lower bound of the fluid regime. In this regime, neoclassical theory and quasilinear theory are decoupled, and modes are also independent of each other because plasmas are collisional enough to prevent particles moving along the magnetic field line from sampling all the modes.

In the plateau regime, equation (7.1.2.6) can be solved by using a Krook model for the collision operator and expanding h and $\tilde{\Phi}$ as $h = \sum_{m,n\neq 0} h_{mn} \exp[i\omega t + i(m\theta - n\zeta + \eta_{mn})]$, and $\tilde{\Phi} = \sum_{m,n\neq 0} \tilde{\Phi}_{mn} \exp[i\omega t + i(m\theta - n\zeta + \eta_{mn})]$, where η_{mn} represents the random phase. Substituting these expressions into equation (7.1.2.6) and taking the $\nu \to 0$ limit, which corresponds to the asymptotic limit of the plateau regime, yield the resonant part of the solution

$$h_{mn} = i\pi\delta\left[\omega_{mn}^E + v_{\|}\left(\hat{n} \cdot \nabla\theta\right)(m - nq)\right] D_{mn}, \tag{7.1.2.11}$$

where

$$D_{mn} = \omega \frac{e\bar{\Phi}_{mn}}{\bar{T}} f_M + f_M\left(V_p - \frac{2}{5} L_1^{(3/2)} \frac{q_p}{\bar{p}}\right)(m)\left(\frac{e\tilde{\Phi}_{mn}}{\bar{T}}\right) + f_M\left(V_t - \frac{2}{5} L_1^{(3/2)} \frac{q_t}{\bar{p}}\right)(n)\left(\frac{e\tilde{\Phi}_{mn}}{\bar{T}}\right). \tag{7.1.2.12}$$

7.1.3. Transport matrix. The distinct feature of the unification is to include the bootstrap current, Ware pinch flux and the modification of the plasma resistivity in the quasilinear theory. The Ware pinch flux is obtained from the parallel flows in the components of the electrostatic forces $\langle eN\boldsymbol{B}_t \cdot \nabla\tilde{\Phi}\rangle$, $\langle(\boldsymbol{B}_t \cdot \boldsymbol{n})Ne\boldsymbol{n} \cdot \nabla\tilde{\Phi}\rangle$, $\langle e[(3/2)\tilde{N}\tilde{T} - \tilde{N}\tilde{T}]\boldsymbol{B}_t \cdot \nabla\tilde{\Phi}\rangle$, and $\langle(\boldsymbol{B}_t \cdot \boldsymbol{B}/B^2)e[(3/2)\tilde{N}\tilde{T} - \tilde{N}\tilde{T}]\boldsymbol{B} \cdot \nabla\tilde{\Phi}\rangle$. These forces play the same roles as the viscous forces in the neoclassical theory. The bootstrap current and the modification on the plasma resistivity are obtained by solving the parallel force balance equations for electrons

$$\langle N_e eB\boldsymbol{n} \cdot \nabla\Phi\rangle - \left\langle N_e eE_{||}^{(A)} B\right\rangle + \langle BF_{1||e}\rangle = 0, \tag{7.1.3.1}$$

and

$$\left\langle e\left(\frac{3}{2}\bar{N}_e\tilde{T}_e - \tilde{N}_e\bar{T}_e\right)B\boldsymbol{n} \cdot \nabla\Phi\right\rangle + \bar{T}_e\langle BF_{2||e}\rangle = 0, \tag{7.1.3.2}$$

obtained by taking the $v_{\|}$ and $v_{\|}(M_e v^2/2 - 5\bar{T}_e/2)$ moments of equation (7.1.2.6). Thus, it is obvious that the forces that drive the fluctuation-induced bootstrap current are the electrostatic forces $\langle N_e eB\boldsymbol{n} \cdot \nabla\Phi\rangle$ and $\langle e[(3/2)\tilde{N}\tilde{T} - \tilde{N}\tilde{T}]\boldsymbol{B} \cdot \nabla\tilde{\Phi}\rangle$.

Evaluating the fluxes using the resonant solution and solving the parallel force balance equations yield the

electron transport matrix [21], in approximate cylindrical coordinates,

$$\begin{pmatrix} \Gamma^{e}_{AN} \\ q^{e}_{AN}/T_e \\ J_{||}/T_e \end{pmatrix} = \begin{pmatrix} D_{nn} & -3D_{nn}/2 & WP \\ -3D_{nn}/2 & 13D_{nn}/4 & -0.87WP \\ WP & -0.87WP & \sigma_{e\Phi}/T_e \end{pmatrix} \times \begin{pmatrix} X_{1e} \\ X_{2e} \\ E^{(A)}_{||} \end{pmatrix}, \quad (7.1.3.3)$$

where

$$X_{1e} = -\left\langle \frac{\omega}{m} \right\rangle_e \frac{eBr}{cT_e} - \frac{T_i}{T_e}\frac{1}{P_i}\frac{dP_i}{dr} - \frac{e}{T_e}\frac{d\Phi}{dr} + \frac{T_e + T_i}{T_e}\frac{1}{P}\frac{dP}{dr} - \frac{3}{2}\frac{1}{T_e}\frac{dT_e}{dr},$$

$$X_{2e} = \frac{1}{T_e}\frac{dT_e}{dr},$$

$$D_{nn} = -\frac{\sqrt{\pi}}{4}\rho^2_{pe}\frac{v_{te}}{Rq}N\left[\sum_{m,n}\left(\frac{e\Phi_{mn}}{\sqrt{2}T_e}\right)^2\frac{m^2}{|m-nq|}\right],$$

$$WP = -\frac{\sqrt{\pi}}{2}\frac{c}{B_p}\frac{v_{te}}{Rq}\frac{N}{v_{ei}}\left[\sum_{m,n}\frac{m\,(m-nq)}{|m-nq|}\left(\frac{e\Phi_{mn}}{\sqrt{2}T_e}\right)^2\right],$$

$$\sigma_{e\phi} = \sigma_s\left[1 - 0.175\sqrt{\pi}\frac{v_{te}/(Rq)}{\nu_{ei}} \times \sum_{mn}|m-nq|\left(\frac{e\Phi_{mn}}{T_e}\right)^2\right],$$

$$\left\langle \frac{\omega}{m} \right\rangle_e = \sum_{m,n}\left(\frac{m\omega}{|m-nq|}\right)\Phi^2_{mn}\left[\sum_{m,n}\left(\frac{m^2}{|m-nq|}\right)\Phi^2_{mn}\right]^{-1},$$

and $\Phi_{mn} = |\tilde{\Phi}_{mn}|$.

The transport matrix is Onsager symmetric because the collision operator is self-adjoint [7]. It is important to note that transport coefficients have different wave vector dependences. The diffusion coefficients depend on the perpendicular wave vector and are strongly anomalous. The bootstrap current and modification on the plasma resistivity on the other hand depend on the parallel wave vector and are not affected significantly by the turbulent fluctuations.

7.1.4. Physics implications of the unified theory. The bootstrap current, Ware pinch fluxes and the modification on the plasma electric conductivity are not usually calculated in the conventional quasilinear theory. The unification of the neoclassical and quasilinear theories is to extend the standard particle and energy fluxes in the conventional quasilinear theory to include these additional transport quantities related to the plasma current. The quasilinear transport matrix in equation (7.1.3.3) is also obtained in [190] using the conventional method for the neoclassical theory.

It is important to note that the fluctuation driven bootstrap current is proportional to the parallel wave vector, i.e. $(m-nq)$. Thus, it vanishes for symmetric modes that centre around the mode rational surfaces where $m = nq$. There are at least two possibilities that the fluctuation driven bootstrap current does not vanish. The first possibility is that when the modes are not symmetric relative to the mode rational surface, e.g., as shown in figure 17. The second possibility is that when the fluctuation spectrum has a radial gradient, i.e. $\sum_{mn}|\Phi_{mn}|^2$ has a radial gradient as shown in figure 18, which is often the case in tokamaks and stellarators. However, in both cases, the fluctuation driven bootstrap current is small relative to the equilibrium bootstrap current [19, 21]. This provides an explanation as to why in turbulent tokamak and stellarator plasmas, the bootstrap current is close to the value predicted by the neoclassical theory.

Similarly, because the modification of the plasma resistivity resulting from the fluctuations is proportional to $|m-nq|$, the experimentally observed plasma resistivity is close to that predicted by the neoclassical theory.

One of the most significant implications of the unified theory is that the parallel momentum and heat flux balanced equations in turbulent toroidal plasmas can be approximated by those used in the neoclassical theory for localized modes that have $m - nq \approx 0$. This implies that the poloidal flow in tokamaks is close to what predicted by the neoclassical theory. It follows that both the bootstrap current and the modification on the plasma resistivity are well approximated by values in the neoclassical theory.

There is a radial electric field in the thermodynamic force X_{1e} in the particle flux. However, because for low frequency

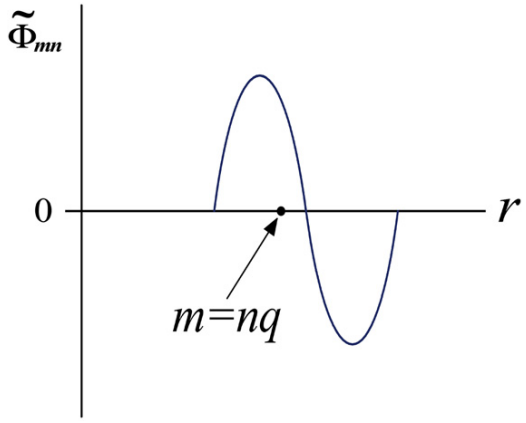

Figure 17. Schematic diagram for a mode that is not symmetric to the mode rational surface.

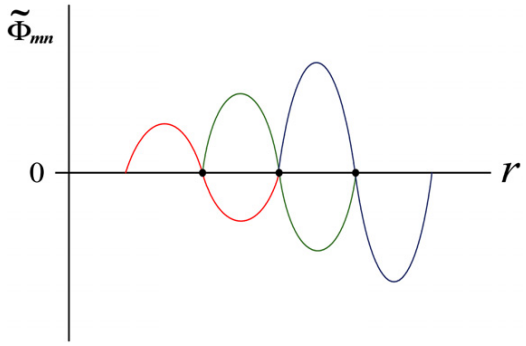

Figure 18. Schematic diagram for the fluctuation spectrum that has a radial gradient. The black dots indicate the positions of the mode rational surfaces.

electrostatic fluctuations quasineutrality is imposed to obtain the dispersion relation, ambipolarity is not maintained by setting the ion particle flux to the electron flux. Thus, when there is a change in the radial electric field, the fluctuation spectrum must change to maintain ambipolarity. This leads to the turbulence suppression theory.

7.2. Toroidal momentum transport

Neoclassical theory usually cannot explain toroidal momentum confinement in tokamaks because the predicted toroidal flow relaxation time is too long [68–70, 134, 180–188]. The theory for the neoclassical toroidal angular momentum flux has been evolving. The recent accepted form has been established basically in [184, 185], where the key insight, that when the potential and density variations along the magnetic field line are taken into account the magnitude of the gyro-viscosity reduces to that of the perpendicular viscosity, is advanced. In terms of Braginskii classification, these are viscosities that depend on ν^0 and ν^1 respectively. Neoclassical toroidal angular momentum flux consists of both perpendicular viscosity and gyro-viscosity. The perpendicular viscosity yields the momentum diffusion, which determines the relaxation time scale, and the gyro-viscosity, independent of the flow, acts like the momentum source. Thus, it has constituents similar to that observed in experiments. To understand the physics of toroidal rotation in experiments, fluctuation driven toroidal stress can be important. The quasilinear theory for the toroidal momentum flux provides a qualitative description for the toroidal rotation when the turbulent fluctuation level is high enough to compete with other mechanisms.

The drift kinetic equation is adopted. In the quasilinear theory, as in most of the neoclassical theories for the axisymmetric toroidal stress for tokamaks [67–70, 134, 180–188], the toroidal stress is derived in the laboratory frame, where the notion of the Coriolis force is not applicable. In the theory for the sonic toroidal rotation [134],the Coriolis force appears in the drift velocity. However, the diamagnetic flow is higher order and is neglected in that theory. A quasilinear theory developed using the same sonic ordering is presented in [191]. Experimentally, the toroidal rotation speed, measured in the laboratory frame, is usually subsonic and is of the order of $v_t\rho_{pi}/L_n$. Thus, the diamagnetic flow must be kept in the theory for toroidal momentum confinement to model experiments. For these reasons, the standard drift kinetic equation for subsonic flow is employed. The gyro-kinetic equation can also be used for the same purpose [192].

7.2.1. Linear drift kinetic equation. The toroidal stress can be derived from the second-order linear drift kinetic equation in the gyro-radius ordering, i.e. $(\rho_{pi}/L)^2$. Again, the perturbed distribution function is expanded as

$$f_1 = h + \frac{2v_{||}V_{||}}{v_t^2} f_M + \frac{2v_{||}^2V_{||}^2}{v_t^4} f_M + \cdots, \tag{7.2.1.1}$$

where $q_{||}$ is neglected for simplicity. Assuming $\varepsilon < 1$, the toroidal flow speed is approximately the same as the parallel flow. Substituting equation (7.2.1.1) into equation (7.1.2.1) and keeping only the perturbed $\boldsymbol{E} \times \boldsymbol{B}$ drift terms yield the second-order equation [174]

$$\frac{\partial h}{\partial t} + \left(v_{||}\boldsymbol{n} + V_E\right) \cdot \nabla h - C\,(h) = -\left(\tilde{D}_0 + \tilde{D}_1 + \tilde{D}_2 + \tilde{D}_3\right), \tag{7.2.1.2}$$

where

$$\tilde{D}_0 = \frac{2v_{||}}{v_t^2} f_M \frac{c\boldsymbol{B} \times \nabla\psi}{B^2} \cdot \left(\nabla\theta \frac{\partial\tilde{\Phi}}{\partial\theta} + \nabla\zeta \frac{\partial\tilde{\Phi}}{\partial\zeta}\right) \frac{\partial V_{||}}{\partial\chi},$$

$$\tilde{D}_1 = -\frac{e}{\bar{T}} f_M \left[\left(V_p - \frac{2}{5}L_1^{(3/2)}\frac{q_p}{\bar{p}}\right)\left(\frac{\partial\tilde{\Phi}}{\partial\theta}\right) + \left(V_t - \frac{2}{5}L_1^{(3/2)}\frac{q_t}{\bar{p}}\right)\left(\frac{\partial\tilde{\Phi}}{\partial\zeta}\right)\right],$$

$$\tilde{D}_2 = -\frac{e}{\bar{T}}\frac{2v_{||}}{v_t^2} f_M V_{||} \left[\left(V_p - \frac{2}{5}L_1^{(3/2)}\frac{q_p}{\bar{p}}\right)\left(\frac{\partial\tilde{\Phi}}{\partial\theta}\right) + \left(V_t - \frac{2}{5}L_1^{(3/2)}\frac{q_t}{\bar{p}}\right)\left(\frac{\partial\tilde{\Phi}}{\partial\zeta}\right)\right],$$

and

$$\tilde{D}_3 = -\frac{e}{\bar{T}} f_M \frac{\partial\tilde{\Phi}}{\partial t}\left(1 + \frac{2v_{||}V_{||}}{v_t^2}\right).$$

Because $q_{||}$ is neglected, it does not appear in the definitions for q_p and q_t in equations (7.1.2.9)–(7.1.2.10). Some of the first-order terms in ρ_pi/L are kept in equation (7.2.1.2) because these terms contribute to the residual stress that is proportional to $m - nq \approx 0$ for localized modes.

Equation (7.2.1.2) can be solved in the plateau regime using the method in section in 7.1.2, and the resonant part of the solution is

$$h_{mn} = \mathrm{i}\pi\delta\left[\omega^E_{mn} + v_{||}\left(m - nq\right)\boldsymbol{n}\cdot\nabla\theta\right]M_{mn}, \qquad (7.2.1.3)$$

where

$$\begin{aligned}M_{mn} = {}& \omega\frac{e\tilde{\Phi}_{mn}}{\bar{T}}f_\mathrm{M}\left(1+\frac{2v_{||}V_{||}}{v_\mathrm{t}^2}\right)\\ &+\frac{e}{\bar{T}}f_\mathrm{M}\left[m\tilde{\Phi}_{mn}\left(V_\mathrm{p}-\frac{2}{5}L_1^{(3/2)}\frac{q_\mathrm{p}}{\bar{p}}\right)\right.\\ &\left.-n\tilde{\Phi}_{mn}\left(V_\mathrm{t}-\frac{2}{5}L_1^{(3/2)}\frac{q_\mathrm{t}}{\bar{p}}\right)\right]\\ &+\frac{e}{\bar{T}}\frac{2v_{||}}{v_\mathrm{t}^2}f_\mathrm{M}V_{||}\left[m\tilde{\Phi}_{mn}\left(V_\mathrm{p}-\frac{2}{5}L_1^{(3/2)}\frac{q_\mathrm{p}}{\bar{p}}\right)\right.\\ &\left.-n\tilde{\Phi}_{mn}\left(V_\mathrm{t}-\frac{2}{5}L_1^{(3/2)}\frac{q_\mathrm{t}}{\bar{p}}\right)\right]\\ &+\frac{2v_{||}}{v_\mathrm{t}^2}f_\mathrm{M}\frac{c\boldsymbol{B}\times\nabla\chi}{B^2}\cdot\left(m\tilde{\Phi}_{mn}\nabla\theta - n\tilde{\Phi}_{mn}\nabla\zeta\right)\frac{\partial V_{||}}{\partial\chi}.\end{aligned}$$

The resonant solution is used to calculate the toroidal component of the stress.

7.2.2. Toroidal momentum equation in neoclassical quasilinear theory. The toroidal angular momentum equation is, in tokamak coordinates,

$$\frac{\partial}{\partial t}\left\langle R^2\nabla\zeta\cdot NM\boldsymbol{V}\right\rangle = -\left\langle R^2\nabla\zeta\cdot\nabla\cdot\overleftrightarrow{\boldsymbol{P}}\right\rangle + \frac{1}{c}\left\langle\boldsymbol{J}\cdot\nabla\chi\right\rangle. \qquad (7.2.2.1)$$

As shown in section 4.2, the radial current density $\langle\boldsymbol{J}\cdot\nabla\chi\rangle$ is related to $\partial\langle\boldsymbol{E}\cdot\nabla\chi\rangle/\partial t$, and can be neglected because it is smaller by a factor of $(V_\mathrm{A}/c)^2$. The flux surface averaged toroidal stress can be expressed in a conservative form [68]

$$\left\langle R^2\nabla\zeta\cdot\nabla\cdot\overleftrightarrow{\boldsymbol{P}}\right\rangle = \frac{1}{V'}\frac{\mathrm{d}}{\mathrm{d}\chi}V'\left\langle R^2\nabla\zeta\cdot\overleftrightarrow{\boldsymbol{P}}\cdot\nabla\chi\right\rangle, \qquad (7.2.2.2)$$

where the kinetic definition for the toroidal momentum flux for the electrostatic fluctuations is [68, 134, 186–188]

$$\left\langle R^2\nabla\zeta\cdot\overleftrightarrow{\boldsymbol{P}}\cdot\nabla\chi\right\rangle = \left\langle\int\mathrm{d}\boldsymbol{v}MR^2\nabla\zeta\cdot\boldsymbol{n}v_{||}\left(\boldsymbol{v}_E\cdot\nabla\chi\right)f\right\rangle, \qquad (7.2.2.3)$$

where $\boldsymbol{v}_E$ is the $\boldsymbol{E}\times\boldsymbol{B}$ drift velocity. The quantity $\langle R^2\nabla\zeta\cdot\overleftrightarrow{\boldsymbol{P}}\cdot\nabla\chi\rangle$ is the toroidal angular momentum flux Γ_ϕ. Using the resonant solution in equation (7.2.1.3) to evaluate $\langle R^2\nabla\zeta\cdot\overleftrightarrow{\boldsymbol{P}}\cdot\nabla\chi\rangle$ in equation (7.2.2.3) yields [174, 175]

$$\Gamma_\phi = \left\langle R^2\nabla\zeta\cdot\overleftrightarrow{\boldsymbol{P}}\cdot\nabla\chi\right\rangle = \left\langle P_1\right\rangle + \left\langle P_2\right\rangle + \left\langle P_3\right\rangle, \qquad (7.2.2.4)$$

where

$$\begin{aligned}\left\langle P_1\right\rangle = {}& -\sqrt{\pi}\frac{NV_\mathrm{t}MI}{B}\sum_{m,n,\omega}\frac{\omega^E_{mn}sgn\left(m-nq\right)}{\left[v_\mathrm{t}\left(m-nq\right)\hat{n}\cdot\nabla\theta\right]^2}\\ &\times\left|\frac{e\Phi_{mn\omega}}{T}\right|^2\mathrm{e}^{-x_0^2}\cdot\left(m\frac{T}{M}\frac{c\boldsymbol{B}\times\nabla\chi\cdot\nabla\theta}{B^2}\right)\\ &\times\left\{\left[\omega+\left(mU_\mathrm{p}-nU_\mathrm{t}\right)-\frac{2}{5}\left(m\frac{q_\mathrm{p}}{p}-n\frac{q_\mathrm{t}}{p}\right)\right.\right.\\ &\left.\left.\times\left(\frac{5}{2}-x_0^2\right)\right]\left(m\frac{T}{M}\frac{\boldsymbol{B}\times\nabla\chi\cdot\nabla\theta}{B\Omega}\right)^{-1}\right\},\\ \left\langle P_2\right\rangle = {}& -2\sqrt{\pi}\frac{NV_{||}MI}{B}\sum_{m,n,}\left(m\frac{T}{M}\frac{\boldsymbol{B}\times\nabla\chi\cdot\nabla\theta}{B^2}\right)^2\\ &\cdot\mathrm{e}^{-x_0^2}\frac{\left(\omega^E_{mn}\right)^2\left|e\Phi_{mn\omega}/T\right|^2}{\left(v_\mathrm{t}\left|m-nq\right|\hat{n}\cdot\nabla\theta\right)^3}\\ &\times\left\{\left[\omega+\left(mU_\mathrm{p}-nU_\mathrm{t}\right)-\frac{2}{5}\left(\frac{5}{2}-x_0^2\right)\left(m\frac{q_\mathrm{p}}{p}-n\frac{q_\mathrm{t}}{p}\right)\right]\right.\\ &\left.\times\left(m\frac{T}{M}\frac{\boldsymbol{B}\times\nabla\chi\cdot\nabla\theta}{\Omega B}\right)^{-1}\right\}\end{aligned}$$

and

$$\begin{aligned}\left\langle P_3\right\rangle = {}& -2\sqrt{\pi}\frac{NMI}{B}\frac{\partial V_{||}}{\partial\chi}\sum_{m,n,}\frac{\mathrm{e}^{-x_0^2}\left(\omega^E_{mn}\right)^2\left|e\Phi_{mn}/T\right|^2}{\left(v_\mathrm{t}\left|m-nq\right|\hat{n}\cdot\nabla\theta\right)^3}\\ &\times\left(m\frac{T}{M}\frac{\boldsymbol{B}\times\nabla\chi\cdot\nabla\theta}{\Omega B}\right)^2.\end{aligned}$$

The $x_0 = \omega^E_{mn}/v_\mathrm{t}\left|m-nq\right|\hat{\boldsymbol{n}}\cdot\nabla\theta$. It is obvious that the magnitude of the ion stress is usually larger than that of electrons.

The toroidal momentum flux consists of three types of fluxes [174, 175]. One is the diffusive flux that is proportional to $\partial V_{||}/\partial\chi$ [179]. Another is the convective flux driven by $V_{||}$ [174, 175, 177, 193]. The other is the residual stress that is independent of $V_{||}$ [174–176]. The convective flux cannot be expressed as $\Gamma_\mathrm{i}^\mathrm{an}V_{||}$, a property consistent with experimental observations. The residual flux is proportional to $m - nq$, which is the same as that in the fluctuation driven bootstrap current. Thus, it changes sign across the mode rational surface.

It is clear that Γ_ϕ depends on the fluctuation spectrum. For

$$\omega^E_{mn} = -\frac{mT\boldsymbol{B}\times\nabla\chi\cdot\nabla\theta}{MB\Omega}\left(\lambda_p\frac{p'}{p}+\lambda_T\frac{T'}{T}\right), \qquad (7.2.2.5)$$

Γ_ϕ can be expressed as

$$\Gamma_\phi = -\chi_\phi\frac{\partial V_{||}}{\partial\chi} - V_\phi V_{||} + \left\langle P_1\right\rangle, \qquad (7.2.2.6)$$

where λ_p and λ_T are two parameters to model the mode frequency, and

$$\begin{aligned}\chi_\phi = {}& 2\sqrt{\pi}\frac{NMI}{B}\frac{\partial V_{||}}{\partial\chi}\sum_{m,n,}\frac{\mathrm{e}^{-x_0^2}\left(\omega^E_{mn}\right)^2\left|e\Phi_{mn}/T\right|^2}{\left(v_\mathrm{t}\left|m-nq\right|\hat{n}\cdot\nabla\theta\right)^3}\\ &\times\left(m\frac{T}{M}\frac{\boldsymbol{B}\times\nabla\chi\cdot\nabla\theta}{\Omega B}\right)^2.\end{aligned} \qquad (7.2.2.7)$$

The convective velocity V_ϕ for this specific frequency is, after neglecting terms that are either proportional to $(m - nq)$ or smaller by a factor of $B_\mathrm{p}/(qB)$,

$$V_\phi = -\chi_\phi\left[\left(\lambda_p-1\right)\frac{p'}{p}+\left(\lambda_T+\frac{5}{2}\right)\frac{T'}{T}\right]. \qquad (7.2.2.8)$$

For different frequencies, the convective velocity will be different.

The residual stress plays a role similar to the toroidal momentum source when there are no externally imposed momentum sources. There are at least two possibilities that make the residual stress finite [174]. One is the asymmetric modes and the other is that the fluctuation spectrum has a radial gradient. They are the same as those that drive a local bootstrap current discussed in section 7.1.4. Here, both of these mechanisms drive a local toroidal flow. The magnitude of the toroidal flow generated from the residual stress is of the order of

$$V_{||} \sim \frac{\rho_{\rm pi}}{L} v_{\rm ti}. \qquad (7.2.2.9)$$

The magnitude of the toroidal flow generated is of the same order as that by the neoclassical toroidal plasma viscosity [194].

7.3. Theory for turbulence suppression

As indicated in the quasilinear theory, when there is a change in the radial electric field profile the fluctuation spectrum must change accordingly to maintain quasineutrality [21, 173]. This leads naturally to the development of the theory for turbulence suppression resulting from the change of the radial electric profile. The theory was first published in 1988 [17]. It is primarily motivated by the need to explain the improved plasma confinement in H-mode in the theory for the L–H transition [15]. The radial electric field profile is usually strongly modified inside the pedestal region of the H-mode and inside the internal transport barriers.

The turbulence suppression theory is not specific for any particular instability by design. It is a dramatic departure from the traditional approach to plasma turbulence theories. It is a generic theory for the consequence of a change in the radial electric field profile. This type of theory is preferable because not only specific underlying instabilities in turbulent plasmas are usually difficult to identify but also turbulence usually already manifests itself without a discernible quiescent phase in toroidal plasmas. This motivates the development of the turbulent suppression theory. The theory is not the same as the theory for the stabilization of the linear instabilities, because usually prior to the change in the radial electric field profile, the plasmas are already turbulent.

7.3.1. De-correlation time The suppression theory is focused on the change of the de-correlation time when the radial electric field profile changes resulting from the momentum balance equation. The fluctuation spectrum and the fluctuation level will respond accordingly.

The basic physics mechanism for turbulence suppression does not depend on the toroidal curvature of the magnetic field. Thus, the theory can be demonstrated in magnetized cylindrical plasmas using the (r, θ, ζ) coordinates. The magnetic field is in the ζ direction. Plasmas are assumed to rotate in the poloidal angle θ direction. Suppose that there are two fluid elements located at two positions (r_1, θ_1, ζ_1) and (r_2, θ_2, ζ_2) with a separation (r_-, θ_-, ζ_-) that is smaller than $(k_0^{-1}, m_0^{-1}, n_0^{-1})$. Here $r_- = r_1 - r_2, \theta_- = \theta_1 - \theta_2, \zeta_- = \zeta_1 - \zeta_2, (k_0^{-1}, m_0^{-1}, n_0^{-1})$ are, respectively, the typical radial mode width, and typical poloidal and toroidal mode numbers. When they are inside the correlation volume, these two fluid elements do not diffuse independently [195]. As a matter of fact, the diffusion coefficient must vanish when (r_-, θ_-, ζ_-) approaches $(0, 0, 0)$. To simplify the illustration without loss of generality, it is assumed that there is no de-correlation mechanism in the ζ direction. Thus, $\langle \zeta_-^2 \rangle$ remains constant. The angular brackets demote ensemble average here. The de-correlation frequency τ_c^{-1} can be estimated from

$$\tau_c^{-1} \left\langle r_-^2 \right\rangle = D \left(k_0^2 \left\langle r_-^2 \right\rangle + m_0^2 \left\langle \theta_-^2 \right\rangle \right), \qquad (7.3.1.1)$$

where D is the turbulence diffusion coefficient when (r_-, θ_-, ζ_-) is outside the correlation volume. The factor $(k_0^2 \langle r_-^2 \rangle + m_0^2 \langle \theta_-^2 \rangle)$ is used to model the effect that when (r_-, θ_-) approaches $(0, 0)$ the two fluid elements are correlated indefinitely. If the plasma rotation frequency ω in the θ direction has a radial gradient, $\langle \theta_-^2 \rangle$ is not a constant, and can be estimated to be

$$\tau_c^{-1} \langle \theta_-^2 \rangle^{1/2} = \omega' \langle r_-^2 \rangle^{1/2}, \qquad (7.3.1.2)$$

where prime denotes $\mathrm{d}/\mathrm{d}r$. The de-correlation frequency thus satisfies a cubic equation

$$\left(\frac{\tau_c^{-1}}{k_0^2 D} \right)^3 - \left(\frac{\tau_c^{-1}}{k_0^2 D} \right)^2 - \frac{D m_0^2}{\left(k_0^2 D \right)^3} \omega'^2 = 0. \qquad (7.3.1.3)$$

This equation is first derived using a two-point theory in [17]. However, the heuristic derivation given here is more physically transparent and is developed in [16]. The dependence of $\tau_c^{-1}/(k_0^2 D)$ as a function of normalized ω' is shown in figure 19, which is also observed in a numerical simulation [196].

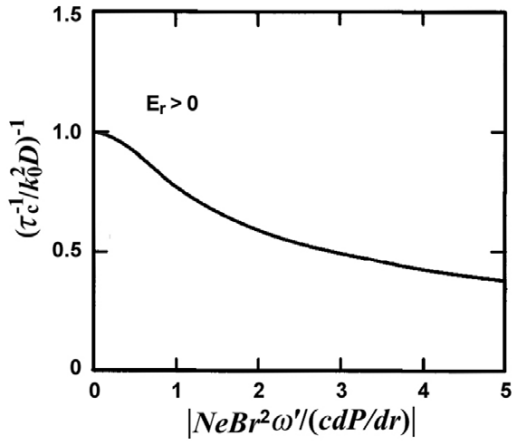

Figure 19. Normalized de-correlation time as a function of the normalized ω'.

The plasma rotation frequency ω can be either poloidal $\boldsymbol{E} \times \boldsymbol{B}$ drift, or $\boldsymbol{E} \times \boldsymbol{B}$ drift and diamagnetic flow depending on the origins of the turbulence [16]. The simplest case is poloidal $\boldsymbol{E} \times \boldsymbol{B}$ drift only. In that case,

$$\omega = \frac{cE_r}{Br}. \qquad (7.3.1.4)$$

When plasmas rotate in the toroidal direction, the roles of θ and ζ are exchanged, and the frequency becomes [17, 173]

$$\omega = q \frac{cE_r}{Br}. \qquad (7.3.1.5)$$

In the limit of $Dm_0^2\omega'^2/(k_0^2D)^3 < 1$, the de-correlation frequency has the approximate expression

$$\tau_c = \frac{(k_0^2D)^2}{(k_0^2D)^3 + Dm_0^2\omega'^2}. \quad (7.3.1.6)$$

This scaling has stronger effects on the improved plasma confinement because the de-correlation time decreases as $1/\omega'^2$ [17]. In this limit, the denominator in equation (7.3.1.6) can be expanded to obtain the expression of τ_c in [17] exactly. In the limit, where $Dm_0^2\omega'^2/(k_0^2D)^3 > 1$, the approximate τ_c is [197]

$$\tau_c = \frac{1}{(Dm_0^2)^{1/3}\omega'^{2/3}}. \quad (7.3.1.7)$$

This scaling has a weaker effect on improving the plasma confinement due to the $\omega'^{-2/3}$ dependence.

In the derivation of equation (7.3.1.3), the turbulent diffusion coefficient D is not assumed as a function of ω. However, in general, D can be a function of ω. This effect is addressed in [198]. It is shown that in the limit, where $Dm_0^2\omega'^2/(k_0^2D)^3 < 1$, the expression for τ_c in equation (7.3.1.6) is not affected by whether D is a function of ω or not. In the limit, where $Dm_0^2\omega'^2/(k_0^2D)^3 > 1$, τ_c in general has stronger than $\omega'^{-2/3}$ dependence if D is a function of ω. The theory of turbulence suppression used for static $\boldsymbol{E}\times\boldsymbol{B}$ flow can also be applied to time varying flow as long as the time variation is much slower than the characteristic fluctuation frequency as shown in [199, 200].

The turbulence suppression theory has often been invoked to explain the observed improved plasma confinement in not only toroidal plasmas but also in mirror machines [201]. The theory has been reviewed in [18] as well, although the work that first presented all the relevant physics, its implications on plasma confinement, and correct τ_c in the limit of $Dm_0^2\omega'^2/(k_0^2D)^3 < 1$, i.e. [17], is not referenced.

8. Tokamaks with broken toroidal symmetry

Tokamaks are toroidally symmetric in principle. However, there are always error fields or MHD activities present in real tokamaks, which break the toroidal symmetry. The broken symmetry leads to enhanced particle, momentum and energy transport in tokamaks. The recent development of the theory for neoclassical toroidal plasma viscosity (NTV) in the low collisionality regimes in part is motivated by the need to understand toroidal rotation damping observed in experiments [38, 202, 203]. The importance of weak broken symmetry on plasma confinement in other symmetric devices has also been recognized [204, 205].

Because of the toroidal symmetry, the axisymmetric neoclassical toroidal plasma viscosity is small; the toroidal momentum diffusion coefficient is of the order of $\nu_{ii}\rho_i^2$ [67–69, 180–188]. When the toroidal symmetry is broken, the neoclassical toroidal plasma viscosity is enhanced. For perturbed magnetic field $\delta B/B \sim 10^{-4}$ or higher, the toroidal momentum dissipation associated with the neoclassical toroidal plasma viscosity can become the dominant mechanism in determining the toroidal momentum confinement in tokamaks.

There are two mechanisms that contribute to the $|\boldsymbol{B}|$ spectrum for tokamaks with broken symmetry. One is the direct addition [206] and the other is the magnetic surface distortion [207]. The combination of these two mechanisms for the non-resonant magnetic field perturbations is first presented in [208]. Later, a term Lagrangian is used to describe the same combined mechanisms [209].

When there is a perturbed magnetic field $\boldsymbol{B}_1 = \boldsymbol{B}_1(V,\theta,\zeta)$ in Hamada coordinates, the $|\boldsymbol{B}|$ spectrum is

$$|\boldsymbol{B}| = |\boldsymbol{B}_0 + \boldsymbol{B}_1|, \quad (8.1)$$

where $\boldsymbol{B}_0$ is the equilibrium magnetic field. If $\boldsymbol{B}_1$ is perpendicular to $\boldsymbol{B}_0$, the contribution of the direction addition mechanism to $|\boldsymbol{B}|$ is quite small for being of the order of $(\delta B/B)^2$. Such is the case for the perturbed magnetic field that forms a magnetic island. However, there is another mechanism that is important for the $|\boldsymbol{B}|$ spectrum when the symmetry is broken. That is the surface distortion [207]. Neoclassical transport fluxes are calculated relative to the magnetic surface. When the flux surface is distorted due to the existence of the perturbed magnetic field, the transport fluxes are defined relative to the distorted flux surface. Thus, it is the $|\boldsymbol{B}|$ spectrum on the distorted magnetic surface that is relevant to the transport fluxes. This mechanism is important even when $\boldsymbol{B}_1$ is perpendicular to $\boldsymbol{B}_0$. In the case of the magnetic island, the contribution to the $|\boldsymbol{B}|$ spectrum due to the surface distortion mechanism is of the order of $\sqrt{\delta B/B}$ [207], which is significant even for $\delta B/B \sim 10^{-4}$. For the non-resonant perturbations, i.e. $m \neq nq$, both mechanisms are important. The $|\boldsymbol{B}|$ on the distorted surface due to surface distortion mechanism can be approximated as [208]

$$B = B(V,\theta,\zeta) + \frac{\partial B}{\partial V}\xi_d^V + \frac{\partial B}{\partial \theta}\xi_d^\theta + \frac{\partial B}{\partial \zeta}\xi_d^\zeta, \quad (8.2)$$

where ξ_d^V, ξ_d^θ and ξ_d^ζ are contravariant components of the plasma displacement vector ξ_d.

The $|\boldsymbol{B}|$ spectrum in a doubly periodic torus can be expressed as

$$B = B_0\Big\{1 - \sum_{m,n}[b_{mnc}\cos(m\theta - n\zeta) + b_{mns}\sin(m\theta - n\zeta)]\Big\}. \quad (8.3)$$

The standard equilibrium $\varepsilon\cos\theta$ harmonic is included in equation (8.3). The presence of the ζ dependence in $|\boldsymbol{B}|$ spectrum implies that the toroidal component of the viscous force is finite. This leads to the damping of the toroidal flow. Physically, this mechanism is analogous to the fluid flow damping in corrugated pipes.

Defining

$$A_n(\theta) = \sum_m \{b_{mnc}\cos[(m - nq)\theta] + b_{mns}\sin[(m - nq)\theta]\}, \quad (8.4)$$

and

$$B_n(\theta) = \sum_m \{-b_{mnc}\sin[(m - nq)\theta] + b_{mns}\cos[(m - nq)\theta]\} \quad (8.5)$$

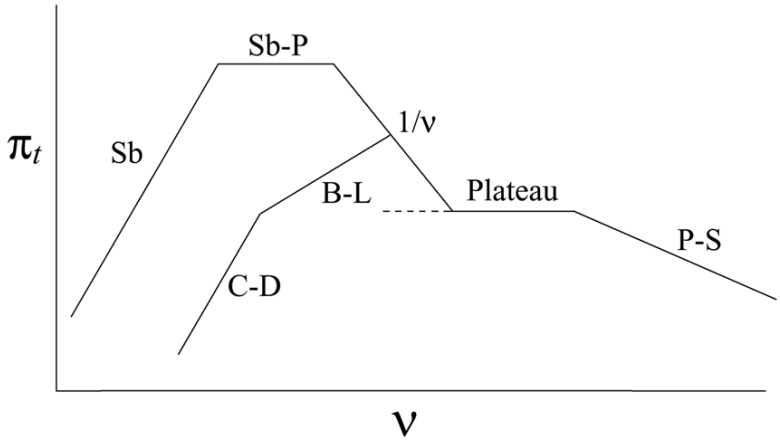

Figure 20. Neoclassical toroidal plasma viscosity π_t versus collision frequency ν in a log–log plot. The superbanana (Sb), superbanana plateau (Sb-P), $1/\nu$, collisional boundary layer (B-L), collisionless detrapping (C-D), plateau, and Pfirsch–Schlüter (P–S) regimes are shown. The dotted line indicates the bounce-transit and drift resonance.

a more compact form for B

$$B = B_0\,(1 - \varepsilon\cos\theta) - B_0\sum_n [A_n\,(\theta)\cos n\zeta_0 + B_n\,(\theta)\sin n\zeta_0] \tag{8.6}$$

is used in the theory to solve the bounce averaged drift kinetic equation, where $\zeta_0 = q\theta - \zeta$ is the field line label.

An alternative form for equation (8.3) is

$$B = B_0\left[1 - \sum_{m.n}\varepsilon_{mn}\mathrm{e}^{\mathrm{i}(m\theta - n\zeta)}\right], \tag{8.7}$$

where ε_{mn} is the Fourier amplitude of the (m,n) mode. Because B is real, $\varepsilon_{mn} = \varepsilon^*_{-m-n}$, where the superscript * denotes the complex conjugate.

The theory for neoclassical toroidal plasma viscosity in tokamaks differs from those for rippled tokamaks [210] and stellarators [3] in that there is only one class of trapped particle. To avoid creating new classes of trapped particles, i.e. particles trapped in the perturbed helical magnetic field, the perturbed magnetic field strength must be weak enough so that there should be no new local maxima or minima of B along the magnetic field line. Thus, the approximate solutions to the equation $\boldsymbol{B}\cdot\nabla B = 0$ to locate local maximum and minimum should be $\theta = 0$ or π. For a single (m, n) mode, the creation of a new class of trapped particles can be approximately prevented when [211]

$$\alpha_{\mathrm{t}} = \frac{\varepsilon}{|m - nq|\,b_{mn}} \gg 1, \tag{8.8}$$

where $b_{mn} = \sqrt{b^2_{mnc} + b^2_{mns}}$. The quantity α_{t} is a simple extension of $\alpha_{\mathrm{r}} = \varepsilon/(nq\delta_{\mathrm{r}})$ in the criterion for local ripple trapping, i.e. in $\alpha^*_{\mathrm{r}} = \alpha_{\mathrm{r}}\sin\theta = 1$ in rippled tokamaks [211]. Here, δ_{r} is the amplitude of the rippled field $B = B_0(1 - \varepsilon\cos\theta - \delta_{\mathrm{r}}\cos n\zeta)$. Equation (8.8) can be generalized to multiple modes to yield

$$\alpha_{\mathrm{t}} = \frac{\varepsilon}{(|m - nq|\,b_{mn})_{\mathrm{M}}\,U_{\mathrm{M}}} \gg 1, \tag{8.9}$$

where $(|m - nq|b_{mn})_{\mathrm{M}}$ is the maximum value of $|m - nq|b_{mn}$ for all modes, U_{M} is the absolute maximum value of the function

$$U = \left|\sum\nolimits_{m,n}\frac{b_{mn}\,(m - nq)}{(b_{mn}\,|m - nq|)_{\mathrm{M}}} \times \sin\left[(m - nq)\,\theta - n\zeta_0 - \chi_{mn}\right]\right|, \tag{8.10}$$

and χ_{mn} is a phase factor defined as $\cos\chi_{mn} = b_{mnc}/\sqrt{b^2_{mnc} + b^2_{mns}}$ and $\sin\chi_{mn} = b_{mns}/\sqrt{b^2_{mnc} + b^2_{mns}}$.

Comparing with the parallel viscous forces in axisymmetric tokamaks, the collision frequency dependence for the neoclassical toroidal plasma viscosity is rather complex and is summarized schematically in figure 20. The theory and the physics involved for each known collisionality regime, which are extensions of the stellarator transport theory [3], are reviewed here.

8.1. Bounce averaged drift kinetic equation

In the limit, where $\nu_* < 1$, it is trapped particles, i.e., bananas that dominate the transport processes in tokamaks with broken symmetry. Because the toroidal canonical momentum p_ζ is no longer conserved, bananas wobble off the magnetic surface to form drift orbits. These drift orbits have a typical width that is of the order of the $\langle \boldsymbol{v}_{\mathrm{d}}\cdot\nabla V\rangle_{\mathrm{b}}/\langle \boldsymbol{v}_{\mathrm{d}}\cdot\nabla\zeta_0\rangle_{\mathrm{b}}$. Here, $\langle \boldsymbol{v}_{\mathrm{d}}\cdot\nabla V\rangle_{\mathrm{b}}$ and $\langle \boldsymbol{v}_{\mathrm{d}}\cdot\nabla\zeta_0\rangle_{\mathrm{b}}$ are the bounce averaged radial drift speed and toroidal drift frequency, respectively. The physics of the drift orbits dynamics is governed by the bounce averaged drift kinetic equation [212].

The physics of wobbling bananas induced transport flux in rippled tokamaks have been reviewed in [210], where stochastic transport loss [213] and transport fluxes in the $1/\nu$, and ν regimes [210, 214, 215] are discussed. However, physics related to superbanana plateau resonance, superbanana, and collisional boundary layer has not been addressed. In this regard, the results reviewed here are also applicable for rippled tokamaks when local ripple trapping is insignificant. There is a topical review on the effects of three-dimensional (3D) magnetic perturbations on toroidal plasmas [217], and a summary on the neoclassical toroidal plasma viscosity in [218].

The drift kinetic equation is

$$v_{\parallel}\boldsymbol{n}\cdot\nabla f + \boldsymbol{v}_{\mathrm{d}}\cdot\nabla f = C(f). \tag{8.1.1}$$

Because $\nu_* < 1$, trapped particles are basically collisionless during their bounce motion. Using ν_* as the small parameter, the leading order equation for equation (8.1.1) is

$$v_\parallel \boldsymbol{n}\cdot\nabla f_0 = 0, \tag{8.1.2}$$

where the subscript 0 in f indicates the ordering. The solution to equation (8.1.2) is

$$f_0 = f_0\left(V, \zeta_0, E, \mu\right). \tag{8.1.3}$$

The next order equation is

$$v_\parallel \boldsymbol{n}\cdot\nabla f_1 + \boldsymbol{v}_\mathrm{d}\cdot\nabla f_0 = C\left(f_0\right). \tag{8.1.4}$$

Equation (8.1.4) is bounce averaged over the trapped particle trajectory subject to the reflection boundary conditions at the turning points of the trapped particles where $v_\parallel = 0$, i.e.

$$f_{1+}\left(V, \zeta_0, \theta_\mathrm{t}, E, \mu\right) = f_{1-}\left(V, \zeta_0, \theta_\mathrm{t}, E, \mu\right), \tag{8.1.5}$$

and

$$f_{1+}\left(V, \zeta_0, -\theta_\mathrm{t}, E, \mu\right) = f_{1-}\left(V, \zeta_0, -\theta_\mathrm{t}, E, \mu\right), \tag{8.1.6}$$

to annihilate $v_\parallel \boldsymbol{n}\cdot\nabla f_1$ term, where the subscript $\pm$ in f_1 indicates the sign of $v_\parallel$ and $\pm\theta_\mathrm{t}$ are the turning points of the trapped particles, i.e. $v_\parallel(\pm\theta_\mathrm{t}) = 0$. Applying the bounce average operator, defined as $\langle\cdot\rangle_\mathrm{b} = \sum_\sigma \left(\oint \mathrm{d}\theta(\cdot)B/|v_\parallel|\right)/\left(\oint \mathrm{d}\theta B/|v_\parallel|\right)$ to equation (8.1.4) yields

$$\langle \boldsymbol{v}_\mathrm{d}\cdot\nabla\zeta_0\rangle_\mathrm{b}\frac{\partial f_0}{\partial\zeta_0} + \langle \boldsymbol{v}_\mathrm{d}\cdot\nabla V\rangle_\mathrm{b}\frac{\partial f_0}{\partial V} = \langle C\left(f_0\right)\rangle_\mathrm{b}, \tag{8.1.7}$$

where $\oint \mathrm{d}\theta = \int_{-\theta_\mathrm{t}}^{\theta_\mathrm{t}} \mathrm{d}\theta$. Note that all the $P_1(v_\parallel/v)f_\mathrm{M}$ like terms, including momentum restoring terms, vanish after bounce averaging.

A subsidiary ordering is used to solve equation (8.1.7). A maximum ordering scheme is adopted by ordering $\langle \boldsymbol{v}_\mathrm{d}\cdot\nabla\zeta_0\rangle_\mathrm{b}\partial f_0/\partial\zeta_0 \sim \langle C(f_0)\rangle_\mathrm{b} > \langle \boldsymbol{v}_\mathrm{d}\cdot\nabla V\rangle_\mathrm{b}\partial f_0/\partial V$. This implies that the radial width of the drift orbits is much smaller than L_n. Thus, the transport process is local in radius. The leading order equation is

$$\langle \boldsymbol{v}_\mathrm{d}\cdot\nabla\zeta_0\rangle_\mathrm{b}\frac{\partial f_{00}}{\partial\zeta_0} = \langle C\left(f_{00}\right)\rangle_\mathrm{b}, \tag{8.1.8}$$

where the second subscript in f indicates the subsidiary ordering. The solution to equation (8.1.8) is a Maxwellian distribution, i.e.

$$f_{00} = f_\mathrm{M}(V). \tag{8.1.9}$$

The next order equation in the subsidiary ordering is

$$\langle \boldsymbol{v}_\mathrm{d}\cdot\nabla\zeta_0\rangle_\mathrm{b}\frac{\partial f_{01}}{\partial\zeta_0} + \langle \boldsymbol{v}_\mathrm{d}\cdot\nabla V\rangle_\mathrm{b}\frac{\partial f_\mathrm{M}}{\partial V} = \langle C\left(f_{01}\right)\rangle_\mathrm{b}, \tag{8.1.10}$$

where f_{01} is the first order correction to $f_{00} = f_\mathrm{M}(V)$.

Equation (8.1.10) governs the physics of wobbling trapped particles and is the equation to be solved to obtain transport fluxes in the regime where $\nu_* < 1$. However, the exact analytic solution to equation (8.1.10) is unattainable for arbitrary plasma parameters. The asymptotic analysis is employed to seek its solution.

The explicit expressions for the bounce averaged toroidal drift frequency, the radial drift speed and the collision operator are [208]

$$\langle \boldsymbol{v}_\mathrm{d}\cdot\nabla\zeta_0\rangle_\mathrm{b} = \frac{c\Phi'}{\chi'} - \frac{c\mu B_0}{e\chi'}\varepsilon'\left[\frac{2E(k)}{K(k)} - 1\right], \tag{8.1.11}$$

$$\langle \boldsymbol{v}_\mathrm{d}\cdot\nabla V\rangle_\mathrm{b} = \frac{c\mu B_0}{e\chi'}\frac{1}{4K(k)} \times\sum_n\oint \mathrm{d}\theta\frac{A_n(\theta)(-n\sin n\zeta_0) + B_n(\theta)(n\cos n\zeta_0)}{\sqrt{k^2 - \sin^2\left(\frac{\theta}{2}\right)}}, \tag{8.1.12}$$

and

$$\langle C(f_{01})\rangle_\mathrm{b} = \frac{\nu_\mathrm{D}}{\varepsilon K(k)}\frac{\partial}{\partial k^2}\left\{\left[E(k) - (1-k^2)K(k)\right]\frac{\partial f_{01}}{\partial k^2}\right\}, \tag{8.1.13}$$

where the prime denotes $\mathrm{d}/\mathrm{d}V$, and $K(k)$ is the complete integral of the first kind. The pitch angle parameter k^2 is defined as

$$k^2 = [E - e\Phi - \mu B_0\left(1-\varepsilon\right)]/(2\mu B_0\varepsilon). \tag{8.1.14}$$

The symbol E without an argument denotes the particle energy and with an argument k denotes the complete elliptic integral of the second kind. The pitch angle parameter k^2 separates trapped particles that are parametrized by $0 \leqslant k^2 \leqslant 1$ from circulating particles categorized by $k^2 \geqslant 1$. The curvature drift, and effects of magnetic shear and finite $\bar{\beta}$, in equations (8.1.11) and (8.1.12) are neglected by assuming $\varepsilon < 1$. Thus, $\mu B_0 \approx E$. Note that only the pitch angle scattering operator is needed because it contains an enhancement factor of $1/\varepsilon$. The effective collision frequency ν_eff is $\nu_\mathrm{D}/\varepsilon$ as can be seen directly from equation (8.1.13).

Examining the derivation of equation (8.1.10) and the general property of its solution, several important physics conclusions can be drawn. It should be noted that the momentum restoring term in the collision operator vanishes after bounce averaging. Thus, the parallel flow velocity does not appear in the bounce averaged collision operator. This also reflects in the thermodynamic forces where the parallel mass flow and parallel heat flow do not appear. In addition, this implies that the solution of the bounce averaged drift kinetic equation does not contribute to the parallel momentum and parallel heat flux balance equations. Thus, transport fluxes derived from the bounce averaged drift kinetic equation only contribute to the momentum balance in the direction that is not parallel to the magnetic field. It has been shown rigorously in a theorem that the solution of the bounce averaged drift kinetic equation (equation (8.1.10)) does not contribute to the parallel viscous forces $\langle \boldsymbol{B}\cdot\nabla\cdot\overleftrightarrow{\pi}\rangle$ and $\langle \boldsymbol{B}\cdot\nabla\cdot\overleftrightarrow{\Theta}\rangle$, i.e. $\langle \boldsymbol{B}\cdot\nabla\cdot\overleftrightarrow{\pi}\rangle = 0$, and $\langle \boldsymbol{B}\cdot\nabla\cdot\overleftrightarrow{\Theta}\rangle = 0$, because f_{01} does not vary along the magnetic field line, i.e. $f_{01} = f_{01}(V, \zeta_0)$ [53]. This also implies that $\langle \boldsymbol{B}_\mathrm{tt}\cdot\nabla\cdot\overleftrightarrow{\pi}\rangle = -\langle \boldsymbol{B}_\mathrm{pp}\cdot\nabla\cdot\overleftrightarrow{\pi}\rangle$, and $\langle \boldsymbol{B}_\mathrm{tt}\cdot\nabla\cdot\overleftrightarrow{\Theta}\rangle = -\langle \boldsymbol{B}_\mathrm{pp}\cdot\nabla\cdot\overleftrightarrow{\Theta}\rangle$, where $\boldsymbol{B} = \boldsymbol{B}_\mathrm{tt} + \boldsymbol{B}_\mathrm{pp}$ for any two vectors $\boldsymbol{B}_\mathrm{tt}$ and $\boldsymbol{B}_\mathrm{pp}$. A particular case of interest is that $\boldsymbol{B}_\mathrm{tt} = \boldsymbol{B}_\mathrm{t} = \psi'\nabla V\times\nabla\theta$, and $\boldsymbol{B}_\mathrm{pp} = \boldsymbol{B}_\mathrm{p} = \chi'\nabla\zeta\times\nabla V$ in Hamada coordinates. This theorem is also valid for f_{01} that is piecewise constant along the magnetic field line. Thus,

the solution does not contribute to the bootstrap current. This implies that to calculate the bootstrap current one must solve the non-bounce averaged drift kinetic equation [53].

The boundary conditions for equation (8.1.10) are that

$$f_{01} = 0 \tag{8.1.15}$$

at $k^2 = 1$ where particles are barely trapped and that

$$\left[E(k) - (1-k^2)K(k)\right]\frac{\partial f_{01}}{\partial k^2} = 0 \tag{8.1.16}$$

at $k^2 = 0$ where particles are trapped at the bottom of the magnetic well [3]. The boundary condition $f_{01} = 0$ at $k^2 = 1$ is a statement that barely circulating particles do not wobble off the magnetic surface significantly relative to the trapped particles after circulating around the torus a few times. Because the distribution function must be continuous, $f_{01} = 0$ for barely trapped particles. At the bottom of the magnetic well, the flux in the pitch angle space must be continuous when the pitch angle scattering operator dominates, which implies $[E(k) - (1-k^2)K(k)]\partial f_{01}/\partial k^2 = 0$ at $k^2 = 0$.

8.2. Neoclassical toroidal plasma viscosity derived from bounce averaged drift kinetic equation

Equation (8.1.11) is solved by examining the relative strength of the toroidal drift frequency and the effective collision frequency. This leads to several collisionality regimes. Because the toroidal drift frequency can vanish at a particular pitch angle parameter k_r^2, particles having $k^2 = k_r^2$ can drift off the flux surface unbounded. This indicates that there is a resonance process occurring at k_r^2. Thus, the solutions are categorized in terms of the non-resonant and resonant fluxes.

8.2.1. $1/\nu$ regime. In this asymptotic regime, the transport fluxes scale as $1/\nu$. It occurs when the toroidal drift frequency is much smaller than the collision frequency and can be neglected. Equation (8.1.10) reduces to

$$\langle \boldsymbol{v}_{\rm d}\cdot\nabla V\rangle_{\rm b}\frac{\partial f_{\rm M}}{\partial V} = \langle C\left(f_{01}\right)\rangle_{\rm b}. \tag{8.2.1.1}$$

Integrating equation (8.2.1.1) over k^2 yields

$$\frac{\partial f_{01}}{\partial k^2} = \frac{\varepsilon}{\nu_{\rm D}}\frac{\int_0^{k^2}{\rm d}k^2\,\langle \boldsymbol{v}_{\rm d}\cdot\nabla V\rangle_{\rm b}\,K(k)\partial f_{\rm M}/\partial V}{E\left(k\right) - \left(1-k^2\right)K\left(k\right)}, \tag{8.2.1.2}$$

after imposing the boundary condition that $\partial f_{01}/\partial k^2$ remains finite at $k^2 = 0$.

The flux surface averaged particle flux $\vec{\Gamma}$ is defined as

$$\left\langle \vec{\Gamma}\cdot\nabla V\right\rangle = \int_0^{2\pi}\frac{{\rm d}\zeta}{2\pi}\int_{-\pi}^{\pi}\frac{{\rm d}\theta}{2\pi}\int {\rm d}\boldsymbol{v} f\boldsymbol{v}_{\rm d}\cdot\nabla V. \tag{8.2.1.3}$$

It is convenient to use ${\rm d}\boldsymbol{v} = 2\pi/M^2\sum_\sigma {\rm d}E\,{\rm d}\mu B/|v_\parallel|$, and ${\rm d}\mu B \approx -2\mu B_0\varepsilon\,{\rm d}k^2$ in performing velocity space integrals equation (8.2.1.3). Only f_{01} contributes to the transport fluxes. Because f_{01} is not a function of the poloidal angle θ, it only contributes to the non-axisymmetric flux $\Gamma^{\rm na}$ and

$$\Gamma^{\rm na} = \int_0^{2\pi}\frac{{\rm d}\zeta_0}{\pi}\int\frac{{\rm d}E}{M^2}v^{-1}\int 2\mu B_0\varepsilon\,{\rm d}k^2\frac{4K(k)}{\sqrt{2\varepsilon}} \times\langle \boldsymbol{v}_{\rm d}\cdot\nabla V\rangle_{\rm b} f_{01}, \tag{8.2.1.4}$$

Replacing $\langle \boldsymbol{v}_{\rm d}\cdot\nabla V\rangle_{\rm b}$ in equation (8.2.1.4) by $\langle C(f_{01})\rangle_{\rm b}$, using either equation (8.2.1.1) or equation (8.1.10), and imposing the boundary conditions for f_{01} yield

$$\Gamma^{\rm na} = -\frac{4}{\sqrt{2\varepsilon}}\int_0^{2\pi}\frac{{\rm d}\zeta_0}{\pi}\int\frac{{\rm d}E}{M}v\nu_D \times\int {\rm d}k^2\frac{\left[E(k) - \left(1-k^2\right)K(k)\right]}{\partial f_{\rm M}/\partial V}\left(\frac{\partial f_{01}}{\partial k^2}\right)^2. \tag{8.2.1.5}$$

The flux surface averaged particle flux is [208], after substituting $\partial f_{01}/\partial k^2$ in equation (8.2.1.2) into equation (8.2.1.5),

$$\Gamma^{\rm na}_{1/\nu} = -N\frac{\varepsilon^{3/2}}{4\sqrt{2}\pi^{3/2}}\left(\frac{Mc}{e\chi'}\right)^2\frac{v_{\rm t}^4}{\nu_{\rm t}}I_{1/\nu} \times\left[\eta_1\left(\frac{p'}{p}+\frac{e\Phi'}{T}\right)+\eta_2\frac{T'}{T}\right], \tag{8.2.1.6}$$

where $\nu_{\rm t} = \sqrt{2}\pi N_{\rm i}e_{\rm i}^4\ln\Lambda/(M_{\rm i}^{1/2}T_{\rm i}^{3/2})$ for ions, and $\nu_{\rm t} = \sqrt{2}\pi N_{\rm i}Z_{\rm i}^2e_{\rm e}^4\ln\Lambda/(M_{\rm e}^{1/2}T_{\rm e}^{3/2})$ for electrons,

$$I_{1/\nu} = \int_0^1 {\rm d}k^2\left[E(k) - \left(1-k^2\right)K(k)\right]^{-1} \times\sum_n n^2\left[\left(\int_{-\theta_{\rm t}}^{\theta_{\rm t}}{\rm d}\theta\left(k^2-\sin^2\frac{\theta}{2}\right)^{1/2}A_n\right)^2 + \left(\int_{-\theta_{\rm t}}^{\theta_{\rm t}}{\rm d}\theta\left(k^2-\sin^2\frac{\theta}{2}\right)^{1/2}B_n\right)^2\right], \tag{8.2.1.7}$$

η_j for j = 1–2 is defined as

$$\eta_j = \int_0^\infty {\rm d}x x^6{\rm e}^{-x^2}\left(x^2-\frac{5}{2}\right)^{j-1}\frac{\nu_{\rm t}}{\nu_{\rm D}}. \tag{8.2.1.8}$$

The turning points of the toroidally trapped particles $\pm\theta_{\rm t}$ are defined as $k^2 = \sin^2(\theta_{\rm t}/2)$.

In this regime, the heat flux is [208]

$$\frac{q^{\rm na}_{1/\nu}}{T} = -N\frac{\varepsilon^{3/2}}{4\sqrt{2}\pi^{3/2}}\left(\frac{Mc}{e\chi'}\right)^2\frac{v_{\rm t}^4}{\nu_{\rm t}}I_{1/\nu} \times\left[\eta_2\left(\frac{p'}{p}+\frac{e\Phi'}{T}\right)+\eta_3\frac{T'}{T}\right], \tag{8.2.1.9}$$

where η_3 is defined in equation (8.2.1.8) with $j = 3$.

The symbol η_j for j = 1–3 is used to denote the coefficients in front of the plasma gradients for neoclassical plasma viscosity in various regimes. Their definitions are valid only in their specific subsections.

The bounds for this asymptotic regime in the collision frequency space are $\nu_* < 1$, but $\nu/\varepsilon > c|\Phi'|/\chi'$, if finite ∇B drift is neglected as is appropriate for $\varepsilon < 1$. The scaling in this regime can be understood in terms of the random walk argument. In the $1/\nu$ regime, the drift orbit trajectories are interrupted by collisions and the step size is $\Delta r \sim \varepsilon v_{\rm dr}/\nu$, where, $v_{\rm dr}$ is the bounce averaged radial drift speed. The fraction of particles that participate in the transport process is of the order of $\sqrt{\varepsilon}$, namely, the fraction of bananas. The de-correlation time is ε/ν. Note that for bananas, the bounce averaged $v_{\rm dr}$ is proportional to the magnitude of the perturbed fields. Substituting all these estimates in the random walk argument leads to the scaling for transport fluxes in the $1/\nu$ regime.

8.2.2. Collisional boundary layer $\nu - \sqrt{\nu}$ regime. When the collision frequency decreases further so that $\langle C(f_{01})\rangle_b < \langle \boldsymbol{v}_d \cdot \nabla\zeta_0\rangle_b$, equation (8.1.10) can be solved by a subsidiary ordering using the small parameter $\langle C(f_{01})\rangle_b/\langle \boldsymbol{v}_d \cdot \nabla\zeta_0\rangle_b$. Note that because $\langle \boldsymbol{v}_d \cdot \nabla\zeta_0\rangle_b \neq 0$ for non-resonant transport fluxes, the ordering is meaningful. The ordered equations are

$$\langle \boldsymbol{v}_d \cdot \nabla\zeta_0\rangle_b \frac{\partial f_{01,0}}{\partial \zeta_0} + \langle \boldsymbol{v}_d \cdot \nabla V\rangle_b \frac{\partial f_M}{\partial V} = 0, \tag{8.2.2.1}$$

and

$$\langle \boldsymbol{v}_d \cdot \nabla\zeta_0\rangle_b \frac{\partial f_{01,1}}{\partial \zeta_0} = \left\langle C\left(f_{01,0}\right)\right\rangle_b, \tag{8.2.2.2}$$

where the third subscript in the perturbed distribution f denotes the ordering for this regime.

The solution to equation (8.2.2.1) is [208]

$$f_{01,0} = -\frac{c\mu B_0}{e\chi' \langle \boldsymbol{v}_d \cdot \nabla\zeta_0\rangle_b} \frac{1}{4K(k)} \frac{\partial f_M}{\partial V} \times \sum_n \oint \mathrm{d}\theta \frac{A_n(\theta)\cos n\zeta_0 + B_n(\theta)\sin n\zeta_0}{\sqrt{k^2 - \sin^2\left(\frac{\theta}{2}\right)}}. \tag{8.2.2.3}$$

The integration constant $f_{01,0}$ is found to be zero by solving the solubility constraint of equation (8.2.2.2). The solution in equation (8.2.2.3) is adequate to calculate the transport fluxes by expressing them in terms of the collision operator as illustrated in equation (8.2.1.5). However, the resultant fluxes diverge logarithmically as $k^2 \to 1$, i.e. approaching the boundary that separates the trapped and circulating particles [216]. This unphysical behaviour must be resolved. The physics origin of the singularity is the logarithmic dependence in the bounce averaged radial drift $\langle \boldsymbol{v}_d \cdot \nabla V\rangle_b$. When $f_{01,0}$ in equation (8.2.2.3) is substituted into the bounce averaged collision operator, the $\partial f_{01,0}/\partial k^2$ diverges as $k^2 \to 1$. This indicates that the ordering scheme used in obtaining equations (8.2.2.1) and (8.2.2.2) becomes invalid in the vicinity of $k^2 = 1$, and implies that the original bounce averaged drift kinetic equation, i.e. equation (8.1.10) must be solved in the boundary layer region. The solution in equation (8.2.2.3) is perfectly acceptable outside the vicinity of $k^2 = 1$. This leads to the conclusion that the singularity can be resolved by a collisional boundary analysis [3]. The solution in equation (8.2.2.3) becomes the outer solution to be matched to the boundary layer solution. In addition because the $\partial f_{01,0}/\partial k^2$ varies slowly relative to the rapid variation of the boundary layer solution, $f_{01,0}$ is also an approximate particular solution to equation (8.1.10). Thus, the boundary layer analysis is to find the homogeneous solution for equation (8.1.10) that is localized in the vicinity of $k^2 = 1$.

The homogeneous equation that is valid in the vicinity of $k^2 = 1$ is

$$\langle \boldsymbol{v}_d \cdot \nabla\zeta_0\rangle_b \frac{\partial f_{01}}{\partial \zeta_0} \approx \frac{\nu_D}{\varepsilon}\left(\ln\frac{4}{\sqrt{1-k^2}}\right)^{-1} \frac{\partial^2 f_{01}}{\partial (k^2)^2}. \tag{8.2.2.4}$$

Because the layer is narrow, only the highest derivative term $\partial^2 f_{01}/\partial\left(k^2\right)^2$ is kept in $\langle C(f_{01})\rangle_b$. The complete elliptic integrals in the vicinity of $k^2 = 1$ are also expanded to obtain equation (8.2.2.4). The $(1-k^2)$ in the argument of the logarithm can be replaced by the width of the layer because the value of the logarithm is not sensitive to its argument. Equation (8.2.2.4) can be cast into a dimensionless form

$$\frac{1}{2}\frac{\partial^2 f_-}{\partial y_b^2} = \sigma_\omega \quad \frac{\partial f_-}{\partial \zeta_0}, \tag{8.2.2.5}$$

where f_- is the distribution function inside the layer, $\sigma_\omega = \pm 1$ indicates the direction of the toroidal drift frequency $\langle \boldsymbol{v}_d \cdot \nabla\zeta_0\rangle_b$, y_b is the stretch variable defined as

$$y_b = \left(1-k^2\right)\left(\frac{\nu_D}{\nu_t}\right)^{-1/2}\left[\nu_{\cdot d}/\ln\left(16/\sqrt{\nu_{\cdot d}}\right)\right]^{-1/2}, \tag{8.2.2.6}$$

and $\nu_{*d} = 4\nu_t/\left(\varepsilon|\langle \boldsymbol{v}_d \cdot \nabla\zeta_0\rangle_b|_{1-\Delta k^2}\right)$. From the definition for y_b, $y_b = 0$ at $k^2 = 1$, and y_b becomes large when k^2<1 in the asymptotic limit of the boundary layer analysis where $\nu_{*d} < 1$.

The width of the layer Δk^2 estimated from equation (8.2.2.5) by setting $y_b = 1$, the edge of the layer, and $\nu_D = \nu_t$, i.e. neglecting the energy dependence in ν_D, is

$$\Delta k^2 = \left[\nu_{\cdot d}/\ln\left(16/\sqrt{\nu_{\cdot d}}\right)\right]^{1/2}. \tag{8.2.2.7}$$

Note that in defining the stretch variable y_b, the width of the layer in equation (8.2.2.7) is used which in turn is used to estimate Δk^2. This procedure yields an accurate solution in the asymptotic limit. The iteration procedure may be solved numerically to yield an accurate value in the transition region from one asymptotic limit to the other [219, 220].

The layer equation equation (8.2.2.5) is solved in y_b that varies from ∞, the region of trapped particles, to 0, the trapped-circulating boundary. Fourier analysing the solution f in terms of $\sin n\zeta_0$and $\cos n\zeta_0$ yields the homogeneous solution

$$f_- = \sum_n A_{n-}\mathrm{e}^{-\sqrt{|n|}y_b} \times \left(\cos\sqrt{|n|}y_b \sin n\zeta_0 - \sigma_\omega \sin\sqrt{|n|}y_b \cos n\zeta_0\right) + \sum_n B_{n-}\mathrm{e}^{-\sqrt{|n|}y_b} \times \left(\cos\sqrt{|n|}y_b \cos n\zeta_0 + \sigma_\omega \sin\sqrt{|n|}y_b \sin n\zeta_0\right), \tag{8.2.2.8}$$

where A_{n-} and B_{n-} are coefficients to be determined from the boundary conditions. Two other linearly independent solutions that diverge as $\mathrm{e}^{\sqrt{|n|}y_b}$ are discarded.

Setting the complete solution, which is the sum of the outer solution equation (8.2.2.3) evaluated at the edge of the boundary layer, i.e. $k^2 = 1 - \Delta k^2$, and the layer solution equation (8.2.2.8), to zero at $y_b = 0$, i.e. $k^2 = 1$, yields

$$B_{n-} = \left[\frac{c\mu B_0}{e\chi' \langle \boldsymbol{v}_d \cdot \nabla\zeta_0\rangle_b} \frac{1}{4K(k)} \oint \mathrm{d}\theta A_n(\theta) \Big/ \sqrt{k^2 - \sin^2(\theta/2)}\right]_{1-\Delta k^2} \frac{\partial f_M}{\partial V}, \tag{8.2.2.9}$$

and

$$A_{n-} = \left[\frac{c\mu B_0}{e\chi' \langle \boldsymbol{v}_d \cdot \nabla\zeta_0\rangle_b} \frac{1}{4K(k)} \oint \mathrm{d}\theta B_n(\theta) \Big/ \sqrt{k^2 - \sin^2(\theta/2)}\right]_{1-\Delta k^2} \frac{\partial f_M}{\partial V}, \tag{8.2.2.10}$$

where the subscript $1-\Delta k^2$ indicates that the quantities inside the square brackets are evaluated at the edge of the boundary layer.

The solution inside the layer is completely determined. It consists of the outer solution equation (8.2.2.3) evaluated at the edge of the boundary layer, the layer solution equation (8.2.2.8), and the coefficients for the layer solution equation (8.2.2.9) and equation (8.2.2.10).

The boundary layer solution including both the homogeneous solution and the particular solution needs to match to the outer solution given in equation (8.2.2.3) to obtain

$$\begin{aligned} f_{01} = &-\frac{c\mu B_0}{e\chi'\langle \boldsymbol{v}_{\rm d}\cdot\nabla\zeta_0\rangle_{\rm b}}\frac{\partial f_{\rm M}}{\partial V}\frac{1}{4K(k)} \\ &\times\Bigg\{\sum_n \oint \frac{{\rm d}\theta}{\sqrt{k^2-\sin^2\left(\frac{\theta}{2}\right)}} \\ &\times\Bigg[A_n(\theta)\left(1-{\rm e}^{-\sqrt{|n|}y_{\rm b}}\cos\sqrt{|n|}y_{\rm b}\right) \\ &+\sigma_\omega B_n(\theta){\rm e}^{-\sqrt{|n|}y_{\rm b}}\sin\sqrt{|n|}y_{\rm b}\Bigg]\cos n\zeta_0 \\ &+\sum_n \oint \frac{{\rm d}\theta}{\sqrt{k^2-\sin^2\left(\frac{\theta}{2}\right)}} \\ &\times\Bigg[B_n(\theta)\left(1-{\rm e}^{-\sqrt{|n|}y_{\rm b}}\cos\sqrt{|n|}y_{\rm b}\right) \\ &-\sigma_\omega A_n(\theta){\rm e}^{-\sqrt{|n|}y_{\rm b}}\sin\sqrt{|n|}y_{\rm b}\Bigg]\sin n\zeta_0\Bigg\}. \end{aligned} \tag{8.2.2.11}$$

As $y_{\rm b}$ approaches infinity, f_{01} in equation (8.2.2.11) reduces to the outer solution given in equation (8.2.2.3).

Substituting f_{01} into the expressions for the flux surface averaged transport fluxes yields [216, 221]

$$\begin{aligned} \Gamma^{\rm na}_{\nu-\sqrt{\nu}} = &-N\frac{v_{\rm t}^4}{\pi^{3/2}}\left(\frac{M}{e\Phi'}\right)^2 \\ &\times\frac{\nu_{\rm t}}{\sqrt{32\varepsilon}}\left[\eta_1\left(\frac{p'}{p}+\frac{e\Phi'}{T}\right)+\eta_2\frac{T'}{T}\right], \end{aligned} \tag{8.2.2.12}$$

and

$$\begin{aligned} \frac{q^{\rm na}_{\nu-\sqrt{\nu}}}{T} = &-N\frac{v_{\rm t}^4}{\pi^{3/2}}\left(\frac{M}{e\Phi'}\right)^2 \\ &\times\frac{\nu_{\rm t}}{\sqrt{32\varepsilon}}\left[\eta_2\left(\frac{p'}{p}+\frac{e\Phi'}{T}\right)+\eta_3\frac{T'}{T}\right], \end{aligned} \tag{8.2.2.13}$$

where for j =1–3, η_j is defined as

$$\begin{aligned} \eta_j = &\int_0^{x_{\rm min}} {\rm d}x x^6\left(x^2-\frac{5}{2}\right)^{j-1} \\ &\times{\rm e}^{-x^2}\frac{\nu_{\rm D}}{\nu_{\rm t}}\int_0^1 {\rm d}k^2\left[E(k)-\left(1-k^2\right)K(k)\right]\sum_n\left(\hat{\alpha}_n^2+\hat{\beta}_n^2\right), \end{aligned} \tag{8.2.2.14}$$

and $\hat{\alpha}_n$ and $\hat{\beta}_n$ are defined, respectively, as

$$\begin{aligned} \hat{\alpha}_n = &\frac{\partial}{\partial k^2}\Bigg\{\oint {\rm d}\theta\frac{(-1/2)}{\sqrt{k^2-\sin^2(\theta/2)}} \\ &\times\Big[A_n(\theta)(1-{\rm e}^{-\sqrt{|n|}y_{\rm b}}\cos(\sqrt{|n|}y_{\rm b})) \\ &+\sigma_\omega B_n(\theta){\rm e}^{-\sqrt{|n|}y_{\rm b}}\sin(\sqrt{|n|}y_{\rm b})\Big]\frac{F_{\rm b}}{K(k)}\Bigg\}, \end{aligned} \tag{8.2.2.15}$$

$$\begin{aligned} \hat{\beta}_n = &\frac{\partial}{\partial k^2}\Bigg\{\oint {\rm d}\theta\frac{(-1/2)}{\sqrt{k^2-\sin^2(\theta/2)}} \\ &\times[B_n(\theta)(1-{\rm e}^{-\sqrt{|n|}y_{\rm b}}\cos(\sqrt{|n|}y_{\rm b})) \\ &-\sigma_\omega A_n(\theta){\rm e}^{-\sqrt{|n|}y_{\rm b}}\sin(\sqrt{|n|}y_{\rm b})]\frac{F_{\rm b}}{K(k)}\Bigg\}, \end{aligned} \tag{8.2.2.16}$$

The factor $F_{\rm b}$ in equations (8.2.2.15) and (8.2.2.16) is defined as

$$F_{\rm b} = \frac{1}{1-\sigma_{e\Phi'}\frac{x^2}{x^2_{\rm min}}\left[\frac{2E(k)}{K(k)}-1\right]}, \tag{8.2.2.17}$$

where

$$x^2_{\rm min} = \left|\frac{c\Phi'}{\chi'}\frac{e\chi'}{Mc}\frac{2}{v_{\rm t}^2\varepsilon'}\right|. \tag{8.2.2.18}$$

The energy integral and the pitch angle integral are coupled even in the case where the energy dependence in $y_{\rm b}$ is neglected. The maximum of the dimensionless energy integral $x_{\rm min}$ is defined so that the toroidal drift frequency does not vanish. This upper limit defines the non-resonant transport fluxes.

The asymptotic limit can be defined when the $\boldsymbol{E}\times\boldsymbol{B}$ drift speed is assumed to be much larger than the ∇B drift speed, which can be satisfied in large aspect ratio tokamaks or for low energy particles. In this case, the upper limit of the dimensionless energy integral can be extended to infinity. Transport fluxes are valid when $\nu/\varepsilon < c|\Phi'|/\chi'$ but $(\nu/\varepsilon)/(c|\Phi'|/\chi') > [(\delta B/B)/\varepsilon]^2$ where $(\delta B/B)$ is the typical magnitude of the perturbed field, e.g., typical values of $|b_{mnc}|$ or $|b_{mns}|$. The fluxes consist of two collision frequency scalings. One scales as ν resulting from the outer solution and the other as $\sqrt{\nu}$ from the boundary layer solution. The boundary layer contribution usually dominates and the transport fluxes can be simplified as [216, 221]

$$\begin{aligned} \Gamma^{\rm na}_{\sqrt{\nu}} = &-\frac{1}{4\sqrt{2}\pi^{3/2}}Nv_{\rm t}^4\frac{\sqrt{\nu_{*\rm d}}}{c\,|{\rm d}\Phi/{\rm d}\chi|}\sqrt{\varepsilon}\left(\frac{Mc}{e\chi'}\right)^2 \\ &\times\left[\ln\left(\frac{16}{\sqrt{\nu_{\cdot\rm d}}}\right)\right]^{1/2}\sum_n\left[\sqrt{n}\left(\alpha_{\rm bn}^2+\beta_{\rm bn}^2\right)\right] \\ &\times\left[\eta_1\left(\frac{p'}{p}+\frac{e\Phi'}{T}\right)+\eta_2\frac{T'}{T}\right], \end{aligned} \tag{8.2.2.19}$$

and

$$\begin{aligned} \frac{q^{\rm na}_{\sqrt{\nu}}}{T} = &-\frac{1}{4\sqrt{2}\pi^{3/2}}Nv_{\rm t}^4\frac{\sqrt{\nu_{*\rm d}}}{c\,|{\rm d}\Phi/{\rm d}\chi|}\sqrt{\varepsilon}\left(\frac{Mc}{e\chi'}\right)^2 \\ &\times\left[\ln\left(\frac{16}{\sqrt{\nu_{\cdot\rm d}}}\right)\right]^{1/2}\sum_n\left[\sqrt{n}\left(\alpha_{\rm bn}^2+\beta_{\rm bn}^2\right)\right] \\ &\times\left[\eta_2\left(\frac{p'}{p}+\frac{e\Phi'}{T}\right)+\eta_3\frac{T'}{T}\right], \end{aligned} \tag{8.2.2.20}$$

where $\alpha_n = [4K(k)]^{-1}\int_{-\theta_{\rm t}}^{\theta_{\rm t}}{\rm d}\theta A_n(\theta)/\sqrt{k^2-\sin^2(\theta/2)}$, $\alpha_{\rm bn} = \alpha_n|_{1-\Delta k^2}$, $\beta_n = [4K(k)]^{-1}\times\int_{-\theta_{\rm t}}^{\theta_{\rm t}}{\rm d}\theta B_n(\theta)/\sqrt{k^2-\sin^2(\theta/2)}$, $\beta_{\rm bn} = \beta_n|_{1-\Delta k^2}$, and for j = 1–3,

$$\eta_j = \int_0^\infty {\rm d}x\left(x^2-\frac{5}{2}\right)^{j-1}x^6{\rm e}^{-x^2}\sqrt{\frac{\nu_{\rm D}}{\nu_{\rm t}}}. \tag{8.2.2.21}$$

Both $\alpha_{\rm bn}$ and $\beta_{\rm bn}$ are evaluated at the edge of the boundary layer where $k^2 = 1-\Delta k^2$ if they diverge as $k^2\to 1$ as

indicated in the subscript, and are evaluated at $k^2 = 1$ if they are well behaved at $k^2 = 1$. There is a possibility that α_{bn} and β_{bn} vanish at a particular radius. In that case, the ν scaling becomes important. For this reason it could be better to use the expressions in equations (8.2.2.12) and (8.2.2.13) for modelling purposes.

The transport scaling in this regime can be understood as follows when $\boldsymbol{E}\times\boldsymbol{B}$ drift frequency dominates. The fraction of particles that participate in the transport process is $\sqrt{\varepsilon}\Delta k^2$, the step size is v_{dr}/ω_{ζ_0}, where $\omega_{\zeta_0} = c|\mathrm{d}\Phi/\mathrm{d}\chi|$ is the angular $\boldsymbol{E}\times\boldsymbol{B}$ drift frequency, and the de-correlation frequency is $(\nu/\varepsilon)/(\Delta k^2)^2$. The Δk^2 is given in equation (8.2.2.7). The scaling of the transport fluxes in this regime follows from the random walk argument.

8.2.3. Collisionless detrapping/retrapping regime. When $(\nu/\varepsilon)/(c|\Phi'|/\chi') < [(\delta B/B)/\varepsilon]^2$, the collisionless detrapping/retrapping layer becomes wider than the collisional boundary layer and the transport fluxes are dominated by particles that undergo detrapping and retrapping processes when the $\boldsymbol{E}\times\boldsymbol{B}$ drift frequency dominates [3, 28, 222]. The detrapping here means that a toroidally trapped particle, i.e. a banana, becomes a circulating particle without suffering collisions. The reverse process is called retrapping. This detrapping-and-retrapping process is unique to tori without any symmetry. The trapping state of particles can change even when there are no collisions involved [3, 28]. This transport mechanism is non-resonant because the $\boldsymbol{E}\times\boldsymbol{B}$ drift speed is assumed to be much larger than the ∇Bdrift speed. The transport fluxes scale with collision frequency in this regime. The particle and heat fluxes are [222]

$$\Gamma_{\nu}^{\mathrm{na}} = -\frac{\sqrt{2\varepsilon}}{\pi^{3/2}} N \left(\frac{M}{e\Phi'}\right)^2 v_t^4 \nu_t (\delta B/B)_{\mathrm{M}} \times \left[\eta_1\left(\frac{p'}{p}+\frac{e\Phi'}{T}\right)+\eta_2\frac{T'}{T}\right], \tag{8.2.3.1}$$

and

$$\frac{q_{\nu}^{\mathrm{na}}}{T} = -\frac{\sqrt{2\varepsilon}}{\pi^{3/2}} N \left(\frac{M}{e\Phi'}\right)^2 v_t^4 \nu_t (\delta B/B)_{\mathrm{M}} \times \left[\eta_2\left(\frac{p'}{p}+\frac{e\Phi'}{T}\right)+\eta_3\frac{T'}{T}\right], \tag{8.2.3.2}$$

where

$$(\delta B/B)_{\mathrm{M}} = \mathrm{Max}\left\{ [4K(k_{\mathrm{d}})]^{-1} \times \int_{-\theta_t}^{\theta_t} \mathrm{d}\theta \frac{1}{\sqrt{k_{\mathrm{d}}^2 - \sin^2\frac{\theta}{2}}} \sum_n (A_n \cos n\zeta_0 + B_n \sin n\zeta_0)\right\}, \tag{8.2.3.3}$$

k_{d} is approximately the same as k defined in equation (8.1.14), and

$$\eta_j = \int_0^{\infty} \mathrm{d}x \left(x^2 - \frac{5}{2}\right)^{j-1} x^6 \mathrm{e}^{-x^2} \frac{\nu_{\mathrm{D}}}{\nu_t}, \tag{8.2.3.4}$$

for $j = 1$–3. The notation Max[s] in equation (8.2.3.3) means the maximum value of the argument s along ζ_0. The fluxes in equations (8.2.3.1) and (8.2.3.2) are a simplified version by approximating an integral as discussed in [222]. This simplified version is easier to implement. The more complicated version in [222] can be adopted if more accuracy is preferred.

The random walk argument for this regime is similar to that for the collisional boundary layer $\sqrt{\nu}$ regime except that the layer width is replaced by the collisionless detrapping/retrapping layer width Δk_{d}^2

$$\Delta k_{\mathrm{d}}^2 \sim \frac{\delta B/B}{\varepsilon} < 1. \tag{8.2.3.5}$$

Note that the ratio $(\delta B/B)/\varepsilon$ is a measure of asymmetry in the $|\boldsymbol{B}|$ spectrum.

8.2.4. Superbanana plateau regime. When the $\boldsymbol{E}\times\boldsymbol{B}$ drift speed is comparable to or smaller than the ∇B drift speed, these two frequencies can resonate, i.e. the toroidal drift frequency vanishes, and the radial step size becomes unbounded if the singularity is unresolved. This leads to the superbanana plateau regime and the superbanana regime. The collision frequency is large enough to resolve the singularity but small enough to prevent the drift orbits from forming in the superbanana plateau regime where $\nu_t < cMv_t^2\varepsilon'/(e\chi')$, but $\nu/(\delta B/B_0) > (\delta B/B_0)^{1/2}\varepsilon^{-1/2} cMv_t^2\varepsilon'/(e\chi')$ [223]. In the superbanana regime, the singularity is resolved by the nonlinear orbit trajectories [224].

8.2.4.1. Resonance away from the phase space boundary. When superbanana plateau resonance occurs at a pitch angle parameter k_r^2 that is away from either $k^2 = 1$ or 0, the dependence of the complete elliptic integrals in the toroidal drift frequency on k^2 can be approximated by a Taylor series expanded in the vicinity of the resonance k_r^2. Specifically,

$$\langle \boldsymbol{v}_{\mathrm{d}}\cdot\nabla\zeta_0\rangle_{\mathrm{b}} \approx \frac{c\Phi'}{\chi'} - \frac{c\mu B_0}{e\chi'}\varepsilon'\left[\frac{2E(k_r)}{K(k_r)} - 1\right] - \frac{c\mu B_0}{e\chi'}\varepsilon'\left(\frac{\mathrm{d}G}{\mathrm{d}k_r^2}\right)\left(k^2 - k_r^2\right), \tag{8.2.4.1.1}$$

where $G(k) = 2E(k)/K(k) - 1$ [66]. From equation (8.2.4.1.1), the resonance condition that determines the resonance pitch angle parameter k_r^2 is

$$\frac{c\Phi'}{\chi'} - \frac{c\mu B_0}{e\chi'}\varepsilon'\left[\frac{2E(k_r)}{K(k_r)} - 1\right] = 0. \tag{8.2.4.1.2}$$

In the vicinity of k_r^2, the toroidal drift becomes

$$\langle \boldsymbol{v}_{\mathrm{d}}\cdot\nabla\zeta_0\rangle_{\mathrm{b}} \approx -\frac{c\mu B_0}{e\chi'}\varepsilon'\left(\frac{\mathrm{d}G}{\mathrm{d}k_r^2}\right)\left(k^2 - k_r^2\right), \tag{8.2.4.1.3}$$

which describes the collisional resonance broadening. The collision operator can be approximated as

$$\langle C(f_{10})\rangle_{\mathrm{b}} \approx \frac{\nu_{\mathrm{D}}}{\varepsilon}\left[\frac{E(k_r)}{K(k_r)} - \left(1 - k_r^2\right)\right]\frac{\partial^2 f_{01}}{\partial\left(k^2\right)^2}, \tag{8.2.4.1.4}$$

for a narrow resonance layer in the vicinity of k_r^2. Substituting results in equations (8.2.4.1.1)–(8.2.4.1.4) into equation (8.1.10) yields the equation that governs the physics of the superbanana plateau resonance:

$$-\frac{c\mu B_0}{e\chi'}\varepsilon'\frac{\mathrm{d}G}{\mathrm{d}k_r^2}\left(k^2 - k_r^2\right)\frac{\partial f_{01}}{\partial\zeta_0} + \langle \boldsymbol{v}_{\mathrm{d}}\cdot\nabla V\rangle_{\mathrm{b}}\frac{\partial f_{\mathrm{M}}}{\partial V} = \frac{\nu_{\mathrm{D}}}{\varepsilon}\left[\frac{E(k_r)}{K(k_r)} - \left(1 - k_r^2\right)\right]\frac{\partial^2 f_{01}}{\partial\left(k^2\right)^2}. \tag{8.2.4.1.5}$$

Equation (8.2.4.1.5) can be solved by expanding f_{01} as

$$f_{01} = \sum_n \left(f_n e^{in\zeta_0} + f_n^* e^{-in\zeta_0} \right), \tag{8.2.4.1.6}$$

where f_n and its complex conjugate f_n^* are Fourier coefficients. The equation for the Fourier amplitude f_n is

$$-\frac{c\mu B_0}{e\chi'}\varepsilon' \left|\frac{dG}{dk_r^2}\right| in y_a f_n + \langle \boldsymbol{v}_d \cdot \nabla V \rangle_{bn} \frac{\partial f_M}{\partial V} = \frac{\nu_D}{\varepsilon}\left[\frac{E(k_r)}{K(k_r)} - \left(1 - k_r^2\right)\right]\frac{\partial^2 f_n}{\partial y^2}, \tag{8.2.4.1.7}$$

where $y_a = k_r^2 - k^2$, $\left(dG/dk_r^2\right) = -|dG/dk_r^2|$ because $\left(dG/dk_r^2\right)$ is negative, and

$$\langle \boldsymbol{v}_d \cdot \nabla V \rangle_{bn} = \frac{c\mu B_0}{e\chi'}\frac{1}{4K(k)}\frac{n}{2}\int_{-\theta_t}^{\theta_t} d\theta \frac{B_n(\theta) + iA_n(\theta)}{\sqrt{k^2 - \sin^2(\theta/2)}}. \tag{8.2.4.1.8}$$

Equation (8.2.4.1.7) can be cast into the standard dimensionless form for the plateau regime in general [6, 225–227]

$$\frac{\partial^2 g_n}{\partial z^2} - z g_n = 1, \tag{8.2.4.1.9}$$

where

$$f_n = -\frac{\langle \boldsymbol{v}_d \cdot \nabla V \rangle_{bn}}{|c\mu B_0 \varepsilon' n/(e\chi')|\left|dG/dk_r^2\right|}\hat{\nu}^{-1/3}\frac{\partial f_M}{\partial V} g_n, \tag{8.2.4.1.10}$$

$$\hat{\nu} = \frac{\nu_D}{\varepsilon}\frac{\left[E(k_r)/K(k)_r - \left(1 - k_r^2\right)\right]}{[c\mu B_0 \varepsilon'/(|e|\,\chi')]\left|dG/dk_r^2\right|}, \tag{8.2.4.1.11}$$

$z = i\sigma_1 \hat{p}$, and $\hat{p} = y_a \hat{\nu}^{-1/3}$. The notation σ_1 is the combined sign of the electric charge e and mode number n: $\sigma_1 = +1$ if e and n have the same signs otherwise $\sigma_1 = -1$. The transport fluxes do not depend on the sign of σ_1. Thus, $\sigma_1 = +1$ is chosen without loss of generality. The width of the resonance layer can be estimated by $\hat{p} \sim 1$ and is

$$\Delta k^2 \sim \hat{\nu}^{1/3}. \tag{8.2.4.1.12}$$

There are two scales in the pitch angle space. One is of the order of unity associated with the equilibrium such as those in $\langle \boldsymbol{v}_d \cdot \nabla V \rangle_b$, and the other is of the order of $\Delta k^2 \approx \hat{\nu}_1^{1/3} \ll 1$ resulting from the resonance. The goal is to find the short scale variation, of the order of the width of the resonance layer, of the perturbed distribution function. Within this scale, the equilibrium variation of k^2 is treated as a parameter. This approximation is the same as that used in the collisional boundary layer analysis in section 8.2.2 [216] and is used in evaluating the transport fluxes.

In the asymptotic limit where $\hat{\nu} < 1$, the layer variable z describes the fast variation in the pitch angle parameter k^2 space. Because the resonance is far away from $k^2 = 0$ or 1, the boundary condition for equation (8.2.4.1.8) is that $g_n \to 0$ as $|\hat{p}| \to \infty$. The solution for equation (8.2.4.1.9) is then

$$g_n = \pi Hi(z), \tag{8.2.4.1.13}$$

where $\pi Hi(z) = \int_0^\infty dt e^{zt - t^3/3}$ [228]. This is the standard dimensionless solution in the plateau regime when the pitch angle scattering operator dominates [6, 225–227].

Substituting equations (8.2.4.1.9)–(8.2.4.1.11) into the definitions for the particle and heat fluxes yields the transport fluxes in the superbanana plateau regime [223]

$$\Gamma_{sb-p}^{na} = -\frac{\pi}{4}\sqrt{2\varepsilon}\frac{2}{|\varepsilon'|}\frac{cM}{|e|\chi'}\frac{Nv_t^2}{\pi^{3/2}}\left[\eta_1\left(\frac{p'}{p} + \frac{e\Phi'}{T}\right) + \eta_2\frac{T'}{T}\right], \tag{8.2.4.1.14}$$

and

$$\frac{q_{sb-p}^{na}}{T} = -\frac{\pi}{4}\sqrt{2\varepsilon}\frac{2}{|\varepsilon'|}\frac{cM}{|e|\chi'}\frac{Nv_t^2}{\pi^{3/2}}\left[\eta_2\left(\frac{p'}{p} + \frac{e\Phi'}{T}\right) + \eta_3\frac{T'}{T}\right]. \tag{8.2.4.1.15}$$

The coefficients η_j for $j = 1$–3 are

$$\eta_j = \int_{x_{min}}^\infty dx 2x^4 \left(x^2 - \frac{5}{2}\right)^{j-1} \times e^{-x^2}\frac{K(k_r)}{\left|dG/dk_r^2\right|}\sum_n |n|(\alpha_n^2 + \beta_n^2)_{k_r}, \tag{8.2.4.1.16}$$

where the subscript k_r indicates that the quantity is evaluated at $k = k_r$, the lower integration limit of the energy integral is set by the resonant condition and is given in equation (8.2.2.18). Note that all the k dependences inside the energy integral in equations (8.2.4.1.16) are evaluated at k_r. The transport fluxes are identical to those obtained in [223] using a Krook model as expected.

When the radial electric field vanishes, $k_r^2 \approx 0.827$ [3], and fluxes reduce to [223]

$$\Gamma_{sb-p}^{na} = -\frac{\pi}{4}\sqrt{2\varepsilon}\frac{2}{|\varepsilon'|}\frac{cM}{|e|\chi'}\frac{Nv_t^2}{\pi^{3/2}}\left[\eta_1\left(\frac{p'}{p} + \frac{e\Phi'}{T}\right) + \eta_2\frac{T'}{T}\right], \tag{8.2.4.1.17}$$

and

$$\frac{q_{sb-p}^{na}}{T} = -\frac{\pi}{4}\sqrt{2\varepsilon}\frac{2}{|\varepsilon'|}\frac{cM}{|e|\chi'}\frac{Nv_t^2}{\pi^{3/2}}\left[\eta_2\left(\frac{p'}{p} + \frac{e\Phi'}{T}\right) + \eta_3\frac{T'}{T}\right], \tag{8.2.4.1.18}$$

where $\eta_j = C_j 4K(k_r)k_r^2(1 - k_r^2)\sum_n |n|(\alpha_n^2 + \beta_n^2)_{k_r}$, and C_j for $j = 1$–3 is defined in section 6.2.2.

The random walk argument for the superbanana plateau scaling goes as follows. Balancing the residual∇B drift frequency $\omega'_{\nabla B}(\Delta k^2)$ with the effective collision frequency $(\nu/\varepsilon)/(\Delta k^2)^2$, after evaluating $\langle \boldsymbol{v}_d \cdot \nabla \zeta_0 \rangle_b$ at $k = k_r$, determines the width of the layer in the k^2 space $(\Delta k^2) \sim [(\nu/\varepsilon)/|\omega'_{\nabla B}|]^{1/3}$, which is basically $\hat{\nu}^{1/3}$, where $\omega'_{\nabla B} = d\omega_{\nabla B}/dk_r^2$, and the ∇B drift frequency $\omega_{\nabla B}$ is $\omega_{\nabla B} = -[c\mu B_0/(e\chi')]\varepsilon'[2E(k)/K(k) - 1]$. The step size is $\Delta r \sim [v_{dr}/(|\omega'_{\nabla B}|\Delta k^2)]$, which remains finite due to collisional resonance broadening. Recognizing that the fraction of particles that participate in the transport process is $\sqrt{\varepsilon}\Delta k^2$, i.e. the particles that are centered around the resonance k_r^2, and the de-correlation frequency is $(\nu/\varepsilon)/(\Delta k^2)^2$, superbanana plateau scaling is obtained as $D \sim \sqrt{\varepsilon}v_{dr}^2/|\omega'_{\nabla B}|$, which is the same scaling as those given in equations (8.2.4.1.14) and (8.2.4.1.15).

The theory discussed here is for the superbanana plateau resonance occurring away from the phase space boundary, i.e. $k^2 = 1$ or 0. The boundary conditions at the phase space boundary can be ignored when the resonance pitch angle parameter k_r^2 is away from the boundary by more than the width of the resonance layer $\Delta k^2 \sim \hat{\nu}^{1/3}$. However, when the

resonance occurs in the vicinity of the phase space boundary, the boundary conditions at $k^2 = 1$ or 0 cannot be ignored and these conditions modify the resonance physics as first noticed in [219, 220].

8.2.4.2. Resonance in the vicinity of $k^2 = 1$. When resonance occurs in the vicinity of $k^2 = 1$, the toroidal drift frequency can be approximated as [66]

$$\langle \boldsymbol{v}_{\rm d} \cdot \nabla \zeta_0 \rangle_{\rm b} \approx \frac{c\Phi'}{\chi'} - \frac{c\mu B_0}{e\chi'}\varepsilon' \times \left[\frac{2}{\ln\left(4/\sqrt{1-k^2}\right)} - k_r^2 + \left(k_r^2 - k^2\right) \right]. \quad (8.2.4.2.1)$$

The proper interpretation of equation (8.2.4.2.1) is that the resonance k_r^2 is determined from the resonance condition

$$\frac{c\Phi'}{\chi'} - \frac{c\mu B_0}{e\chi'}\varepsilon' \left[\frac{2}{\ln\left(4/\sqrt{1-k^2}\right)} - k_r^2 \right] = 0. \quad (8.2.4.2.2)$$

The $1 - k^2 = \Delta k^2$ in the argument of the logarithmic function is the width of the resonance layer to be determined. Thus, in the vicinity of the resonance,

$$\langle \boldsymbol{v}_{\rm d} \cdot \nabla \zeta_0 \rangle_{\rm b} \approx -\frac{c\mu B_0}{e\chi'}\varepsilon' \left(k_r^2 - k^2\right), \quad (8.2.4.2.3)$$

which describes the collisional resonance broadening. For a narrow resonance layer, the collision operator is approximated in the vicinity of $k^2 = 1$ as [66]

$$\langle C\left(f_{01}\right)\rangle = 2\frac{\nu_{\rm D}}{\varepsilon}\frac{1}{\ln\left[16/\left(1-k^2\right)\right]}\frac{\partial^2 f_{01}}{\partial y_1^2}, \quad (8.2.4.2.4)$$

where $y_1 = k_r^2 - k^2$. Thus, the equation that governs the resonance in the vicinity of $k^2 = 1$ is

$$-\frac{c\mu B_0}{e\chi'}\varepsilon' y_1 \frac{\partial f_{01}}{\partial \zeta_0} + \langle \boldsymbol{v}_{\rm d} \cdot \nabla V \rangle_{\rm b} \frac{\partial f_{\rm M}}{\partial V} = 2\frac{\nu_{\rm D}}{\varepsilon}\frac{1}{\ln\left[16/\left(\Delta k^2\right)\right]}\frac{\partial^2 f_{01}}{\partial y_1^2}. \quad (8.2.4.2.5)$$

Using the same procedure in solving equation (8.2.4.1.5), a dimensionless equation for the Fourier amplitude f_{1n}, defined in $f_{01} = \sum_n \left(f_{1n}e^{in\zeta_0} + f_{1n}^* e^{-in\zeta_0}\right)$, is

$$\frac{\partial^2 g_{1n}}{\partial z_1^2} - z_1 g_{1n} = 1, \quad (8.2.4.2.6)$$

where $z_1 = i\sigma_1 \hat{\nu}_1^{-1/3} y_1$, $\hat{\nu}_1 = (2\nu_{\rm D}/\varepsilon)\left[\ln\left(16/\Delta k^2\right)\right]^{-1} \times \left[|e|\,\chi'/\left(c\mu B_0 \varepsilon'\right)\right]$, and σ_1 is the combined sign of the charge e and the mode number n as defined previously. The dimensionless function g_{1n} is defined as

$$f_{1n} = -\frac{\langle \boldsymbol{v}_{\rm d} \cdot \nabla V \rangle_{{\rm b}n}}{\hat{\nu}_1 \left|c\mu B_0 \varepsilon' n/(e\chi')\right|}\hat{\nu}_1^{2/3}\frac{\partial f_{\rm M}}{\partial V} g_{1n}. \quad (8.2.4.2.7)$$

The width of the resonance layer can be estimated from the definition for z_1 to be $\Delta k^2 \approx \hat{\nu}_1^{1/3}$, and can be used in the argument of the logarithmic function. An accurate numerical evaluation for the layer width can be made using the iteration procedure for the best fit to the numerical solution of the bounce average drift kinetic equation in the transition region [229].

Equation (8.2.4.2.6) is the standard equation for the plateau resonances derived previously. It is to be solved subject to the boundary conditions that $g_{1n} = 0$ at $k^2 = 1$ and vanishes far away from the resonance k_r^2, i.e. $g_{1n} \to 0$ when $k^2 \ll k_r^2$. These boundary conditions are different from those that require the perturbed distribution function vanishes far away from the resonance for standard plateau resonances away from the phase space boundary in section 8.2.4.1. There, the boundary conditions at the phase space boundary are not important because the resonance layer is narrow.

The solution to equation (8.2.4.2.6) consists of the particular solution and the homogeneous solution. The particular solution $g_{1n,{\rm p}}$ that is compatible with the boundary condition is [6, 66, 225–227]

$$g_{1n,{\rm p}} = \pi Hi\left(z_1\right). \quad (8.2.4.2.8)$$

Note that $g_{1n,{\rm p}}$ is the standard solution for the plateau resonances because it satisfies the boundary conditions given in section 8.2.4.1 and there are no homogeneous solutions that are compatible with the boundary conditions when the resonance is away from the phase space boundary. However, to impose the boundary condition at $k^2 = 1$, homogeneous solution must be included. For $\sigma_1 = +1$, the homogeneous solution that is compatible with the boundary conditions is $Ai\left(z_1 e^{-i2\pi/3}\right)$. Here, Ai is Airy function [228]. For $\sigma_1 = -1$, it is $Ai\left(z_1 e^{i2\pi/3}\right)$. These two functions are mirror images of each other [228]. Thus, $\sigma_1 = +1$ is chosen without loss of the generality. The complete solution compatible with the boundary conditions is

$$g_{1n} = I_{c1} Ai\left(z_1 e^{-i2\pi/3}\right) + \pi Hi\left(z_1\right), \quad (8.2.4.2.9)$$

where I_{c1} is a constant determined from the boundary condition that $g_n = 0$ at $k^2 = 1$ and is

$$I_{c1} = -\frac{\pi Hi\left(z_{11}\right)}{Ai\left(z_{11}e^{-i2\pi/3}\right)}, \quad (8.2.4.2.10)$$

where z_{11} is defined as $z_{11} = i\hat{\nu}_1^{-1/3}\left(k_r^2 - 1\right)$.

Substituting the solution into the expressions for the transport fluxes yields [66]

$$\Gamma_{\rm sb\_p\_1}^{\rm na} = -\frac{\pi}{4}\frac{N v_{\rm t}^2}{\pi^{3/2}}\frac{cM}{|e|\,\chi'}\frac{2\sqrt{2\varepsilon}}{\varepsilon'}\sum_n |n|\left(\alpha_n^2 + \beta_n^2\right)\Big|_{k_r} \times K\left(k_r\right)\left[\eta_1\left(\frac{p'}{p} + \frac{e\Phi'}{T}\right) + \eta_2\frac{T'}{T}\right], \quad (8.2.4.2.11)$$

and

$$\frac{q_{\rm sb\_p\_1}^{\rm na}}{T} = -\frac{\pi}{4}\frac{N v_{\rm t}^2}{\pi^{3/2}}\frac{cM}{|e|\,\chi'}\frac{2\sqrt{2\varepsilon}}{\varepsilon'}\sum_n |n|\left(\alpha_n^2 + \beta_n^2\right)\Big|_{k_r} \times K\left(k_r\right)\left[\eta_2\left(\frac{p'}{p} + \frac{e\Phi'}{T}\right) + \eta_3\frac{T'}{T}\right], \quad (8.2.4.2.12)$$

where for $j = 1$–3

$$\eta_j = \int_{x_{\min}}^{\infty} {\rm d}x 2x^4 \left(x^2 - \frac{5}{2}\right)^{j-1} e^{-x^2} C_{\rm p1}, \quad (8.2.4.2.13)$$

and

$$C_{\rm p1} = \int_{-\left(1-k_r^2\right)\hat{\nu}_1^{-1/3}}^{\infty} {\rm d}\,|z_1|\,Re\left\{Hi\left(z_1\right) - \left[\frac{Hi\left(z_{11}\right)}{Ai\left(z_{11}e^{-i2\pi/3}\right)}\right. \left.Ai\left(z_1 e^{-i2\pi/3}\right)\right]\right\}. \quad (8.2.4.2.14)$$

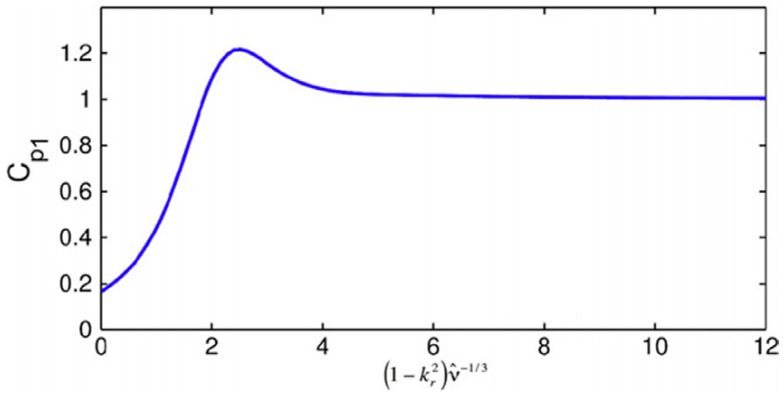

Figure 21. The form factor C_{p1} as a function of $\left(1-k_r^2\right)\hat{\nu}_1^{-1/3}$ is shown. When resonance is at $k^2=1$, $C_{p1}\approx 1/6$; when $\left(1-k_r^2\right)\hat{\nu}_1^{-1/3}\gg 1$, C_{p1} approaches unity.

The factor C_{p1} as a function of $\left(1-k_r^2\right)\hat{\nu}_1^{-1/3}$ is shown in figure 21 [66]. When $\left(1-k_r^2\right)\hat{\nu}_1^{-1/3}\gg 1$, $C_{p1}=1$, which is the same value obtained when the resonance occurs away from phase space boundary discussed in section 8.2.4.1. When the resonance occurs at $k^2=1$, $C_{p1}\approx 1/6$, an indication that the strength of the resonance is weakened. There is an overshoot in the transition from the phase space boundary to the interior. The integrand of C_{p1} is shown in figure 22 [66]. The boundary condition at $k^2=1$ modifies the shape of the resonance significantly when $\left(1-k_r^2\right)\hat{\nu}_1^{-1/3}\ll 1$. When the resonance is away from $k^2=1$, the shape of the resonance becomes centrally peaked.

8.2.4.3 Resonance in the vicinity of $k^2=0$. In the vicinity of $k^2=0$, $\langle \boldsymbol{v}_d\cdot\nabla\zeta_0\rangle_b$ can be expressed as [66]

$$\langle \boldsymbol{v}_d\cdot\nabla\zeta_0\rangle_b\approx\frac{c\Phi'}{\chi'}-\frac{c\mu B_0}{e\chi'}\varepsilon'\left[1-k_r^2+\left(k_r^2-k^2\right)\right]. \tag{8.2.4.3.1}$$

Thus, the resonance for $\langle \boldsymbol{v}_d\cdot\nabla\zeta_0\rangle_b$ occurs at

$$\frac{c\Phi'}{\chi'}-\frac{c\mu B_0}{e\chi'}\varepsilon'\left(1-k_r^2\right)=0, \tag{8.2.4.3.2}$$

which is an equation for the resonance k_r^2. The residual $\langle \boldsymbol{v}_d\cdot\nabla\zeta_0\rangle_b$ for the collisional resonance broadening is

$$\langle \boldsymbol{v}_d\cdot\nabla\zeta_0\rangle_b=-\frac{c\mu B_0}{e\chi'}\varepsilon'\left(k_r^2-k^2\right). \tag{8.2.4.3.3}$$

In the vicinity of $k^2=0$, the collision operator can be approximated as [66]

$$\langle C(f_{10})\rangle_b\approx\frac{\nu_D}{2\varepsilon}\frac{\partial}{\partial k^2}\left(k^2\frac{\partial f_{10}}{\partial k^2}\right). \tag{8.2.4.3.4}$$

It should be noted that even though the resonance layer is narrow, the $\partial/\partial k^2$ term is of the same order as $\partial^2/\left(\partial k^2\right)^2$ because k^2 is small. Employing equations (8.2.4.3.3) and (8.3.4.3.4), the bounce averaged drift kinetic equation in the vicinity of $k^2=0$ that governs the resonance becomes

$$-\frac{c\mu B_0}{e\chi'}\varepsilon'\left(k_r^2-k^2\right)\frac{\partial f_{01}}{\partial\zeta_0}+\langle \boldsymbol{v}_d\cdot\nabla V\rangle_b\frac{\partial f_M}{\partial V}=\frac{\nu_D}{2\varepsilon}\frac{\partial}{\partial k^2}\left(k^2\frac{\partial f_{10}}{\partial k^2}\right), \tag{8.2.4.3.5}$$

which can be solved by expanding $f_{01}=\sum_n(f_{0n}e^{in\zeta_0}+f_{0n}^*e^{-in\zeta_0})$. The function f_{0n} satisfies

$$\frac{c\mu B_0}{e\chi'}\varepsilon'\left(k^2-k_r^2\right)in f_{0n}+\langle \boldsymbol{v}_d\cdot\nabla V\rangle_{bn}\frac{\partial f_M}{\partial V}=\frac{\nu_D}{2\varepsilon}\frac{\partial}{\partial k^2}\left(k^2\frac{\partial f_{0n}}{\partial k^2}\right). \tag{8.2.4.3.6}$$

Defining $u=k^2\left[\sigma_1\hat{\nu}_0/(i\,|n|)\right]^{-1/2}$ and $u_0=k_r^2[\sigma_1\hat{\nu}_0/(i\,|n|)]^{-1/2}$, equation (8.2.4.3.6) is cast into

$$\frac{\partial^2 f_{0n}}{\partial u^2}+\frac{1}{u}\frac{\partial f_{0n}}{\partial u}-\frac{u-u_0}{u}f_{0n}=\frac{1}{u}\langle \boldsymbol{v}_d\cdot\nabla V\rangle_{bn}\times\frac{\partial f_M}{\partial V}\left(\frac{\sigma_1\hat{\nu}_0}{i\,|n|}\right)^{1/2}\frac{1}{\hat{\nu}_0}\left(\frac{c\mu B_0}{|e|\,\chi'}\right)^{-1}, \tag{8.2.4.3.7}$$

where $\hat{\nu}_0=(2\nu_D/\varepsilon)\left[|e|\,\chi'/\left(c\mu B_0\varepsilon'\right)\right]$. Defining $g_n=\sqrt{u}\,f_{0n}$ to remove the first derivative, and then changing variable from u to $w=2u$, equation (8.2.4.3.7) becomes a Whittaker's equation [66]:

$$\frac{\partial^2 g_n}{\partial w^2}+\left(\frac{1}{4w^2}-\frac{1}{4}+\frac{u_0/2}{w}\right)g_n=\frac{\sqrt{2}}{4\sqrt{w}}\langle \boldsymbol{v}_d\cdot\nabla V\rangle_{bn}\times\frac{\partial f_M}{\partial V}\left(\frac{\sigma_1\hat{\nu}_0}{i\,|n|}\right)^{1/2}\frac{1}{\hat{\nu}_0}\frac{|e|\,\chi'}{c\mu B_0}. \tag{8.2.4.3.8}$$

Solving equation (8.2.4.3.8) in terms of Whittaker's functions yields

$$f_{0n}=\frac{\langle \boldsymbol{v}_d\cdot\nabla V\rangle_{bn}}{\hat{\nu}_0\,|c\mu B_0\varepsilon'/(e\chi')|}\left(\frac{\sigma_1\hat{\nu}_0}{i\,|n|}\right)^{1/2}\frac{\partial f_M}{\partial V}h_n, \tag{8.2.4.3.9}$$

where

$$h_n=I_1\frac{Y_1}{\sqrt{w}}+I_2\frac{Y_2}{\sqrt{w}}-\frac{Y_1}{2\sqrt{w}}\int_0^w dw\frac{Y_2/\sqrt{w}}{W(Y_1,Y_2)}+\frac{Y_2}{2\sqrt{w}}\int_0^w dw\frac{Y_1/\sqrt{w}}{W(Y_1,Y_2)}, \tag{8.2.4.3.10}$$

and I_1 and I_2 are constants to be determined. The Y_1 and Y_2 are Whittaker's functions defined as [228]

$$Y_1=e^{-w/2}\sqrt{w}M\left(\frac{1}{2}-\lambda_r,1,w\right), \tag{8.2.4.3.11}$$

and

$$Y_2=e^{-w/2}\sqrt{w}U\left(\frac{1}{2}-\lambda_r,1,w\right), \tag{8.2.4.3.12}$$

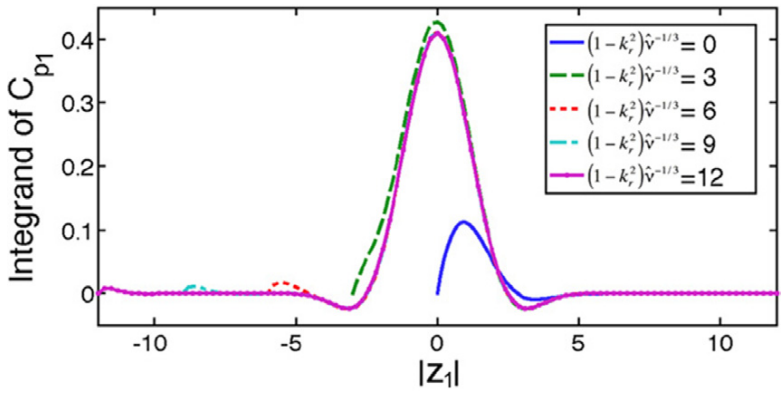

Figure 22. The integrand of the integral C_{p1} as a function of $|z_1|$. When $\left(1-k_r^2\right)\hat{\nu}^{-1/3} \ll 1$. The boundary condition at $k^2=1$ modifies the resonant integrand significantly. When $\left(1-k_r^2\right)\hat{\nu}^{-1/3} \gg 1$, the integrand becomes centrally peaked as expected.

where $M(a,b,w)$ and $U(a,b,w)$ are Kummer's functions [228], and $\lambda_r = u_0/2$. The $W(Y_1,Y_2) = -1/\Gamma(a)$ is the Wronskian, and $a = (1/2-\lambda_r)$. Because Y_2 diverges logarithmically as $w \to 0$, $I_2 = 0$. For localized solution, the dimensionless function $g_n \to 0$ as $w \to \infty$, and the constant I_1 is

$$I_1 = \frac{1}{2}\int_0^\infty \mathrm{d}w \frac{Y_2/\sqrt{w}}{W(Y_1,Y_2)}. \tag{8.2.4.3.13}$$

The function g_n that satisfies boundary conditions is then

$$g_n = \frac{Y_1}{2\sqrt{w}}\int_w^\infty \mathrm{d}w \frac{Y_2/\sqrt{w}}{W(Y_1,Y_2)} + \frac{Y_2}{2\sqrt{w}}\int_0^w \mathrm{d}w \frac{Y_1/\sqrt{w}}{W(Y_1,Y_2)}, \tag{8.2.4.3.14}$$

and f_{0n} is also determined.

The transport fluxes calculated using the solution for f_{01} are [66]

$$\Gamma^{\mathrm{na}}_{\mathrm{sb\_p\_0}} = -\frac{\pi}{4}\frac{Nv_t^2}{\pi^{3/2}}\frac{cM}{|e|\chi'}\frac{2\sqrt{2\varepsilon}}{\varepsilon'}\sum_n |n|\left(\alpha_n^2+\beta_n^2\right)_{k_r^2} K(k_r) \times\left[\eta_1\left(\frac{p'}{p}+\frac{e\Phi'}{T}\right)+\eta_2\frac{T'}{T}\right], \tag{8.2.4.3.15}$$

and

$$\frac{q^{\mathrm{na}}_{\mathrm{sb\_p\_0}}}{T} = -\frac{\pi}{4}\frac{Nv_t^2}{\pi^{3/2}}\frac{cM}{|e|\chi'}\frac{2\sqrt{2\varepsilon}}{\varepsilon'}\sum_n |n|\left(\alpha_n^2+\beta_n^2\right)_{k_r^2} K(k_r) \times\left[\eta_2\left(\frac{p'}{p}+\frac{e\Phi'}{T}\right)+\eta_3\frac{T'}{T}\right], \tag{8.2.4.3.16}$$

where coefficient η_j is defined as, for $j = 1$–3,

$$\eta_j = \int_{x_{\min}}^\infty \mathrm{d}x 2x^4\left(x^2-\frac{5}{2}\right)^{j-1}\mathrm{e}^{-x^2}C_{\mathrm{p0}}, \tag{8.2.4.3.17}$$

and the form factor that describes the transition is

$$C_{\mathrm{p0}} = \frac{1}{2\pi}\int_0^\infty \mathrm{d}|w| Re\left\{\frac{\sqrt{2}}{2}(1-i)\frac{\Gamma(a)}{2} \times\left[\frac{Y_1}{\sqrt{w}}\int_w^{\infty\mathrm{e}^{\mathrm{i}\pi/4}}\mathrm{d}w'\frac{Y_2}{\sqrt{w'}}+\frac{Y_2}{\sqrt{w}}\int_0^w \mathrm{d}w'\frac{Y_1}{\sqrt{w'}}\right]\right\}. \tag{8.2.4.3.18}$$

Note that C_{p0} depends on the parameter $\lambda_r = u_0/2$ which is a function of energy. If thermal quantities are used for the energy to evaluate λ_r, C_{p0} becomes a function of temperature and can be taken out of the energy integral. If the energy dependence in λ_r is treated rigorously, there can be a different collision frequency scaling in the transition region.

The factor C_{p0} as a function of λ_r is shown in figure 23 [66]. When the resonance occurs at $k^2=0$, $C_{\mathrm{p0}} \approx 1/4$, an indication that the resonance strength is weakened. When $\lambda_r \gg 1$, $C_{\mathrm{p0}} \to 1$ as expected. There is also an overshoot in the transition region. The integrand of C_{p0} for several values of λ_r is shown in figure 24 [66]. When $\lambda_r \gg 1$, the effects of the boundary condition at $k^2=0$ diminish.

8.2.5. Superbanana regime. In this regime, the singularity resulting from the resonance between the $\boldsymbol{E}\times\boldsymbol{B}$ drift frequency and the ∇B drift frequency is resolved by the non-linear drift trajectories, i.e. superbananas, similar to the standard banana regime. It onsets when the effective collision frequency for superbananas is less than the superbanana bounce frequency, i.e. $\nu_{\mathrm{eff}} \sim \nu/(\delta B/B_0) < (\delta B/B_0)^{1/2}\varepsilon^{-1/2}cMv_t^2\varepsilon'/(|e|\chi')$ so that collisionless drift orbits can form [3, 224].

To solve the bounce averaged drift kinetic equation, it is necessary to know the toroidal drift frequency for superbananas. To this end, the constant of motion of the second adiabatic invariant $J_2 = \oint \mathrm{d}\theta|v_\parallel|$ is needed, which is valid when curvature drift like terms and magnetic shear are neglected. Here, the integral is performed in between the turning points of the trapped particles, i.e. $\oint \mathrm{d}\theta = \int_{-\theta_t}^{\theta_t}\mathrm{d}\theta$, where $v_{||}(\pm\theta_t) = 0$. Using the magnetic field spectrum for $|\boldsymbol{B}|$ in equation (8.3) and assuming that $|A_n(\theta)|$, and $|B_n(\theta)|$ are much smaller than ε yield

$$J_2 = 8\sqrt{\frac{\mu B_0\varepsilon}{M}}[E(k)-(1-k^2)K(k)] + \frac{1}{2\varepsilon}\sqrt{\frac{\mu B_0\varepsilon}{M}}\sum_n(\bar{A}_n\cos n\zeta_0+\bar{B}_n\sin n\zeta_0), \tag{8.2.5.1}$$

where $\bar{A}_n = \oint \mathrm{d}\theta A_n(\theta)/\sqrt{k^2-\sin^2(\theta/2)}$, and $\bar{B}_n = \oint \mathrm{d}\theta B_n(\theta)/\sqrt{k^2-\sin^2(\theta/2)}$.

Because the toroidal symmetry is broken, trapped particles drift off the flux surface following a constant J_2 surface. Thus, at any two points on the constant J_2 surface,

$$J_2(V,\zeta_0) = J_2(V_0,\zeta_{00}), \tag{8.2.5.2}$$

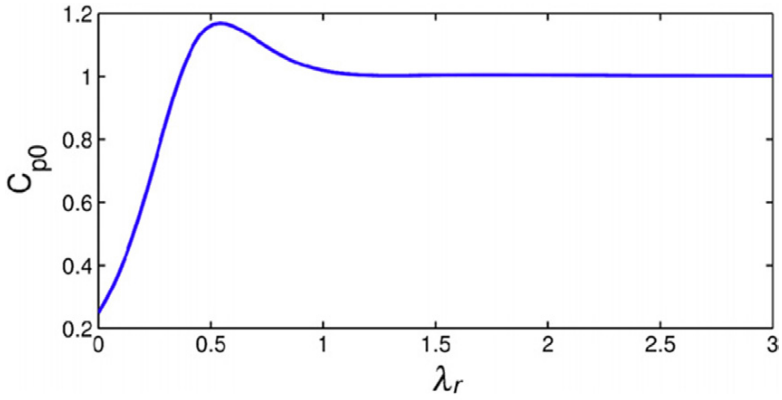

Figure 23. The form factor C_{p0} as a function of λ_r. When resonance at the $k^2 = 0$, $C_{p0} \approx 1/4$. When the resonance is far away from $k^2 = 0$, C_{p0} approaches unity as expected.

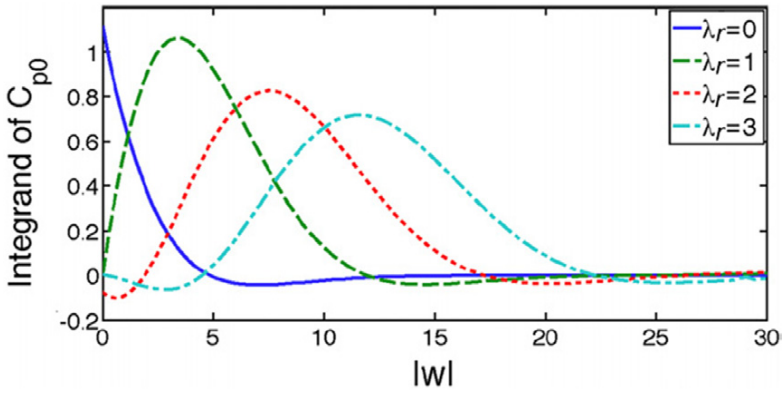

Figure 24. The integrand of the integral C_{p0} as a function of $|w|$. When the resonance occurs at the $k^2 = 0$, the integrand is modified significantly by the boundary condition. When the resonance is far away from $k^2 = 0$, the integrand approaches a centrally peaked resonant function.

where (V_0, ζ_{00}) are the coordinates of the reference point on the drift trajectory. Assuming the width of the orbits is smaller than the radial gradient scale length of J_2, equation (8.2.5.2) can be expanded to obtain an equation for the orbit width $(V - V_0)$ [224]:

$$\frac{1}{2}(V - V_0)^2 \frac{\partial^2 \bar{J}_2}{\partial V_0^2} + (V - V_0)\frac{\partial \bar{J}_2}{\partial V_0} + \frac{1}{2\varepsilon_0}\sqrt{\frac{\mu B_0 \varepsilon_0}{M}} \sum_n [\bar{A}_n(\cos n\zeta_0 - \cos n\zeta_{00}) + \bar{B}_n(\sin n\zeta_0 - \sin n\zeta_{00})] = 0, \quad (8.2.5.3)$$

where $\bar{J}_2 = 8\sqrt{\mu B_0 \varepsilon / M}[[E(k) - (1 - k^2)K(k)]$, and the additional subscript '0' is to indicate the quantity is evaluated at (V_0, ζ_{00}). Solving equation (8.2.5.3) yields the orbit width

$$(V - V_0) = \left[-\frac{\partial \bar{J}_2}{\partial V_0} \pm \left\{ \left(\frac{\partial \bar{J}_2}{\partial V_0}\right)^2 - \frac{\partial^2 \bar{J}_2}{\partial V_0^2}\frac{1}{\varepsilon_0}\sqrt{\frac{\mu B_0 \varepsilon_0}{M}} \times \sum_n [\bar{A}_n(\cos n\zeta_0 - \cos n\zeta_{00}) + \bar{B}_n(\sin n\zeta_0 - \sin n\zeta_{00})] \right\}^{1/2} \right] \left[\partial^2 \bar{J}_2 / \partial V_0^2\right]^{-1}. \quad (8.2.5.4)$$

The toroidal angular velocity ω_{tb} can now be calculated. The bounce averaged toroidal drift velocity can be written as

$$\omega_{tb} = \langle \boldsymbol{v}_d \cdot \nabla \zeta_0 \rangle_b = -\frac{Mc}{e\chi'} \frac{\partial J_2 / \partial V}{M \partial J_2 / \partial E}, \quad (8.2.5.5)$$

Because $M\partial J_2/\partial E$ appears in all terms in the bounce averaged drift kinetic equation, it is not necessary to perform any operation on it. Expanding $\partial J_2/\partial V$ in the numerator of equation (8.2.5.5) in the vicinity of V_0 yields

$$\omega_{tb} \approx \omega_0 + \omega_0'(V - V_0), \quad (8.2.5.6)$$

where $\omega_0 = \langle \boldsymbol{v}_d \cdot \nabla \zeta_0 \rangle_b$ evaluated at V_0. To obtain equation (8.2.5.6), it is noted that the variation of ω_{tb} on a given flux surface is much weaker than that of ω_{tb} on the drift surface. Substituting the width of the superbanana given in equation (8.2.5.4) into equation (8.2.5.6) yields a simple expression for ω_{tb} on the drift surface [224]

$$\omega_{tb} = \sigma_{sb}\hat{\omega}_{tb}\sqrt{\hat{k}^2 - F(\zeta_0)}, \quad (8.2.5.7)$$

where σ_{sb} denotes the sign of ω_{tb},

$$\hat{\omega}_{tb} = \left|\frac{Mc}{e\chi'}\right| \left[2\frac{\partial^2 \bar{J}_2}{\partial V_0^2}\frac{\delta B/B_0}{2\varepsilon}\left(\frac{\mu B_0 \varepsilon}{M}\right)^{1/2}\right]^{1/2} \times \frac{1}{2K(k)}\left(\frac{\mu B_0 \varepsilon}{M}\right)^{1/2}, \quad (8.2.5.8)$$

the effective pitch angle parameter is

$$\hat{k}^2 = \frac{\left(\partial \bar{J}_2/\partial V_0\right)^2}{2\left|\frac{\partial^2 \bar{J}_2}{\partial V_0^2}\right| \frac{\delta B/B_0}{2\varepsilon}\left(\frac{\mu B_0 \varepsilon}{M}\right)^{1/2}}, \tag{8.2.5.9}$$

the effective magnetic well is

$$F(\zeta_0) = \frac{\sigma_j}{\delta B/B_0}\sum_n [\bar{A}_n(\cos n\zeta_0 - \cos n\zeta_{00}) + \bar{B}_n(\sin n\zeta_0 - \sin n\zeta_{00})], \tag{8.2.5.10}$$

the normalized perturbed magnetic field strength is

$$\frac{\delta B}{B_0} = \sum_n [\bar{A}_n(\cos n\zeta_{0\mathrm{M}} - \cos n\zeta_{0m}) + \bar{B}_n(\sin n\zeta_{0\mathrm{M}} - \sin n\zeta_{0m})], \tag{8.2.5.11}$$

$\zeta_{0\mathrm{M}}$ is the angle at which $\sum_n \left(\bar{A}_n \cos n\zeta_{0\mathrm{M}} + \bar{B}_n \sin n\zeta_{0\mathrm{M}}\right)$ is the global maximum, ζ_{0m} is the angle at which $\sum_n \left(\bar{A}_n \cos n\zeta_{0m} + \bar{B}_n \sin n\zeta_{0m}\right)$ is the global minimum, and σ_j denotes the sign of $\partial^2 \bar{J}_2/\partial V_0^2$. The angle ζ_{00} is chosen according to the sign of $\partial^2 \bar{J}_2/\partial V_0^2$. If $\partial^2 \bar{J}_2/\partial V_0^2 > 0$, i.e. $\sigma_j = +1$, $\zeta_{00} = \zeta_{0m}$, otherwise $\zeta_{00} = \zeta_{0\mathrm{M}}$. Thus, superbananas can be trapped either on the side of ζ_{0m} or on the side of $\zeta_{0\mathrm{M}}$ depending on the sign of $\partial^2 \bar{J}_2/\partial V_0^2$. There is a possibility that the quantity $\sum_n \left(\bar{A}_n \cos n\zeta_0 + B_n \sin n\zeta_0\right)$ can have local maxima and minima. In that case, there can be multiple trapping regions. The function $F(\zeta_0)$ is an effective magnetic field well that can trap bananas to form superbananas. The effective pitch angle for the superbananas is $\hat{k}^2$. Because $F(\zeta_0) \leqslant 1$, $\hat{k}^2 \leqslant 1$ for superbananas, and $\hat{k}^2 \geqslant 1$ for circulating drift bananas.

The superbanana orbits have $\omega_0 \approx 0$, i.e. the $\boldsymbol{E} \times \boldsymbol{B}$ and ∇B drifts almost cancel each other. In order for the cancellation to occur, the normalized energy $x^2 = v^2/v_\mathrm{t}^2$ must be larger than $x_{\min}^2$. Note that the resonant condition $\omega_0 \approx 0$ can be satisfied for any species regardless of the electric charge of the species and the sign of the radial electric field.

The typical magnitude of $\hat{\omega}_{\mathrm{tb}}$ is of the order of $(\delta B/B_0)^{1/2}\,\varepsilon^{-1/2}|\omega_\mathrm{t}|$, where ω_t is the typical angular frequency of the circulating drift bananas

$$\omega_\mathrm{t} \sim \left|\frac{c\mu B_0}{e\chi'}\varepsilon'\right|. \tag{8.2.5.12}$$

Thus, the onset of the superbanana regime is when $\nu_{\mathrm{eff}} \sim \nu/(\delta B/B_0) < (\delta B/B_0)^{1/2}\,\varepsilon^{-1/2}|\omega_\mathrm{t}|$. The collisions are so infrequent that trapped particles can complete their drift trajectories before suffering collisions. The fraction of the superbananas f_{sb} can be inferred from the definition of $\hat{\omega}_{\mathrm{tb}}$. It is the fraction of the banana particles $\sqrt{\varepsilon}$ times the fraction of the superbananas among the bananas, which is $(\delta B/B_0)^{1/2}\,\varepsilon^{-1/2}$, and $f_{\mathrm{sb}} \sim (\delta B/B_0)^{1/2}$.

The bounce averaged drift kinetic equation is solved using the same method used to calculate transport fluxes caused by orbits with finite width such as the drift orbits in bumpy tori, the potato orbits, and squeezed banana orbits in tokamaks in section 6 [110, 111, 120].

The linear bounce averaged drift kinetic equation for trapped particles is

$$\langle \boldsymbol{v}_\mathrm{d}\cdot\nabla\zeta_0\rangle_\mathrm{b}\frac{\partial f_{01}}{\partial\zeta_0} + \langle \boldsymbol{v}_\mathrm{d}\cdot\nabla V\rangle_\mathrm{b}\frac{\partial f_{01}}{\partial V} + \langle \boldsymbol{v}_\mathrm{d}\cdot\nabla V\rangle_\mathrm{b}\frac{\partial f_\mathrm{M}}{\partial V} = \langle C(f_{01})\rangle_\mathrm{b}. \tag{8.2.5.13}$$

The normally higher order $\langle \boldsymbol{v}_\mathrm{d}\cdot\nabla V\rangle_\mathrm{b}\partial f_{01}/\partial V$ term must be kept because $\partial f_{01}/\partial V \sim \partial f_\mathrm{M}/\partial V$. In the superbanana regime, equation (8.2.5.13) is solved by a subsidiary expansion exploring the small parameter $[\nu/(\delta B/B_0)]/[(\delta B/B_0)^{1/2}\,\varepsilon^{-1/2}|\omega_\mathrm{t}|] < 1$. The leading order equation is

$$\langle \boldsymbol{v}_\mathrm{d}\cdot\nabla\zeta_0\rangle_\mathrm{b}\frac{\partial f_{01,1}}{\partial\zeta_0} + \langle \boldsymbol{v}_\mathrm{d}\cdot\nabla V\rangle_\mathrm{b}\frac{\partial f_{01,1}}{\partial V} + \langle \boldsymbol{v}_\mathrm{d}\cdot\nabla V\rangle_\mathrm{b}\frac{\partial f_\mathrm{M}}{\partial V} = 0, \tag{8.2.5.14}$$

and the next order equation is

$$\langle \boldsymbol{v}_\mathrm{d}\cdot\nabla\zeta_0\rangle_\mathrm{b}\frac{\partial f_{01,2}}{\partial\zeta_0} + \langle \boldsymbol{v}_\mathrm{d}\cdot\nabla V\rangle_\mathrm{b}\frac{\partial f_{01,2}}{\partial V} = \left\langle C(f_{01,1})\right\rangle_\mathrm{b}, \tag{8.2.5.15}$$

where the second set of the subscript denotes the subsidiary ordering. Changing independent variables from (V, ζ_0, E, μ) to (J_2, ζ_0, E, μ), equations (8.2.5.14) and (8.2.5.15) become

$$\langle \boldsymbol{v}_\mathrm{d}\cdot\nabla\zeta_0\rangle_\mathrm{b}\frac{\partial f_{01,1}}{\partial\zeta_0} + \langle \boldsymbol{v}_\mathrm{d}\cdot\nabla V\rangle_\mathrm{b}\frac{\partial f_\mathrm{M}}{\partial V} = 0, \tag{8.2.5.16}$$

and

$$\langle \boldsymbol{v}_\mathrm{d}\cdot\nabla\zeta_0\rangle_\mathrm{b}\frac{\partial f_{01,2}}{\partial\zeta_0} = \left\langle C(f_{01,1})\right\rangle_\mathrm{b}, \tag{8.2.5.17}$$

Equation (8.2.5.16) is solved either by integrating it directly or utilizing the fact that J_2 is a constant on the drift surface [212, 224]. Because J_2 is constant on the drift trajectory,

$$\mathrm{d}J_2 = \frac{\partial J_2}{\partial V}\mathrm{d}V + \frac{\partial J_2}{\partial\zeta_0}\mathrm{d}\zeta_0 = 0. \tag{8.2.5.18}$$

Since $\langle \boldsymbol{v}_\mathrm{d}\cdot\nabla V\rangle_\mathrm{b}$ is proportional to $\partial J_2/\partial\zeta_0$, and $\langle \boldsymbol{v}_\mathrm{d}\cdot\nabla\zeta_0\rangle_\mathrm{b}$ is proportional to $\partial J_2/\partial V$, equation (8.2.5.16) can be integrated to obtain, utilizing equation (8.2.5.18),

$$f_{01,1} = -\Delta V\frac{\partial f_\mathrm{M}}{\partial V} + C_V, \tag{8.2.5.19}$$

where ΔV is the width of the orbits, and C_V is an integration constant. Using $(V - V_0)$ in equation (8.2.5.4) and expressing it in terms of ω_{tb} yield

$$f_{01,1} = -\frac{\omega_{\mathrm{tb}}}{\omega_0'}\frac{\partial f_\mathrm{M}}{\partial V} + g_{\mathrm{sb}}, \tag{8.2.5.20}$$

where g_{sb} is an integration constant with $\partial g_{\mathrm{sb}}/\partial\zeta_0 = 0$. To determine g_{sb}, the constraint equation of equation (8.2.5.17) is solved so that $f_{01,2}$ is periodic. For superbananas, g_{sb} vanishes, i.e. $g_{\mathrm{sb}} = 0$, because of the reflection boundary condition at the turning points and $\partial g_{\mathrm{sb}}/\partial\zeta_0 = 0$. To determine g_{sb} for circulating bananas, an explicit form for the collision operator is needed.

The approximate collision operator in equation (8.1.13) is appropriate for $\langle C(f_{01,1})\rangle_\mathrm{b}$ in equation (8.2.5.17). Changing variable from k to ω_{tb}, and expressing it in terms of $\hat{k}$ yield

$$\left\langle C(f_{01,1})\right\rangle_\mathrm{b} \approx \frac{\nu_\mathrm{D}}{\varepsilon}\left[\frac{E(k)}{K(k)} - (1-k^2)\right] \times \left(\frac{\partial\omega_{\mathrm{tb}}}{\partial k^2}\right)^2 \frac{\omega_{\mathrm{tb}}}{\hat{k}\hat{\omega}_{\mathrm{tb}}^2}\frac{\partial}{\partial\hat{k}}\frac{\omega_{\mathrm{tb}}}{\hat{k}\hat{\omega}_{\mathrm{tb}}^2}\frac{\partial f_{01,1}}{\partial\hat{k}}. \tag{8.2.5.21}$$

The physical meaning is that the dominant effect of collisions is to scatter particles across the boundary marked by

$\omega_{tb} \approx \omega_0 \approx 0$. The effective collision frequency deduced from equation (8.2.5.21) scales as $\nu_D/(\delta B/B_0)$.

Substituting $f_{01,1}$ in equation (8.2.5.20) into the constraint equation for equation (8.2.5.17), i.e. $\oint d\zeta_0 \langle C(f_{01,1})\rangle_b/\omega_{tb} = 0$, yields

$$\frac{\partial g_{sb}}{\partial \hat{k}} = C_g \frac{\hat{k}\hat{\omega}_{tb}^2}{\langle \omega_{tb}\rangle_{\zeta_0}}, \tag{8.2.5.22}$$

where C_g is an integration constant, and $\langle A\rangle_{\zeta_0} = \oint d\zeta_0 A/2\pi$. The constant C_g is determined from the condition that $\partial f_{01,1}/\partial \hat{k} \to 0$ as $\hat{k} \to \infty$. Thus,

$$\frac{\partial f_{01,1}}{\partial \hat{k}} = -\frac{\hat{k}\hat{\omega}_{tb}^2}{\omega_0'}\left(\frac{1}{\omega_{tb}} - \frac{H(\hat{k}-1)}{\langle \omega_{tb}\rangle_{\zeta_0}}\right)\frac{\partial f_M}{\partial V}, \tag{8.2.5.23}$$

where $H(\hat{k}-1)$ is the step function. There is a boundary layer between the trapped and circulating bananas in the vicinity of $\hat{k} = 1$. This leads to a modification to the transport fluxes and the plasma viscosity that scales as $\sqrt{\nu}$. Such a modification is neglected here. With $\partial f_{01,1}/\partial \hat{k}$, the transport fluxes in the superbanana regime can be calculated.

The transport fluxes must be radially averaged besides the usual flux surface average because the width of the orbits is finite as discussed in section 6. Thus, the particle flux is defined as

$$\langle \Gamma \cdot \nabla V\rangle_V = \left\langle \int d\boldsymbol{v} f \boldsymbol{v}_d \cdot \nabla V \right\rangle_V, \tag{8.2.5.24}$$

where the angular brackets denote both the flux surface and the radial averages:

$$\langle A\rangle_V = \int \frac{dV}{\Delta V}\int \frac{d\theta}{2\pi}\int \frac{d\zeta}{2\pi} A. \tag{8.2.5.25}$$

Expressing the particle flux in terms of the collision operator and using $\partial f_{01,1}/\partial \hat{k}$ given in equation (8.2.5.23) yield [224]

$$\Gamma_{sb}^{na} = -\frac{8\sqrt{2}}{\pi^{3/2}}\frac{N\nu_t}{\varepsilon}\sqrt{\delta B/B_0}\left[\eta_1\left(\frac{p'}{p} + \frac{e\Phi'}{T}\right) + \eta_2\frac{T'}{T}\right], \tag{8.2.5.26}$$

and

$$\frac{q_{sb}^{na}}{T} = -\frac{8\sqrt{2}}{\pi^{3/2}}\frac{N\nu_t}{\varepsilon}\sqrt{\delta B/B_0}\left[\eta_2\left(\frac{p'}{p} + \frac{e\Phi'}{T}\right) + \eta_3\frac{T'}{T}\right], \tag{8.2.5.27}$$

where the coefficients η_j for $j = 1$–3 are defined as

$$\eta_j = \int_{x_{min}}^{\infty} dx \frac{\nu_D}{\nu_t} x^2 \left(x^2 - \frac{5}{2}\right)^{j-1} e^{-x^2} \frac{\sqrt{\varepsilon}}{\sqrt{\delta B/B_0}} I_k \times \left\{\left[E(k) - (1-k^2)K(k)\right]\left|\frac{\partial \omega_0}{\partial k^2}\right|\frac{\hat{\omega}_{tb}}{(\partial\omega_0/\partial V)^2}\right\}, \tag{8.2.5.28}$$

and all terms inside the curly brackets are evaluated at $\omega_0 = 0$. Specifically, k^2 is determined from $\omega_0 = 0$ equation in terms of the energy and the radial electric field. After that, the energy integral is performed. The pitch angle integral I_k appeared in equation (8.2.5.28) is defined as

$$I_k = \int_0^{\infty} d\hat{k}\left[\hat{k}\left(\left\langle\frac{\hat{\omega}_{tb}}{|\omega_{tb}|}\right\rangle_{\zeta_0} - H\frac{\hat{\omega}_{tb}}{\langle|\omega_{tb}|\rangle_{\zeta_0}}\right)\right], \tag{8.2.5.29}$$

where $|\hat{\omega}_{tb}/\omega_{tb}| = 1/\sqrt{\hat{k}^2 - F(\zeta_0)}$.

The transport fluxes in the superbanana regime can be understood as follows. The superbanana orbit width scales as

$$(\Delta r)_{sb} \sim r\sqrt{(\delta B/B)/\varepsilon}, \tag{8.2.5.30}$$

which only depends on the geometry. Strong magnetic field strength cannot reduce the step size. The fraction of superbananas is estimated to be $f_{sb} \sim \sqrt{(\delta B/B)}$. Thus, the scaling for the transport coefficients is [3, 224]

$$D \sim \nu\frac{\sqrt{(\delta B/B)}}{\varepsilon}r^2, \tag{8.2.5.31}$$

which can be significant even for small $\delta B/B$. It should be noted that superbananas discussed here are an ideal rendition of the real orbit trajectories, which can be more complicated. However, superbanana transport scaling becomes relevant to plasma confinement when the tips of the superbananas exist inside the confined region because they experience the largest radial drift in the vicinity of those tips.

It should be emphasized that the same transport fluxes in the superbanana plateau regime can also obtained by solving equation (8.2.5.13) as demonstrated in [230]. By including the radial motion in the theory, the mirror like force that pulls the drift orbits back from the resonance positions in the phase space becomes explicit. Neglecting the mirror like force sets the lower bound in the collision frequency domain for the superbanana plateau regime.

8.2.6. Approximate analytic expression for neoclassical toroidal plasma viscosity. The results presented in sections 8.2.1–8.2.5 are the asymptotic limits for not only the transport fluxes but also the neoclassical toroidal viscosity from the flux–force relation in section 4. Knowing these limits a formula that joins all of them together can be constructed. There is only one requirement for the formula that is that it reproduces all the analytic asymptotic expressions in the appropriate limits. The rational approximation inside the energy integral that has been used to join neoclassical transport fluxes in tokamaks and stellarators is adopted [6, 7, 105, 231].

Three non-resonant regimes, namely, $1/\nu$, collisional boundary layer ν–$\sqrt{\nu}$, and collisionless detrapping/retrapping ν regimes are joined by defining energy dependent kernels for these regimes [218],

$$k_{1/\nu} = \frac{\varepsilon}{\nu_D} I_{1/\nu}, \tag{8.2.6.1}$$

$$k_{\nu-\sqrt{\nu}} = \frac{\nu_t}{\varepsilon}\left(\frac{\chi'}{c\Phi'}\right)^2\frac{\nu_D}{\nu_t}\int_0^1 dk^2\left[E(k) - \left(1-k^2\right)K(k)\right] \times \sum_n\left(\hat{\alpha}_n^2 + \hat{\beta}_n^2\right) \tag{8.2.6.2}$$

and

$$k_\nu = \frac{8\nu_D}{\left(c\Phi'/\chi'\right)^2}(\delta B/B)_M. \tag{8.2.6.3}$$

The deflection frequency $\nu_D = \nu_D^{ii}$ for ions and $\nu_D = \nu_D^{ee} + \nu_D^{ei}$ for electrons. The logarithmic function $\ln\left(16/\sqrt{\nu_{*d}}\right)$, causing unphysical result in the transition region between the collisional boundary layer regime and the $1/\nu$ regime when $\nu_{*d} \gg 1$, is modified to $\ln\left[16/\sqrt{\nu_{*d}/(1+\nu_{*d})}\right]$ [218]. The reason for this approximation is that the slope in $\ln\nu$ at the

transition region is determined by the asymptotic limit, which can be extrapolated to the transition region. This is a proper procedure as evidenced by the excellent agreement between the connection formula and the numerical results shown in [219].

The factor F_b in $\hat{\alpha}_n^2$ and $\hat{\beta}_n^2$ is modified slightly to accommodate the possible singularity in the expression. The modified form is [221]

$$F_b = \frac{x_{min}^2\left\{x_{min}^2 - \sigma_{e\Phi'}x^2\left[2E(k)/K(k)-1\right]\right\}}{\left\{x_{min}^2 - \sigma_{e\Phi'}x^2\left[2E(k)/K(k)-1\right]\right\}^2 + \left(\Delta k^2\right)^2}, \tag{8.2.6.4}$$

where Δk^2 is the width of the layer for the superbanana plateau resonance and can be approximated as $\Delta k^2 \approx \hat{\nu}^{1/3}$ defined in equation (8.2.4.1.12).

Using these kernels, a single expression that joins three non-resonant regimes to obtain the flux surface averaged non-resonant particle flux Γ_{non} is [218]

$$\Gamma_{non} = -N\frac{\varepsilon^{1/2}}{4\sqrt{2}\pi^{3/2}}\left(\frac{Mc}{e\chi'}\right)^2 v_t^4 \times\left[\lambda_1\left(\frac{p'}{p}+\frac{e\Phi'}{T}\right)+\lambda_2\frac{T'}{T}\right], \tag{8.2.6.5}$$

and the corresponding Onsager symmetric heat flux q_{non} is

$$\frac{q_{non}}{T} = -N\frac{\varepsilon^{1/2}}{4\sqrt{2}\pi^{3/2}}\left(\frac{Mc}{e\chi'}\right)^2 v_t^4 \times\left[\lambda_2\left(\frac{p'}{p}+\frac{e\Phi'}{T}\right)+\lambda_3\frac{T'}{T}\right], \tag{8.2.6.6}$$

where for j =1–3

$$\lambda_j = \int_0^{x_{min}} dx x^6\left(x^2-\frac{5}{2}\right)^{j-1} e^{-x^2} \times\frac{k_{\nu-\sqrt{\nu}}}{\left(1+k_{\nu-\sqrt{\nu}}/k_\nu\right)\left(1+k_{\nu-\sqrt{\nu}}/k_{1/\nu}\right)}. \tag{8.2.6.7}$$

Note that the upper limit of the energy integral is x_{min}, which is unambiguously defined in equation (8.2.2.18). The reason for the limit is because only normalized energy less than x_{min} can participate in the non-resonant transport processes.

The resonant transport fluxes, including superbanana plateau and superbanana regimes, are also joined in the same way. However, because the $1/\nu$ regime is the collisional end of the superbanana plateau regime, it should also be included in the single expression for the resonant transport fluxes. Two kernels for the superbanana plateau regime k_{sb-p} and the superbanana regime k_{sb} can be defined and they are [66]

$$k_{sb-p} = \frac{8\pi}{\varepsilon'\frac{cM}{|e|\chi'}v_t^2 x}\left\{\frac{\left[1-e^{-(1-k_r^2)/\hat{\nu}^{1/3}}\right]}{\left|dG/dk_r^2\right|}+C_{p1}e^{-(1-k_r^2)/\hat{\nu}^{1/3}}\right\} \times K(k_r)\sum_n |n|(\alpha_n^2+\beta_n^2)|_{k_r} \tag{8.2.6.8}$$

for $0.827 \leqslant k^2 \leqslant 1$,

$$k_{sb-p} = \frac{8\pi}{\varepsilon'\frac{cM}{|e|\chi'}v_t^2 x}C_{p0}K(k_r)\sum_n |n|(\alpha_n^2+\beta_n^2)|_{k_r} \tag{8.2.6.9}$$

for $0 \leqslant k_r^2 \leqslant 0.827$, and

$$k_{sb} = \frac{64}{\varepsilon}\left(\frac{e\chi'}{Mcv_t^2 x}\right)^2 \nu_D I_k\left\{\left[E(k)-(1-k^2)K(k)\right] \times\left|\frac{\partial\omega_0}{\partial k^2}\right|\frac{\hat{\omega}}{(\partial\omega_0/\partial V)^2}\right\}. \tag{8.2.6.10}$$

Of course, quantities inside the curly brackets and I_k should be evaluated at $\omega_0 = 0$ as indicated in the theory for the transport fluxes in the superbanana regime.

Using the same rational approximation procedure, a single expression for the flux surface averaged resonant particle flux Γ_{res} is [218]

$$\Gamma_{res} = -N\frac{\varepsilon^{1/2}}{4\sqrt{2}\pi^{3/2}}\left(\frac{Mc}{e\chi'}\right)^2 v_t^4 \times\left[\lambda_1\left(\frac{p'}{p}+\frac{e\Phi'}{T}\right)+\lambda_2\frac{T'}{T}\right], \tag{8.2.6.11}$$

and the Onsager symmetric resonant heat flux q_{res} is

$$\frac{q_{res}}{T} = -N\frac{\varepsilon^{1/2}}{4\sqrt{2}\pi^{3/2}}\left(\frac{Mc}{e\chi'}\right)^2 v_t^4 \times\left[\lambda_2\left(\frac{p'}{p}+\frac{e\Phi'}{T}\right)+\lambda_3\frac{T'}{T}\right], \tag{8.2.6.12}$$

where for j = 1–3

$$\lambda_j = \int_{x_{min}}^{\infty} dx x^6\left(x^2-\frac{5}{2}\right)^{j-1} e^{-x^2} \times\frac{k_{sb-p}}{\left(1+k_{sb-p}/k_{sb}\right)\left(1+k_{sb-p}/k_{1/\nu}\right)}. \tag{8.2.6.13}$$

The lower limit for the energy integral is x_{min} because only particles with energy higher than x_{min} can contribute to the resonant transport processes. In the collisional limit of the resonant transport fluxes, the asymptotic limit of the $1/\nu$ regime is reproduced. The interval of the energy integral in the collisional limit of the combined resonant and non-resonant fluxes is from 0 to ∞ as expected to reproduce the asymptotic limit of the $1/\nu$ regime.

The overall flux surface averaged transport fluxes, and thus neoclassical toroidal plasma viscosity, derived from the solutions of the bounce averaged drift kinetic equation, are the sum of both the resonant and the non-resonant transport fluxes, i.e. [218]

$$\Gamma = \Gamma_{non} + \Gamma_{res} \tag{8.2.6.14}$$

and

$$\frac{q}{T} = \frac{q_{non}}{T} + \frac{q_{res}}{T}. \tag{8.2.6.15}$$

Because typical magnitude for the perturbed fields $\delta B/B$ resulting from the error fields or MHD activities is of the order of 10^{-3} or smaller in experiments, the collisionless detrapping/retrapping regime and the superbanana regime are not usually accessible for most tokamak plasmas. In that case, one could choose to neglect both of these regimes and simplify equations (8.2.6.14) and (8.2.6.15) by setting quantities $\left(1+k_{\nu-\sqrt{\nu}}/k_\nu\right)$ in equation (8.2.6.7) and $\left(1+k_{sb-p}/k_{sb}\right)$ in equation (8.2.6.13) to unity. These simplified analytic expressions reproduce the asymptotic limits accurately as shown in [229].

The accuracy of the connection formula can be further improved by determining the layer widths in the theories for the collisional boundary layer and superbanana plateau resonance using iterative procedures following their definitions as is done in [229].

8.2.7. Implications on the modelling of toroidal flow and steady-state intrinsic toroidal flow. The non-axisymmetric particle flux $\Gamma^{\rm na}$ is proportional to the toroidal plasma viscosity $\langle \boldsymbol{B}_{\rm t}\cdot\nabla\cdot\overleftrightarrow{\pi}\rangle$ from the flux–force relation in equation (4.1.1.6). Thus, it can be responsible for the toroidal flow damping observed in experiments when the perturbed magnetic field strength is of the order of 10^{-4} or larger.

Except in the $1/\nu$ regime, the transport fluxes depend on the radial electric field non-linearly. The resonant transport fluxes decrease exponentially when the magnitude of the radial electric field increases. The non-resonant transport fluxes, on the other hand, decrease algebraically. These non-linear dependences can cause the toroidal momentum equation to have bifurcated solutions for the radial electric field [208], as demonstrated in [229].

The steady-state solution of the toroidal momentum equation determines the radial electric field that makes plasmas ambipolar. If the ion particle flux dominates, the radial electric field is negative and is [208], approximately,

$$\left(\frac{p_{\rm i}'}{p_{\rm i}}+\frac{e_{\rm i}\Phi'}{T_{\rm i}}\right)=-\frac{\eta_{2i}}{\eta_{1i}}\frac{T_{\rm i}'}{T_{\rm i}}. \tag{8.2.7.1}$$

The radial electric field is positive when the electron particle flux dominates and is approximately [208]

$$\left(\frac{p_{\rm e}'}{p_{\rm e}}+\frac{e_{\rm e}\Phi'}{T_{\rm e}}\right)=-\frac{\eta_{2e}}{\eta_{1e}}\frac{T_{\rm e}'}{T_{\rm e}}. \tag{8.2.7.2}$$

When electron and ion particle fluxes are comparable, there can be multiple solutions just like the bifurcated solutions in the L–H transition theory.

The thermodynamic forces can also be expressed in terms of the components of the plasma flows. Using the radial force balance equations in the Hamada coordinates [208]

$$\left(\frac{p'}{p}+\frac{e\Phi'}{T}\right)=-\frac{e}{cT}\left(\chi' V^{\zeta}-\psi' V^{\theta}\right) \tag{8.2.7.3}$$

all the transport fluxes presented in sections 8.2 can be expressed in terms of the components of flow velocity. The existence of the ambipolar radial electric field implies a steady-state intrinsic toroidal flow. The poloidal flow V^{θ} can be determined from the parallel component of the momentum equation as shown in section 6. The intrinsic steady-state toroidal flow is, when ion viscous force dominates [208],

$$V^{\zeta}=qV^{\theta}+\frac{\eta_{2i}}{\eta_{1i}}\frac{cT_{\rm i}}{e_{\rm i}\chi'}\frac{T'}{T_{\rm i}}. \tag{8.2.7.4}$$

When electron viscous force dominates, V^{ζ} can reverse the direction and becomes [208]

$$V^{\zeta}=qV^{\theta}+\frac{\eta_{2e}}{\eta_{1e}}\frac{cT}{e_{\rm e}\chi'}\frac{T_{\rm e}'}{T_{\rm e}}+\frac{P'}{Ne_{\rm e}\chi'}. \tag{8.2.7.5}$$

In between these two limits, the toroidal flow can have bifurcated solutions. The magnitude of the intrinsic steady-state toroidal flow is of the order of $v_{\rm t}\rho_{\rm pi}/L_n$ [208], which is the same as that determined from the residual stress discussed in section 7.

From the flux–force relation, the transport fluxes derived from the bounce averaged drift kinetic equation can be employed in modelling the toroidal flow damping when there are error fields or MHD activities present in tokamaks. This can be accomplished when the neoclassical toroidal plasma viscosity is implemented in the NCLASS code [89].

8.3. Neoclassical toroidal plasma viscosity derived from the drift kinetic equation

When $\nu_*>1$, the collision frequency is high enough to interrupt collisionless orbits, the proper equation to solve for the neoclassical plasma viscosity is the drift kinetic equation shown in equation (6.4.6). There are two regimes in this limit. One is the Pfirsch–Schlüter regime and the other is the plateau regime. The plateau regime is the resonance between the parallel particle motion $v_{||}\boldsymbol{n}$ and the $\left(V_{||}n+V_E\right)$. The results of these two regimes can be unified with a judiciously chosen collision frequency in the Krook model [135].

In the limit of $\nu_*<1$, the toroidal drift frequency can resonate either with the bounce frequency of the trapped particles [232–236], or with the transit frequency of the circulating particles [236]. These resonances result in a toroidal viscosity that is independent of the collision frequency similar to that in the plateau regime. The magnitude is also similar. Theory for the superbanana formation and its transport consequences for the resonance between the bounce frequency and the toroidal drift frequency has also been developed in detail in [233, 234], and a superbanana transport scaling similar to D in equation (8.2.5.31) has been obtained.

8.3.1. Plateau–Pfirsch–Schlüter regime. The perturbed distribution function in this regime can be obtained by solving equation (6.4.6) with a Krook model, where the collision frequency ν_T is chosen to be $\nu_T=3\nu_{\rm D}+\nu_E$. The resultant components of the viscous forces in Hamada coordinates are [135]

$$\left\langle B_{\rm p}\cdot\nabla\cdot\overleftrightarrow{\pi}\right\rangle=\frac{\sqrt{\pi}}{4}NMv_{\rm t}B \times\left\{\sum_{m,n}\left[I_{mn}^{(1)}\left(b_{mnc}^2+b_{mns}^2\right)m\left(mV^{\theta}-nV^{\zeta}\right)\right] +\sum_{m,n}\left[I_{mn}^{(2)}\left(b_{mnc}^2+b_{mns}^2\right)m\frac{2}{5p}\left(mq^{\theta}-nq^{\zeta}\right)\right]\right\}, \tag{8.3.1.1}$$

$$\left\langle \boldsymbol{B}_{\rm t}\cdot\nabla\cdot\overleftrightarrow{\pi}\right\rangle=\frac{\sqrt{\pi}}{4}NMv_{\rm t}B \times\left\{\sum_{m,n}\left[I_{mn}^{(1)}\left(b_{mnc}^2+b_{mns}^2\right)(nq)\left(-mV^{\theta}+nV^{\zeta}\right)\right] +\sum_{m,n}\left[I_{mn}^{(2)}\left(b_{mnc}^2+b_{mns}^2\right)(nq)\frac{2}{5p}\left(-mq^{\vartheta}+nq^{\zeta}\right)\right]\right\}, \tag{8.3.1.2}$$

and

$$\left\langle \boldsymbol{B}\cdot\nabla\cdot\overleftrightarrow{\pi}\right\rangle=\frac{\sqrt{\pi}}{4}NMv_{\rm t}B \times\left\{\sum_{m,n}\left[I_{mn}^{(1)}\left(b_{mnc}^2+b_{mns}^2\right)(m-nq)\left(mV^{\theta}-nV^{\zeta}\right)\right] +\sum_{m,n}\left[I_{mn}^{(2)}\left(b_{mnc}^2+b_{mns}^2\right)(m-nq)\frac{2}{5p}\left(mq^{\theta}-nq^{\zeta}\right)\right]\right\}, \tag{8.3.1.3}$$

where $R_{mn} = \nu_T/[(m\omega_\theta - n\omega_\zeta)^2 + \nu_T^2]$, $\omega_\theta = (v_{||} + V_{||})\chi'/B + \boldsymbol{V}_E \cdot \nabla\theta$, $\omega_\zeta = (v_{||} + V_{||})\psi'/B + \boldsymbol{V}_E \cdot \nabla\zeta$, and

$$I_{mn}^{(j)} = (2/\pi)\int_0^\infty \mathrm{d}x x^5 \mathrm{e}^{-x^2}\left(x^2 - 5/2\right)^{j-1} \times \int_{-1}^{1} \mathrm{d}y \left(1 - 3y^2\right)^2 \left(v\chi'/B\right) R_{mn}, \quad (8.3.1.4)$$

for $j = 1$ and 2. The expressions for $\langle \boldsymbol{B}_\mathrm{p} \cdot \nabla \cdot \overleftrightarrow{\Theta} \rangle$, $\langle \boldsymbol{B}_\mathrm{t} \cdot \nabla \cdot \overleftrightarrow{\Theta} \rangle$ and $\langle \boldsymbol{B} \cdot \nabla \cdot \overleftrightarrow{\Theta} \rangle$ are the same as the corresponding viscous forces except replacing $I_{mn}^{(1)}$ by $I_{mn}^{(2)}$ and $I_{mn}^{(2)}$ by $I_{mn}^{(3)}$, with $I_{mn}^{(3)}$ is defined in equation (8.3.1.4) with $j = 3$. The non-linear viscous forces in equations (8.3.1.1)–(8.3.1.4) are valid for an arbitrary magnetic field spectrum in a doubly periodic torus, including stellarators. It should be emphasized that the mirror force terms for all modes are neglected by the definition for the plateau resonances.

It is important to note that the upper limit for the energy integral in $I_{mn}^{(j)}$ is ∞. This indicates that $I_{mn}^{(j)}$ is the asymptotic limit of the plateau–Pfirsch–Schlüter regime. For practical applications, it is often chosen to limit the upper limit to $(\nu_*^{(mn)_m})^{1/4}$, where $\nu_*^{mn} = \nu Rq/(v_\mathrm{t}\varepsilon_{mn}^{3/2}|m - nq|)$ and $\nu_*^{(mn)_m}$ is the minimum value of ν_*^{mn} for all (m, n) modes [237]. Thus, for particles with normalized energy $x^2 < (\nu_*^{(mn)_m})^{1/2}$ are in the plateau–Pfirsch–Schlüter regime; while particles with $x^2 > (\nu_*^{(mn)_m})^{1/2}$ are in the low collisionality regime for that particular (m, n) mode. This is an approximation to model a torus with complicated magnetic field spectrum.

The components of the viscous forces are a non-linear function of the radial electric field. The generic dependence on the radial electric field is similar to that in the non-linear plasma viscosity for the axisymmetric tokamaks. The only possible difference is that as the magnitude of the radial electric field increases, viscous forces can have more than one local maximum as demonstrated in [238]. They can have several local maxima and minima depending on the magnetic field spectra. This can lead to bifurcated solution for the radial electric field.

8.3.2. Bounce-transit and drift resonance. When $\nu_* < 1$, either the bounce frequency of the trapped particles or the transit frequency of the circulating particles can resonate with the toroidal drift frequency. The physics of bounce and drift resonance on plasma transport has been discussed for tandem mirrors [232]. The resonance between the bounce frequency and toroidal drift frequency has been found to enhance transport loses for energetic particles in rippled tokamaks [233, 234]. The theory includes not only the superbanana plateau like scaling but also the superbanana like scaling. The same mechanism is used in the context of the theory for neoclassical toroidal plasma viscosity. This leads to the plateau-like neoclassical toroidal plasma viscosity [235, 236]. However, because the bounce averaged toroidal drift frequency is smaller than the bounce-transit frequency by a factor of ρ/L_n, the magnitude of the superbanana plateau fluxes is larger than that resulting from the bounce-transit and drift resonance scaling wise.

The bounce averaged drift kinetic equation cannot describe the resonance between the characteristic frequency of the bounce motion and the toroidal drift frequency. The drift kinetic equation is used for this purpose. The standard approach is to solve the drift kinetic equation by integrating along the unperturbed orbit, i.e. by following the banana orbits [93, 239, 240]. This is Lagrangian in nature. In this approach, only a Krook model can be used when collisional dissipation becomes important. An Eulerian approach is developed to complement the Lagrangian approach [236]. The advantage of the Eulerian approach is that it can treat dissipation using a realistic collision operator. The method can be used to describe transit and drift resonance as well.

The kinetic part of equation (6.4.6) is two dimensional when toroidal symmetry is broken. Changing variables from (θ, ζ) to (θ, ζ_0) in the low collisionality regime yields

$$\left[\left(v_\parallel + V_{||}\right)\boldsymbol{n} + \boldsymbol{V}_E\right] \cdot \nabla h = \left(\frac{v_\parallel + V_{||}}{B}\chi' + \boldsymbol{V}_E \cdot \nabla\theta\right)\frac{\partial h}{\partial\theta} + \frac{c\Phi'}{\chi'}\frac{\partial h}{\partial\zeta_0}. \quad (8.3.2.1)$$

To focus on the bounce-transit and drift resonance, equation (8.3.2.1) is simplified by neglecting $\left(V_{||}\chi'/B + \boldsymbol{V}_E \cdot \nabla\theta\right)$ term. This term is related to the effects of orbit squeezing [110] and the shift of the tips of the bananas to higher energy that leads to non-linear plasma viscosity [135].

The drift kinetic equation to be solved for the bounce-transit and drift resonance is then

$$\frac{v_\parallel}{B}\chi'\frac{\partial h}{\partial\theta} + \frac{c\Phi'}{\chi'}\frac{\partial h}{\partial\zeta_0} - C(h) = 2\frac{v^2}{v_\mathrm{t}^2}\left(\frac{1}{2} - \frac{3}{2}\frac{v_\parallel^2}{v^2}\right) f_M \times \left(\frac{V \cdot \nabla B}{B} - \frac{2}{5}L_1^{(3/2)}\frac{\boldsymbol{q} \cdot \nabla B}{Bp}\right), \quad (8.3.2.2)$$

where magnetic drift is neglected assuming $\varepsilon < 1$.

8.3.2.1. Bounce and Drift Resonance. For the bounce and drift resonance to occur, the two terms in the kinetic part of equation (8.3.2.2) must be comparable. In the Eulerain approach, the Jacobian elliptic function is used in solving equation (8.3.2.2). The parallel particle speed $|v_\parallel|$ can be expressed as

$$|v_\parallel| = 2\sqrt{\frac{\mu B_0\varepsilon}{M}}\left(k^2 - \sin^2\frac{\theta}{2}\right)^{1/2}. \quad (8.3.2.1.1)$$

The pitch angle parameter k^2 is the same as that in equation (8.1.14); for trapped particles, $k^2 < 1$, and for circulating particles, $k^2 > 1$.

For trapped particles, an angle η is defined such that [236]

$$\eta = \frac{\pi}{2K(k)}\int_0^\varphi \frac{\mathrm{d}x}{\left(k^2 - \sin^2 x\right)^{1/2}} = \frac{\pi}{2K(k)} F\left(\sin^{-1}\left(\frac{\sin\varphi}{k}\right), k\right), \quad (8.3.2.1.2)$$

where $F(\phi, k)$ is the elliptic integral of the first kind, and $\varphi = \theta/2$ [241]. When trapped particles complete their full bounce trajectories, i.e. particles make a round trip from one turning point to the other and back, η goes from $-\pi$ to π. Thus, in terms of η, trapped particles are periodic with a period of 2π. Using the angle η, the operator $|v_\parallel|\,\partial/\partial\theta$ in equation (8.3.2.2) can be cast as

$$|v_\parallel|\frac{\partial}{\partial\theta} = \frac{\pi}{2}\sqrt{\frac{\mu B_0\varepsilon}{M}}\frac{1}{K(k)}\frac{\partial}{\partial\eta}. \quad (8.3.2.1.3)$$

The magnetic field variations also need to be expressed in terms of η. Using Fourier series, $\partial B/\partial\theta$ and $\partial B/\partial\zeta_0$ become

$$\frac{1}{B}\frac{\partial B}{\partial\theta} = -\sum_{m,n} \mathrm{i}(m-nq)\varepsilon_{mn}\mathrm{e}^{\mathrm{i}[(m-nq)\theta+n\zeta_0]} = \sum_{n,l} a_{nl}\mathrm{e}^{\mathrm{i}(l\eta+n\zeta_0)}, \tag{8.3.2.1.4}$$

and

$$\frac{1}{B}\frac{\partial B}{\partial\zeta_0} = -\sum_{m,n} \mathrm{i}n\varepsilon_{mn}\mathrm{e}^{\mathrm{i}[(m-nq)\theta+n\zeta_0]} = \sum_{n,l} b_{nl}\mathrm{e}^{\mathrm{i}(l\eta+n\zeta_0)}. \tag{8.3.2.1.5}$$

The complete θ dependence in $|\boldsymbol{B}|$ spectrum is expanded in terms of the angle η, because the poloidal mode number m is not a good quantum number. Since a_{nl} and b_{nl} are Fourier coefficients of real quantities, $a_{nl} = a^*_{-n-l}$ and $b_{nl} = b^*_{-n-l}$. The $\sin\theta$ term resulting from the equilibrium magnetic field is excluded in equation (8.3.2.1.4) because it only yields the standard transport fluxes and does not contribute to the toroidal plasma viscosity.

In the bounce-drift plateau regime, the role of the collisions is to remove the singularity in the kinetic part of the drift kinetic equation and the details of the collision operator are not important after the momentum conservation property of the collision operator is taken into account. For this reason, the Krook model is adopted, i.e. $C(h) = -\nu h$.

Equation (8.3.2.2) is solved by expanding the perturbed distribution function h as

$$h = \sum_{n,l} h_{nl}\mathrm{e}^{\mathrm{i}(l\eta+n\zeta_0)}, \tag{8.3.2.1.6}$$

where h_{nl}s are Fourier coefficients. For each (n,l) mode, h_{nl} satisfies

$$\mathrm{i}\sigma l\omega_\mathrm{b}h_{nl} + \mathrm{i}n\omega_E h_{nl} + \nu h_{nl} = 2\frac{v^2}{v_\mathrm{t}^2}\left(\frac{1}{2} - \frac{3}{2}\frac{v_\parallel^2}{v^2}\right) f_\mathrm{M} \times \left(a_{nl}D_\theta + b_{nl}D_\zeta\right), \tag{8.3.2.1.7}$$

where $\omega_\mathrm{b} = (\pi/2)\sqrt{\mu B_0\varepsilon/M}\left(\chi'/B\right)[K(k)]^{-1}$, $D_\theta = V^\theta - (2/5)\,L_1^{(3/2)}q^\theta/p$, and $D_\zeta = \boldsymbol{V}\cdot\nabla\zeta_0 - (2/5)\,L_1^{(3/2)}\boldsymbol{q}\cdot\nabla\zeta_0/p$. If bounce average had been performed over the trapped particle trajectory, the driving term D_θ would have been averaged to zero and only D_ζ would have survived as evidenced in the bounce averaged drift kinetic equation discussed in section 8.1. The solution to equation (8.3.2.1.7) is

$$h_{nl} = 2\frac{v^2}{v_\mathrm{t}^2}\left(\frac{1}{2} - \frac{3}{2}\frac{v_\parallel^2}{v^2}\right) f_\mathrm{M}\frac{-\mathrm{i}\left(\sigma l\omega_\mathrm{b} + n\omega_E + \mathrm{i}\nu\right)}{\left(\sigma l\omega_\mathrm{b} + n\omega_E\right)^2 + \nu^2} \times \left(a_{nl}D_\theta + b_{nl}D_\zeta\right), \tag{8.3.2.1.8}$$

which contains both the resonant and non-resonant parts. Only the resonant part contributes to the flux surface averaged transport quantities. The resonant part of h_{nl}, denoted as $h_{nl,r}$, is

$$h_{nl,r} = 2\frac{v^2}{v_\mathrm{t}^2}\left(\frac{1}{2} - \frac{3}{2}\frac{v_\parallel^2}{v^2}\right) f_\mathrm{M}\frac{\nu}{\left(\sigma l\omega_\mathrm{b} + n\omega_E\right)^2 + \nu^2} \times \left(a_{nl}D_\theta + b_{nl}D_\zeta\right). \tag{8.3.2.1.9}$$

Because the transport fluxes are even moments of $v_\parallel$ of the distribution function, an even function $h_{nl,re}$ is defined:

$$h_{nl,re} = \frac{v^2}{v_\mathrm{t}^2}\left(\frac{1}{2} - \frac{3}{2}\frac{v_\parallel^2}{v^2}\right) f_\mathrm{M}\left(a_{nl}D_\theta + b_{nl}D_\zeta\right) \times \left[\frac{\nu}{\left(\sigma l\omega_\mathrm{b} + n\omega_E\right)^2 + \nu^2} + \frac{\nu}{\left(-\sigma l\omega_\mathrm{b} + n\omega_E\right)^2 + \nu^2}\right]. \tag{8.3.2.1.10}$$

Only one term inside the square brackets in $h_{nl,re}$ can resonate for a given set of parameters in the bounce-drift resonance plateau regime. Both terms contribute when all the (n,l) modes are summed. In the asymptotic limit of the bounce-drift resonance plateau regime, i.e. $\nu\to 0$ so that $\nu/\varepsilon < |l|\omega_\mathrm{b}$, $h_{nl,re}$ becomes

$$h_{nl,re} = \pi\frac{v^2}{v_\mathrm{t}^2}\left(\frac{1}{2} - \frac{3}{2}\frac{v_\parallel^2}{v^2}\right) f_\mathrm{M}\left(a_{nl}D_\theta + b_{nl}D_\zeta\right) \times \left[\delta\left(\sigma l\omega_\mathrm{b} + n\omega_E\right) + \delta\left(-\sigma l\omega_\mathrm{b} + n\omega_E\right)\right]. \tag{8.3.2.1.11}$$

Substituting $h_{nl,re}$ into the definitions for the viscous forces yields [236]

$$\left\langle \boldsymbol{B}_\mathrm{t}\cdot\nabla\cdot\overleftrightarrow{\pi}\right\rangle = NM\left\langle B^2\right\rangle \times \left[\mu_{\mathrm{p}1}V^\theta + \mu_{\mathrm{t}1}V^\zeta + \frac{2}{5}\mu_{\mathrm{p}2}\frac{q^\theta}{p} + \frac{2}{5}\mu_{\mathrm{t}2}\frac{q^\zeta}{p}\right], \tag{8.3.2.1.12}$$

and

$$\left\langle \boldsymbol{B}_\mathrm{t}\cdot\nabla\cdot\overleftrightarrow{\Theta}\right\rangle = NM\left\langle B^2\right\rangle \times \left[\mu_{\mathrm{p}2}V^\theta + \mu_{\mathrm{t}2}V^\zeta + \frac{2}{5}\mu_{\mathrm{p}3}\frac{q^\theta}{p} + \frac{2}{5}\mu_{\mathrm{t}3}\frac{q^\zeta}{p}\right], \tag{8.3.2.1.13}$$

where the viscous coefficients are defined as, for $j = 1$–3,

$$\begin{pmatrix}\mu_{\mathrm{p}j}\\ \mu_{\mathrm{t}j}\end{pmatrix} = v_\mathrm{t}\frac{\sqrt{\pi}}{2}\frac{\psi'}{B\chi'} \times \sum_{n,l}\frac{1}{|l|}\int_{x_\mathrm{min}}^\infty \mathrm{d}x 2x^5\mathrm{e}^{-x^2}\frac{K(k_0)}{\pi/2}\frac{(x-5/2)^{j-1}}{\left|\mathrm{d}G_{nl}/\mathrm{d}k_r^2\right|} \times \begin{pmatrix}-\left(a_{nl}b_{-n-l} + q|b_{nl}|^2\right)\\ |b_{nl}|^2\end{pmatrix}_{k_r}, \tag{8.3.2.1.14}$$

and the subscript k_r indicates the quantities are evaluated at the resonant pitch angle k_r for a given energy. The resonant k_r is defined as the zero of the function G determined from the argument of $\delta(s)$ and is

$$G_{nl}(k) = \frac{|n|\,c|}{\chi'}\frac{\left|\Phi'\right|}{|l|\,x\sqrt{\varepsilon}\chi' v_\mathrm{t}}\frac{\sqrt{2}B}{} - \frac{\pi/2}{K(k)}. \tag{8.3.2.1.15}$$

Thus, the resonant pitch angle k_r satisfies

$$G_{nl}(k_r) = 0. \tag{8.3.2.1.16}$$

Because $1 \geqslant (\pi/2)/K(k) \geqslant 0$, equation (8.3.2.1.16) can be satisfied if

$$x \geqslant x_\mathrm{min} = \left(\left|\frac{n}{l}\frac{c\Phi'}{\chi'}\right|\sqrt{\frac{2}{\varepsilon}}\frac{B}{\chi'}\frac{1}{v_\mathrm{t}}\right). \tag{8.3.2.1.17}$$

The $v_\parallel^2/v^2$ factor is neglected in evaluating the viscosity as is appropriate for $\varepsilon < 1$.

8.3.2.2. Transit-drift resonance. The characteristic frequency of the circulating particles can also resonate with the toroidal drift frequency [236]. There is a difference between the non-linear plasma viscosity and the transit-drift resonance viscosity to be discussed in this subsection. In the plateau regime of the non-linear plasma viscosity, the collision frequency is high enough to prevent the particle trapping inside the equilibrium and perturbed magnetic fields from occurring. Thus, the mirror force is neglected completely, and each individual mode is independent from each other. For the transit-drift resonance viscosity only the mirror force of the equilibrium magnetic field is included. The role of the mirror force is to modulate the parallel particle speed of the circulating particles. For circulating particles having $k > 1$, a different angle [236]

$$\xi = \frac{\pi k}{K(1/k)} \int_0^{\varphi} \frac{\mathrm{d}x}{\left(k^2 - \sin^2 x\right)^{1/2}} = \frac{\pi}{K(1/k)} F\left(\varphi, 1/k\right), \tag{8.3.2.2.1}$$

is defined. When a circulating particle goes from $-\pi$ to π, so does ξ. The operator $|v_\parallel|\partial/\partial\theta$ in equation (8.3.2.2) can be written as

$$\left|v_\parallel\right| \frac{\partial}{\partial\theta} = 2\sqrt{\frac{\mu B_0 \varepsilon}{M}} k \frac{\pi/2}{K(1/k)} \frac{\partial}{\partial\xi}. \tag{8.3.2.2.2}$$

Using the same solution procedure for the bounce-drift resonance, the perturbed distribution for circulating particles is

$$h_{nl} = 2\frac{v^2}{v_\mathrm{t}^2}\left(\frac{1}{2} - \frac{3}{2}\frac{v_\parallel^2}{v^2}\right) f_\mathrm{M} \frac{-\mathrm{i}\left(\sigma l \omega_\mathrm{tr} + n\omega_E + \mathrm{i}\nu\right)}{\left(\sigma l \omega_\mathrm{tr} + n\omega_E\right)^2 + \nu^2} \times \left(c_{nl} D_\theta + d_{nl} D_\zeta\right), \tag{8.3.2.2.3}$$

where $\omega_\mathrm{tr} = 2\sqrt{\mu B_0 \varepsilon / M} k \left(\pi/2\right)\left(\chi'/B\right)\left[K(1/k)\right]^{-1}$ is the transit frequency for circulating particles, and c_{nl} and d_{nl} are Fourier coefficients defined as

$$\frac{1}{B}\frac{\partial B}{\partial\theta} = -\sum_{m,n} \mathrm{i}(m - nq)\varepsilon_{mn} \mathrm{e}^{\mathrm{i}[(m-nq)\theta + n\zeta_0]} = \sum_{n,l} c_{nl} \mathrm{e}^{\mathrm{i}(l\xi + n\zeta_0)}, \tag{8.3.2.2.4}$$

and

$$\frac{1}{B}\frac{\partial B}{\partial\zeta_0} = -\sum_{m,n} \mathrm{i}n\varepsilon_{mn} \mathrm{e}^{\mathrm{i}[(m-nq)\theta + n\zeta_0]} = \sum_{n,l} d_{nl} \mathrm{e}^{\mathrm{i}(l\xi + n\zeta_0)}. \tag{8.3.2.2.5}$$

The difference between the solution for the trapped particles and that for the circulating particles is that the bounce frequency ω_b of the trapped particles is replaced by the transit frequency ω_tr of the circulating particles and the Fourier coefficients a_{nl} and b_{nl} are substituted by c_{nl} and d_{nl}.

Only the resonant part of the solution that is even in $|v_\parallel|$ contributes to the flux surface averaged transport quantities, and it is

$$h_{nl,re} = \frac{v^2}{v_\mathrm{t}^2}\left(\frac{1}{2} - \frac{3}{2}\frac{v_\parallel^2}{v^2}\right) f_\mathrm{M}\left(c_{nl} D_\theta + d_{nl} D_\zeta\right) \times \left[\frac{\nu}{\left(\sigma l \omega_\mathrm{tr} + n\omega_E\right)^2 + \nu^2} + \frac{\nu}{\left(-\sigma l \omega_\mathrm{tr} + n\omega_E\right)^2 + \nu^2}\right]. \tag{8.3.2.2.6}$$

Taking $\nu \to 0$ limit, which corresponds to $\nu < |l|\omega_\mathrm{tr}$, yields

$$h_{nl,re} = \frac{v^2}{v_\mathrm{t}^2}\left(\frac{1}{2} - \frac{3}{2}\frac{v_\parallel^2}{v^2}\right) f_\mathrm{M}\left(a_{nl} D_\theta + b_{nl} D_\zeta\right) \times \pi\left[\delta\left(\sigma l \omega_\mathrm{tr} + n\omega_E\right) + \delta\left(-\sigma l \omega_\mathrm{tr} + n\omega_E\right)\right]. \tag{8.3.2.2.7}$$

The transit-drift resonance toroidal plasma viscosity calculated using $h_{nl,re}$ has the same form as those for the bounce-drift resonance except the viscous coefficients are different and they are [236]

$$\begin{pmatrix}\mu_{\mathrm{p}j} \\ \mu_{\mathrm{t}j}\end{pmatrix} v_\mathrm{t}\sqrt{\pi}\frac{\psi'}{B\chi'}\sum_{n,l}\frac{1}{|l|}\int_{x_\mathrm{min}}^{\infty}\mathrm{d}x 2x^5 \mathrm{e}^{-x^2} \times \frac{K\left(1/k_r\right)}{\pi/2}\frac{\left(x - 5/2\right)^{j-1} k_r^2 F(k_r)}{\mathrm{d}H_{nl}/\mathrm{d}(1/k_r^2)} \times \begin{pmatrix} -\left(c_{nl} d_{-n-l} + q\left|d_{nl}\right|^2\right) \\ \left|d_{nl}\right|^2 \end{pmatrix}_{k_r}, \tag{8.3.2.2.8}$$

where

$$H_{nl}(k) = \frac{|n|\, c|\Phi'|}{\chi'}\frac{B}{|l|\sqrt{x}\chi' v_\mathrm{t}} - \frac{\pi/2}{K\left(1/k\right)}\sqrt{\frac{2\varepsilon k^2}{2\varepsilon k^2 + (1 - \varepsilon)}}, \tag{8.3.2.2.9}$$

$$F\left(k_r\right) = \frac{\sqrt{2\varepsilon k_r^2}}{\left[2\varepsilon k_r^2 + (1 - \varepsilon)\right]^{3/2}}\left[\frac{1}{2} - \frac{3}{2}\frac{2\varepsilon k_r^2}{2\varepsilon k_r^2 + (1 - \varepsilon)}\right]^2, \tag{8.3.2.2.10}$$

and

$$x_\mathrm{min} = \left(\left|\frac{n}{l}\frac{c\Phi'}{\chi'}\right|\frac{B}{\chi'}\frac{1}{v_\mathrm{t}}\right). \tag{8.3.2.2.11}$$

The subscript k_r indicates that the quantity is evaluated at k_r which is the zero of the function $H_{nl}(k)$, i.e.

$$H_{nl}\left(k_r\right) = 0. \tag{8.3.2.2.12}$$

The origin of x_min is from the fact that the term involves $K\left(1/k\right)$ in $H_{nl}(k)$ is bounded between 0 and 1 when k varies from 1 to ∞, and to have solution for $H_{nl}\left(k_r\right) = 0$, the dimensionless energy parameter x must be equal or greater than x_min. The $x_\mathrm{min}$for circulating particles shown in equation (8.3.2.2.11) is smaller than that for trapped particles given in equation (8.3.2.1.17) by a factor of $\sqrt{\varepsilon}$. Thus, particles need to have higher energy to have bounce-drift resonance.

The poloidal angle variation in $|v_{||}|$ is neglected when evaluating $\left[(1/2) - (3/2)\left(v_\parallel/v\right)^2\right]$ approximately to obtain viscous coefficients. The terms inside the large square brackets of $F\left(k_r\right)$ are results of such an approximation. The qualitative behaviour of these terms is consistent with the expectation. In the limit, where $k_r \to \infty$ for very circulating particles, the factor $(3/2)\left(v_\parallel/v\right)^2$ approaches (3/2). When $k_r \to 1$, namely, at the trapped-circulating boundary, $(3/2)\left(v_\parallel/v\right)^2$ approaches $(3/2)(2\varepsilon)$ in the large aspect ratio limit.

8.3.2.3. Validity and relation to non-linear plasma viscosity. For trapped particles to contribute to the plasma viscosity in the bounce-drift resonance plateau regime, $\nu/\varepsilon < |l|\omega_\mathrm{b}$. In this asymptotic limit, both trapped particles and circulating particles contribute. When $\nu/\varepsilon > |l|\omega_\mathrm{b}$ but $\nu < |l|\omega_\mathrm{tr}$, only circulating particles contribute to transit-drift resonance. If resonances overlap, particle trajectories in the phase space

become chaotic, and bounce-transit and drift resonance plateau regime persists. If the resonances do not overlap, the bounce-transit and drift resonance plateau regime ends when the closed collisionless non-linear trajectories in the phase space form. This is similar to the superbanana regime [224, 233, 234]. When $\nu > |l|\omega_t$, the plasma viscosity enters the Pfirsch–Schlüter regime [236].

Viscous coefficients for bounce-transit and drift resonance have a similar scaling to that for the non-linear viscosity in the plateau regime, because the physics mechanisms involved are similar. The difference is only in the treatment of the parallel particle speed in the drift kinetic equation. Thus, when the bounce-transit and drift resonance viscosity becomes important, the non-linear plasma viscosity should be important as well.

When the radial electric field vanishes, the resonance occurs at $k_r = 1$ and the neoclassical toroidal plasma viscosity in the bounce-transit and drift resonance plateau regime vanishes in the approximation adopted here. In that case, the superbanana plateau regime becomes important.

8.4. Neoclassical toroidal plasma viscosity in the vicinity of a magnetic island

Symmetry breaking effects in tokamaks are most pronounced in the vicinity of a magnetic island. Because the perturbed magnetic field is perpendicular to the equilibrium magnetic field, the surface distortion mechanism dominates [207]. The magnitude of the perturbed $|\boldsymbol{B}|$ on the island magnetic surface scales as $\sqrt{\delta B/B_0}$. Thus, even for $\delta B/B_0 \sim 10^{-4}$, the symmetry breaking effects are significant. This leads to the enhanced neoclassical plasma viscosity, and the corresponding increases in particle, energy and momentum losses in the vicinity of magnetic islands. The most interesting feature of the enhanced neoclassical plasma viscosity is that it determines a radial electric field in the vicinity of the magnetic islands that can suppress turbulence fluctuations and improve confinement. This provides an explanation as to why plasma confinement is improved in the vicinity of the magnetic island observed in experiments or in the vicinity of the low-order rational surface [207, 242].

8.4.1. $|\boldsymbol{B}|$ on the island magnetic surface. Because transport processes are defined on the magnetic surface, when the magnetic surface is distorted, transport fluxes are calculated on the distorted magnetic surface. In low $\bar{\beta}$ plasmas, the perturbed magnetic field resulting from the magnetic island can be described by the perturbed poloidal flux $\delta\chi = \tilde{\chi}\cos\xi_I$. Here, $\tilde{\chi}$ is the amplitude of the perturbed poloidal flux, $\xi_I = \theta - \zeta/q_s$ for a static magnetic island, and q_s is the safety factor at the rational surface χ_s where the island resides. The island magnetic surface can be described by a helical flux function Ψ, where

$$\Psi = -\frac{q_s'}{2q_s}(\chi - \chi_s)^2 + \tilde{\chi}\cos m\xi_I, \qquad (8.4.1.1)$$

and $q_s' = \mathrm{d}q/\mathrm{d}\chi|_{\chi_s}$ [243]. All the transport fluxes are now defined on the constant Ψ contours.

The $|\boldsymbol{B}|$ on the constant Ψ surface can be obtained from the equilibrium magnetic field $B = B_0(1 - \varepsilon\cos\theta)$ by Taylor expansion of the radial dependence in the vicinity of the magnetic island, i.e.

$$\frac{B}{B_0} = 1 - \left[\frac{r_s}{R} \pm \frac{r_w}{R}\left(\bar{\Psi} + \cos m\xi_I\right)^{1/2}\right]\cos\theta, \qquad (8.4.1.2)$$

where r_s is the minor radius at χ_s, normalized helical flux function $\bar{\Psi} = -\Psi/\tilde{\chi}$, and $r_w = \left[2q_s^2\tilde{\chi}/\left(q_s' B_0 r_s\right)\right]^{1/2}$ is proportional to the island width [207]. The $\pm$ sign in equation (8.4.1.2) is chosen to be '+' for $\chi > \chi_s$ and '−' for $\chi < \chi_s$. In general, for a finite aspect ratio tokamak, $|\boldsymbol{B}|$ on the island magnetic surface can be obtained is

$$B = B_s + (\partial B/\partial\chi_s)(\chi - \chi_s). \qquad (8.4.1.3)$$

8.4.2. Transport fluxes in the vicinity of a magnetic island and implications on plasma confinement. It is most convenient to solve the drift kinetic equation (equation (8.1.1)) in (Ψ, θ, ξ_I) coordinates for the perturbed distribution. For $\nu_* < 1$, the bounce averaged drift kinetic equation is [207]

$$\left(1 - \frac{q}{q_s}\right)\frac{\partial f_{01}}{\partial\xi_I} H(\mu_c - \mu) + \langle \boldsymbol{v}_d\cdot\nabla\xi_I\rangle_b \frac{\partial f_{01}}{\partial\xi_I} + \langle \boldsymbol{v}_d\cdot\nabla\Psi\rangle_b \times\frac{\partial f_{00}}{\partial\Psi} = \langle C(f_{01})\rangle_b, \qquad (8.4.2.1)$$

where $f_{00} = f_M(\Psi)$, f_{01} is the correction to $f_M(\Psi)$, H is the step function, and μ_c is the critical magnetic moment that separates trapped particles from circulating particles.

When the collision frequency is larger than the $\langle \boldsymbol{v}_d\cdot\nabla\xi\rangle_b$, it is in the $1/\nu$ regime. The particle flux in this regime is [207]

$$\Gamma_I^{na} = -\frac{C_I}{2}\frac{(I\boldsymbol{n}\cdot\nabla\theta)^2}{\Omega^2}\left(\frac{q_s'}{q_s}r_w\right)^2 m^2\delta_w^2\varepsilon_s^{3/2}\frac{F_I\left(\bar{\Psi}\right)\sqrt{1+\bar{\Psi}}}{K(k_I)} \times\int \mathrm{d}\bar{w}\frac{\bar{w}^{5/2}}{\nu_D}\frac{\partial f_M}{\partial\bar{\Psi}}, \qquad (8.4.2.2)$$

where $\Gamma_I^{na} = \langle N\boldsymbol{V}\cdot\nabla\Psi\rangle_I$ is the particle flux that is averaged over the island magnetic surface, $C_I = 0.684$, $F_I\left(\bar{\Psi}\right) = \oint \mathrm{d}\xi_I \sin^2 m\xi_I\left(\Delta/\varepsilon_s\right)^{3/2}/\sqrt{\bar{\Psi}+\cos m\xi_I}$, $\Delta = \varepsilon_s \pm \delta_w\sqrt{\bar{\Psi}+\cos m\xi_I}$, $\varepsilon_s = r_s/R$, $\delta_w = r_w/R$, and $k_I^2 = 2/\left(1+\bar{\Psi}\right)$. This flux is valid outside the island separatrix where $k_I^2 < 1$. It is assumed that $\partial f_M/\partial\Psi$ vanishes inside the island. However, this does not have to be the case. The gradients inside the island separatrix can be maintained by good plasma confinement due to turbulence suppression by the steep gradient of the radial electric field.

If both electrons and ions are in the $1/\nu$ regime, $\sum_j \Gamma_{Ij}^{na} = 0$ determines a radial electric field

$$\left(\frac{p_i'}{p_i} + \frac{e_i\Phi'}{T_i}\right) = -2.37\frac{T_i'}{T_i}, \qquad (8.4.2.3)$$

where prime denotes $\mathrm{d}/\mathrm{d}\Psi$. The radial electric field in equation (8.4.2.3) is well known for the $1/\nu$ regime in rippled tokamaks and stellarators [3, 210, 211, 244].

The non-axisymmetric flux Γ_I^{na} in the collisional boundary layer regime has also been calculated [245]. The particle flux from the outer solution has been used to demonstrate that there can be bifurcated states for the radial electric field similar to the L–H transition processes [242]. The resultant radial electric field can suppress turbulence fluctuations and improve plasma confinement according to the turbulence suppression theory in section 7 because it has a scale length of the order of the width of the island.

9. Neoclassical transport theory for stellarators

The $|\boldsymbol{B}|$ spectrum for real stellarators does not possess any symmetry even with modern optimization [27]. In the low collisionality regimes, particle dynamics, especially that of the trapped particles, is crucial to the solution of the linear drift kinetic equation. Particles can be trapped either inside the toroidal magnetic field well or inside one of the many helical magnetic wells as shown in figure 5. Thus, in stellarators there can be at least two or more classes of trapped particles. This makes the development of an analytic transport theory for stellarators in the low collisionality regimes much more difficult. However, in relatively collisional regimes, there are analytic theories for arbitrary magnetic field spectrum at least in the large aspect ratio limit.

Because there does not exist a unique configuration, it is more difficult to develop a neoclassical theory that is valid for all collisionality regimes for all stellarators currently operating around the world. Some of the gross features of the transport consequences of the neoclassical theory, however, might have been observed in all stellarators. One such example is the transition of the radial electric field from a negative value to a positive value when the electron loss rate dominates the ion loss rate as the collision frequency decreases [246–249]. The other is that neoclassical losses can be reduced by manipulating the $|\boldsymbol{B}|$ spectrum in stellarators [249, 250]. When neoclassical theory is applicable, the machine performance is more predictable. The goal here is to discuss the basic physics involved in each asymptotic limit where an analytic treatment is possible. As the collision frequency decreases, the analytic model for $|\boldsymbol{B}|$ becomes simpler and is less able to describe subtler physics.

9.1. Pfirsch–Schlüter regime

In this regime, collisions are frequent enough to dominate the kinetic part in the linear drift kinetic equation. Following the expansion scheme developed for calculating the plasma viscosity in the Pfirsch–Schlüter regime for axisymmetric tokamaks and using $|\boldsymbol{B}| = B(\theta, \zeta)$ yield

$$-2\frac{v^2}{v_t^2}\left(\frac{1}{2}-\frac{3}{2}\frac{v_{||}^2}{v^2}\right)\left(\frac{\boldsymbol{V}\cdot\nabla B}{B}-\frac{2}{5p}L_1^{(3/2)}\frac{\boldsymbol{q}\cdot\nabla B}{B}\right)f_M = C(h). \tag{9.1.1}$$

The difference between equations (9.1.1) and (6.2.3.1) is that besides the θ dependence $|\boldsymbol{B}|$ spectrum also has the ζ dependence in stellarators.

Equation (9.1.1) can be solved either by expanding h in terms of Laguerre and Legendre polynomials or approximating the collision operator by a Krook model, i.e. $C(h) = -\nu_T h$ [7]. The later approach is chosen here to obtain

$$h = 2\nu_T^{-1}\frac{v^2}{v_t^2}\left(\frac{1}{2}-\frac{3}{2}\frac{v_{||}^2}{v^2}\right)\times\left(\frac{\boldsymbol{V}\cdot\nabla B}{B}-\frac{2}{5p}L_1^{(3/2)}\frac{\boldsymbol{q}\cdot\nabla B}{B}\right)f_M. \tag{9.1.2}$$

Substituting h into the definitions for the parallel components of the viscous forces yields

$$\left\langle \boldsymbol{B}\cdot\nabla\cdot\overleftrightarrow{\pi}\right\rangle = NM\left\langle B^2\right\rangle \times\left[\left\langle\frac{\partial B/\partial\theta}{B}\frac{\boldsymbol{B}\cdot\nabla B}{B}\right\rangle\left(\mu_1 V^\theta+\frac{2}{5}\mu_2\frac{q^\theta}{p}\right) +\left\langle\frac{\partial B/\partial\zeta}{B}\frac{\boldsymbol{B}\cdot\nabla B}{B}\right\rangle\left(\mu_1 V^\zeta+\frac{2}{5}\mu_2\frac{q^\zeta}{p}\right)\right] \tag{9.1.3}$$

and

$$\left\langle \boldsymbol{B}\cdot\nabla\cdot\overleftrightarrow{\Theta}\right\rangle = NM\left\langle B^2\right\rangle \times\left[\left\langle\frac{\partial B/\partial\theta}{B}\frac{\boldsymbol{B}\cdot\nabla B}{B}\right\rangle\left(\mu_2 V^\theta+\frac{2}{5}\mu_3\frac{q^\theta}{p}\right) +\left\langle\frac{\partial B/\partial\zeta}{B}\frac{\boldsymbol{B}\cdot\nabla B}{B}\right\rangle\left(\mu_2 V^\zeta+\frac{2}{5}\mu_3\frac{q^\zeta}{p}\right)\right], \tag{9.1.4}$$

where parallel viscous coefficients are

$$\mu_j = \frac{8}{5\sqrt{\pi}}v_t^2\frac{1}{\langle B^2\rangle}\left[\int_0^\infty \mathrm{d}x x^6\left(x^2-\frac{5}{2}\right)^{j-1}\mathrm{e}^{-x^2}\frac{1}{\nu_T}\right], \tag{9.1.5}$$

for $j = 1$–3. The geometric factors can also be absorbed into the definitions of the viscous coefficients, and viscous coefficients become

$$\mu_{jp} = \mu_j\left\langle[(\partial B/\partial\theta)/B]\,[(\boldsymbol{B}\cdot\nabla B)/B]\right\rangle, \tag{9.1.6}$$

and

$$\mu_{jt} = \mu_j\left\langle[(\partial B/\partial\zeta)/B]\,[(\boldsymbol{B}\cdot\nabla B)/B]\right\rangle. \tag{9.1.7}$$

Similarly, the toroidal components of the viscous forces are

$$\left\langle \boldsymbol{B}_t\cdot\nabla\cdot\overleftrightarrow{\pi}\right\rangle = NM\left\langle B^2\right\rangle \times\left[\left\langle\frac{\partial B/\partial\theta}{B}\frac{\boldsymbol{B}_t\cdot\nabla B}{B}\right\rangle\left(\mu_1 V^\theta+\frac{2}{5}\mu_2\frac{q^\theta}{p}\right) +\left\langle\frac{\partial B/\partial\zeta}{B}\frac{\boldsymbol{B}_t\cdot\nabla B}{B}\right\rangle\left(\mu_1 V^\zeta+\frac{2}{5}\mu_2\frac{q^\zeta}{p}\right)\right], \tag{9.1.8}$$

and

$$\left\langle \boldsymbol{B}_t\cdot\nabla\cdot\overleftrightarrow{\Theta}\right\rangle = NM\left\langle B^2\right\rangle \times\left[\left\langle\frac{\partial B/\partial\theta}{B}\frac{\boldsymbol{B}_t\cdot\nabla B}{B}\right\rangle\left(\mu_2 V^\theta+\frac{2}{5}\mu_3\frac{q^\theta}{p}\right) +\left\langle\frac{\partial B/\partial\zeta}{B}\frac{\boldsymbol{B}_t\cdot\nabla B}{B}\right\rangle\left(\mu_2 V^\zeta+\frac{2}{5}\mu_3\frac{q^\zeta}{p}\right)\right]. \tag{9.1.9}$$

In Hamada coordinates, $\boldsymbol{B}_t = \psi'\nabla V\times\nabla\theta$. The poloidal components of the viscous forces have the same forms as the toroidal components except that $\boldsymbol{B}_t$ is replaced by $\boldsymbol{B}_p = \chi'\nabla\zeta\times\nabla V$ in equations (9.1.8) and (9.1.9). The more accurate viscous coefficients obtained by inverting the collision operator can be found in [7, 53, 236]. The components of the viscous force obtained here are the parallel viscosity with coefficient η_0 in terms of Braginskii's classification except that the heat flow is included as an independent variable [1]. The same viscous components are also obtained in [251, 252].

The importance of the components of the viscous forces is that they determine the flow damping and, thus, the steady-state radial electric field and the components of plasma flow velocity in stellarators. The viscous driven particle and heat fluxes are subdominant in this regime for large aspect ratio stellarators.

9.1.1. Plasma flows and radial electric field. Because the radial electric field and parallel flow are neglected in the kinetic part of the kinetic equation, the viscous forces are linear functions of the radial electric field and the parallel flow. The magnitudes of the ion viscous forces are larger than those of electron viscous forces by a factor of $\sqrt{M_\mathrm{i}/M_\mathrm{e}}$. The large aspect ratio assumption is not needed to conclude that $V_{||\mathrm{i}} \approx V_{||\mathrm{e}} \approx V_{||}$, $q_{||\mathrm{i}} \approx 0$ and $q_{||\mathrm{e}} \approx 0$ because the collision frequency is larger than the particle transit frequency for each mode. Thus, the approximate solutions to the parallel momentum and heat flux balance equations yield the common equilibrium parallel flow. From $\sum_j e_j \Gamma_j^{\mathrm{bp}} = 0$, which implies the relaxation of the parallel momentum equation [60, 61],

$$\frac{\langle V_{||} B\rangle}{\langle B^2\rangle} = -G_{\mathrm{ps}} \frac{cT_\mathrm{i}}{e_\mathrm{i}\langle B^2\rangle}\left(\frac{p_\mathrm{i}'}{p_\mathrm{i}} + \frac{e_\mathrm{i}\Phi'}{T_\mathrm{i}} + \frac{\mu_{2\mathrm{i}}}{\mu_{1\mathrm{i}}}\frac{T_\mathrm{i}'}{T_\mathrm{i}}\right), \tag{9.1.1.1}$$

where the geometric factor G_{ps} is

$$G_{\mathrm{ps}} = \frac{\langle (\boldsymbol{n}\cdot\nabla B)\,(1/B)\,\partial B/\partial\theta\rangle}{\langle (\boldsymbol{n}\cdot\nabla B)^2\rangle}\langle \boldsymbol{B}\times\nabla\boldsymbol{V}\cdot\nabla\theta\rangle + \frac{\langle (\boldsymbol{n}\cdot\nabla B)\,(1/B)\,\partial B/\partial\zeta\rangle}{\langle (\boldsymbol{n}\cdot\nabla B)^2\rangle}\langle \boldsymbol{B}\times\nabla\boldsymbol{V}\cdot\nabla\zeta\rangle\,. \tag{9.1.1.2}$$

The geometry factor G_{ps} is valid for tori with arbitrary symmetry property and depends only on the $|\boldsymbol{B}|$ spectrum.

For a classic $|\boldsymbol{B}|$ spectrum for stellarators given in equation (1.2.1) in Hamada coordinates, G_{ps} can be evaluated explicitly and is

$$G_{\mathrm{ps}} = \frac{F}{\chi'}\frac{1 + m\,(m-nq)\,\varepsilon_h^2/\varepsilon_\mathrm{t}^2 + (G/F)\,n\,(m-nq)\,\varepsilon_h^2/\varepsilon_\mathrm{t}^2}{1 + (m-nq)^2\,\varepsilon_h^2/\varepsilon_\mathrm{t}^2}. \tag{9.1.1.3}$$

If $\varepsilon_h = 0$,

$$G_{\mathrm{ps}} = \frac{F}{\chi'}, \tag{9.1.1.4}$$

which is the standard result for axisymmetric tokamaks. If $\varepsilon_\mathrm{t} = 0$, which corresponds to a helically symmetric torus,

$$G_{\mathrm{ps}} = \frac{F}{\chi'}\frac{m + (G/F)\,n}{m - nq}. \tag{9.1.1.5}$$

The direction of the parallel flow reverses when $nq > m$. If $m = 0$, which corresponds to a rippled tokamak,

$$G_{\mathrm{ps}} = \frac{F}{\chi'}\frac{1 - (G/F)\,qn^2\varepsilon_h^2/\varepsilon_\mathrm{t}^2}{1 + (nq)^2\,\varepsilon_h^2/\varepsilon_\mathrm{t}^2}. \tag{9.1.1.6}$$

The direction of $V_{||}$ and the symmetry property of $|\boldsymbol{B}|$ spectrum can be understood in terms of the viscous damping [53]. For simplicity, the heat flow is neglected in the discussion. When the system is toroidally symmetric, parallel viscous forces damp the poloidal flow due to the bumpiness of the magnetic field strength in the poloidal direction. However, the diamagnetic flow, which is perpendicular to the magnetic field, always has a poloidal component. In order for the poloidal component of the flow velocity to vanish, i.e. $V\cdot\nabla\theta = 0$, there must be a parallel flow $V_{||}\boldsymbol{n}$ so that the poloidal component of $V_{||}\boldsymbol{n}$ cancels that of the diamagnetic flow. During the damping processes, the toroidal component of the flow remains approximately constant due to the weakness of the toroidal viscous force when compared with the parallel viscous force.

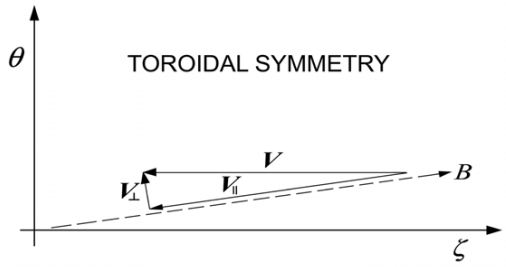

Figure 25. Schematic diagram for plasma flow in a toroidally symmetric torus.

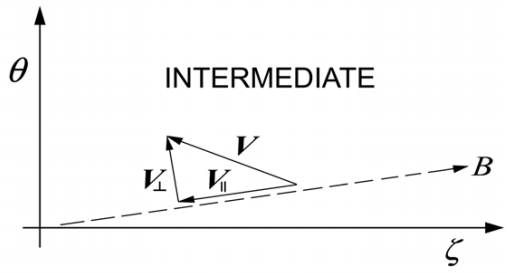

Figure 26. Schematic diagram for plasma flow in a non-axisymmetric torus.

What really happens is that the radial electric field adjusts to make $V\cdot\nabla\theta = 0$, at the same time keeping the toroidal angular momentum constant. A simple physics picture for the process discussed is shown in figure 25.

When the toroidal symmetry is broken, the bumpiness of $|\boldsymbol{B}|$ in the toroidal direction also damps the toroidal component of the flow. In this case, the plasma flows approximately on the constant $|\boldsymbol{B}|$ contour to minimize the viscous damping. This can be seen by casting the viscous forces in the following forms:

$$\left\langle \boldsymbol{B}\cdot\nabla\cdot\overleftrightarrow{\pi}\right\rangle = NM\langle B^2\rangle\mu_1\left\langle\frac{\boldsymbol{B}\cdot\nabla B}{B}\frac{\boldsymbol{V}\cdot\nabla B}{B}\right\rangle, \tag{9.1.1.7}$$

and

$$\left\langle \boldsymbol{B}_\mathrm{t}\cdot\nabla\cdot\overleftrightarrow{\pi}\right\rangle = NM\langle B^2\rangle\mu_1\left\langle\frac{\boldsymbol{B}_\mathrm{t}\cdot\nabla B}{B}\frac{\boldsymbol{V}\cdot\nabla B}{B}\right\rangle, \tag{9.1.1.8}$$

when the heat flow is neglected. This flow pattern in between toroidal and poloidal symmetry is shown in figure 26.

When the toroidal bumpiness increases further so that the torus is almost poloidally symmetric, the plasma can now flow freely in the poloidal direction and the toroidal flow is damped by the viscous forces. In this case, the toroidal component of the diamagnetic flow must be cancelled by the toroidal component of the parallel flow. The resultant parallel flow is in the direction opposite to that of the toroidally symmetric tori and the magnitude of the flow is smaller by a factor of $(B_\mathrm{p}/B)^2$. This process is shown in figure 27.

The toroidal component of the viscous force damps the parallel flow eventually. The issue is if there is a steady-state parallel flow after damping. This is manifest in the solution of the equation for the radial electric field. To completely specify the plasma flow velocity, the radial electric field must also be determined. This is accomplished by setting $\sum_j e_j\Gamma_j^{\mathrm{na}} = 0$

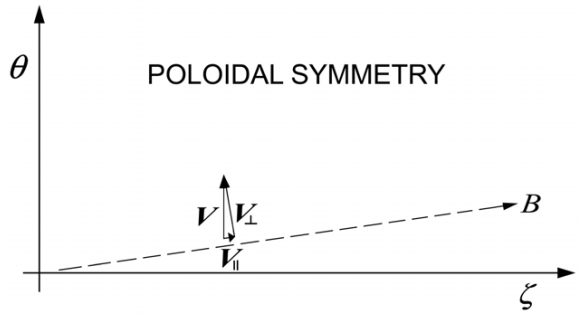

Figure 27. Schematic diagram for plasma flow in a poloidally symmetric torus.

[60, 61]. Because ion viscous coefficients are larger than electron viscous coefficients by a factor of $\sqrt{M_i/M_e}$, the approximate equation for the radial electric field is

$$\left\langle \boldsymbol{B}_t \cdot \nabla \cdot \overleftrightarrow{\pi}_i \right\rangle = 0, \tag{9.1.1.9}$$

and the solution is

$$\frac{p_i'}{p_i} + \frac{e_i \Phi'}{T_i} + \frac{\mu_{2i}}{\mu_{1i}} \frac{T_i'}{T_i} = 0. \tag{9.1.1.10}$$

Thus, at the steady state,

$$\frac{\langle V_{||} B \rangle}{\langle B^2 \rangle} = 0. \tag{9.1.1.11}$$

After the parallel flow $\langle V_{||} B \rangle$ and the radial electric field Φ' are determined, the plasma flow on the magnetic surface is specified completely, or explicitly,

$$V^\theta = -\frac{cT_i F}{e_i \langle B^2 \rangle} \frac{\mu_{2i}}{\mu_{1i}} \frac{T_i'}{T_i}, \tag{9.1.1.12}$$

and

$$V^\zeta = \frac{cT_i G}{e_i \langle B^2 \rangle} \frac{\mu_{2i}}{\mu_{1i}} \frac{T_i'}{T_i}. \tag{9.1.1.13}$$

The components of the residual flow are driven by the temperature gradient. The source of the momentum is the non-cancellation of the particle momenta from neighbouring orbits [194].

9.1.2. Particle and heat fluxes. In this regime, the friction forces driving particle and heat fluxes dominate. Friction forces can be evaluated using a set of more accurate numerical coefficients for this purpose [253]. It is obvious that V^θ and V^ζ do not contribute to the Pfirsch–Schlüter fluxes. Only the diamagnetic flows contribute.

The ambipolar particle flux is, for electron–proton plasmas [6, 253],

$$\Gamma^{ps} = -\left(\frac{c}{e\chi'}\right)^2 p_e M_e \nu_{ei} \left(0.675 \frac{P'}{p_e} - 0.56 \frac{T_e'}{T_e}\right) \times \left(\left\langle \frac{I_h^2}{B^2} \right\rangle - \frac{\langle I_h \rangle^2}{\langle B^2 \rangle}\right), \tag{9.1.2.1}$$

where $P' = p_i' + p_e'$, and $I_h = B \cdot \nabla V \times \nabla \theta$. The electron and ion heat fluxes are

$$\frac{q_e^{ps}}{T_e} = -\left(\frac{c}{e\chi'}\right)^2 p_e M_e \nu_{ei} \left(1.97 \frac{T_e'}{T_e} - 0.56 \frac{P'}{p_e}\right) \times \left(\left\langle \frac{I_h^2}{B^2} \right\rangle - \frac{\langle I_h \rangle^2}{\langle B^2 \rangle}\right), \tag{9.1.2.2}$$

and

$$\frac{q_i^{ps}}{T_i} = -1.13 \left(\frac{c}{e_i \chi'}\right)^2 p_i M_i \nu_{ii} \frac{T_i'}{T_i} \left(\left\langle \frac{I_h^2}{B^2} \right\rangle - \frac{\langle I_h \rangle^2}{\langle B^2 \rangle}\right). \tag{9.1.2.3}$$

The electron particle and heat fluxes are Onsager symmetric.

The bootstrap current and Ware pinch flux in this regime scale as ν^{-2} and are not significant except perhaps in unity aspect ratio stellarators.

9.2. Plateau regime

As discussed in section 6, all plateau regimes are caused by the singularity or the resonance in the kinetic part of the kinetic equation when the mirror force can be neglected [46, 103]. The only difference here is that there are multiple resonances in stellarators because there can be multiple classes of trapped particles. When all modes are in the plateau regimes, compact analytic expressions for transport fluxes can be obtained. It should be emphasized that the mirror forces for all the modes have to be negligible for the analytic theory to be valid. In that case, the equation to be solved is

$$v_{||} \boldsymbol{n} \cdot \nabla h - C(h) = 2 \frac{v^2}{v_t^2} \left(\frac{1}{2} - \frac{3}{2} \frac{v_{||}^2}{v^2}\right) \times \left(\frac{\boldsymbol{V} \cdot \nabla B}{B} - \frac{2}{5p} L_1^{(3/2)} \frac{\boldsymbol{q} \cdot \nabla B}{B}\right) f_M. \tag{9.2.1}$$

Using a Krook model for $C(h) = -\nu h$, equation (9.2.1) can be easily solved to obtain the components of the plasma viscosity in the plateau asymptotic limit [46, 67]

$$\left\langle \boldsymbol{B} \cdot \nabla \cdot \overleftrightarrow{\pi} \right\rangle = NM \langle B^2 \rangle \times \left(\mu_{1p} V^\theta + \mu_{1t} V^\zeta + \frac{2}{5} \mu_{2p} \frac{q^\theta}{p} + \frac{2}{5} \mu_{2t} \frac{q^\zeta}{p}\right), \tag{9.2.2}$$

and

$$\left\langle \boldsymbol{B} \cdot \nabla \cdot \overleftrightarrow{\Theta} \right\rangle = NM \langle B^2 \rangle \times \left(\mu_{2p} V^\theta + \mu_{2t} V^\zeta + \frac{2}{5} \mu_{3p} \frac{q^\theta}{p} + \frac{2}{5} \mu_{3t} \frac{q^\zeta}{p}\right), \tag{9.2.3}$$

where parallel viscous coefficients are

$$\mu_{jp} = \frac{\sqrt{\pi}}{2} C_j \sum_{m,n} \left\langle \frac{\partial B_{mn}}{\partial \theta} \frac{\boldsymbol{B} \cdot \nabla B}{B} \right\rangle \frac{v_t}{B_0 |m\chi' - n\psi'|}, \tag{9.2.4}$$

$$\mu_{jt} = \frac{\sqrt{\pi}}{2} C_j \sum_{m,n} \left\langle \frac{\partial B_{mn}}{\partial \zeta} \frac{\boldsymbol{B} \cdot \nabla B}{B} \right\rangle \frac{v_t}{B_0 |m\chi' - n\psi'|}, \tag{9.2.5}$$

and C_j for $j = 1$–3 is defined in section 6. Similarly, the toroidal components of the viscous forces are

$$\left\langle \boldsymbol{B}_{\rm t}\cdot\nabla\cdot\overleftrightarrow{\pi}\right\rangle = NM\left\langle B^2\right\rangle \times\left(\mu_{1{\rm tp}}V^{\theta}+\mu_{1{\rm tt}}V^{\zeta}+\frac{2}{5}\mu_{2{\rm tp}}\frac{q^{\theta}}{p}+\frac{2}{5}\mu_{2{\rm tt}}\frac{q^{\zeta}}{p}\right), \tag{9.2.6}$$

and

$$\left\langle \boldsymbol{B}_{\rm t}\cdot\nabla\cdot\overleftrightarrow{\Theta}\right\rangle = NM\left\langle B^2\right\rangle \times\left(\mu_{2{\rm tp}}V^{\theta}+\mu_{2{\rm tt}}V^{\zeta}+\frac{2}{5}\mu_{3{\rm tp}}\frac{q^{\theta}}{p}+\frac{2}{5}\mu_{3{\rm tt}}\frac{q^{\zeta}}{p}\right), \tag{9.2.7}$$

where toroidal viscous coefficients are

$$\mu_{j{\rm tp}} = \frac{\sqrt{\pi}}{2}C_j\sum_{m,n}\left\langle\frac{\partial B_{mn}}{\partial\theta}\frac{\boldsymbol{B}_{\rm t}\cdot\nabla B}{B}\right\rangle\frac{v_{\rm t}}{B_0\left|m\chi'-n\psi'\right|}, \tag{9.2.8}$$

and

$$\mu_{j{\rm tt}} = \frac{\sqrt{\pi}}{2}C_j\sum_{m,n}\left\langle\frac{\partial B_{mn}}{\partial\zeta}\frac{\boldsymbol{B}_{\rm t}\cdot\nabla B}{B}\right\rangle\frac{v_{\rm t}}{B_0\left|m\chi'-n\psi'\right|}, \tag{9.2.9}$$

for j =1–3. The magnetic field strength is expressed as $B = B_0[1+\sum_{m,n}B_{mn}(V,\theta,\zeta)]$. The poloidal components of the viscous and heat viscous forces can be easily obtained by taking the difference between the parallel and toroidal components of the forces, i.e. $\langle\boldsymbol{B}_{\rm p}\cdot\nabla\cdot\overleftrightarrow{\pi}\rangle = \langle\boldsymbol{B}\cdot\nabla\cdot\overleftrightarrow{\pi}\rangle - \langle\boldsymbol{B}_{\rm t}\cdot\nabla\cdot\overleftrightarrow{\pi}\rangle$.

Comparing the components of the viscous forces in the Pfirsch–Schlüter regime and those in the plateau regime, it is noted that as the collision frequency decreases, the feature of each individual mode appears. This is because the particle dynamics become important when collisions become less frequent. In the plateau regime, the collision frequency is small enough so that resonance for each individual mode appears in the viscous coefficients.

9.2.1. Plasma flows and radial electric field. From the parallel momentum and heat flux balance equations, the standard results on the parallel flows and heat flows for large aspect ratio tori are still valid, i.e. $V_{||{\rm i}}\approx V_{||{\rm e}}\approx V_{||}$, $q_{||{\rm i}}\approx 0$, and $q_{||{\rm e}}\approx 0$. The reason for this is that friction forces are larger than viscous forces in the electron force balance equations and in the ion heat flux balance equation. This implies that the equilibrium parallel flow is, from $\sum_j e_j\Gamma_j^{\rm bp}=0$, or equivalently, $\sum_j\langle\boldsymbol{B}\cdot\nabla\cdot\overleftrightarrow{\pi}_j\rangle = 0$,

$$\frac{\left\langle V_{||}B\right\rangle}{\left\langle B^2\right\rangle} = -G_{\rm p}\frac{cT_{\rm i}}{e_{\rm i}\left\langle B^2\right\rangle}\left(\frac{p_{\rm i}'}{p_{\rm i}}+\frac{e_{\rm i}\Phi'}{T_{\rm i}}+\frac{\mu_{2{\rm i}}}{\mu_{1{\rm i}}}\frac{T_{\rm i}'}{T_{\rm i}}\right), \tag{9.2.1.1}$$

where $\mu_{2{\rm pi}}/\mu_{1{\rm pi}} = \mu_{2{\rm ti}}/\mu_{1{\rm ti}} = \mu_{2{\rm i}}/\mu_{1{\rm i}} = 1/2$, and the geometric factor $G_{\rm p}$ is

$$G_{\rm p} = \frac{\mu_{1{\rm pi}}\left\langle\boldsymbol{B}\cdot\nabla V\times\nabla\theta\right\rangle+\mu_{1{\rm ti}}\left\langle\boldsymbol{B}\cdot\nabla V\times\nabla\zeta\right\rangle}{\mu_{1{\rm pi}}\boldsymbol{B}\cdot\nabla\theta+\mu_{1{\rm ti}}\boldsymbol{B}\cdot\nabla\zeta}. \tag{9.2.1.2}$$

For classic stellarators,

$$G_{\rm p} = \frac{F}{\chi'}\left[\varepsilon_t^2+m\left(m-nq\right)\varepsilon_h^2/\left|m-nq\right| + (G/F)\,n\left(m-nq\right)\varepsilon_h^2/\left|m-nq\right|\right]\left[\varepsilon_{\rm t}^2+\left|m-nq\right|\varepsilon_h^2\right]^{-1}. \tag{9.2.1.3}$$

The factor $G_{\rm p}$ differs from $G_{\rm ps}$ for classic stellarators because of the resonances in the plateau regime. If $\varepsilon_h = 0$, i.e. an axisymmetric tokamak,

$$G_{\rm p} = \frac{F}{\chi'}. \tag{9.2.1.4}$$

For a helically symmetric torus, $\varepsilon_{\rm t}=0$, and

$$G_{\rm p} = \frac{1}{\chi'}\frac{mF+nG}{m-nq}. \tag{9.2.1.5}$$

Thus, the direction of the parallel flow again reverses if $nq > m$. For a straight bumpy torus, $\varepsilon_{\rm t}=0$, and $m=0$,

$$G_{\rm p} = -\frac{1}{\chi'}\frac{G}{q}. \tag{9.2.1.6}$$

The geometric factor $G_{\rm p}$in a rippled tokamak, i.e. $m=0$, is

$$G_{\rm p} = \frac{F}{\chi'}\frac{\varepsilon_{\rm t}^2-(G/F)\,n\varepsilon_h^2}{\varepsilon_{\rm t}^2+nq\varepsilon_h^2}. \tag{9.2.1.7}$$

The radial electric field determined from $\sum_j e_j\Gamma_j^{\rm na}=0$, i.e. $\sum_j\langle\boldsymbol{B}_{\rm t}\cdot\nabla\cdot\overleftrightarrow{\pi}_j\rangle = 0$, is, approximately,

$$\frac{p_{\rm i}'}{p_{\rm i}}+\frac{e_{\rm i}\Phi'}{T_{\rm i}}+\frac{\mu_{2{\rm i}}}{\mu_{1{\rm i}}}\frac{T_{\rm i}'}{T_{\rm i}} = 0, \tag{9.2.1.8}$$

to the leading order in $\sqrt{M_{\rm e}/M_{\rm i}}$ ordering.

The parallel flow is damped by the toroidal viscous force. The steady-state parallel flow is

$$\frac{\left\langle V_{||}B\right\rangle}{\left\langle B^2\right\rangle} = 0, \tag{9.2.1.9}$$

and the corresponding poloidal and toroidal flows are

$$V^{\theta} = -\frac{cT_{\rm i}F}{e_{\rm i}\left\langle B^2\right\rangle}\frac{\mu_{2{\rm i}}}{\mu_{1{\rm i}}}\frac{T_{\rm i}'}{T_{\rm i}}, \tag{9.2.1.10}$$

and

$$V^{\zeta} = \frac{cT_{\rm i}G}{e_{\rm i}\left\langle B^2\right\rangle}\frac{\mu_{2{\rm i}}}{\mu_{1{\rm i}}}\frac{T_{\rm i}'}{T_{\rm i}}. \tag{9.2.1.11}$$

Thus, the steady-state flows in the plateau regime are similar to those in the Pfirsch–Schlüter regime except the ratio of the viscous coefficients is different. The components of the residual flow are again driven by the ion temperature gradient.

9.2.2. Transport fluxes in the plateau regime and examples. With the knowledge of the components of the viscous forces, and the steady-state plasma flows, the viscous force driven transport fluxes can be then evaluated using the flux–force relation [46].

The ambipolar banana–plateau particle flux $\Gamma_{\rm e}^{\rm bp}$ is

$$\Gamma_{\rm e}^{\rm bp} = -\frac{c^2\left\langle I_h\right\rangle}{e^2\left\langle B^2\right\rangle\chi'}N_{\rm e}M_{\rm e}T_{\rm e} \times\left(\mu_{1{\rm pe}}\left\langle\boldsymbol{B}\cdot\nabla V\times\nabla\theta\right\rangle+\mu_{1{\rm te}}\left\langle\boldsymbol{B}\cdot\nabla V\times\nabla\zeta\right\rangle\right) \times\left(\frac{P'}{p_{\rm e}}+\frac{1}{2}\frac{T_{\rm i}'+ZT_{\rm e}'}{ZT_{\rm e}}\right), \tag{9.2.2.1}$$

and non-axisymmetric particle flux Γ_e^{na} is

$$\Gamma_e^{na} = -\frac{c^2}{e^2\chi'\psi'} N_e M_e \times \left(\mu_{1tpe}\langle \boldsymbol{B}\cdot\nabla V\times\nabla\theta\rangle + \mu_{1tte}\langle \boldsymbol{B}\cdot\nabla V\times\nabla\zeta\rangle\right) \times\left(\frac{P'}{p_e}+\frac{1}{2}\frac{T_i'+ZT_e'}{ZT_e}\right). \quad (9.2.2.2)$$

The total ambipolar particle flux Γ_e is

$$\Gamma_e = \Gamma_e^{bp} + \Gamma_e^{na}. \quad (9.2.2.3)$$

The ion heat fluxes are

$$\frac{q_i^{bp}}{T_i} = -\frac{6c^2\langle I_h\rangle}{e_i^2\langle B^2\rangle\chi'} N_i M_i T_i \times\left(\mu_{2pi}\langle \boldsymbol{B}\cdot\nabla V\times\nabla\theta\rangle + \mu_{2ti}\langle \boldsymbol{B}\cdot\nabla V\times\nabla\zeta\rangle\right)\frac{T_i'}{T_i}, \quad (9.2.2.4)$$

and

$$\frac{q_i^{na}}{T_i} = \frac{6c^2}{e_i^2\chi'\psi'} N_i M_i T_i \times\left(\mu_{2tpi}\langle \boldsymbol{B}\cdot\nabla V\times\nabla\theta\rangle + \mu_{2tti}\langle \boldsymbol{B}\cdot\nabla V\times\nabla\zeta\rangle\right)\frac{T_i'}{T_i}. \quad (9.2.2.5)$$

The electron heat fluxes are

$$\frac{q_e^{bp}}{T_e} = -\frac{c^2\langle I_h\rangle}{e^2\langle B^2\rangle\chi'} N_e M_e T_e\Big(\mu_{2pe}\langle \boldsymbol{B}\cdot\nabla V\times\nabla\theta\rangle + \mu_{2te}\langle \boldsymbol{B}\cdot\nabla V\times\nabla\zeta\rangle\Big) \times\left(\frac{P'}{p_e}+\frac{1}{2}\frac{T_i'+13ZT_e'}{ZT_e}\right), \quad (9.2.2.6)$$

and

$$\frac{q_e^{na}}{T_e} = \frac{c^2}{e^2\chi'\psi'} N_e M_e T_e\Big(\mu_{2tpe}\langle \boldsymbol{B}\cdot\nabla V\times\nabla\theta\rangle + \mu_{2tte}\langle \boldsymbol{B}\cdot\nabla V\times\nabla\zeta\rangle\Big) \times\left(\frac{P'}{p_e}+\frac{1}{2}\frac{T_i'+13ZT_e'}{ZT_e}\right). \quad (9.2.2.7)$$

The total heat flux for each species is

$$\frac{q_j}{T_j} = \frac{q_j^{bp}}{T_j} + \frac{q_j^{na}}{T_j}, \quad (9.2.2.8)$$

where $j = \mathrm{i}$ for ions and $j = \mathrm{e}$ for electrons. The bootstrap current is

$$\langle j_{||b} B\rangle = -\frac{\sigma_s M_e}{N_e e^2} c p_e \left(\mu_{1pe}\langle \boldsymbol{B}\cdot\nabla V\times\nabla\theta\rangle + \mu_{1te}\langle \boldsymbol{B}\cdot\nabla V\times\nabla\zeta\rangle\right) \times\left[\frac{P'}{p_e}\left(1+\frac{l_{12}^e}{l_{22}^e}\frac{\mu_{2e}}{\mu_{1e}}\right)+\frac{1}{2}\frac{T_i'+ZT_e'}{ZT_e} +\frac{1}{2}\frac{l_{12}^e}{l_{22}^e}\frac{\mu_{2e}}{\mu_{1e}}\frac{T_i'+13ZT_e'}{ZT_e}\right]. \quad (9.2.2.9)$$

The Ware pinch flux can be inferred from the bootstrap current because they are Onsager conjugates of each other.

To gain physical insights on the transport fluxes in non-axisymmetric tori, it is helpful to have explicit expressions for these quantities for a classic stellarator using approximate cylindrical coordinates [46]. The ambipolar particle fluxes are

$$\left(\Gamma_e^{bp}\right)_r = -\frac{\sqrt{\pi}}{4} N_e \rho_{pe}^2 \frac{v_{te}}{Rq}\left(\varepsilon_t^2 - m\varepsilon_h^2 - nq\frac{B_p^2}{B_t^2}\varepsilon_h^2\right) \times\left(\frac{P'}{p_e}+\frac{1}{2}\frac{T_i'+ZT_e'}{ZT_e}\right), \quad (9.2.2.10)$$

and

$$\left(\Gamma_e^{na}\right)_r = -\frac{\sqrt{\pi}}{4} N_e \rho_{pe}^2 \frac{v_{te}}{Rq}\left(m+nq\frac{B_p^2}{B_t^2}\right)\left|1-\frac{m}{nq}\right|^{-1}\varepsilon_h^2 \times\left(\frac{P'}{p_e}+\frac{1}{2}\frac{T_i'+ZT_e'}{ZT_e}\right), \quad (9.2.2.11)$$

where the subscript r denotes the quantity is evaluated in (r,θ,ζ) coordinates, $nq > m$ has been used, and prime denote $\mathrm{d}/\mathrm{d}r$ in transport fluxes that have subscripted by r. The total ambipolar particle flux is

$$\left(\Gamma_e^{total}\right)_r = -\frac{\sqrt{\pi}}{4} N_e \rho_{pe}^2 \frac{v_{te}}{Rq} \times\left[\varepsilon_t^2 + \left(\left|1-\frac{m}{nq}\right|^{-1}-1\right)\left(m+nq\frac{B_p^2}{B_t^2}\right)\varepsilon_h^2\right] \times\left(\frac{P'}{p_e}+\frac{1}{2}\frac{T_i'+ZT_e'}{ZT_e}\right). \quad (9.2.2.12)$$

The ambipolar particle fluxes in rippled tokamaks can be obtained by setting $m = 0$. Thus, the total particle flux is the same as that in axisymmetric tokamaks. The toroidal magnetic field ripples have no effect on the total ambipolar particle flux in the plateau regime. The total ion heat flux is

$$\left(\frac{q_i^{total}}{T_i}\right)_r = -\frac{3\sqrt{\pi}}{4} N_i \rho_{pi}^2 \frac{v_{ti}}{Rq} \times\left[\varepsilon_t^2 + \left(\left|1-\frac{m}{nq}\right|^{-1}-1\right)\left(m+nq\frac{B_p^2}{B_t^2}\right)\varepsilon_h^2\right]\frac{T_i'}{T_i}, \quad (9.2.2.13)$$

and the total electron heat flux is

$$\left(\frac{q_e^{total}}{T_e}\right)_r = -\frac{\sqrt{\pi}}{8} N_e \rho_{pe}^2 \frac{v_{te}}{Rq} \times\left[\varepsilon_t^2 + \left(\left|1-\frac{m}{nq}\right|^{-1}-1\right)\left(m+nq\frac{B_p^2}{B_t^2}\right)\varepsilon_h^2\right] \times\left(\frac{P'}{p_e}+\frac{1}{2}\frac{T_i'+13ZT_e'}{ZT_e}\right). \quad (9.2.2.14)$$

The toroidal magnetic field ripples again do not affect the heat transport for both ions and electrons in the plateau regime. The bootstrap current is

$$\left(J_{||b}\right)_r = -\frac{\sigma_s M_e}{N_e e^2} c p_e \frac{v_{te}}{Rq}\frac{2\sqrt{\pi}}{B_p}\left(\varepsilon_t^2 - m\varepsilon_h^2 - nq\frac{B_p^2}{B_t^2}\varepsilon_h^2\right) \times\left[\frac{P'}{p_e}\left(1+\frac{l_{12}^e}{l_{22}^e}\frac{\mu_{2e}}{\mu_{1e}}\right)+\frac{1}{2}\frac{T_i'+ZT_e'}{ZT_e} +\frac{1}{2}\frac{l_{12}^e}{l_{22}^e}\frac{\mu_{2e}}{\mu_{1e}}\frac{T_i'+13ZT_e'}{ZT_e}\right]. \quad (9.2.2.15)$$

The bootstrap current in this regime is smaller than that in the banana regime by a factor of the order of $1/\nu_*$. The $1/\nu$ like scaling is often observed in DKES code results [108] when

the collision frequency decreases so that one mode becomes collisionless and the current increases towards its collisionless value [254]. Just like the parallel flow, the bootstrap current can reverse direction when $m\varepsilon_h^2 > \varepsilon_t^2$ in stellarators. Toroidal magnetic field ripples have little effects on the bootstrap current in this regime.

9.2.3. Additional remarks. The analytic expression for the transport fluxes in this regime are in agreement with the numerical results obtained using the DKES code [108, 255]. However, when not all modes are in the plateau regime, the prediction based on all modes being in the plateau regime presented here is obviously not applicable. An example of such is given in [159], where mirror force from one mode becomes non negligible. Thus, not all modes are in the plateau regime in that case. Because the mirror force terms depend on the poloidal and toroidal angles non-linearly, distinguishing individual mode from one another is difficult. The analytic treatment for such a situation is not known.

9.3. Parallel plasma viscosity and bootstrap current in the low collisionality regime

In the low collisionality regime, i.e. when particles' bounce motion is not interrupted by collisions, particle dynamics becomes important in solving the drift kinetic equation. In non-axisymmetric tori, there is no compact analytic description for particle trajectories. Thus, parallel plasma viscous forces in this regime cannot be calculated as accurately as those in the plateau–Pfirsch–Schlüter regime. However, because of the importance of the bootstrap current to plasma confinement in stellarators, it is useful at least to obtain an approximate expression for the parallel viscosity in the collisionless regime.

As discussed in section 9.2.3, it is difficult to treat analytically the case where only a few modes are collisionless. However, when all modes are collisionless, it is possible to obtain an approximate solution.

9.3.1. Parallel plasma viscosity. One way to calculate the parallel plasma viscosity approximately is to demand that the expression is exact, in the sense of the gyro-radius ordering, in any symmetric limit. To this end, the radial drift speed is decomposed as [257]

$$v_{\mathrm{d}}\cdot\nabla V = \frac{v_{||}}{B}\boldsymbol{B}\cdot\nabla\left(\frac{1}{2}\frac{v_{||}}{\Omega}H_1+\frac{1}{2}\frac{v_{||}}{\Omega}\frac{B^2H_2}{\chi'\psi'}\right) + \frac{v_{||}}{B}\left[\frac{\partial}{\partial\theta}\left(\frac{v_{||}}{\Omega\chi'}\mathsf{R}B^2\right)-\frac{\partial}{\partial\zeta}\left(\frac{v_{||}}{\Omega\chi'}\mathsf{S}B^2\right)\right], \tag{9.3.1.1}$$

where

$$H_1 = \frac{\psi'\boldsymbol{B}\times\nabla V\cdot\nabla\theta+\chi'\boldsymbol{B}\times\nabla V\cdot\nabla\zeta}{\psi'\chi'}, \tag{9.3.1.2}$$

$$H_2 = \frac{\left\langle(\partial B/\partial\theta)^2\right\rangle - q^2\left\langle(\partial B/\partial\zeta)^2\right\rangle}{\left\langle(\partial B/\partial\theta+q\partial B/\partial\zeta)^2\right\rangle}, \tag{9.3.1.3}$$

$$\mathsf{R} = \frac{\langle(\partial B/\partial\theta)(\partial B/\partial\zeta)\rangle + q\left\langle(\partial B/\partial\zeta)^2\right\rangle}{\left\langle(\partial B/\partial\theta+q\partial B/\partial\zeta)^2\right\rangle}, \tag{9.3.1.4}$$

and

$$\mathsf{S} = \frac{\left\langle(\partial B/\partial\theta)^2\right\rangle + q\,\langle(\partial B/\partial\theta)(\partial B/\partial\zeta)\rangle}{\left\langle(\partial B/\partial\theta+q\partial B/\partial\zeta)^2\right\rangle}. \tag{9.3.1.5}$$

The purpose of the representation in equation (9.3.1.1) is to separate the axisymmetric part from the non-axisymmetric part of the radial drift speed. The axisymmetric part, valid for any torus that possesses certain symmetry in the $|\boldsymbol{B}|$ spectrum, is the term that involves $\boldsymbol{B}\cdot\nabla$. The terms that involve R and S are the non-axisymmetric part and vanish in any symmetric torus. The decomposition of the drift velocity is motivated by the solution of the density conservation law [257].

The equation to be solved is the linear drift kinetic equation, i.e. equation (5.2). In the collisionless regime, the solution is complex and depends on the details of the solution of the linear bounce averaged drift kinetic equation for stellarators [3, 53]. However, the solution of the bounce averaged drift kinetic equation does not contribute to the parallel viscosity as proven rigorously in [53]. To approximate, the linear drift kinetic equation is solved as if the torus is symmetric. In this approximation, the solution becomes exact in any symmetric limit. Because there are infinite but countable number of symmetric tori, this imposes a powerful constraint on the solution of the linear drift kinetic equation. This provides a plausible explanation for the reasonable agreement between the bootstrap current calculated analytically based on the approximate parallel plasma viscosity and that calculated numerically using DKES [254]. The method of solution to be discussed, which follows from that in [254, 257], is different but equivalent to the original method developed in [53]. This method utilizes Fourier series in solving the magnetic differential equation instead of integrating along the magnetic field line.

The linear drift kinetic equation in the collisionless regime is solved by expanding it, using a small parameter $\nu_{\mathrm{eff}}/\omega_{\mathrm{tb}}$, where ω_{tb} is the typical bounce frequency for all relevant trapped particles, to obtain the leading order equation

$$v_{||}\boldsymbol{n}\cdot\nabla f_{10} + v_{\mathrm{d}}\cdot\nabla V\frac{\partial f_{\mathrm{M}}}{\partial V} = 0, \tag{9.3.1.6}$$

and the next order equation

$$v_{||}\boldsymbol{n}\cdot\nabla f_{11} + ev_{||}\boldsymbol{n}\cdot\boldsymbol{E}^{(A)}\frac{\partial f_{\mathrm{M}}}{\partial E} = C\left(f_{10}\right), \tag{9.3.1.7}$$

where the second subscript in f_1 indicates the order in the auxiliary expansion. The difference between equations (9.3.1.6) and (9.3.1.7), and equations (6.2.1.1) and (6.2.1.2) is that $n\cdot\nabla$ is a two-dimensional operator for non-axisymmetric tori such as stellarators. The advantage in expressing $v_{\mathrm{d}}\cdot\nabla V$ in equation (9.3.1.1) becomes transparent. Using equation (9.3.1.1), equation (9.3.1.6) can be integrated to obtain

$$f_{10} = -\frac{v_{||}}{2\Omega}H_1\frac{\partial f_{\mathrm{M}}}{\partial V} - \frac{v_{||}}{2\Omega}\frac{B^2H_2}{\chi'\psi'}\frac{\partial f_{\mathrm{M}}}{\partial V} + \frac{v}{\Omega}\frac{qBB_{\mathrm{M}}}{\chi'\psi'}\tilde{h}\frac{\partial f_{\mathrm{M}}}{\partial V} + g_{\mathrm{st}}\left(V\right), \tag{9.3.1.8}$$

where $g_{\mathrm{st}}(V)$ is an integration constant,

$$\tilde{h} = -\sigma\sum_{m,n\neq0}\frac{m\mathsf{R}+n\mathsf{S}}{m-nq}\alpha_{mn}\left[\mathrm{e}^{\mathrm{i}(m\theta-n\zeta)}-\mathrm{e}^{\mathrm{i}(m\theta_{\mathrm{M}}-n\zeta_{\mathrm{M}})}\right], \tag{9.3.1.9}$$

$(\theta_{\rm M}, \zeta_{\rm M})$ are the coordinates of $B_{\rm M}$ where B is the global maximum on the magnetic surface, σ denotes the sign of $v_{||}$,

$$\alpha_{mn} = \frac{1}{4\pi^2}\int_0^{2\pi} {\rm d}\theta \int_0^{2\pi} {\rm d}\zeta \frac{B}{B_{\rm M}}\left(1-\frac{\lambda B}{B_{\rm M}}\right)^{1/2} {\rm e}^{-{\rm i}(m\theta - n\zeta)}, \tag{9.3.1.10}$$

and $\lambda = \mu B_{\rm M}/(Mv^2/2)$. The integration constant $g_{\rm st}(V)$ is determined using the same method that is used in calculating the parallel viscosity in [7]. As a result, the flux surface averaged parallel plasma viscosity is

$$\begin{pmatrix} \left\langle \boldsymbol{B}\cdot\nabla\cdot\overleftrightarrow{\pi}\right\rangle \\ \left\langle \boldsymbol{B}\cdot\nabla\cdot\overleftrightarrow{\Theta}\right\rangle \end{pmatrix} = NM\left\langle B^2\right\rangle \begin{pmatrix} \mu_1 & \mu_2 \\ \mu_2 & \mu_3 \end{pmatrix} \begin{pmatrix} \bar{V}^\theta \\ \frac{2}{5}\frac{\bar{q}^\theta}{p} \end{pmatrix}, \tag{9.3.1.11}$$

where

$$\bar{V}^\theta = \frac{V_{||}}{B} + \frac{v_{\rm t}^2}{4}\left(\frac{H_1}{B\Omega} + \frac{BH_2}{\Omega\chi'\psi'} - \frac{1}{f_{\rm t}}\frac{qB}{\Omega\chi'\psi'}\frac{3}{2}\int_0^1 {\rm d}\lambda \frac{\lambda W(\lambda)}{\left\langle |v_{||}|/v\right\rangle}\right) \times\left(\frac{p'}{p} + \frac{e\Phi'}{T}\right), \tag{9.3.1.12}$$

$$\frac{\bar{q}^\theta}{p} = \frac{q_{||}}{pB} + \frac{5}{2}\frac{v_{\rm t}^2}{4} \times\left(\frac{H_1}{B\Omega} + \frac{BH_2}{\Omega\chi'\psi'} - \frac{1}{f_{\rm t}}\frac{qB}{\Omega\chi'\psi'}\frac{3}{2}\int_0^1 {\rm d}\lambda \frac{\lambda W(\lambda)}{\left\langle |v_{||}|/v\right\rangle}\right)\frac{T'}{T}, \tag{9.3.1.13}$$

$$W(\lambda) = \sum_{m,n}\frac{m{\rm R}+n{\rm S}}{m-nq} \times\left[-2\frac{\partial\alpha_{mn}}{\partial\lambda}\left\langle \frac{|v_{||}|}{v}{\rm e}^{{\rm i}(m\theta-n\zeta)}\right\rangle + \frac{1}{f_c}\frac{\left\langle B^2\right\rangle}{B_{\rm M}^2}{\rm e}^{{\rm i}(m\theta_{\rm M}-n\zeta_{\rm M})}\left(\frac{3\alpha_{mn}(1)}{2}+d_{mn}\right)\right], \tag{9.3.1.14}$$

and

$$d_{mn} = \frac{1}{4\pi^2}\int_0^{2\pi}{\rm d}\theta\int_0^{2\pi}{\rm d}\zeta\left(1-\frac{B}{B_{\rm M}}\right)^{3/2}{\rm e}^{-{\rm i}(m\theta-n\zeta)}. \tag{9.3.1.15}$$

The definitions for f_c and $f_{\rm t}$ are the same as those for the axisymmetric tokamaks in equation (6.2.1.12) except that B and $B_{\rm M}$ are different. The expressions for the viscous coefficients μ_js are cast into forms that are the same as those for axisymmetric tokamaks in equation (6.2.1.11) except that the magnetic field spectrum $|\boldsymbol{B}|$ used is different.

9.3.2. Parallel flow and bootstrap current. Having the information of the parallel viscous forces, the parallel flow and the bootstrap current in this regime can be obtained.

In the large aspect ratio limit, there is a common parallel flow as shown in section 6 and [6, 7]. Using the parallel viscous forces in this regime, the common parallel flow is [53, 254]

$$\frac{\left\langle V_{||}B\right\rangle}{\left\langle B^2\right\rangle} = -G_{\rm b}\frac{cT_{\rm i}}{e_{\rm i}\left\langle B^2\right\rangle}\left(\frac{p_{\rm i}'}{p_{\rm i}} + \frac{e_{\rm i}\Phi'}{T_{\rm i}} + \frac{\mu_{2{\rm i}}}{\mu_{1{\rm i}}}\frac{T_{\rm i}'}{T_{\rm i}}\right), \tag{9.3.2.1}$$

where $\mu_{2{\rm i}}/\mu_{1{\rm i}} = -1.17$ and the geometric factor $G_{\rm b}$ is

$$G_{\rm b} = \frac{\langle H_1\rangle}{2} + \frac{\left\langle B^2\right\rangle H_2}{2\chi'\psi'} - \frac{3}{4}\frac{1}{f_{\rm t}}\frac{q\left\langle B^2\right\rangle}{\chi'\psi'}\int_0^1 {\rm d}\lambda\frac{\lambda W(\lambda)}{\left\langle |v_{||}|/v\right\rangle}. \tag{9.3.2.2}$$

If the doubly periodic tori possess any symmetry property in the $|\boldsymbol{B}|$ spectrum, the geometric factor simplifies to

$$G_{\rm b} = \frac{\langle H_1\rangle}{2} + \frac{\left\langle B^2\right\rangle H_2}{2\chi'\psi'}. \tag{9.3.2.3}$$

For a helically symmetric torus,

$$G_{\rm b} = \frac{1}{\chi'}\frac{mF+nG}{m-nq}, \tag{9.3.2.4}$$

which is the same as $G_{\rm ps}$ and $G_{\rm p}$. For axisymmetric tokamaks, $m = 1$ and $n = 0$, and for the poloidally symmetric tori, $m = 0$. For a helically symmetric torus, the parallel flow is in the opposite direction to that of a tokamak if $m < nq$.

The bootstrap current is

$$J_{||{\rm b}} = -2.96 f_{\rm t} c\frac{G_{\rm b}B}{\left\langle B^2\right\rangle}\left[P'\left(1+\frac{l_{12}^{\rm e}}{l_{22}^{\rm e}}\frac{\mu_{2{\rm e}}}{\mu_{1{\rm e}}}\right) + \left(1+\frac{\mu_{2{\rm e}}}{\mu_{1{\rm e}}}\frac{l_{12}^{\rm e}}{l_{22}^{\rm e}}\right) \times\frac{\mu_{2{\rm i}}}{\mu_{1{\rm i}}}NT_{\rm i}' + \left(\frac{\mu_{2{\rm e}}}{\mu_{1{\rm e}}} + \frac{l_{12}^{\rm e}}{l_{22}^{\rm e}}\frac{\mu_{3{\rm e}}}{\mu_{1{\rm e}}}\right)NT_{\rm e}'\right]. \tag{9.3.2.5}$$

The direction of the bootstrap current is controlled by the geometric factor $G_{\rm b}$. The bootstrap current in stellarators is often in the opposite direction to that in tokamaks and has a smaller magnitude. Even though there is no ohmic current in stellarators in principle, the existence of the bootstrap current can modify the q profile and thus MHD stability property [258, 259]. It is necessary to include it in the MHD equilibrium and stability calculations [260–264]. The bootstrap current in stellarators also depends on the radial electric field in the transition from the plateau regime to the banana regime, and in the case where ions and electrons are in different regimes [254, 265, 266].

In practical application, a connection formula for the bootstrap current that joins all the asymptotic limits is needed. However, such a formula is not available. From the numerical results for the bootstrap current from DKES for a classic stellarator [254], it seems that mode-by-mode transition might be a way to join various asymptotic limits. As the collision frequency decreases, one mode becomes collisionless first, i.e. enters the plateau regime. The bootstrap current increases according to the $1/\nu$ scaling for the bootstrap current in the plateau regime, and trying to reach the asymptotic value of that particular mode in the collisionless regime until the other mode becomes collisionless. The asymptotic value in the collisionless regime is approximately the bootstrap current in the symmetric limit for that single mode. After both modes become collisionless, the bootstrap current strives to reach the approximate asymptotic value calculated here. The collision frequency scaling during the transition may follow the scaling from the boundary layer analysis [267].

9.3.3. Neoclassical modification of electrical conductivity. As in axisymmetric tokamaks, when there are trapped particles, the electrical conductivity along the magnetic line is reduced.

The reduced conductivity can be obtained from the solution of the parallel momentum and heat flux balance equations. In the low collisionality regime where all trapped particles are collisionless, the modified conductivity $\sigma_{\rm eff}$ in stellarators is $\sigma_{\rm eff} = (N_{\rm e}e)^2 l_{22}^{\rm eb}/[l_{11}^{\rm eb}l_{22}^{\rm eb} - (l_{12}^{\rm eb})^2]$, where $l_{11}^{\rm eb} = l_{11}^{\rm e} + N_{\rm e}M_{\rm e}\mu_{1\rm e}$, $l_{12}^{\rm eb} = l_{12}^{\rm e} - N_{\rm e}M_{\rm e}\mu_{2\rm e}$ and $l_{22}^{\rm eb} = l_{22}^{\rm e} + N_{\rm e}M_{\rm e}\mu_{3\rm e}$. The $\sigma_{\rm eff}$ has exactly the same form as that for tokamaks in equation (6.2.1.36) except that the details of the viscous coefficients are defined differently. The expression for $\sigma_{\rm eff}$ is also valid in the plateau and Pfirsch–Schlüter regimes. When all modes are either in the plateau regime or in the Pfirsch–Schlüter regime, μ_{je} in $\sigma_{\rm eff}$ is replaced by $\mu_{jpe}\chi' + \mu_{jte}\psi'$ for $j = 1$–3 with the corresponding viscous coefficients defined in equations (9.1.6), (9.1.7), (9.2.4) and (9.2.5).

9.3.4. Transport fluxes in helically symmetric tori and isomorphic transformation. Transport fluxes in helically symmetric tori are similar to those for tokamaks in the banana regime because symmetric tori are isomorphic [268]. The isomorphic transformation is to replace I in tokamaks with $(mF + nG)/(m - nq)$, and to calculate $f_{\rm t}$ using the appropriate $|\boldsymbol{B}|$ spectrum. The Hamada coordinates are used here, i.e. the prime denotes $\mathrm{d}/\mathrm{d}V$.

For example, in the banana regime the parallel flow in helically symmetric tori is

$$\frac{\langle V_\parallel B\rangle}{\langle B^2\rangle} + \frac{(mF+nG)\,cT_{\rm i}}{(m-nq)\,e_{\rm i}\chi'\langle B^2\rangle}\frac{e_{\rm i}\Phi'}{T_{\rm i}} = -\frac{(mF+nG)\,cT_{\rm i}}{(m-nq)\,e_{\rm i}\chi'\langle B^2\rangle}\left(\frac{p_{\rm i}'}{p_{\rm i}} + \frac{\mu_{2\rm i}}{\mu_{1\rm i}}\frac{T_{\rm i}'}{T_{\rm i}}\right), \tag{9.3.4.1}$$

and ion heat conductivity is

$$\frac{q_{\rm i}^{\rm bp}}{T_{\rm i}} = -N_{\rm i}M_{\rm i}\frac{c^2}{e_{\rm i}^2}\frac{(mF+nG)^2}{(m-nq)^2\chi'^2\langle B^2\rangle}\mu_{3\rm i}\left(1 - \frac{\mu_{2\rm i}^2}{\mu_{1\rm i}\mu_{3\rm i}}\right)\frac{\mathrm{d}T_{\rm i}}{\mathrm{d}V} \tag{9.3.4.2}$$

using the flux–force relation for helically symmetric tori in section 4, and transport fluxes in section 6. The electron ambipolar particle flux and heat flux are

$$\Gamma_{\rm e}^{\rm bp} = -N_{\rm e}M_{\rm e}\frac{c^2}{e^2}\frac{(mF+nG)_{\rm i}^2}{(m-nq)^2\chi'^2\langle B^2\rangle}\mu_{1\rm e} \times\left(\frac{P'}{N_{\rm e}} + \frac{\mu_{2\rm e}}{\mu_{1\rm e}}T_{\rm e}' + \frac{\mu_{2\rm i}}{\mu_{1\rm i}}\frac{1}{Z}T_{\rm i}'\right), \tag{9.3.4.3}$$

and

$$\frac{q_{\rm e}^{\rm bp}}{T_{\rm e}} = -N_{\rm e}M_{\rm e}\frac{c^2}{e_{\rm i}^2}\frac{(mF+nG)_{\rm i}^2}{(m-nq)^2\chi'^2\langle B^2\rangle}\mu_{2\rm e} \times\left(\frac{P'}{N_{\rm e}} + \frac{\mu_{3\rm e}}{\mu_{2\rm e}}T_{\rm e}' + \frac{\mu_{2\rm i}}{\mu_{1\rm i}}\frac{1}{Z}T_{\rm i}'\right). \tag{9.3.4.4}$$

A scaling the same as the one in the particle flux shown in equation (9.3.4.3) is also obtained in [269]. The Ware pinch fluxes can also be obtained by applying the isomorphic transformation to results in section 6 if the inductive electric field does not vanish in helically symmetric tori. The effects of orbit squeezing can also be included when the orbit squeezing factor is transformed to [270]

$$S = 1 + \frac{(mF+nG)^2}{(m-nq)^2\chi'^2\Omega^2}\frac{e\Phi_0''}{M}, \tag{9.3.4.5}$$

using the isomorphic transformation. The transport fluxes in the vicinity of the magnetic axis including the effects of orbit squeezing for helically symmetric tori have been calculated in [270]. The results can be obtained by applying the isomorphic transformation to the potato transport fluxes in tokamaks.

9.4. Bounce averaged drift kinetic equation and $1/\nu$ regime

The radial electric field is not yet determined in the low collisionality regime in equation (9.3.2.1). Modern efforts to optimize stellarator configurations are to minimize or even to eliminate the symmetry breaking components in the $|\boldsymbol{B}|$ spectrum to reduce the radial drift speed of trapped particles [27]. However, symmetry breaking components always exist in real configurations with meaningful magnitudes, i.e. typical $\delta B/B$ is larger than 10^{-3}, regardless of the optimization goals. Thus, the radial electric field is determined by the toroidal component of the viscous force resulting from trapped particles drifting off the magnetic surface. In stellarators, it is usually the helically trapped particles that dominate the transport processes.

The $|\boldsymbol{B}|$ spectrum in real stellarators is complex and in general the drift kinetic equation is not amenable to analytic treatment in the low collisionality regime for arbitrary $|\boldsymbol{B}|$ spectrum. However, there is one class of the $|\boldsymbol{B}|$ spectrum for which analytic transport theory can be developed. That class of the $|\boldsymbol{B}|$ spectrum consists of one helical harmonic with multiple poloidal sidebands [271]:

$$\frac{B}{B_0} = 1 + \varepsilon_{\rm t}\cos\theta + \varepsilon_{\rm d}\cos j\theta + \sum_{l=-\infty}^{\infty}\varepsilon^{(l)}\cos(l\theta+\alpha), \tag{9.4.1}$$

where $\alpha = m\theta - n\zeta$ is the main helical harmonic, $\varepsilon^{(l)}$ denotes the amplitude of the lth harmonic of the poloidal sideband, $\varepsilon_{\rm d}$ and $\varepsilon_{\rm t}$ are the amplitudes of the $\cos j\theta$ and $\cos\theta$ harmonics. In this model, arbitrary numbers of the poloidal side bands can be kept. Using the identity $\cos(\pm l\theta + \alpha) = \cos l\theta\cos\alpha \mp \sin l\theta\sin\alpha$, equation (9.4.1) can be cast into [271]

$$\frac{B}{B_0} = 1 + \varepsilon_{\rm t}\cos\theta + \varepsilon_{\rm d}\cos j\theta + \left(C^2+D^2\right)^{1/2} \times\left[\frac{C}{\left(C^2+D^2\right)^{1/2}}\cos\alpha - \frac{D}{\left(C^2+D^2\right)^{1/2}}\sin\alpha\right], \tag{9.4.2}$$

where $C = \varepsilon^{(0)} + [\varepsilon^{(+1)} + \varepsilon^{(-1)}]\cos\theta + [\varepsilon^{(+2)} + \varepsilon^{(-2)}]\cos 2\theta$ and $D = [\varepsilon^{(+1)} - \varepsilon^{(-1)}]\sin\theta + [\varepsilon^{(+2)} - \varepsilon^{(-2)}]\sin 2\theta$ when only two lth-harmonics are kept. It is obvious that the same procedure can be used when there are arbitrary numbers of poloidal sidebands in the magnetic field spectrum. An angle ς can be defined such that $\cos\varsigma = C/(C^2+D^2)^{1/2}$, and $\sin\varsigma = D/(C^2+D^2)^{1/2}$, and equation (9.4.2) can be simplified to [271]

$$\frac{B}{B_0} = 1 + \varepsilon_{\rm T} + \varepsilon_{\rm H}\cos(\alpha+\varsigma), \tag{9.4.3}$$

where $\varepsilon_{\rm T} = \varepsilon_{\rm t}\cos\theta + \varepsilon_{\rm d}\cos j\theta$ and $\varepsilon_{\rm H} = (C^2+D^2)^{1/2}$. The expression in equation (9.4.3) can be reduced to a model

$$\frac{B}{B_0} = 1 - \varepsilon_{\rm t}\cos\theta - \varepsilon_h(1 - \sigma_{\rm M}\cos\theta)\cos\alpha, \tag{9.4.4}$$

used in [272] to improve plasma confinement in stellarators, by setting $\varepsilon^{(+1)} = \varepsilon^{(-1)}$, and $\varepsilon^{(+2)} = \varepsilon^{(-2)} = 0$, where σ_M is a parameter.

The main difference between the theory for stellarators and that for neoclassical toroidal plasma viscosity in tokamaks is that there are, at least, two classes of trapped particles in stellarators. Trapped particles can be roughly classified as toroidally trapped particles that are trapped in the $\varepsilon_t \cos\theta$ variation and the helically trapped particles that are trapped in the helical variation $\varepsilon_H \cos(\alpha + \zeta)$. The helical harmonic in stellarators usually has the property that $nq > m$. With this property, the bounce frequency for the helically trapped particles is higher than that of the toroidally trapped particles by a factor of $|m - nq| \sim nq \gg 1$ for comparable magnitudes of ε_T and ε_H. Thus, as the collision frequency decreases, helically trapped particles become collisionless first. For this reason, when the effective collision frequency $\nu_{eff} \sim \nu/|\varepsilon_H|$ is less than the bounce frequency of the helically trapped particles $\omega_{bh} \sim v_t\sqrt{|\varepsilon_H|}|m - nq|/(Rq)$, helically trapped particles can complete their collisionless bounce motions. For the model presented in equation (9.4.3), the only analytic formulas for transport fluxes developed so far are for $1/\nu$ [271, 272], and the superbanana plateau regimes [230].

9.4.1. Bounce averaged drift kinetic equation for helically trapped particles. Similar to the theory for the neoclassical toroidal plasma viscosity in the low collisionality regimes in tokamaks discussed in section 8, the drift orbit dynamics is governed by the bounce averaged drift kinetic equation for helically trapped particles when $\nu/|\varepsilon_H| < \omega_{bh}$.

It is convenient to choose spatial coordinates as (V, θ_0, ζ) in Hamada coordinates where $\theta_0 = \theta - \zeta/q$ is the label for the field line and ζ is the coordinate along the field line. Obviously, $\boldsymbol{B} \cdot \nabla\theta_0 = 0$.

In the low collisionality regimes, the drift kinetic equation can be expanded using the small parameter $\nu_{eff}/\omega_{bh} < 1$. Because the bounce frequency of the helically trapped particles is larger than the drift frequencies and collision frequency, the leading order equation is

$$v_{||}\boldsymbol{n} \cdot \nabla\zeta \frac{\partial f_0}{\partial \zeta} = 0, \tag{9.4.1.1}$$

where f_0 is the leading particle distribution function. The solution to equation (9.4.1.1) is

$$f_0 = f_0(V, \theta_0). \tag{9.4.1.2}$$

The next order equation is

$$v_{||}\boldsymbol{n} \cdot \nabla\zeta \frac{\partial f_{0,1}}{\partial \zeta} + \boldsymbol{v}_d \cdot \nabla\theta_0 \frac{\partial f_0}{\partial \theta_0} + \boldsymbol{v}_d \cdot \nabla V \frac{\partial f_0}{\partial V} = C(f_0), \tag{9.4.1.3}$$

where $f_{0,1}$ is the perturbed particle distribution function to f_0. To guarantee that $f_{0,1}$ is periodic in ζ, equation (9.4.1.3) is bounce averaged over the trajectories of the helically trapped particles and results in the bounce averaged drift kinetic equation

$$\langle \boldsymbol{v}_d \cdot \nabla\theta_0 \rangle_{bh} \frac{\partial f_0}{\partial \theta_0} + \langle \boldsymbol{v}_d \cdot \nabla V \rangle_{bh} \frac{\partial f_0}{\partial V} = \langle C(f_0) \rangle_{bh}. \tag{9.4.1.4}$$

The bounce average operation $\langle A \rangle_{bh}$ is defined as $\langle A \rangle_{bh} = \sum_\sigma (\int_{-\zeta_t}^{\zeta_t} d\zeta AB/|v_{||}|)/(\int_{-\zeta_t}^{\zeta_t} d\zeta B/|v_{||}|)$, where the turning points $\pm\zeta_t$ are defined as $v_{||}(\pm\zeta_t) = 0$. Of course, bounce average operation also annihilates the momentum restoring term in the collision operator as discussed in section 8.

As in the theory for neoclassical toroidal plasma viscosity in tokamaks, there are resonant and non-resonant transport processes categorized by whether $\langle \boldsymbol{v}_d \cdot \nabla\theta_0 \rangle_{bh}$ vanishes. For the non-resonant transport processes, equation (9.4.1.4) can be further expanded by assuming that the poloidal drift frequency is comparable to the collision frequency and much larger than the radial drift frequency to allow for the local transport theory. The leading order equation is then

$$\langle \boldsymbol{v}_d \cdot \nabla\theta_0 \rangle_{bh} \frac{\partial f_{00}}{\partial \theta_0} = \langle C(f_{00}) \rangle_{bh}, \tag{9.4.1.5}$$

where the second subscript indicates the subsidiary ordering. The solution to equation (9.4.1.5) is

$$f_{00} = f_{00}(V) = f_M. \tag{9.4.1.6}$$

The next order equation is

$$\langle \boldsymbol{v}_d \cdot \nabla\theta_0 \rangle_{bh} \frac{\partial f_{01}}{\partial \theta_0} + \langle \boldsymbol{v}_d \cdot \nabla V \rangle_{bh} \frac{\partial f_M}{\partial V} = \langle C(f_{01}) \rangle_{bh}. \tag{9.4.1.7}$$

Equation (9.4.1.7) is the linear bounce averaged equation to be solved for the non-resonant transport processes.

For the resonant transport processes, the linear drift kinetic equation to be solved is

$$\langle \boldsymbol{v}_d \cdot \nabla\theta_0 \rangle_{bh} \frac{\partial f_{01}}{\partial \theta_0} + \langle \boldsymbol{v}_d \cdot \nabla V \rangle_{bh} \frac{\partial f_{01}}{\partial V} + \langle \boldsymbol{v}_d \cdot \nabla V \rangle_{bh} \frac{\partial f_M}{\partial V} = \langle C(f_{01}) \rangle_{bh}. \tag{9.4.1.8}$$

The radial drift term $\langle \boldsymbol{v}_d \cdot \nabla V \rangle_{bh} \partial f_{01}/\partial V$ describing the radial motion of the drift orbit must be kept to complete the drift trajectories for the resonant helically trapped particles, because $\partial f_{01}/\partial V$ is comparable to $\partial f_M/\partial V$ for resonant transport processes [111, 230].

To calculate the bounce averaged drift velocity, it is assumed that $nq > m$ so that helical angle $\alpha = [m\theta_0 + (m/q - n)\zeta] \approx m\theta_0 - n\zeta$. The difference between θ and θ_0 is also neglected because of the assumption that $nq > 2\pi$. With these approximations, using the model magnetic field in equation (9.4.3) yields [271]

$$\langle \boldsymbol{v}_d \cdot \nabla\theta \rangle_{bh} = \frac{c\Phi'}{\psi'} - \frac{c\mu B_0}{e\psi'} \left\{ \left[\frac{2E(k_h)}{K(k_h)} - 1 \right] \frac{\partial \varepsilon_H}{\partial V} - \frac{\partial \varepsilon_T}{\partial V} \right\}, \tag{9.4.1.9}$$

and

$$\langle \boldsymbol{v}_d \cdot \nabla V \rangle_{bh} = \frac{c\mu B_0}{e\psi'} \left\{ \left[\frac{2E(k_h)}{K(k_h)} - 1 \right] \frac{\partial \varepsilon_H}{\partial \theta} - \frac{\partial \varepsilon_T}{\partial \theta} \right\}, \tag{9.4.1.10}$$

where the pitch angle parameter k_h^2 is defined as

$$k_h^2 = \frac{E - e\Phi - \mu B_0(1 + \varepsilon_T - \varepsilon_H)}{2\mu B_0 \varepsilon_H}. \tag{9.4.1.11}$$

The bounce averaged collision operator is

$$\langle C\left(f_{01}\right)\rangle_{bh} = \frac{\nu_D}{\varepsilon_H}\frac{1}{K\left(k_h\right)}\frac{\partial}{\partial k_h^2} \times\left\{\left[E\left(k_h\right)-\left(1-k_h^2\right)K\left(k_h\right)\right]\frac{\partial f_{01}}{\partial k_h^2}\right\}, \quad (9.4.1.12)$$

where the energy scattering operator is neglected as is appropriate for large aspect ratio tori.

The solution of the bounce averaged drift kinetic equation does not contribute to the flux surface averaged parallel viscous forces as discussed in section 8. It does not have any direct effects on the bootstrap current, nor does it modify the electrical conductivity.

9.4.2. $1/\nu$ regime. The $1/\nu$ regime is the most studied collisionality regime in the transport theory for non-axisymmetric tori and in particular in stellarators in part because transport coefficients scale unfavourably as $T^{7/2}$ for high-temperature plasmas [3, 246, 271, 272, 273–275]. If the scaling persists it could make stellarators a much less viable candidate as thermonuclear fusion reactors [276].

In this regime, collisions are infrequent so that one class of the trapped particles can complete their bounce motions. Complicated analytic expressions for the transport fluxes for a realistic magnetic field spectrum have been derived [273, 275]. To illustrate physics of the theory, the magnetic field model in equation (9.4.3) is used to obtain relative simple transport fluxes in this regime.

In the $1/\nu$ regime, the effective collision frequency is larger than the poloidal drift frequency. The transport process is non-resonant. The equation to be solved is then

$$\langle \boldsymbol{v}_d\cdot\nabla V\rangle_{bh}\frac{\partial f_M}{\partial V} = \langle C\left(f_{01}\right)\rangle_{bh}. \quad (9.4.2.1)$$

Integrating equation (9.4.2.1), and imposing the boundary condition at $k_h^2=0$, i.e. $[E(k_h)-(1-k_h^2)K(k_h)]\partial f_{01}/\partial k_h^2 = 0$, yield

$$\frac{\partial f_{01}}{\partial k_h^2} = \frac{\varepsilon_H}{\nu_D}\frac{c\mu B_0}{e\psi'}\frac{\partial f_M}{\partial V}\left[\int_0^{k^2}\mathrm{d}k_h^2\left\{\left[2E\left(k_h\right)-K\left(k_h\right)\right]\times\left(\partial\varepsilon_H/\partial\theta\right)-K\left(k_h\right)\left(\partial\varepsilon_T/\partial\theta\right)\right\}\right] \times\left[E\left(k_h\right)-\left(1-k_h^2\right)K\left(k_h\right)\right]^{-1}. \quad (9.4.2.2)$$

Knowing $\partial f_{01}/\partial k_h^2$ is adequate to calculate transport fluxes, and they are [271]

$$\Gamma^{na}_{s,1/\nu} = -\frac{N}{\sqrt{2}\pi^2}\left(\frac{Mc}{e\psi'}\right)^2\frac{v_t^4}{\nu_t}I_{s,1/\nu} \times\left[\eta_1\left(\frac{p'}{p}+\frac{e\Phi'}{T}\right)+\eta_2\frac{T'}{T}\right], \quad (9.4.2.3)$$

and

$$\frac{q^{na}_{s,1/\nu}}{T} = -\frac{N}{\sqrt{2}\pi^2}\left(\frac{Mc}{e\psi'}\right)^2\frac{v_t^4}{\nu_t}I_{s,1/\nu} \times\left[\eta_2\left(\frac{p'}{p}+\frac{e\Phi'}{T}\right)+\eta_3\frac{T'}{T}\right], \quad (9.4.2.4)$$

where η_j for $j=1$–3 is the same as the one defined in equation (8.2.1.8),

$$I_{s,1/\nu} = \int_0^{2\pi}\mathrm{d}\theta\varepsilon_H^{3/2}\left[G_1\left(\frac{\partial\varepsilon_T}{\partial\theta}\right)^2-2G_2\frac{\partial\varepsilon_T}{\partial\theta}\frac{\partial\varepsilon_H}{\partial\theta} +G_3\left(\frac{\partial\varepsilon_H}{\partial\theta}\right)^2\right],$$

$G_1=16/9, G_2=16/15$ and $G_3=0.684$. Both the particle and normalized heat fluxes scale as $T^{7/2}$. This unfavourable temperature scaling can have significant impact on the confinement for fusion-born alpha particles [276]. The difference between stellarator transport fluxes and the neoclassical toroidal viscosity in the $1/\nu$ regime is that the role of the toroidal magnetic field variation has changed. In stellarators, helically trapped particles drift off the magnetic surface as a result of the toroidal magnetic field variation. In the theory of neoclassical toroidal viscosity, particles trapped in the toroidal magnetic field variation drift off the magnetic surface due to the helically perturbed magnetic field.

Another difference between the transport fluxes for the stellarators and those for tokamaks with broken symmetry is the mode number dependences. There are no explicit mode number dependences for stellarator transport fluxes, while the mode number dependences for neoclassical toroidal plasma viscosity are important. The reason for the difference lies in the approximation $nq > m$ used in the theory for stellarators.

The radial electric field is not determined yet in the low collisionality regime. In the $1/\nu$ regime, the radial electric field can be determined by setting $\sum_j e_j\Gamma^{na}_{s,1/\nu,j}=0$, which is equivalent to $\sum_j\langle \boldsymbol{B}_t\cdot\nabla\cdot\overleftrightarrow{\pi}_j\rangle=0$, or $\sum_j\langle \boldsymbol{B}_p\cdot\nabla\cdot\overleftrightarrow{\pi}_j\rangle=0$, because the solution of the bounce averaged drift kinetic equation does not contribute to $\langle \boldsymbol{B}\cdot\nabla\cdot\overleftrightarrow{\pi}\rangle$ [53]. Thus, the radial electric field is [3, 211]

$$\frac{e_i\Phi'}{T_i} = -\frac{p_i'}{p_i}+\frac{\eta_{2i}}{\eta_{1i}}\frac{T_i'}{T_i}, \quad (9.4.2.5)$$

after neglecting the electron contribution because $\sqrt{M_e/M_i}<1$. Together with the parallel flow in equation (9.3.2.1), the plasma flows are completely determined in this regime.

9.4.3. Other low collisionality regimes. When the collision frequency is even lower, boundary layer $\sqrt{\nu}$ regime, collisionless detrapping/retrapping regime, superbanana plateau regime and superbanana regime will become important for plasma confinement in stellarators [3]. For a classic stellarator, transport fluxes in all these regimes can be calculated following the asymptotic analysis developed for the theory for neoclassical toroidal plasma viscosity in section 8 and the physics reviewed in [3].

The collisional boundary layer $\sqrt{\nu}$ regime is too narrow in the collision frequency domain for comparable magnitudes of ε_t and ε_h, to be meaningful for asymptotic analysis as demonstrated in [277] using the DKES code. Indeed, a connection formula without including $\sqrt{\nu}$ scaling fits numerical results better. However, in the limit where $\varepsilon_h \gg \varepsilon_t$, the physics of the collisional boundary layer can be important. The asymptotic boundary layer analysis is to make the outer solution vanish at the trapped-circulating boundary. This leads to the $\sqrt{\nu}$ scaling [3].

The collisional boundary layer solution for the bounce averaged drift kinetic equation in the regime where $\nu/\varepsilon_h < c|\Phi'|/\psi'$ but $(\nu/\varepsilon_h)/(c|\Phi'|/\psi') > (\varepsilon_t/\varepsilon_h)^2$ has been given in [3]. Details of the analytic method are shown in section 8. The transport fluxes are

$$\Gamma^{\rm na}_{\sqrt{\nu}} = -\frac{1}{4\sqrt{2}\pi^{3/2}} N v_t^4 \frac{2\varepsilon_t^2\sqrt{\nu_{*dh}}}{c\,|{\rm d}\Phi/{\rm d}\psi|}\sqrt{\varepsilon_h}\left(\frac{Mc}{e\psi'}\right)^2 \times\left[\ln\left(\frac{16}{\sqrt{\nu_{\cdot dh}}}\right)\right]^{1/2}\times\left[\eta_1\left(\frac{p'}{p}+\frac{e\Phi'}{T}\right)+\eta_2\frac{T'}{T}\right], \tag{9.4.3.1}$$

and

$$\frac{q^{\rm na}_{\sqrt{\nu}}}{T} = -\frac{1}{4\sqrt{2}\pi^{3/2}} N v_t^4 \frac{2\varepsilon_t^2\sqrt{\nu_{*dh}}}{c\,|{\rm d}\Phi/{\rm d}\psi|}\sqrt{\varepsilon_h}\left(\frac{Mc}{e\psi'}\right)^2 \times\left[\ln\left(\frac{16}{\sqrt{\nu_{\cdot dh}}}\right)\right]^{1/2}\left[\eta_2\left(\frac{p'}{p}+\frac{e\Phi'}{T}\right)+\eta_3\frac{T'}{T}\right], \tag{9.4.3.2}$$

where $\nu_{*dh} = 4(\nu_t/\varepsilon_h)|c\Phi'/\psi'|^{-1}$, and η_j for $j = 1$–3 is defined in equation (8.2.2.21). It can be seen that when the magnitudes of ε_t and ε_h are comparable the region in the collision frequency domain for the $\sqrt{\nu}$ scaling is too narrow to render a valid asymptotic analysis. Thus, it is not very useful to insert a $\sqrt{\nu}$ scaling in the connection formula that joins all the asymptotic limits.

The transport fluxes in the superbanana plateau regime for the spectrum in equation (9.4.3) have been obtained in [230]. The same analysis can be extended to calculate transport fluxes in the superbanana regime. It should be emphasized that the superbanana plateau transport fluxes can be obtained with or without $\langle \boldsymbol{v}_{\rm d}\cdot\nabla V\rangle_{{\rm b}h}\partial f_{01}/\partial V$ in equation (9.4.1.8) as demonstrated in [224, 230].

The DKES code [108] has been used to calculate the plasma viscosity and to determine the radial electric field in stellarators using the moment approach [278, 279]. It can describe almost all relevant transport physics in stellarators except that the superbanana plateau resonance is excluded in the formulation. Thus, it is perfectly suited in the region where the value of the radial electric field is finite, which is true for most plasmas. Besides DKES, several numerical codes are devoted to calculate the transport matrix for a variety of stellarator configurations [280–288]. The benchmark of the transport coefficients from all these codes is given in [289].

A connection formula for a classic stellarator, with $\varepsilon_h > \varepsilon_t$ and $nq > m$, has been constructed to join $1/\nu$, collisionless detrapping, superbanana plateau and superbanana regimes following the physics reviewed in [3]. It can be casted in a form as, when $\nu R/(v_t n\varepsilon_h^{3/2}) \ll 1$,

$$\left(\Gamma^{\rm na}\right)_r = -N\varepsilon_t^2\varepsilon_h^{1/2}\left(\frac{cT}{eBr}\right)^2\int_0^\infty {\rm d}x 2x^6 {\rm e}^{-x^2}\frac{\nu_{\rm D}(x)}{\varepsilon_h} \times\left[\frac{p'}{p}+\frac{e\Phi'}{T}+\left(x^2-\frac{5}{2}\right)\frac{T'}{T}\right] \times\left\{1.67\frac{\varepsilon_t}{\varepsilon_h}\left(\omega_E+\omega_{\nabla B}\right)^2+\left(\frac{\varepsilon_t}{\varepsilon_h}\right)^{3/2} \times\left[\frac{\omega_{\nabla B}^2}{4}+0.6\left|\omega_{\nabla B}\right|\frac{\nu_{\rm D}}{\varepsilon_h}\left(\frac{\varepsilon_t}{\varepsilon_h}\right)^{-3/2}\right]+3\left(\frac{\nu_{\rm D}}{\varepsilon_h}\right)^2\right\}^{-1}, \tag{9.4.3.3}$$

where $\omega_E = cE_r/(Br)$, and $\omega_{\nabla B} = -cT\varepsilon_h' x/(eBr)$ [231]. The pitch angle dependence in $\omega_{\nabla B}$ is neglected. Thus, the resonance can only exist in one of the plasma species for a given sign of the radial electric field. This is in contrast to the connection formula for the neoclassical toroidal plasma viscosity in section 8 where the pitch angle dependence is not neglected. Note that there are no parallel plasma flows in the thermodynamic forces because $(\Gamma^{\rm na})_r$ is calculated from the solution of the bounce averaged drift kinetic equation.

The E_r for the ambipolar state is determined by $\sum_j e_j(\Gamma^{\rm na}_j)_r = 0$. This equation has bifurcated solutions because the equation is a non-linear function of E_r [290, 291]. When ion particle transport dominates, E_r is negative. This is called the ion root. The radial electric field is positive, when the electron particle flux dominates. This is called the electron root. In between these two roots, there can be multiple solutions. Some of the roots are unstable. The stability of the roots can be classified according to the extremes of the generalized heat production rate [231]. The stable roots are at the minima of the heat production rate and the unstable roots correspond to the maximum production rate. The transition of ion root to electron root or vice versa can be a mechanism for the formation of the improved confinement region in stellarators. There are other bifurcation mechanisms that could be responsible for the L–H in the edge region of stellarators [237].

9.4.4. H-mode. High confinement mode also exists in stellarators. In the edge region of the stellarators besides the orbit loss mechanism, the bifurcation can be triggered by $(\Gamma^{\rm na})_r$ in equation (9.4.2.3) together with the non-linear plasma viscosity in the plateau–Pfirsch–Schlüter regime in section 8. The dimensionless steady-state poloidal momentum balance equation for a classic stellarator in cylindrical coordinates is [237]

$$-\frac{32}{9(2\pi)^{3/2}}\frac{\varepsilon_t}{|m-nq|\,\nu_*^h}\left[I^{(1)}_{1/\nu}\left(M_{\rm p}-U_{\rm p,p}\right)-I^{(2)}_{1/\nu}U_{{\rm p},T}\right] = \frac{\sqrt{\pi}}{4}\sum\nolimits_{m,n}\varepsilon_{mn}^2 m^2 \times\left[I^{(1)}_{mn}\left(M_{\rm p}-U_{\rm p,p}\right)-I^{(2)}_{mn}U_{{\rm p},T}\right] +\varepsilon_t^2\frac{\nu_{\rm cx}}{v_t/(Rq)}\frac{1+2q^2}{q^2}\left(M_{\rm p}-U_{\rm p,p}\right), \tag{9.4.4.1}$$

where $\nu_*^h = \nu Rq/(v_t\varepsilon_h^{3/2}|m-nq|)$, $M_{\rm p} = cE_r/(v_t B_{\rm p})$, $U_{\rm p,p} = -cp'/(Nev_t B_{\rm p})$, $U_{{\rm p},T} = -cT'/(Nev_t B_{\rm p})$, $\nu_{\rm cx} = N_n\langle\sigma v\rangle_{\rm cx}$ is to denote charge exchange frequency, N_n is the density for neutral particles, $\langle\sigma v\rangle_{\rm cx}$ is the charge exchange cross section, $I^{(j)}_{1/\nu} = \int_{\sqrt{\nu_*^h}}^\infty {\rm d}x 2x^9(x^2-5/2)^j{\rm e}^{-x^2}$ by approximating the energy dependence in the collision frequency as x^{-3}, and

$$I^{(j)}_{mn} = \pi^{-1}\int_0^{(\nu_*^h)^{1/4}}{\rm d}x 2x^5\left(x^2-5/2\right)^j \times{\rm e}^{-x^2}\int_{-1}^1 {\rm d}y\left(1-3y^2\right)^2 R_{mn}\nu\chi'/B, \tag{9.4.4.2}$$

for $j = 1$, and 2. The coupling between $M_{\rm p}$ and $V_{||}/v_t$ is neglected in equation (9.4.4.1) by assuming that $|V_{||}/v_t| \ll 1$ for simplicity. The definition for $I^{(j)}_{mn}$ is the same as that in

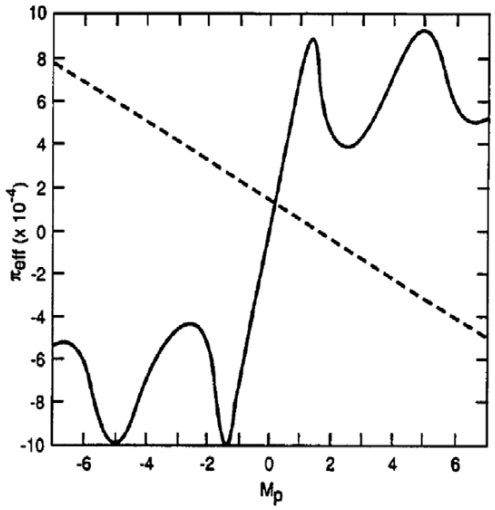

Figure 28. The graphic solution for M_p in L-mode plasmas with $\nu_* = 15$, and $U_{p,p} = U_{p,T} = 0.25$. The dashed line is for the term on the left-hand side of equation (9.4.4.1) and the solid line is the non-linear plasma viscosity from the right-hand side of equation (9.4.4.1).

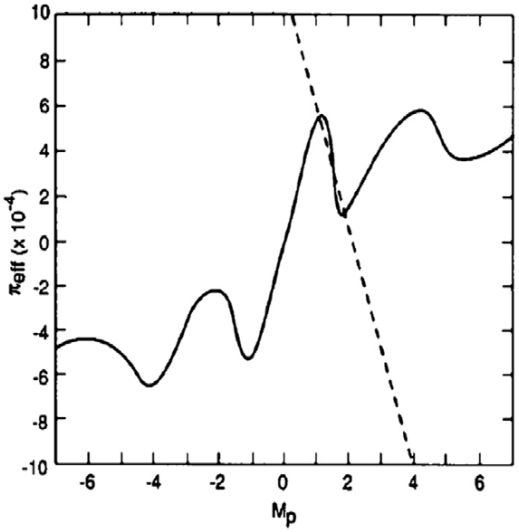

Figure 29. Multiple solutions for M_p with $\nu_* = 7.5$, and $U_{p,p} = U_{p,T} = 0.50$. The dashed and solid lines are from the left- and right-hand sides of equation (9.4.4.1) respectively.

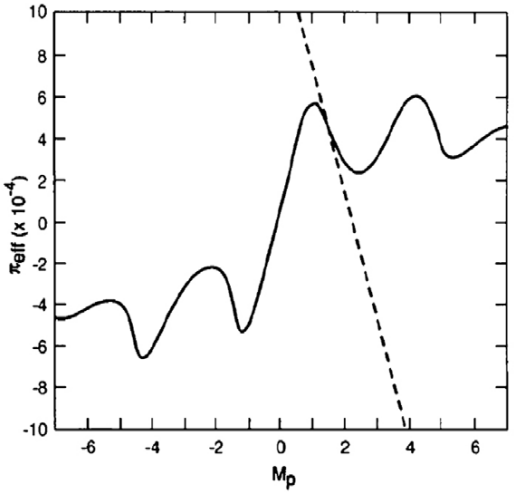

Figure 30. The H-mode solution for M_p with $\nu_* = 7.0$, and $U_{p,p} = U_{p,T} = 0.55$.

equation (8.3.1.4) except that the upper integration limit is $(\nu_*^h)^{1/4}$ instead of ∞ to account for the fact that particles with normalized speed faster than $(\nu_*^h)^{1/4}$ are not in the plateau–Pfirsch–Schlüter regime. It is assumed that these higher speed particles are in the $1/\nu$ regime and is modelled on the left-hand side of equation (9.4.4.1).

The steady-state solutions for equation (9.4.4.1) are found using a graphic method for a given set of parameters: $\varepsilon_t = 0.053, \varepsilon_h = 0.025, q = 1.92, m = 2, n = 5, \nu_{cx} Rq/v_t = 0.01$ and $U_{p,p} = U_{p,T} = 0.25$ [237]. In figure 28, $\nu_* = 15$, there is only one solution, which is the L-mode solution. There are two local maxima in the non-linear plasma viscosity when M_p is positive. The first local maximum, which is slightly larger than 1, is from the Pfirsch–Schlüter regime associated with the $(1, 0)$ toroidal mode. The second local maximum is from the (2,5) helical mode that is in the plateau regime. As ν_* decreases to 0.75 and $U_{p,p} = U_{p,T} = 0.50$, there are three solutions as shown in figure 29. The one in the middle is unstable. The new solution with higher value of M_p is the H-mode solution. When ν_* decreases further to 0.70 and $U_{p,p} = U_{p,T} = 0.55$, there is only one solution which is the H-mode solution (figure 30). The turbulence is suppressed according to the turbulence suppression theory in section 7, and confinement is improved.

The L–H transition theory in equation (9.4.4.1) is also applicable for a rippled tokamak. In that case, only (1,0) toroidal mode contributes to the non-linear plasma viscosity. The $(0,n)$ ripple mode contributes to the $1/\nu$ transport flux. The $1/\nu$ transport flux in a rippled tokamak differs from those in stellarators and tokamaks with broken symmetry in that the new class of ripple trapped particles exists only in part of the (r, ϑ) plane [211]. Thus, there is an additional geometric factor in the $1/\nu$ transport flux [211].

The generic non-linear behaviour for the bifurcated solutions for the momentum equation is similar for tokamaks and stellarators as expected. The important physics is the non-linearity in the plasma viscosity, which is derived from the solution of the drift kinetic equation. It should be noted that when the poloidal plasma flow is sonic, a shock can form and plasma viscosity will be greatly enhanced [132].

In many aspects, the confinement of H-mode plasmas in stellarators is similar to that in tokamaks. However, there is one significant difference. In tokamaks, orbit squeezing leads to reduced neoclassical transport losses. However, orbit squeezing can increase the neoclassical losses in stellarators. For example, in the $1/\nu$ regime, ion transport loss is increased as a result of the increased fraction of trapped particles due to orbit squeezing [292]. In this regard, the confinement improvement factor in H-mode in stellarators may not be as large as that in tokamaks.

9.4.5. Non-linear plasma viscosity driven fluxes. From the flux–force relation, the non-linear plasma viscosity in section 8 also drives transport fluxes in the plateau and Pfirsch–Schlüter regimes in stellarators. The magnitudes of the transport fluxes are usually smaller than the friction force driven fluxes in the Pfirsch–Schlüter regimes. Because both parallel flow speed and radial electric field appear in the viscous forces, the viscous force driven transport fluxes can be obtained after these quantities are determined from the coupled non-linear force balance equations. The procedure is the same as that demonstrated in sections 9.1 and 9.2.

10. Neoclassical toroidal viscosity: experimental results from stellarators and implications to ITER

10.1. Parallel viscosity

In general, neoclassical parallel viscosity plays a role only in the poloidal direction in flow damping and there is no neoclassical toroidal (CGL) viscosity in an axisymmetric system (in tokamaks). Neoclassical toroidal (CGL) viscosity appears only when the toroidal symmetry is broken by a perturbation magnetic field. Therefore, the neoclassical toroidal viscosity is tested by comparing the response of the plasma rotation to the perturbation magnetic field. In stellarators, the neoclassical parallel viscosity plays a role both in the toroidal and poloidal directions and plasma tends to flow along the symmetric direction where the parallel viscosity is minimum when there is no toroidal torque input. In the non-axisymmetric system both toroidal and poloidal flows (not just the toroidal flow) are compared with that predicted by neoclassical theory for a 3D magnetic structure in a stellarator [46, 108].

Parallel viscosity is the mechanism of flow damping due to collisions between trapped particles and transit particles. The parallel viscosity due to collisions with banana orbit particles appears in the poloidal direction as poloidal viscosity in a tokamak, while the parallel viscosity due to collisions with helical ripple trapped particles appears in the poloidal and toroidal directions in helical systems. When there is a magnetic island in the plasma, the magnetic flux surface loses toroidal symmetry even in a tokamak, and this symmetry breaking causes additional viscosity in the plasma. In experiment, the parallel viscosity in a helical system and the viscosity due to symmetry breaking such as by a magnetic island have been investigated.

10.1.1. Toroidal viscosity. In helical plasmas, there is no symmetry in the toroidal direction. Therefore, the toroidal flow tends to damp due to the non-axisymmetric magnetic field. This is the damping mechanism due to collisions between the trapped particles and passing particles, which is called the parallel viscosity. The parallel viscosity becomes important only in the poloidal flow in an axisymmetric magnetic configuration such as in a tokamak.

In contrast, the parallel viscosity becomes important both in toroidal and poloidal flows in the cases where the toroidal symmetry is broken such as by a magnetic island or in a helical device. In general, both toroidal and poloidal flows are determined by the balance between the damping force and the driving force. The driving force in the poloidal direction is dominated only by the non-ambipolar flux, while the driving force in the toroidal direction can be dominated by the toroidal torque from a tangentially injected neutral beam (NB).

In the compact helical system (CHS), the toroidal flow profiles were measured in the plasma with tangentially injected NB in order to compare the parallel viscosity evaluated experimentally to that predicted by neoclassical theory [293, 294]. Since the magnitude of the parallel viscosity depends on the magnitude of the ripple, it can be significantly changed by the magnetic axis shift in a Heliotron configuration. In the configuration with an outer axis shift, where the parallel viscosity is large enough, the toroidal torque injected by NBI is balanced by the neoclassical parallel viscosity and the parallel viscosity experimentally determined agrees with the neoclassical prediction within a factor. In contrast, when the parallel viscosity becomes small in the configuration with an inner axis shift, the toroidal rotation observed in the plasma is much smaller than that predicted by neoclassical parallel viscosity. This is due to the flow damping due to anomalous perpendicular viscosity. Figure31(a) shows the radial profiles of the neoclassical toroidal viscosity coefficient [295, 296], $\mu_{||}$, calculated by including all magnetic field Fourier spectral components of the finite $\bar{\beta}$ equilibrium in the plateau regime in the CHS. Here the toroidal viscosity coefficient is defined as

$$\mu_{\parallel} = 2\frac{\sqrt{2eT_i/M_i F}}{\lambda_{\mathrm{PL}\zeta} R B_\zeta}, \qquad (10.1.1.1)$$

where $2\pi F$ is the poloidal current outside the flux surface and N, M_i and T_i, are ion density, mass and temperature, respectively. In CHS, ions are in the plateau collisionality regime and $\lambda_{\mathrm{PL}\zeta}$ is defined as

$$\frac{1}{\lambda_{\mathrm{PL}\zeta}} = \left(\frac{\sqrt{\pi}(F + (\iota/2\pi)G)}{2\langle B^2\rangle}\right)\left\langle\left(\frac{B_\zeta\cdot\nabla B}{B}\right)\right.$$
$$\left.\times\sum_{mn}\frac{1}{|m(\iota/2\pi)+M_\mathrm{t}n|}\left(\frac{\hat{n}\cdot\nabla B}{B}\right)_{mn} \mathrm{e}^{\mathrm{i}(m\theta+M_\mathrm{t}n\zeta)}\right\rangle,$$

where m and n are the poloidal and toroidal period numbers of the magnetic field spectrum, and M_t is the toroidal field periodicity in the helical device. By replacing the terms of the Fourier series with $1/(m(\iota/2\pi)+M_\mathrm{t}n)(\hat{n}\cdot\nabla B/B)$, making the approximation of single helicity ($n = 1$, $m = 2$, then $M_\mathrm{t} \gg m\,(i/2\pi)$), ignoring the difference between parallel and toroidal viscosity ($B_\zeta \approx B$ and $(B_\zeta\cdot\nabla B)/B \approx \hat{n}\cdot\nabla B$), and taking the large aspect ratio limit ($F \approx B_\zeta R$) with no net current ($G = 0$), this formula is approximated to be $(1/2)(\sqrt{\pi}R\gamma^2)/M_\mathrm{t}$. Then the viscosity coefficient is simplified as $\mu_{\parallel} \approx \sqrt{\pi}\gamma^2(R/M_\mathrm{t})/\sqrt{2eT_iM_i}$. This formula is identical to the Shaing formula [81] by replacing ω_ti with $\omega_{\hbar\mathrm{i}} = (\nu_{\mathrm{th}}M_\mathrm{t}/R)$.

The toroidal viscosity coefficient increases very rapidly towards the plasma edge, which gives strong damping of the toroidal rotation velocity. As the magnetic axis, R_ax is shifted outward, the toroidal viscosity coefficient increases even near the plasma centre. The increase of the toroidal viscosity coefficient by shifting the plasma from 89.9 cm, where there is negligible ripple, to 97.4 cm, where the helical ripple is more than 2%, is one order of magnitude near the plasma centre. As seen in figure 31(b), the central inverse parallel

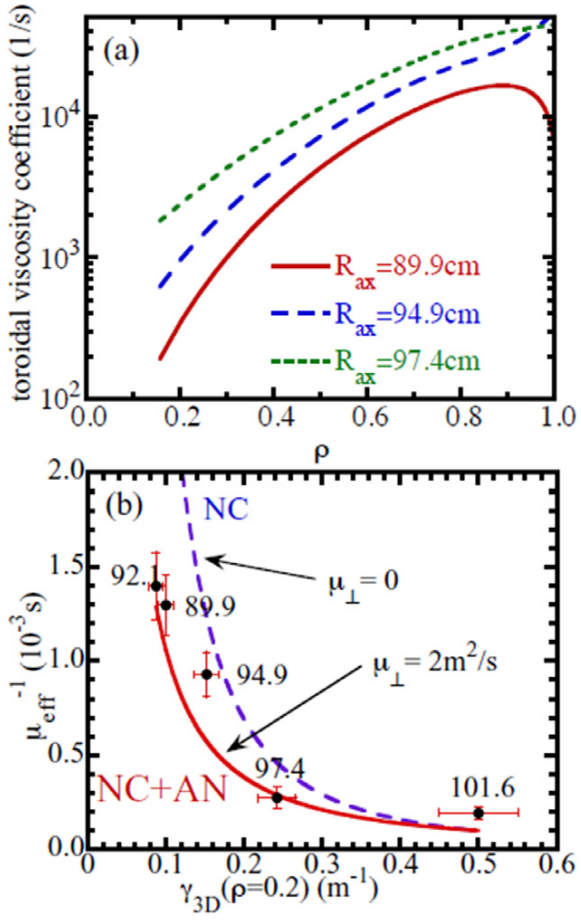

Figure 31. (*a*) Radial profile of the toroidal viscosity coefficient in the CHS torsatron/heliotron for the vacuum magnetic axes of $R_{ax} = 89.9$, 94.9 and 97.4 cm and (*b*) inverse central parallel viscosity derived from the measured central parallel viscosity, density and momentum input as a function of the central modulation of magnetic field strength. The dashed line is an estimate by the neoclassical parallel viscosity and the solid line shows the radial-diffusion-of-momentum effect on the measurements (from figures 2 and 4 in [294]).

viscosity evaluated from the torque input from tangential NBI and toroidal rotation measured with charge exchange spectroscopy decreases as the modulation of the magnetic field strength γ_{3D} increases. Here γ_{3D} is defined as $\gamma_{3D}^2 = \mu_\parallel/(\sqrt{2\pi e T_i/M_i}(R/M_t))$. When the γ_{3D} is less than 0.3 m^{-1}, the damping of toroidal rotation due to the perpendicular viscosity (transport of momentum) becomes comparable to the damping due to the parallel viscosity. The perpendicular viscosity is evaluated to be 2 m^2 s^{-1} in the plasma with $\gamma_{3D} \sim 0$ and assumed to be unchanged for all configurations with different γ_{3D}. By adopting the parallel viscosity predicted by the neoclassical value, the experimental data show good agreement with predictions. Therefore, the experiment in CHS clearly demonstrates that the neoclassical prediction [46, 81] agrees with the measurements.

A comparison of parallel viscosity between the experimental results and neoclassical prediction was made in the helically symmetric experiment (HSX). The plasma flow is driven by the $\boldsymbol{J} \times \boldsymbol{B}$ force due to the radial current drawn by an electrode inserted inside the last closed magnetic surface. The plasma flow is measured with Mach probes. The magnitude of the parallel viscosity can be decreased by changing the configuration from a mirror configuration to a quasi-helically symmetric (QHS) configuration [297, 298]. The spin-up and decay rates of the parallel flow are measured with the Mach probe after the onset and turn-off of the electrode pulse. As seen in figure 32, the spin-up and decay rate is 1–3 kHz (0.3–1 ms) near the plasma periphery ($r/a = 0.7$–1.0) and the spin-up rate is higher for the mirror configuration than the QHS configuration. The spin-up rate for both configurations shows good agreement with the neoclassical prediction. Significant reduction of the damping rate of flow in the QHS configurations is observed as predicted by neoclassical theory. The time scale of the spin-up rate of the flow at the onset of electrode voltage is consistent with the neoclassical prediction. However, the rate at which the flows are damped is not consistent with neoclassical theory; the measured damping dates are much larger than the prediction by a factor of approximately 10 for the QHS configuration and 5 for the mirror configuration. One of the candidates causing the fast damping of flow after the electrode voltage is turned off is the viscosity due to the collision with neutrals.

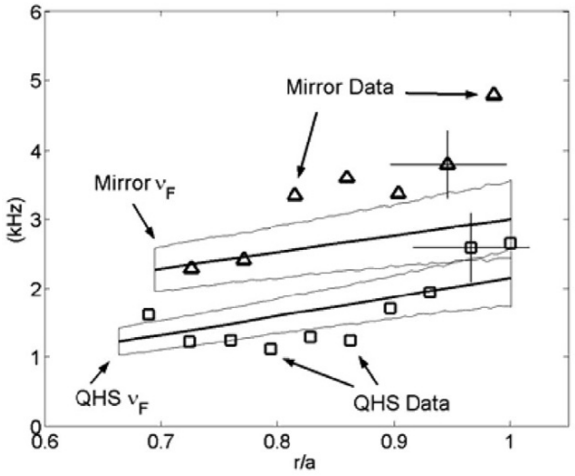

Figure 32. Measured spin-up rate of parallel flow after the onset of electrode bias in the QHS configuration and mirror configuration. The theoretical rates predicted by neoclassical theory are also indicated with ν_F (from figure 1 in [297]).

The experiment in HSX contrasts with the experiment in CHS. The magnitude of parallel viscosity is decreased by changing the configuration towards the increase of toroidal symmetry in CHS and helical symmetry in HSX. The driving force was the toroidal torque from NBI in CHS, while it is the $\boldsymbol{J} \times \boldsymbol{B}$ force from the electrode. The plasma flows were measured with Doppler shift of the impurity line in CHS, while it is with Mach probe in HSX. In both experiments, the plasma flow is consistent with the neoclassical prediction, but some mechanism increasing the viscosity in the plasma was pointed out, which is anomalous perpendicular viscosity in CHS and neutral drag in HSX. In both experiments, the observation shows reasonable agreement with the prediction from neoclassical parallel viscosity [81].

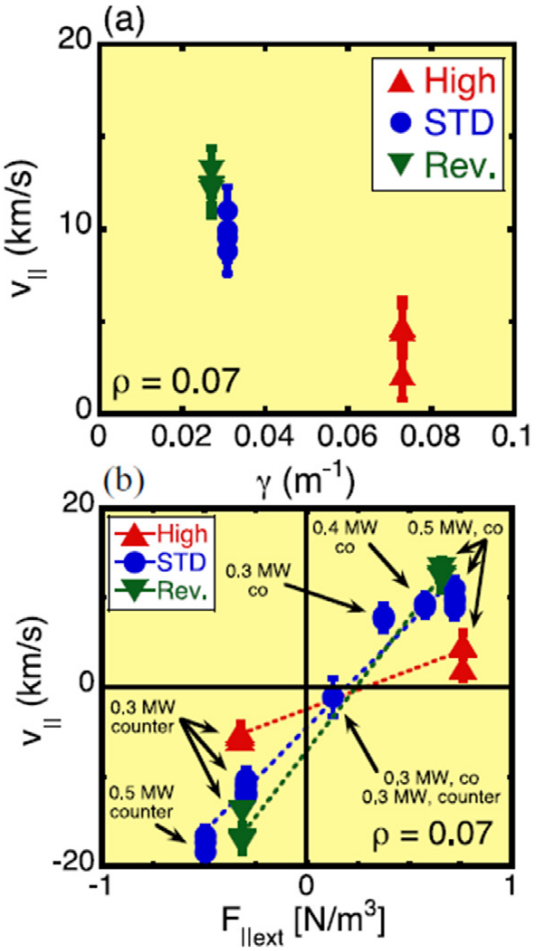

Figure 33. Measured parallel flow velocities (a) as a function of the magnetic ripple strength and (b) as a function of the external momentum input in the three mirror configurations at $r = 0.07$ in Heliotron-J (from figures 9 and 10 in [299]).

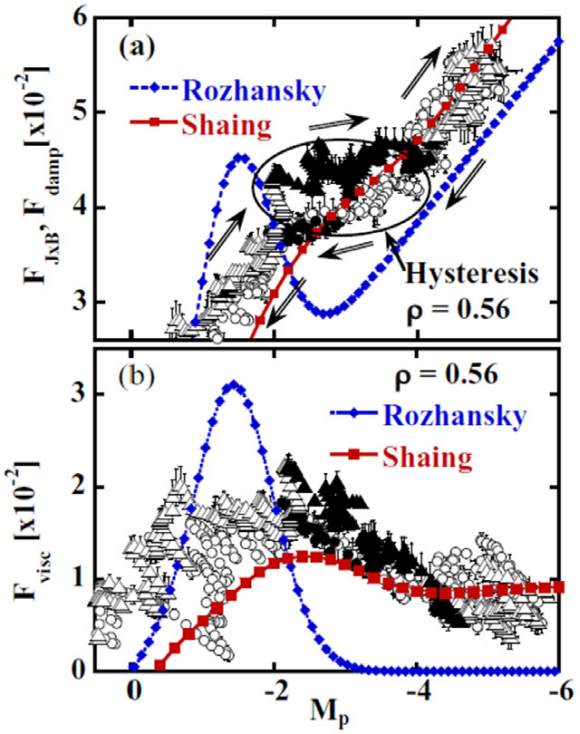

Figure 34. The dependence of (a) poloidal driving force, $F_{J\times B}$, and momentum damping force, $F_{\rm damp}$, and (b) the ion viscosity, $F_{\rm visc}$, on poloidal Mach number, $M_{\rm p}$, at $r = 0.56$. The line with closed diamonds shows the calculation data for ion viscosity applied to the Rozhansky and Tendler model and that with closed squares to the Shaing model. The closed symbols in the experimental results correspond to the data in the negative resistance region. The local maximum of the ion viscosity at $M_{\rm p} \sim 2$ was observed both for the theoretical prediction and the experimental results (from figure 7 in [302]).

The offset of rotation in the counter-direction was observed in Heliotron-J [299]. The parallel velocities are measured with charge exchange spectroscopy in the plasmas with both for co- and counter-NBI for high, standard and reversed mirror configurations, where the magnetic ripple strength changes from 0.073, 0.031 to 0.027 $\rm m^{-1}$. As seen in figure 33(a), the measured parallel flow decreases as the magnetic ripple strength, γ, is increased. This γ dependence of parallel flow observed is quite consistent with the previous results reported in CHS. It is interesting that the offset of rotation (non-zero parallel flow and the zero external momentum input) is observed in this experiment as seen in figure 33(b), which was not identified in CHS experiments. The offset parallel flow is recognized as the neoclassical toroidal viscosity torque, which has been discussed in tokamaks [300].

10.1.2. Poloidal viscosity. In stellarators both poloidal and toroidal viscosities are important to determine the flow pattern in the plasma. According to neoclassical theory, when the poloidal rotation velocity exceeds critical values, the poloidal Mach number, $M_p = (B_\zeta/B_\theta)(V_{E\times B}/v_{\rm th})$ of unity, the neoclassical parallel viscosity starts to decrease and therefore a large sudden increase in poloidal rotation velocity and radial electric field is expected. The poloidal viscosity is measured in the biasing experiment with an emissive polarization probe in the Tohoku Heliac [301, 302]. Figure 34(a) shows the damping force due to the poloidal viscosity and friction with neutral particles. The solid lines and dashed lines are the neoclassical ion viscous damping forces including the friction term with neutral particles predicted by the Shaing model [237] and the Rozhansky and Tendler model [303].

Because of the low edge temperature, the friction with neutral particle can be significant in this experiment. The damping force increases more or less linearly as the poloidal Mach number is increased and the peak near the poloidal Mach number $-M_{\rm p}$ of $\sim$2 is due to the contribution of the neoclassical poloidal viscosity. Figure 34(b) shows the ion poloidal viscosity as a function of the poloidal Mach number. Here the friction with neutral particles is subtracted in order to compare the experimental results with the neoclassical poloidal viscosity. The viscosity drops to zero in the Rozhansky and Tendler model, while the Shaing model gives finite viscosity at higher poloidal Mach numbers $-M_{\rm p} > 3$. The poloidal viscosity measured starts to decrease when the poloidal Mach

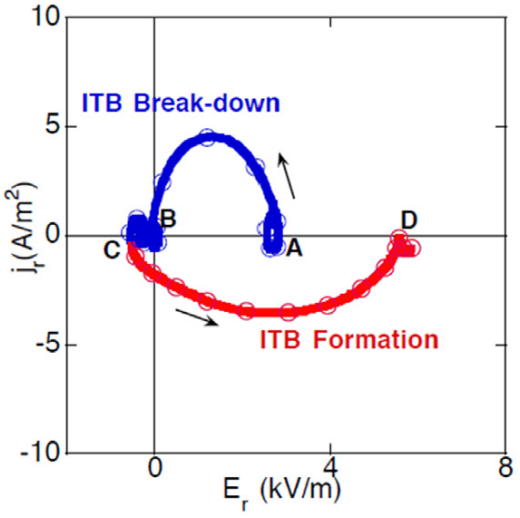

Figure 35. Experimental radial current, j_r, as a function of radial electric field, E_r. The open circles are plotted every 64 μs (modified from figure 3 in [305]).

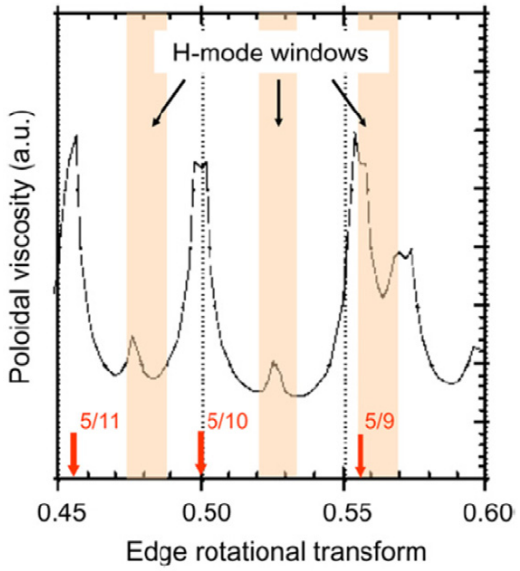

Figure 36. Poloidal viscosity versus edge rotational transform for W7-AS vacuum field conditions. The maxima are linked to the edge island chains which vary in this iota range from 5/11 to 5/10 to 5/9. The H-mode windows are linked to the periodic field structure. Two windows are located at the viscosity minima (from figure 16 in [308]).

number $-M_p = 1 - 2$ but does not completely drop to zero, which is more consistent with the Shaing model.

The biasing experiment can be done only near the plasma edge, where the effects of neutral cannot be neglected. Since the radial current due to the ion non-ambipolar flux is cancelled by the electron radial current, the net radial current is always zero in the steady state in the core plasma. Therefore, it is not easy to evaluate the ion non-ambipolar flux in experiment. However, a radial current, which produces the $\boldsymbol{J} \times \boldsymbol{B}$ force to make the plasma rotate can be evaluated from the change in the radial electric field, because the time scale of the transition of the radial electric field is connected to the magnitude of the radial current [304]. The radial current which drives the poloidal flow and the radial electric field can be evaluated in the transient phase where the radial electric field changes rapidly at the events of the transition from an L-mode plasma to an ITB plasma and back transitions. Figure 35 shows the radial current evaluated from the time derivative of the radial electric field at the formation and termination of the ITB, where the large positive radial electric field is produced. The radial current measured is consistent with the neoclassical prediction [305, 306], which also supports the idea that the poloidal viscosity is close to that predicted by neoclassical theory.

The poloidal viscosity is expected to drop in the plasma with higher temperature and/or low neutral density as the poloidal Mach number exceeds unity. Therefore, the spin-up of the poloidal rotation due to the reduction of poloidal viscosity is one of the candidates of the L- to H-mode transition [15]. The reduction of the poloidal viscosity near the critical poloidal Mach number well explains the poloidal rotation profiles at the L-mode to H-mode transition in JFT-2M [307]. The width of the large poloidal flow region is determined by the neoclassical poloidal viscosity and turbulent perpendicular viscosity. The study of the H-mode boundaries in W7-AS gave strong evidence of the role of neoclassical poloidal damping for the H-mode transition conditions [308, 309]. Figure36 shows the neoclassical poloidal damping due to specific field Fourier coefficients, which compose the field structure at the edge of W7-AS. The H-mode can be realized in W7-AS at a low power threshold but only in isolated iota windows. Apart from the high-iota window, the quiescent H-modes develop at the minima of poloidal damping. These windows are periodically linked to the island chains 5/11, 5/10 and 5/9 whose associated chain of natural islands establishes the inner separatrix.

In Heliotron-J, the transition from the L-mode to the H-mode is observed in a wide range of iota window. However, there are iota windows for the good H-mode discharges. HISS95-factors exceed 1.3 in the regions where the $\iota/(2\pi)$ values are close to the low order of resonances of $n/m = 4/8$, 4/7 and 12/22 [310]. In LHD, the transition from L-mode to the H-mode is observed only in the configuration with an outward magnetic axis shift of $R_{ax} = 3.9{-}4.1$ m, where the low order of resonances of $n/m = 1/1$ are located in the stochastic region near the plasma edge. There is no L- to H-mode transition observed in the standard and inner shifted configuration ($R_{ax} > 3.9$ m), where the $n/m = 1/1$ resonance surface is located in the interior region of the plasma [311]. The relation between ELM activity and rational surfaces is also investigated in LHD. The ELM activity vanishes with a small change of the edge rotational transform. A precise profile measurement of the edge density bursts confirmed that ELM activity occurs at the $\iota/(2\pi) = 1$ position [312]. These experiments suggest the importance of poloidal viscosity damping and the magnetic structure of the rational surfaces and the magnetic island, which will be discussed in section 10.3.

10.2. Plasma flow along minimum viscosity

10.2.1. Parallel flow in the plasma with large radial electric field. In helical plasmas, both toroidal and poloidal flows are affected by the damping process due to parallel viscosity. The

symmetric direction, where the parallel viscosity is minimum, is between the toroidal and poloidal directions. In a tokamak, this symmetric direction is the toroidal direction and the toroidal flow is parallel to the $\langle \boldsymbol{E}_r \times \boldsymbol{B}_\theta \rangle$ drift direction. However, in helical plasmas, the toroidal flow anti-parallel to the $\langle \boldsymbol{E}_r \times \boldsymbol{B}_\theta \rangle$ drift direction is observed because of the pitch angle of the symmetric direction is larger than the averaged pitch angle of the magnetic field [313].

Plasma flow along the symmetric direction is observed in HSX [314] and CHS, when a large electric field exists in the plasma and the plasma flow is mainly determined by the intrinsic flow. The reversal of the toroidal flow is observed when the second electron cyclotron heating (ECH) pulse is applied to the NBI plasma and the electron temperature gradient and poloidal rotation velocity in the ion diamagnetic direction becomes large (hot electron mode) as shown in figure 37(a). The poloidal and toroidal rotations for the discharges without the second ECH pulse are also plotted as a reference. The electron temperature increases up to 2 keV (hot electron mode), while it is only 0.2 keV when there is no second ECH pulse. During the second ECH pulse, the electron collisionality is low enough to make the plasma to be in the electron root (positive electric field), which is consistent with neoclassical prediction. The positive radial electric field is mainly contributed by the poloidal flow in the ion diamagnetic direction. Figure 37(b) shows the contours of the magnetic field strength on the magnetic flux surface at $r = 0.3$. The minimum ∇B direction is roughly parallel to the pitch angle of the helical coils of $\theta/\zeta = 4$, where θ and ζ are the poloidal and toroidal angles, respectively. On the other hand, the averaged pitch of the magnetic field is only 0.7. The flow reversal in the plasma with ECH shows that the plasma tends to flow along the minimum ∇B direction rather than the direction of the $\langle \boldsymbol{E}_r \times \boldsymbol{B}_\theta \rangle$ drift. In contrast, in the NBI heated plasma without a second ECH, the radial electric field and poloidal flow are small and the toroidal flow is parallel to the direction of the torque input from the NBI. In LHD, the flow in the core region is dominated by the flow driven by the NBI torque. However, the toroidal flow anti-parallel to the $\langle \boldsymbol{E}_r \times \boldsymbol{B}_\theta \rangle$ drift direction is also observed near the plasma periphery in LHD [315].

Plasma flow parallel to the symmetry direction is more pronounced in the HSX plasma which has more complete helical symmetry. Flow velocity profiles are shown in figure 38(a) for 50 kW and 100 kW ECH input power. The symmetry flow increases across almost the entire plasma radius when the input power is increased. The cross symmetry flow did not change measurably. This is because the parallel viscosity has a minimum in the symmetry direction and plasma tends to flow along the minimum viscosity direction. The neutral beam is injected perpendicular to the plasma and there is no external torque and flows indicated in this figure are considered to be intrinsic plasma flows. Viscosity in the direction perpendicular to the direction of symmetry leads to the appearance of a large parallel flow. If the viscosity in the direction of symmetry was exactly zero, the sum of the parallel and perpendicular flows would produce a net flow that moved completely in the direction of symmetry, as shown in figure 38(b). These experiments show that the strong coupling between the toroidal and poloidal flows is important in a stellarator because the symmetry direction,

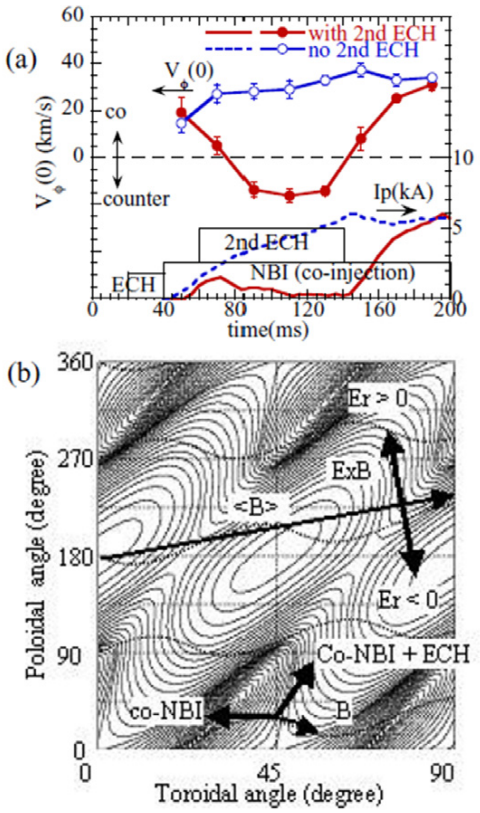

Figure 37. (a) Time evolution of toroidal rotation velocity for the L-mode plasma without a second ECH and the hot electron mode plasma with a second ECH where the large electron temperature gradient is produced and (b) contours of magnetic field strength on the magnetic flux surface at $\rho = 0.3$ (from figure 11.1 in [313] and figure 3 in [316]).

where the neoclassical parallel viscosity becomes minimum, is tilted from the toroidal direction. Therefore, both toroidal and poloidal viscosities should be taken into account to predict the flow structure.

10.2.2. Comparison of flow structure between a stellarator and a tokamak. Because of the 3D effect of viscosity, there is a strong coupling between the toroidal and poloidal flows (or the radial electric field) especially in helical plasmas. This effect drives the 'toroidal flow due to the radial electric field' and can be large enough to exceed the toroidal torque driven by neutral beams and cause a reversal of the toroidal flow. In experiment, the reversal of the toroidal flow is observed in the CHS in the plasma with an electron internal transport barrier, where the strong positive radial electric field and the poloidal flow appear [313]. In this experiment, the toroidal flow is in the co-direction in the NBI heated plasma with a small negative radial electric field. After the onset of the ECH pulse, a large poloidal flow in the ion diamagnetic direction and a positive radial electric field appears in the whole plasma. After a significant increase in the poloidal flow, the toroidal flow in the co-direction (parallel to the current increasing the rotational transform produced by external coil currents) decreases and finally the plasma flow reverses direction in

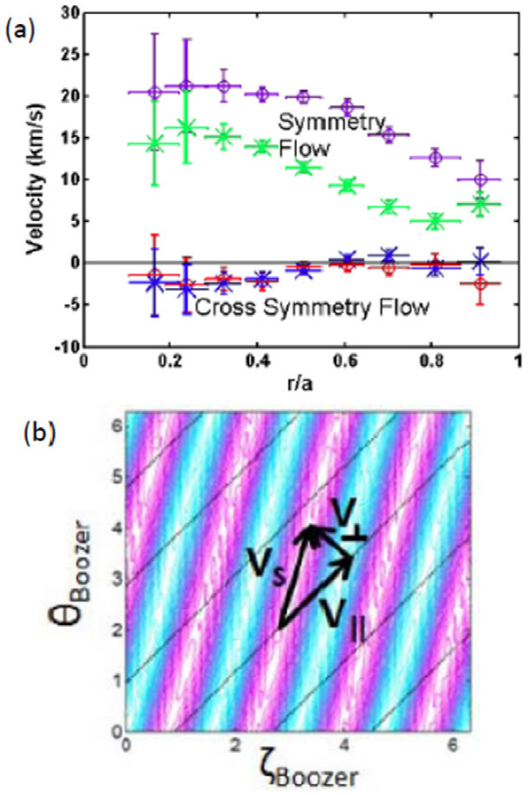

Figure 38. Flow components: (*a*) the measured flow in HSX is primarily in the symmetry direction with a small cross symmetry flow. The flow increases with increasing heating power; ○: 100 kW heating, ×: 50 kW heating. (*b*) Idealized flow component vectors are plotted over magnetic field strength contours and selected magnetic field lines (from figure 13 in [314]).

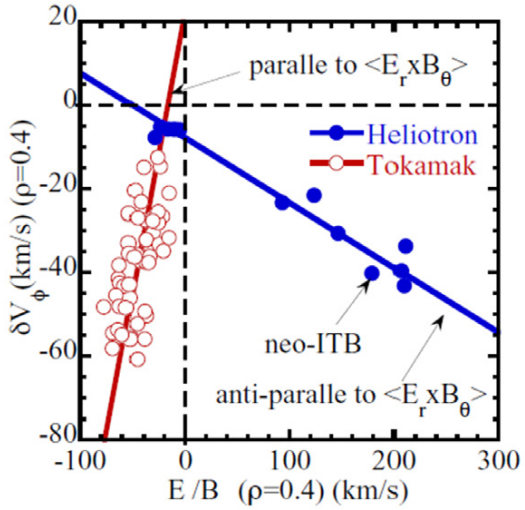

Figure 39. Spontaneous toroidal flow velocity as a function of E_r/B_θ at $\rho = 0.4$ for tokamak and helical plasmas. The solid lines are best fits for the measured data and $\delta V_\phi = -1.5(E_r/B_\theta) - 0.79$ for a heliotron plasma and $\delta V_\phi = 1.34(E_r/B_\theta) + 22.3$ for a tokamak plasma. The positive slope shows the flow parallel to the $\langle E_r \times B_\theta \rangle$ drift direction and the negative slope shows the flow anti-parallel to the $\langle E_r \times B_\theta \rangle$ direction (from figure 7 in [316]).

the counter-direction (anti-parallel to the current increasing the rotational transform). This experiment clearly shows the strong coupling between the poloidal flow and the toroidal flow. Since the pitch of the helical symmetry (the direction of minimum parallel viscosity) is larger than the pitch of the magnetic field averaged over a magnetic flux surface, the poloidal flow in the ion diamagnetic direction (positive radial electric field) contributes to the toroidal flow in the counter-direction. This is in contrast to the poloidal flow in the electron diamagnetic direction (negative electric field) contributing to the toroidal flow in the counter-direction in a tokamak, where there is almost zero parallel viscosity in the toroidal direction because of toroidal symmetry. The differences in the direction of the toroidal flow driven by this mechanism are discussed based on observations in CHS and the JFT-2M tokamak [316].

The spontaneous toroidal flow observed in the plasma in CHS is anti-parallel to the direction of the $\boldsymbol{E}_r \times \boldsymbol{B}_\theta$ drift. This is in contrast to the spontaneous toroidal flow in the direction parallel to the direction of the $\boldsymbol{E}_r \times \boldsymbol{B}_\theta$ drift in tokamak plasmas, which is clearly demonstrated in figure 39. Here the spontaneous toroidal flow is given by the difference of magnitude of toroidal flow velocity between co-injection and counter-injection with a similar magnitude of momentum input. In general, the toroidal flow in a Heliotron plasmas is much smaller than that in a tokamak, because of the toroidal viscosity due to helical ripple [298] which does not exist in tokamak plasmas. However, the spontaneous flow observed in CHS is comparable to that observed in the JFT-2M tokamak. This is because the radial electric field in the CHS plasma with an internal transport barrier is much larger than that in the L-mode plasma in the JFT-2M tokamak. It should be noted that the ratio of the spontaneous flow velocity to the radial electric field normalized by the poloidal field in CHS is 0.15, which is much smaller than that observed in a tokamak (∼1.34) by an order of magnitude. At the internal transport barrier in a tokamak, a spontaneous toroidal flow larger by one order of magnitude than that observed in CHS is expected.

10.3. Damping of poloidal flow inside the magnetic island

The plasma flow inside the magnetic island is an important issue because it affects the growth or healing of the magnetic island. When the magnetic island rotates with the $\boldsymbol{E} \times \boldsymbol{B}$ flow, there is no flow shear at the boundary of the magnetic island. However, when the magnetic island stops or rotates with a speed different from the $\boldsymbol{E} \times \boldsymbol{B}$ velocity, the flow shear should appear at the boundary of the magnetic island. Figure 40 shows the radial profile of poloidal flow measured with high resolution charge exchange spectroscopy in LHD [317, 318].

A magnetic island in a helical plasma usually does not rotate although there is a finite poloidal flow in the plasma. The poloidal flow inside the magnetic island was measured and it was found that the poloidal flow is zero inside the magnetic island, which indicates a flat space potential inside the magnetic island for small and medium sized magnetic islands. Then the strong flow shear appears at the boundary of the magnetic island and it may contribute to the reduction of transport near the boundary of the magnetic island through turbulence suppression by $\boldsymbol{E} \times \boldsymbol{B}$ shear. The

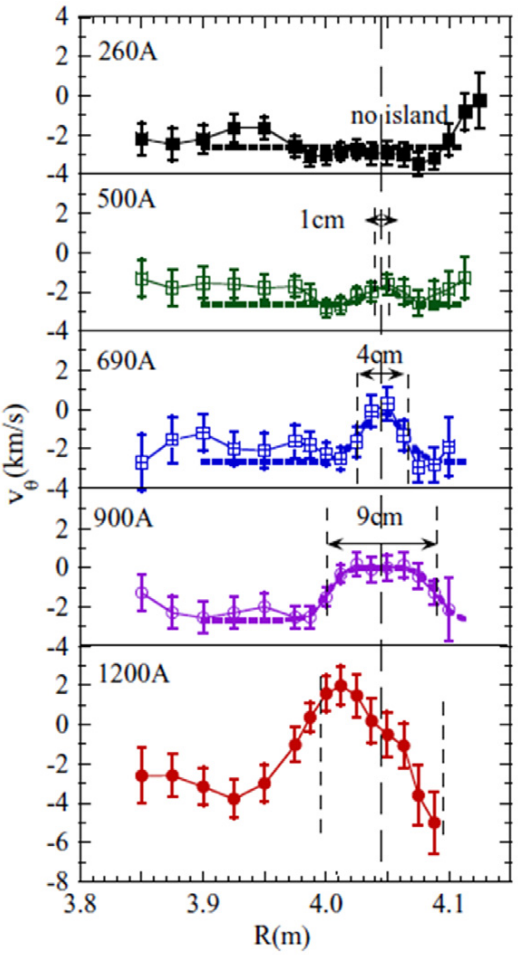

Figure 40. Radial profiles of poloidal rotation velocity for various currents of $n/m = 1/1$ external perturbation coils. The last closed surface is at $R = 4.10$ m at the vertically elongated cross section. The major radius for the centre of the magnetic island, R_i, is indicated with a line as a reference. The dashed lines are profiles of poloidal velocity fitted to the measured values (from figure 2 in [317]).

E_r shear at the boundary of the magnetic island exceeds a few hundred kV m^{-2}, where the turbulence suppression is expected, although the shear region is narrow (1–2 cm). The scale length of the E_r shear is similar to that observed in a zonal flow while the magnitude of shear is much larger than that of a zonal flow [319, 320]. Therefore, the E_r shear at the boundary of the magnetic island should have a strong impact on the transport. In a tokamak, the magnetic island is believed to rotate at the same speed as the $\boldsymbol{E} \times \boldsymbol{B}$ rotation. However, it is not clear whether there is a 'slip' of the rotation. It should be noted that the difference in plasma flow between inside and outside of the magnetic island observed in LHD is only 2 km s^{-1}, which is masked by the uncertainty of the flow measurements in many cases. The width of this island is controlled by external coils and can be varied between 0% and 20% of the minor radius. As a result of the finite ion temperature in LHD, the profile flattening inside the island gives rise to a jump in the ion drift velocity across the separatrix. To satisfy the no-slip condition, this jump is compensated by a discontinuity in the electric field, which may contribute to turbulence suppression. Because the region of E_r shear is narrow even a small jump in the radial electric field may be enough to affect the transport. The interaction of turbulence and magnetic islands is an important issue and theoretical research for this issue has been reported [321].

A theory to determine the radial electric field in the vicinity of a magnetic island based on the island-induced symmetry-breaking transport flux is proposed (see section 8.4) [207]. In this model, the radial electric field is governed by a non-linear equation that can have multiple equilibrium solutions as plasma parameters change (see section 8.4.2) [242]. This results in a bifurcated state of the radial electric field which is observed in the experiments in LHD, when the size of the magnetic island becomes large enough. This theory predicts an important role in the plasma confinement in the vicinity of the lower order rational surfaces and may explain the plasma confinement improvement in the vicinity of the lower order rational surfaces observed in the stellarator and tokamak experiments [322–324]. The mechanism of the transport reduction near the rational surface is not fully understood yet; however, the radial electric field shear near the rational surface is one of the candidates for suppressing the turbulence.

Another interesting observation of the poloidal flow in the magnetic island is the bifurcation phenomena. When the width of a magnetic island exceeds a critical size, a spin-up of the poloidal flow inside the magnetic island is observed. This spin-up causes a finite radial electric field and a peaked space potential profile inside the magnetic island, although the temperature profile is flat inside the magnetic island. This spin-up of the poloidal flow is due to the difference in poloidal flows at the two boundaries of the magnetic island (the boundary inner side and the boundary outer side). It is an important fact that the spin-up of the poloidal flow appears abruptly, which suggests the strong non-linearity of flow damping and/or generation in the vicinity of the magnetic island. The multiple equilibrium solutions of the radial electric field in the vicinity of the magnetic island are also predicted theoretically (section 8.4.2) [242]. It should be noted that the E_r shear at the boundary of the magnetic island tends to disappear when the spin-up takes place for the large size magnetic island. Therefore, strong E_r shear is expected in a plasma with a small magnetic island.

This E_r shear is one of the candidates for the transport improvement mechanism near rational magnetic surfaces, where small magnetic islands may exist. The TJ-II stellarator device was the ideal device to explore the effects of rational surfaces and possible small magnetic islands on the transport, because the rotational transform can be scanned over a wide range $\iota/(2\pi) = 0.9$–2.2 during the discharge [325, 326]. Figure 41 shows the contours of the electron thermal diffusivity in the helical coil current scan during a discharge [327]. The electron thermal diffusivity is derived from the electron temperature gradient measured with ECE, which gives precise relative values, although the absolute value of the gradient may have a large uncertainty due to the calibration. It is clearly demonstrated that the electron thermal diffusivity is strongly coupled with the low order rational surface of $\iota/(2\pi)$ =8/5 and 5/3 indicated with solid lines.

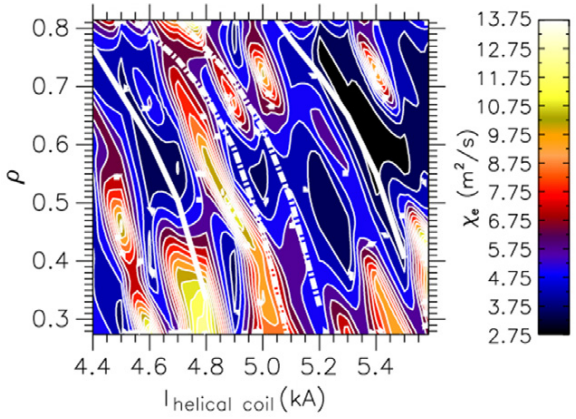

Figure 41. Profiles of electron thermal diffusivity as a function of helical coil current. The vacuum low order rationals $(\iota/(2\pi)) = 8/5$ and 5/3 are shown with white lines. Two higher order rationals $(\iota/(2\pi)) = 13/8$ and 18/11) are indicated with dashed lines (from figure 8 in [327]).

10.4. Implications for ITER

Experiments on toroidal and poloidal viscosities demonstrated that these viscosities have reasonable agreement with that expected from neoclassical theory. At the plasma edge, friction with neutral particle has a significant role and it can be larger than the poloidal viscosity. Since the friction with neutral particles decreases as the edge temperature becomes higher, the friction may not be crucial in large devices such as ITER. Therefore, the experiments on toroidal and poloidal flow suggest that the theory of neoclassical viscosity can give a reasonable prediction of the flow pattern (toroidal and poloidal flows) for the plasma with normal nested magnetic flux surface in future devices such as ITER.

In contrast, the physics of a complicated magnetic topology (magnetic flux surface with magnetic island) is not well understood. For example, the flattening of temperature inside the magnetic island is commonly observed; however, this flattening of the temperature is not due to the enhancement of cross field transport (large thermal diffusivity) but due to the change of topology. The heat flux parallel to the magnetic field becomes significant in this region and most heat flux in the radial direction is through the X-point of the magnetic island [328]. In fact, heat pulse propagation experiments suggest reduction of cross field transport (low thermal diffusivity) inside the magnetic island [329]. The existence of a magnetic island would be crucial in ITER, when the resonance magnetic perturbation field is applied to control the ELM. The magnetic island causes a significant poloidal asymmetry of radial heat flux and also significant complicated flow patterns in the plasma. Therefore, the toroidal and poloidal viscosities in the plasma with a magnetic island should be investigated more in detail, because the toroidal flow plays an important role to stabilize the MHD mode at the plasma edge, while the poloidal flow as well as the zonal flow plays important roles to suppress the turbulence and contribute to the increase in the pressure gradient and MHD activity. Further comparisons of neoclassical viscosity theory to explore are desirable in order to understand the 3D effect on viscosities and to predict the flow at the plasma boundary in ITER.

11. Neoclassical toroidal viscosity in tokamak experiments

11.1. Importance of theoretical NTV expectations for tokamak experiments

The non-ambipolar transport caused by broken toroidal field symmetry in tokamaks has important ramifications for present and future tokamaks. The effects of three-dimensional (3D) magnetic fields with normalized magnetic perturbations $\delta B/B \sim \mathrm{O}\left(10^{-3}\right)$ are currently being used to alter tokamak transport, with a highly notable example being the use of resonant magnetic perturbations to alter the density profile in the pedestal region of tokamaks, to control edge localized modes with direct application to ITER [330]. Tokamak experiments on NTV have focused more directly on the effect of the enhanced plasma viscosity caused by the associated non-ambipolar transport. Studies have logically been more closely tied to the effects of how NTV may alter plasma stability through the variation of the plasma rotation profile, examining the ramifications of slowing or increasing the toroidal plasma rotation, and changing its profile. The effects of toroidal rotation and its shear on MHD modes, e.g. tearing modes and resistive wall modes (RWMs) are well known [331–334].

Verification and understanding of the basic characteristics and scalings of NTV, an inherently 3D effect in tokamaks, is especially important because the particle diffusivity, to which the magnitude of the NTV is related, increases at reduced collisionality (figure 20). Future devices such as ITER [335], FNSF [336, 337] or DEMO [338] will operate at collisionalities of about two orders of magnitude smaller than tokamaks today, and so it will be important to experimentally verify the dependence of NTV on ν, which shown by figure 20 is somewhat complex. The behaviour of NTV in regimes spanning the Pfirsch–Schlüter, plateau, $1/\nu$, B–L, and C–D regimes will be important. Also, very important is the verification of the superbanana plateau (Sb-P) regime, which will create increased NTV at sufficiently low ω_{E}. Determining potential alteration of Sb-P generated NTV at different levels of ν is important. The NTV offset rotation might provide important intrinsic rotation for mode stabilization or sustained H-mode operation in slowly rotating plasmas. As NTV is strongly related to the perturbed 3D field, the ramifications of the amplification of that field due to stable or unstable plasma response is important to understand. NTV can also be used to tailor the plasma rotation and its shear to avoid MHD instabilities by using pre-programmed currents, or in closed-loop feedback using applied 3D fields as actuators. Understanding the dependence of NTV on the key plasma parameters is critical for the successful use of NTV in either pre-programmed or closed-loop feedback. For instance, one must be wary of potential non-linearities, or possible hysteresis due to variations of NTV as the plasma traverses the operating space of a given tokamak.

Bridging from present-day tokamaks to the lower collisionality of ITER and DEMO takes NTV from the $1/\nu$ (section 8.2.1) to the collisional boundary layer $\nu - \mathrm{sqrt}(\nu)$ regime (section 8.2.2) and the collisionless detrapping/retrapping regimes (section 8.2.3) [208, 222]. The superbanana plateau regime (section 8.2.4) can exist in all regimes at reduced collisionality with $\nu_{\mathrm{i}}^{*} < 1$. These

regimes have distinct dependences on plasma collisionality, summarized as follows for ions: the torque due to NTV, $T_{\mathrm{NTVi}} \propto n_{\mathrm{i}}^{K1} T_{\mathrm{i}}^{K2}$, where $K1 = 0$, $K2 = 5/2$ for the $1/\nu$ regime, $K1 = 3/2$, $K2 = 1/4$ for the $\nu - \mathrm{sqrt}(\nu)$ regime, and $K1 = 1$, $K2 = 0$ for the superbanana plateau regime. Simplified, these scalings show a strong increase in the strength of τ_{NTVi} as the plasma becomes collisionless (here defined as collisionality falls below $\nu_{\mathrm{i}}^{*} < 1$), then saturates at lower ν. The extended theory states that at sufficiently low ν, τ_{NTVi} may eventually begin to decrease with decreasing ν. Of particular note is that when the superbanana plateau criterion is met, the T_{NTVi} dependence on ν changes significantly, and increases in magnitude, even though the plasma rotation may be small. Based on these observations, attention should be placed on the potential deleterious effects of strong NTV reducing plasma rotation, and possibly leading to locked tearing modes and global MHD instabilities leading to disruptions at low ν, and separately in the Sb-P regime.

11.2. Non-resonant rotation alteration by applied fields and modes in tokamaks

11.2.1. Non-resonant NTV versus resonant damping, key experimental characteristics. The terms 'non-resonant' and 'resonant' rotation damping are often used to segregate observations of rotation damping in tokamaks by 3D perturbations generated in the plasma by either applied fields and their potential amplification by stable, but weakly damped MHD modes, or MHD instabilities. While they can often become confused with similar terminology on related subjects (e.g. stabilizing resonant kinetic effect applied to MHD modes), these two designations are important because they generally describe torques on a tokamak plasma with critically different dependences on the magnitude of the toroidal plasma rotation frequency, ω_{ϕ}. Extending the classification by Fitzpatrick [339] for low-beta, large aspect ratio tokamak equilibria, Fourier harmonics of modes and error fields can be separated into two classes: 'resonant' when there exists a 'rational flux surface' inside the plasma for which $\boldsymbol{k} \cdot \boldsymbol{B} = 0$, where $\boldsymbol{k}$ is the wave vector associated with the harmonic. A non-resonant harmonic has no such rational surface inside the plasma. A simple example of a resonant mode is a tearing mode, for which the rotation damping due to the electromagnetic interaction of the mode and tokamak error field has been studied [340].

Generally, the damping torque exerted on a rotating plasma due to a resonant harmonic importantly has an inverse dependence on ω_{ϕ}. Therefore, a rotating mode exposed to a resonant braking torque that continually slows the plasma rotation will eventually generate a catastrophic loss of torque balance [339], causing the mode to lock to the typically static resonant error field harmonic, typically causing a plasma disruption (significant thermal collapse, or full current quench). In stark contrast, a non-resonant braking torque typically scales with ω_{ϕ} in such a way that it cannot produce a catastrophic loss of torque balance, which is clearly beneficial in that it will not cause mode locking and associated disruptions. Non-resonant NTV as described in earlier sections exhibits such a characteristic (e.g. NTV scales linearly with ω_{ϕ} in most regimes of interest).

The following brief summary of key characteristics of non-resonant NTV plasma rotation damping compared to resonant damping is useful to help identify the different mechanisms in tokamak experiments.

(A) *Resonant rotation damping.*

(i) Exhibits a localized peak in rotation damping near a rational surface, initially showing a clear outward diffusion of momentum across the rational surface. This increases rotation on the outboard side of the rational surface and decreases it on the inboard side, as the island creates a localized radial flattening of the rotation across the rational surface.

(ii) If momentum input is sufficient to maintain the torque balance, the steady-state evolution of the plasma rotation frequency inside of the rational surface is a rigid rotor ($\omega_{\phi}(\psi) = \mathrm{constant} = \omega_{\phi s}$, which is the value of the plasma rotation at the rational surface).

(iii) Since the magnetic braking torque near the rational surface scales as $1/\omega_{\phi}$, the plasma is subject to loss of torque balance and consequent mode locking. Assuming that the island is locked to the plasma flow (no-slip condition [340]), the plasma slows to zero rotation at the rational surface.

(B) *Non-resonant NTV rotation damping.*

(i) Non-resonant NTV is radially extended and not highly localized, as it is a convolution of a non-resonant perturbed field spectrum (which is typically radially extended in a tokamak plasma), the plasma temperature profile, and the plasma toroidal rotation profile.

(ii) Since the plasma temperature and rotation profiles tend to zero at the plasma boundary, the NTV torque density and related change in toroidal rotation due to NTV tend to zero in this region regardless of the magnetic field perturbation strength in this region.

(iii) There is no clear momentum transfer across a particular rational surface, and no clear localization of momentum damping at rational surfaces. Therefore, when the plasma rotation frequency is significantly greater than the NTV offset frequency, the change in the rotation frequency due to NTV by an applied 3D field retains the same sign versus the minor radial coordinate, in contrast to resonant braking where the change in rotation changes sign across the rational surface.

(iv) For usual tokamak radial profiles, the NTV magnitude changes as a function of flux surface, therefore the profile of the plasma rotation frequency can be changed by NTV, depending on the non-resonant field spectrum applied, or non-resonant mode activity that appears. The local NTV torque density and its profile are therefore important, as its alteration allows more control of the rotation profile than afforded by a highly localized, or integrated external torque.

These characteristics allow the identification of observed magnetic braking in tokamak experiments as either resonant or non-resonant. However, the superposition of these two effects can confuse their interpretation. Therefore, tokamak experiments aimed to study NTV are generally required to have insignificant sources of resonant breaking, e.g. the

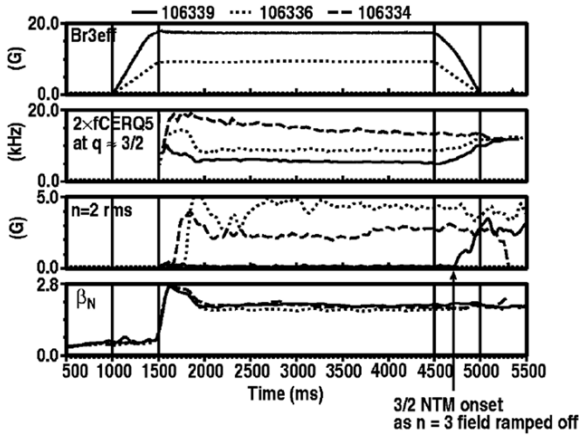

Figure 42. Reduced plasma rotation (frame 2) in DIII-D due to the variation of an applied $n = 3$ field (frame 1).

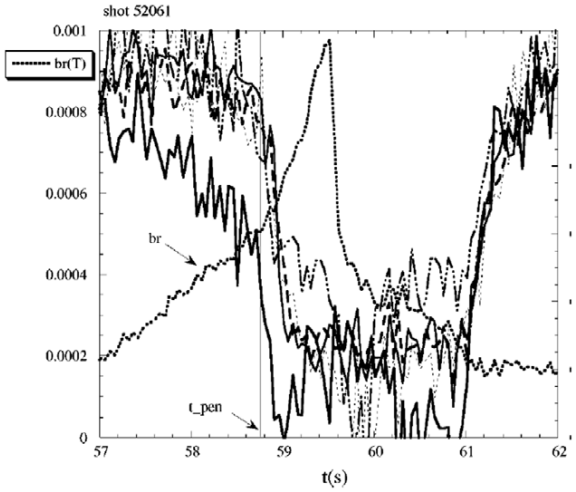

Figure 43. Evolution of measured $m = 2, n = 1$ radial field perturbation (dashed, labelled line) and various radial channels of charge exchange recombination spectroscopy measurements in JET. The time of mode penetration is labelled and indicated with a vertical line.

elimination of strong tearing mode activity. The potential loss of torque balance generated by resonant braking mechanisms also precludes non-resonant NTV studies at low rotation speeds below the threshold for mode locking [341].

Theory and modelling [340–342] of resonant rotation damping preceded the experimental identification of non-resonant NTV. This may have been due to an apparent lack of connection between plasma rotation damping due to resonant (e.g. tearing perturbations of the magnetic field) and non-resonant modes (e.g. ideal perturbations of the magnetic field). The successful model of rotation damping due to tearing modes [340] identified the drag force as an electromagnetic $\boldsymbol{J} \times \boldsymbol{B}$ drag caused by the perturbed currents of the mode interacting with a resonant error field. However, it can be shown that for an ideal plasma perturbation, the corresponding torque is zero.

11.2.2. Early connections to rotation damping induced by applied fields. In research primarily addressing NTM control, it was observed in DIII-D that an applied $n = 3$ perturbation led to a decrease on plasma rotation [37] (figure 42). An important conclusion of the study was that a resonant electromagnetic $\boldsymbol{J} \times \boldsymbol{B}$ force model was not compatible with the observed drag. A key defense made for this statement is related to the $1/\omega_\phi$ dependence of the resonant drag torque. It was argued that mode locking should have occurred once the rotation dropped to half of the steady-state rotation frequency [340]. Instead, a simple empirical model of $n = 3$ ripple field-induced drag related to transit time magnetic pumping (TTMP) [343] was used to fit the experimental results, with a good fit to the observed plasma rotation frequency evolution.

The paper purposefully did not attempt a first-principles computation of TTMP. Also, it is important to note that the magnitude of the radial field perturbation was used in the empirical fits, which would have been insufficient in producing quantitative agreement with NTV theory, which requires the total field perturbation as input. Unlike the majority of the NTV regimes described in section 8, TTMP has a plateau characteristic in that the induced particle diffusivity is not dependent on collisionality.

At about the same time, connection between non-resonant perturbation field harmonics and measured magnetic braking was made for JET plasmas [38]. A new hypothesis was needed to address the JET results, which showed an anomalous fast bulk braking of the plasma toroidal rotation which could not be explained by the resonant braking model. Specifically, the non-resonant $m = 0, n = 1$ sideband of an $m = 2, n = 1$ tearing mode was computed to cause a significant neoclassical toroidal viscous force which could explain the rotation damping by applied resonant error fields, or MHD mode activity. Results from the experiment are shown in figure 43. Here, a resonant $m = 2, n = 1$ field is applied by coils in a slow linear ramp. Before, and up to the time of mode penetration, the resonant braking theory [340] applies, showing localized braking at the rational surface only. Also expected from the theory, the time of mode penetration corresponds to the ω_ϕ at the $q = 2$ surface reaching half of its initial steady-state value. However, after the time of mode penetration, the braking was no longer localized to the rational surface, and unexpectedly the ω_ϕ profile decreases self-similarly ($\omega_\phi(r,t)/\omega_\phi(r,t_0)$ is a function of time alone). Once the applied $n = 1$ field is turned off at $t \sim 59.5$ s, the plasma was observed to recover (figure 43), and it was remarked that the initial ω_ϕ profile was reached in a manner that was also self-similar during the subsequent plasma acceleration phase.

To address the experiment, [38] considered the neoclassical toroidal viscous force $\langle \hat{e}_\varphi \bullet \nabla \bullet \overleftrightarrow{\prod}_i \rangle$ in the plateau regime (section 8.3.1). A key element of the modelling was the inclusion of the non-resonant $m = 0, n = 1$ sideband in the neoclassical toroidal viscous force. This consideration allowed the model to represent the global, non-resonant characteristic of the rotation braking force, as this harmonic had a radially extended profile with significant amplitude in the plasma core. This, superposed with the $m = 2, n = 1$ radial profile, formed the simple perturbed magnetic field spectrum used in the model (figure 44). An *ad hoc* model of the time dependence was used to simulate the experimental time variation of the applied field. The model qualitatively reproduced the self-similar braking

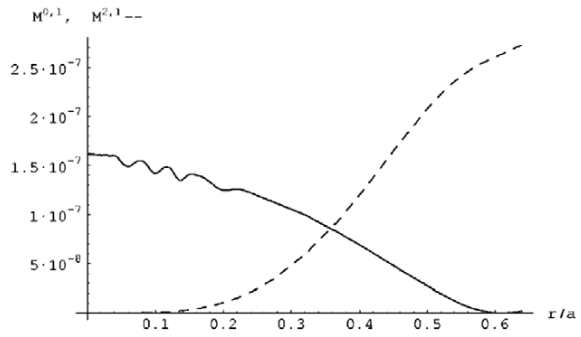

Figure 44. Profiles of the two components used to model the perturbed field in the JET experiment: $m = 2, n = 1$ (dashed line) and the $m = 0, n = 1$ non-resonant sideband (solid line).

characteristic of the experimental results, although the final braking amplitude was too low, indicating that the magnitude of the neoclassical toroidal viscous force was underestimated.

It was recognized that the plateau regime modelling of the neoclassical toroidal viscous force was not adequate, as the region of the plasma near the $q = 2$ surface in these experiments was in the ion banana regime ($\nu_i^* < 1$), and that extension of the model to lower collisionality (section 8.2), specifically highlighting that the $1/\nu$ regime [208, 271] (section 8.2.1) needed to be considered. An estimate was made to determine if the inclusion of the $1/\nu$ regime in the model could bring the calculations closer to the experiment results. An increase of two orders of magnitude was estimated for the braking force in the $1/\nu$ regime compared to the plateau regime. At this level, the observed experimental braking rate would be comparable to the experimental observations.

11.2.3. Early connections to rotation damping by non-resonant global modes. The experimental results shown in section 11.2.2 displayed resonant mode activity, or utilized applied fields resonant with low-order tearing modes (e.g. $m = 2, n = 1$) that can significantly alter plasma stored energy and rotation when destabilized. Studies addressing non-resonant, radially extended plasma rotation braking without strong resonant harmonics or modes are therefore desired. Early experimental demonstrations of such braking were reported in NSTX in connection with ideal plasma RWMs [344]. Such modes have ideal field perturbations in the plasma which typically have a large radial extent (i.e. a global mode). The plasmas used in the studies of non-resonant magnetic braking were shown not to exhibit resonant mode activity, and comparisons of the ω_ϕ profile evolution in cases with non-resonant global RWM activity were compared to cases with saturated $n = 2$ and 3 rotating modes of significant amplitude. The demonstration that an ideal, non-resonant field perturbation alone (here, generated by an ideal plasma RWM) can cause global rotation damping supported the need for a non-resonant theory of toroidal viscosity, since the resonant electromagnetic $\boldsymbol{J} \times \boldsymbol{B}$ force model typically applied at rational surfaces produces no internal torque on an ideal perturbation. This initial finding was further substantiated in continued studies of strong, global plasma rotation damping during RWM destabilization in NSTX [39, 40], which furthered observations that were qualitatively consistent with non-resonant NTV: (i) strong, global rotation damping during RWM activity measured by internal kinetic and external magnetic diagnostics, with (ii) a self-similar decrease of the ω_ϕ profile, significantly different in form compared to the localized, resonant ω_ϕ damping dynamics found during saturated tearing mode activity (which exhibited a clear radially outward momentum transfer across dominant rational surfaces), and (iii) essentially no change in the plasma rotation near the edge of the plasma, regardless of the field perturbation strength.

A computation of the non-resonant NTV torque density profile observed during ideal plasma RWM activity in NSTX [40] was made using the NTV model appropriate for plasmas in the plateau regime (section 8.3.1). These calculations were analogous to the calculations made for JET [38] (described above), except with a significantly different magnetic perturbation profile. In the NSTX calculations, the difference in the electron temperature profile measured by Thomson scattering was used as a proxy for the magnetic perturbation profile. Similar to the result found for JET, the NTV torque density profile qualitatively matched the change in the angular momentum profile based on Thomson scattering and charge exchange recombination spectroscopy (CXRS) measurements of plasma density and ω_ϕ (figure 45).

11.2.4. Observation of non-resonant NTV by applied fields and RWMs. The first quantitative comparison of non-resonant NTV theory that included both the plateau and $1/\nu$ regime formulation with experiment was conducted for NSTX plasmas in conditions that included $n = 1$ applied field configurations, $n = 3$ applied field configurations, significant amplification of the $n = 1$ applied field, and unstable $n = 1$ RWMs [41]. The theoretical calculations followed the models in section 8 utilizing Hamada coordinates. Note the use of the word 'configuration' here. Actually, for each configuration, the full Fourier spectrum of the perturbations generated by a midplane RWM control coil set was computed using the Biot–Savart law on a full 3D model of the coils (which have 3D features), using the time-varying experimental coil currents. It was noted, for instance, that the '$n = 1$ applied field configuration' in fact had higher n components of significant amplitude due to the 3D nature of the coil set. The entire spectrum was used in the computations to make the best comparison to experiment. When viewed as individual components in the NTV model, the effect of the $n = 5$ component is actually larger than the $n = 1$ component, and even $n = 11$ is appreciable (figure 46). The '$n = 3$ configuration' did have $n = 3$ as the dominant component, with a smaller but still appreciable $n = 9$ component.

Some cases using the $n = 1$ applied field configuration showed an experimentally measured resonant field amplification which was used to increase the computed vacuum field. In all of the cases studied, the plasmas were carefully prepared to eliminate measurable tearing modes, so that the non-resonant NTV could be accurately evaluated. The $n = 3$ applied field cases were particularly notable, as the measured resonant field amplification was insignificant, and the applied field spectrum was non-resonant. $N = 3$ instabilities were not observed in the plasmas investigated.

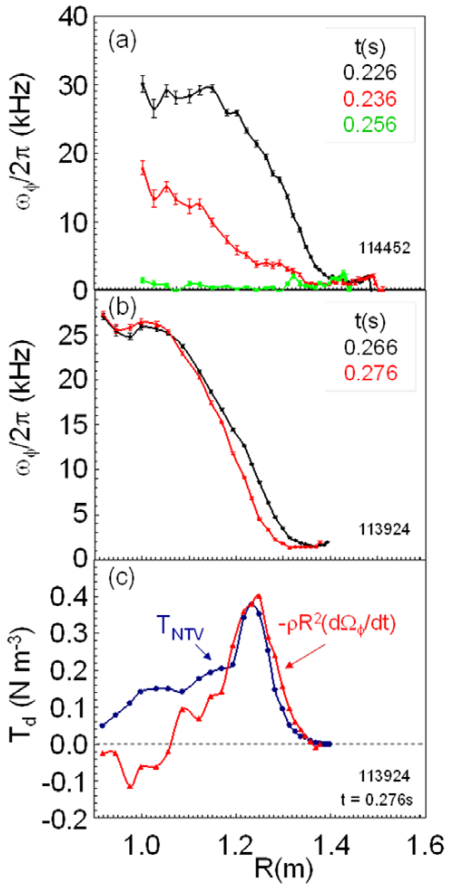

Figure 45. Toroidal rotation profile evolution during RWM activity in NSTX (*a*), (*b*) and a simplified calculation of the NTV torque density profile in the plateau regime (scaled) overlaid with the measured change in the plasma angular momentum (*c*).

In these experiments, a perturbative technique was used in which the applied non-axisymmetric fields were switched on quickly (significantly faster than the plasma momentum diffusion time) and the change in the plasma moment of inertia, I, and the angular momentum profile was determined using full two-dimensional equilibrium reconstructions, and Thomson scattering and CXRS measurements of plasma density and ω_ϕ. This perturbative technique was used to eliminate most components of the momentum diffusion equation, allowing a direct comparison of the measured change of the plasma angular momentum to the computed NTV torque density profile (figure 47). Quantitative agreement was found between experiment and theory. Thirty different equilibria were modelled for cases with the applied field configurations mentioned, with the mean value of the ratio of $(T_{\rm NTV})/(\mathrm{d}(I\omega_\phi)/\mathrm{d}t)$ being 1.59 using the peak values along the radial profile, with a standard deviation of 0.87. This $O(1)$ agreement was considered close given that prior research showed theory and experiment differing by more than two orders of magnitude.

In addition to the comparison of NTV theory to experiment for applied non-axisymmetric field perturbations, a similar comparison was made for ideal plasma RWMs, and the plasma amplification response generated by stable RWMs, again with good quantitative agreement (figure 48). Improved agreement between theory and experiment was found when a simple model of the measured plasma amplification of the vacuum field was included (rather than using the applied vacuum field alone). Agreement was further improved when the spatial variation of the plasma amplification was modelled using an ideal $n = 1$ RWM eigenfunction computed by the DCON code [345].

Subsequent to these experiments, the $n = 3$ applied field configuration was routinely and extensively used in many experiments spanning different areas of research on NSTX including stability and transport to provide open-loop toroidal rotation profile control [333, 334, 346, 347]. This application of non-resonant NTV was to slow the plasma rotation generated by the unidirectional neutral beam configuration of the device. Due to the non-resonant nature of NTV in this field configuration, resonant mode locking due to the applied field does not occur, even at plasma rotation speeds near zero at key rational surfaces, such as $q = 2$ or 3. In addition, small changes in the magnitude of the current generating the applied field can be made to generate similarly small and reproducible changes in ω_ϕ. These are both favourable characteristics for more general experiments, and provide significant advantages over changing the plasma rotation via modulation of the neutral beam sources. Such modulation generally produces coarser variations in ω_ϕ, and alters other key plasma parameters that are often preferred to be held constant, such as stored energy, or β_N.

11.3. Further investigation of NTV characteristics in tokamak experiments at various ν

The success in reaching quantitative agreement between NTV theory and experiment, as shown in section 11.2.4 was due to the suggestion and application of the substantial increase in viscosity predicted by theory in the $1/\nu$ regime (section 8.2.1) as the plasma collisionality drops below $\nu_i^* = 1$, when particle collisions become sub-dominant to particle bounce motion. This gave greater confidence that NTV could more generally reproduce related aspects of plasma rotation dynamics in tokamaks in the different NTV collisionality regimes at low $\nu_i^* < 1$. This has led to a significant number of more recent experiments in several devices testing aspects of NTV physics.

11.3.1. Varied applied field spectra. Several experiments have used varying applied field spectra to produce non-resonant NTV, with results that further support theoretical expectations. Earlier work from JET was followed up with more recent experiments using an $n = 1$ applied field configuration producing significant global damping of the plasma rotation [348] (figure 49(*a*)). The maximum torque was observed to be in the plasma core (within normalized radial coordinate $\rho = 0.4$). The rotation profile was reduced by about 50% in these experiments due to the applied field (figure 49(*b*)). The plasma was computed to be in the transition between the $1/\nu$, and ν–$\nu^{0.5}$ regimes (sections 8.2.1 and 8.2.2). Strong tearing mode activity was absent in these experiments.

Due to the different 3D geometry of the coil sets, the Fourier spectrum of the $n = 1$ applied field configuration

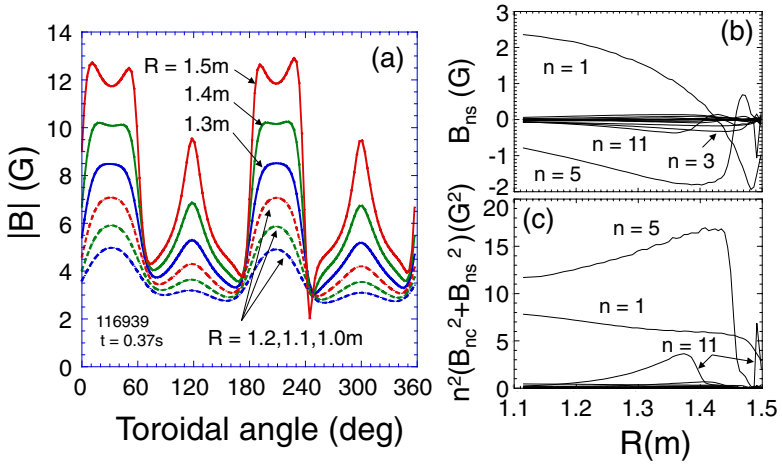

Figure 46. (*a*) Magnitude of the total field perturbation versus toroidal angle and major radius for the '$n = 1$ applied field configuration' in NSTX, (*b*) the major radial profile of the sine components of the field perturbation for this configuration, and (*c*) the flux surface averaged field component summation relevant to the NTV calculation.

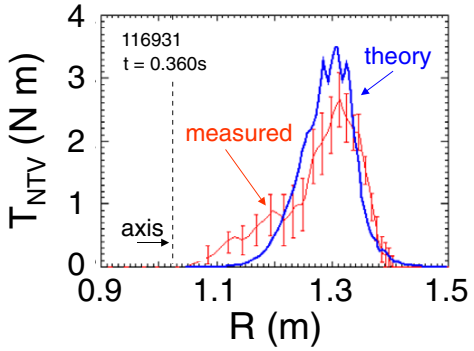

Figure 47. Comparison of measured $\mathrm{d}(I\omega_\phi)/\mathrm{d}t$ profile with the theoretically computed NTV torque for an $n = 3$ applied field configuration in NSTX.

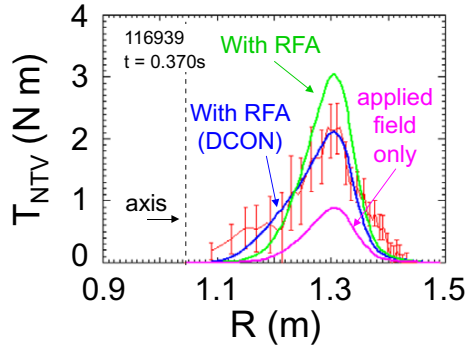

Figure 48. Comparison of measured $\mathrm{d}(I\omega_\phi)/\mathrm{d}t$ profile with the theoretically computed NTV torque for an $n = 1$ applied field configuration in NSTX. NTV calculations using the applied vacuum field, the measured plasma amplification of this field (RFA), and with a spatial variation of the plasma amplification modelled using an ideal $n = 1$ RWM eigenfunction are compared.

yielding NTV in JET is significantly different than the equivalently named applied field configuration in NSTX. In the JET case, the dominant component is $n = 1$, with $n = 2$ amplitude about two orders of magnitude lower, and the $n = 1$ component makes the dominant contribution to the non-resonant NTV (recall from section 11.2.4, the $n = 5$ component was computed to yield the dominant non-resonant NTV magnitude in the '$n = 1$ configuration'). The NTV torque was computed in several ways in this work, with the best agreement between theory and experiment occurring when the effect of the resonant components of the field were assumed to be shielded. The computation of the experimental torque density profile on the plasma (computed by a transport code) was compared to the NTV torque for the low collisionality $\nu - \nu^{0.5}$, and $1/\nu$ regimes, with the closest quantitative agreement occurring with the $1/\nu$ regime formulation, and the calculated torque about an order of magnitude larger than expected (figure 50). Note that the paper also shows results for an Eulerian formulation of the field perturbation, which agrees with the experimental observation to order unity [349]. Since the core of these JET plasmas appeared to be in the lower collisionality $\nu - \nu^{0.5}$ regime, it is unclear why the $1/\nu$ formulation provides superior agreement. It was postulated that plasma amplification effects added in the $\nu - \nu^{0.5}$ formulation may bring those calculations closer to experiment.

Experimental results on non-resonant NTV due to $n = 2$ applied field configurations have been reported in NSTX [334], JET [349], KSTAR [350] MAST [351] and TEXTOR [352]. Experiments on NSTX have demonstrated controlled, non-resonant toroidal rotation braking by an $n = 2$ field configuration, and that the NTV braking torque increases with ion temperature, consistent with the scaling $T_{\mathrm{NTV}} \sim \delta B^2 \varepsilon^{1.5} p_\mathrm{i}/\nu_\mathrm{i} \sim T_\mathrm{i}^{5/2}$ [334] expected by NTV theory in the $1/\nu$ regime. A factor of two increase in toroidal rotation damping was found in plasmas with higher ion temperature, consistent with the $T_\mathrm{i}^{5/2}$ scaling in the region of peak NTV torque (figure 51). It was also observed that the toroidal rotation damping profile was broader when using the $n = 2$ applied field configuration than for $n = 3$ fields, which is theoretically expected due to the broader field spectrum and reduced radial falloff of the $n = 2$ field.

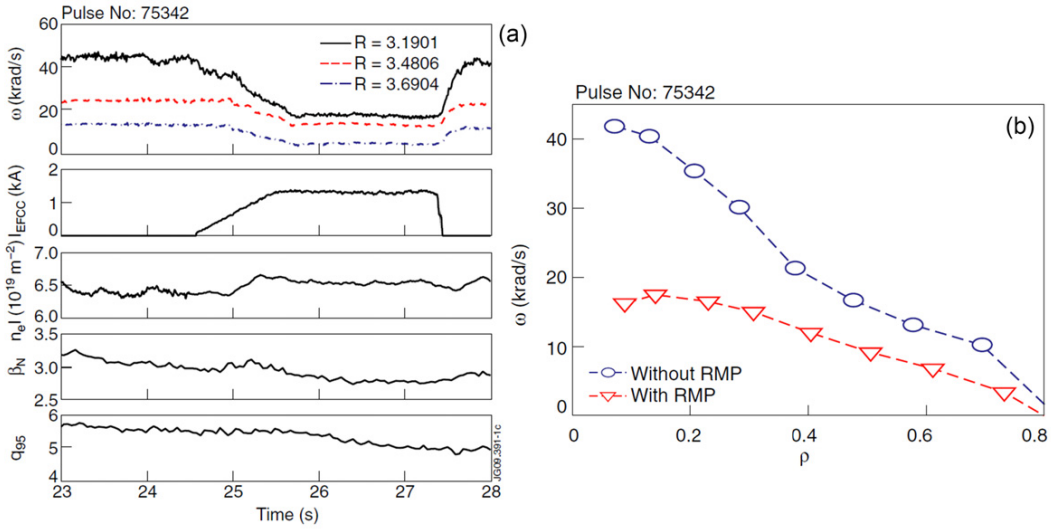

Figure 49. Global toroidal plasma rotation damping in JET by an $n = 1$ applied field. (a) shows the time evolution of the toroidal rotation from three CXRS channels, the magnitude of the $n = 1$ applied field current, the line-integrated density, normalized beta and q_{95}. (b) shows the steady-state rotation profiles without, and with the $n = 1$ field applied.

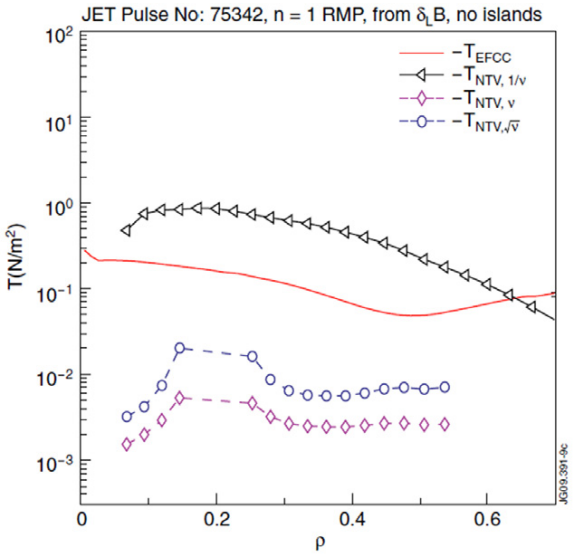

Figure 50. Torque density profile (computed by the JETTO transport code from experimental measurements) in JET experiments with an $n = 1$ applied field compared to NTV torque calculations appropriate for various collisionality regimes in the Shaing formulation.

Rotation damping for both $n = 2$ and $n = 1$ applied field configurations was reported in JET experiments focused on ELM control [349]. No clear dependence of the toroidal plasma rotation braking on q_{95} was observed in the range 3–4.9. Curiously, a hysteresis was reported in the plasma toroidal rotation evolution when comparing the interval of rotation braking to rotation spin-up as the applied non-axisymmetric field current was increased, then decreased. No explanation of this effect was reported. However, the variation of the applied field and rotation data plotted was made in the same discharge, and it clear that the rotation data had not reached a steady-state value at each value of the applied field plotted. The NTV braking torque in the core of JET was shown to increase with decreasing collisionality [352] (figure 52), similar to the increase observed on NSTX further out in the plasma (figure 51). However, it was remarked that the collisionality dependence was weaker than $1/\nu$, and closer to $1/\nu^{0.5}$.

The KSTAR device has also produced controlled rotation braking in initial experiments using applied $n = 2$ fields [350]. In recent experiments on KSTAR using long applied field pulses significantly longer than the momentum diffusion time, so that a steady-state was reached at each level of the applied $n = 2$ field current (figure 53), the rotation profile measured by CXRS is observed to be of nearly identical shape and magnitude at a given applied field current whether the plasma rotation is reduced towards the steady state, or if it is increased towards the steady state [365]. There is no evidence of hysteresis in this process, indicating that that the technique will be useful for future closed-loop rotation control in the device. The experiments were conducted using a combination of the KSTAR in-vessel control coils that were located on the plasma midplane. As the off-midplane coils were not used, there was no preferred pitch of the applied field with respect to the helical plasma equilibrium field.

A non-axisymmetric $n = 2$ applied field configuration has produced non-resonant NTV rotation damping in MAST using ex-vessel coils [351]. The plasma toroidal rotation evolution measured by CXRS is shown in figure 54 for a plasma heated by neutral beam injection (NBI) aimed counter to the direction of the plasma current. Clear global braking was observed, reducing the rotation by a factor of two. No tearing or ideal instabilities were observed in these experiments to isolate the effect of the non-axisymmetric applied field on the plasma. This experimental braking was compared with the theoretically expected NTV torque, and a factor of five difference was found. However, similar to the result found for JET, by reducing the resonant component for two harmonics around a given

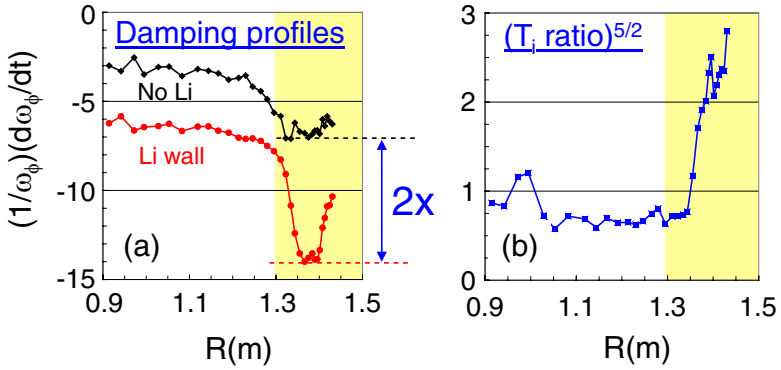

Figure 51. (*a*) Toroidal rotation damping profiles in NSTX in plasmas with different ion temperature profiles (higher ion temperature occurs in the plasmas with lithium wall conditioning), (*b*) the ion temperature ratio in these plasmas, raised to the 5/2 power. The region of peak non-resonant NTV magnetic braking torque is indicated by the shaded region.

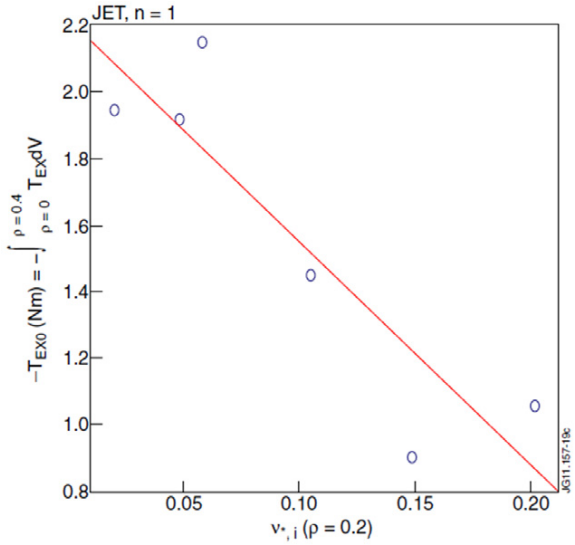

Figure 52. Integrated total torque inside the $\rho = 0.4$ surface in a JET plasma with applied $n = 1$ field configuration versus collisionality (ν_i^* at $\rho = 0.2$).

resonant surface by a factor of 0.5 (where 1 is complete plasma shielding), the agreement was improved, suggesting a strong plasma shielding of the resonant components of the field.

The possibility of significant non-resonant NTV was examined in a significantly different applied field spectrum in TEXTOR [352]. While the configuration was $n = 2$, the dynamic ergodic divertor (DED) coils [353], which are located on the inboard (small R) side of the torus, were utilized. This is in contrast to all other experiments reviewed in section 11 which utilized coils located on the outboard (large R) side of the torus. Specifically, it was shown that the strength of the vacuum field perturbation for the $n = 2$ applied field decreased strongly from $\delta B/B \sim 0.6\%$ at the plasma edge for the strongest poloidal harmonics down nearly an order of magnitude to $\delta B/B \sim 0.075\%$ only 20% into the plasma (in terms of a minor radial coordinate $\rho =$ (normalized toroidal flux)$^{0.5}$). This is compared to the vacuum perturbation of the $n = 1$ applied field configuration in JET, which maintains large magnitude into the core (figure 55). Consequently, the computed NTV torque generated by this field was small—four orders of magnitude smaller than the NTV from the $n = 1$ applied field configuration in JET [352]. This is consistent with the non-resonant braking experiments on TEXTOR using this configuration, which showed no significant reduction of the measured toroidal rotation (figure 56).

The results shown in this section, examining non-resonant NTV in a diverse set of tokamaks with various non-axisymmetric applied field spectra, displaying the characteristics of non-resonant NTV in each case, and agreeing to within an order of magnitude with NTV theory, give added confidence that non-resonant NTV physics can explain the observed phenomena. However, challenges remain to further improve the quantitative agreement of the non-resonant NTV torque with the observed change in the plasma angular momentum, the largest being an accurate and verified experimental and theoretical determination of the internal plasma response that may significantly modify the vacuum field (e.g. addressed in [352]). This is a relatively insignificant issue for applied fields with mostly non-resonant components (e.g. the $n = 3$ field configuration in NSTX (figure 47)—the $n = 3$ component of the resonant field amplification measured by RWM sensors has been shown to be small, even in high β_N NSTX plasmas). Codes such as IPEC [354] and MARS-F [355] have been used successfully to generate the ideal plasma response for applied fields with relatively high sensitivity for amplification or shielding of the applied field. At present, NTV results attempting such modification generally yield stronger non-resonant NTV than observed. Use of the vacuum applied field should provide a quantitative lower limit of the non-resonant NTV profile, with understandably greater accuracy for applied fields that have components that are not strongly affected by the plasma (e.g. spectra with higher n components). Fortunately, these two approaches for computing the non-axisymmetric field in the plasma apparently provide upper and lower bounds for non-resonant NTV calculations. It is noteworthy that NTV calculations for JET [348] and MAST [351] have shown success by reducing the magnitude of key resonant components in the plasma, which generally represent the field

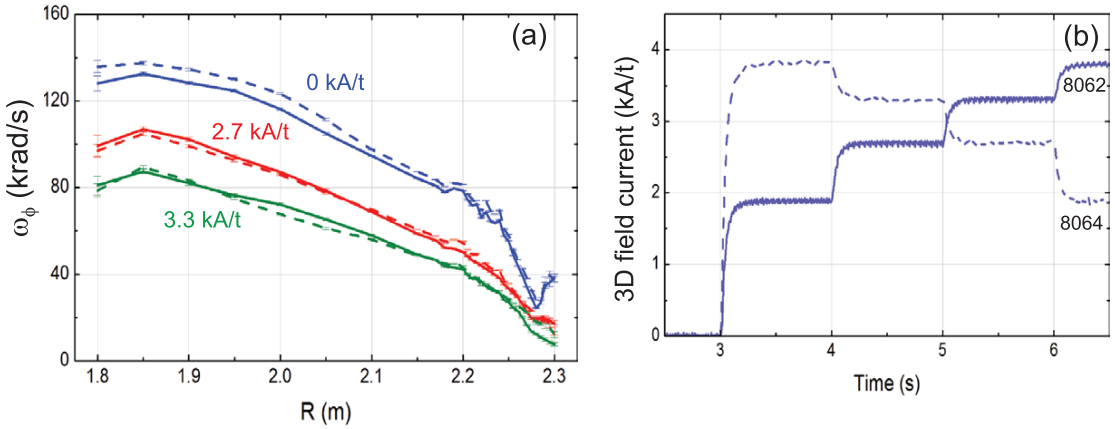

Figure 53. (*a*) Plasma toroidal rotation frequency profile evolution from non-resonant NTV rotation damping with $n = 2$ applied field current stepped-up (solid lines) and stepped-down (dashed lines), with (*b*) corresponding applied 3D field current waveforms. Rotation profiles reach a steady state between current steps, and the dynamic shows no hysteresis—the same profile is reached at the same applied 3D field current regardless of whether the plasma accelerates or decelerates towards each steady state.

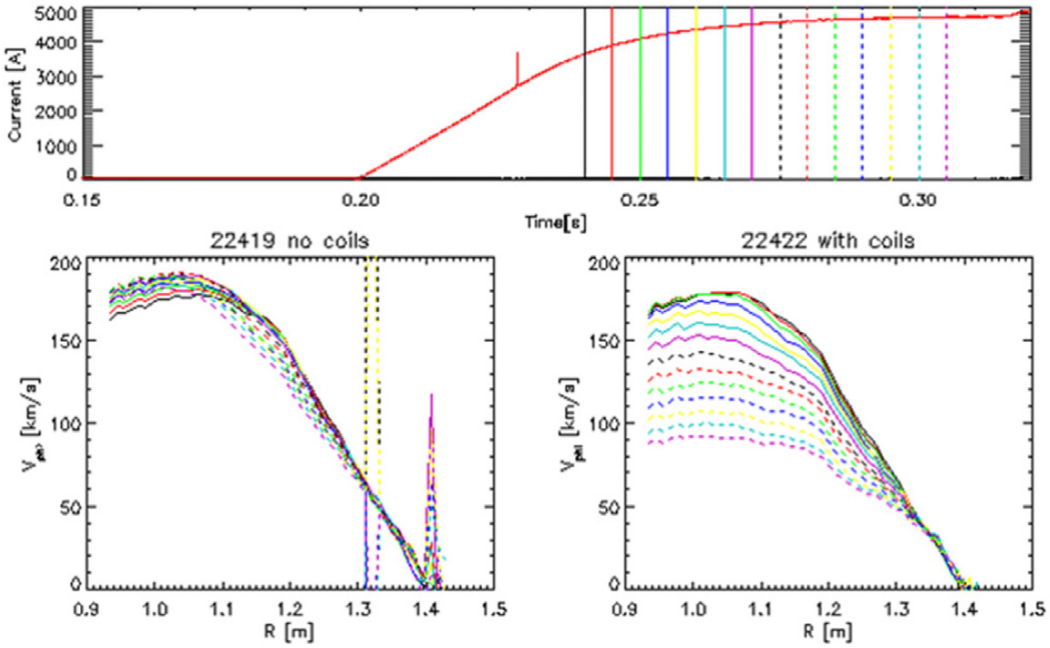

Figure 54. Non-resonant NTV rotation braking in MAST from external coils circuited in an $n = 2$ applied field configuration.

components that have the greatest uncertainty regarding the plasma response.

11.3.2. Offset rotation. The anticipated NTV offset rotation was observed in experiments conducted on DIII-D [300, 356]. In these experiments, a static, non-resonant field with a dominant $n = 3$ component was applied to relatively slowly rotating plasmas in the device. Evidence of an offset rotation in the direction opposed to the plasma current was observed by examining the evolution of the ω_ϕ profile towards a steady state (figure 57) Because the experiments were conducted with initially slowly rotating plasmas, with rotation speeds on the order of the offset rotation itself, the results have notably demonstrated the positive result that non-resonant NTV can increase the plasma rotation locally, rather than just decrease it. This capability has been used to support the important QH mode operational scenario in DIII-D. In preliminary experiments using $n = 3$ fields in this way at ITER-relevant low NBI torque, QH mode was generated and sustained in DIII-D plasmas with low $q_{95} = 3.4$ having reached high equivalent fusion gain [357]. The NTV offset rotation may be more generally useful in future experiments operating with relatively low injected neutral beam torque (e.g. in ITER) to influence plasma stability and/or confinement properties.

The NTV offset rotation remains a topic of research as results from various experiments have shown varying results. Non-resonant NTV operation with an $n = 3$ field configuration over the full range of neutral beam operation in NSTX has

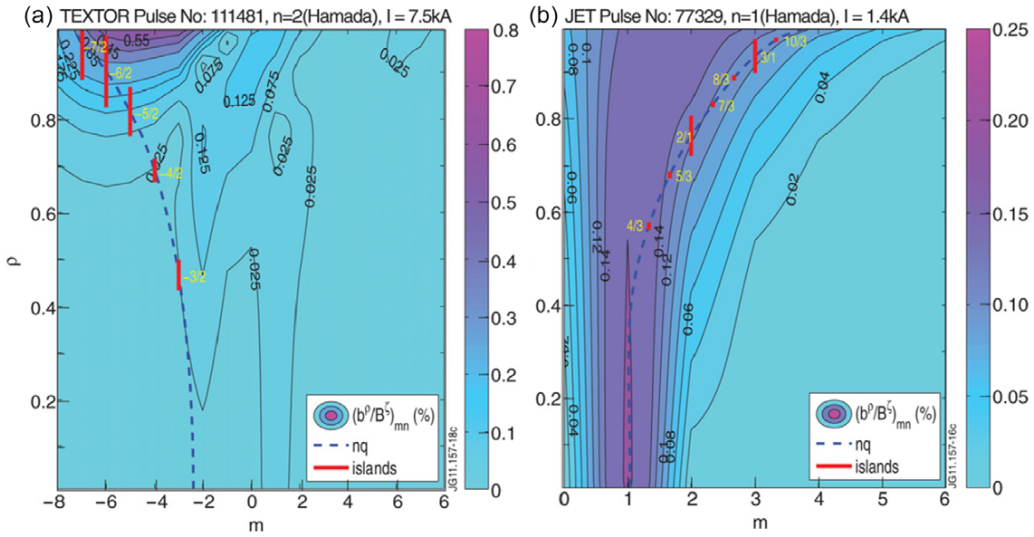

Figure 55. Percentage magnitude of the normalized vacuum non-axisymmetric field perturbation for (*a*) $n = 2$ applied DED configuration in TEXTOR, and (*b*) $n = 1$ applied field configuration in JET.

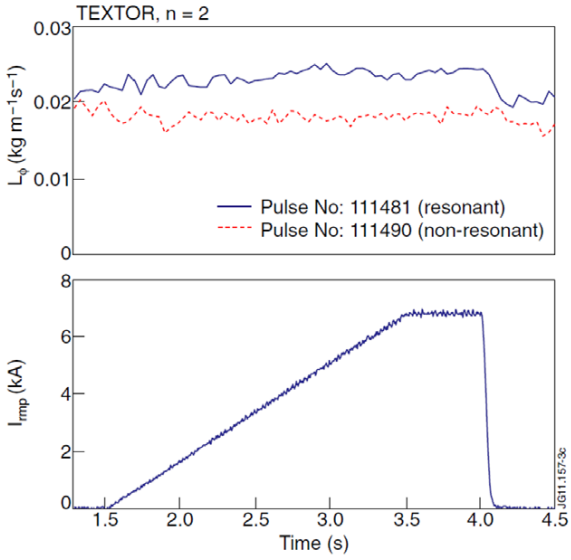

Figure 56. Toroidal angular momentum density evolution near the plasma core for both resonant (solid line, top frame) and non-resonant (dashed line, top frame) $n = 2$ DED field configurations in TEXTOR; corresponding DED coil current waveform (bottom frame).

shown that the NTV offset rotation was small, with saturated values of ω_ϕ approaching zero, rather than to a finite offset in the counter-I_p direction [334, 358]. The conclusion was similar for NSTX operation with an $n = 2$ field configuration. NTV studies on JET have pointed out the potential importance of the electron contribution to NTV in the low collisionality core plasma, with a corresponding component to the offset rotation in the co-I_p direction, with magnitude on the order of the electron diamagnetic frequency [352]. Research on TCV [359] (discussed further in section 11.3.3) investigating a mixture of non-resonant and resonant sources of rotation damping has also shown that an offset rotation in the co-I_p direction best fits the experimental data. These results indicate that the physics of the NTV offset rotation still needs to be verified across devices to give the highest confidence for extrapolation to future devices.

11.3.3. Plasma modes causing non-resonant NTV. Non-resonant plasma modes can provide the non-axisymmetric field perturbation in the plasma to generate non-resonant NTV. To influence the plasma rotation, a mode with an ideal perturbation needs to couple to other modes with non-ideal perturbations, or to external fields which could be generated by a coil set, by eddy currents in conducting structure, or provided by device error fields. An early example of this effect was shown in section 11.2.3, with non-resonant NTV generated by unstable, ideal plasma RWMs in NSTX [40]. In this case, the plasma momentum is transferred to the lab frame through the inherent coupling of the RWM to the tokamak device conducting structure.

A further study examining non-resonant NTV as a cause for rotation damping by ideal MHD mode perturbations was shown in MAST for a large saturated kink instability, termed the 'long-lived mode' [360], which produced toroidal rotation damping in the plasma core. It was remarked that high resolution temperature measurements using Thomson scattering did not indicate local profile flattening, and no phase inversions were observed between neighbouring channels of poloidal cross-section soft x-ray cameras, indicating that no strong magnetic islands were found during the time of strong magnetic braking. However, the measured global toroidal rotation damping was not self-similar, and a clear outward momentum transfer is observed at a well-defined major radial position in the profile $R = 1.15$ m. The structure of the eigenmode, measured to be $n = 1$, was estimated using the CASTOR code and soft x-ray measurements. In the core plasma, at minor radial positions corresponding to being inside $R = 1.15$ m, the mode appears to be a kink. Calculation of the

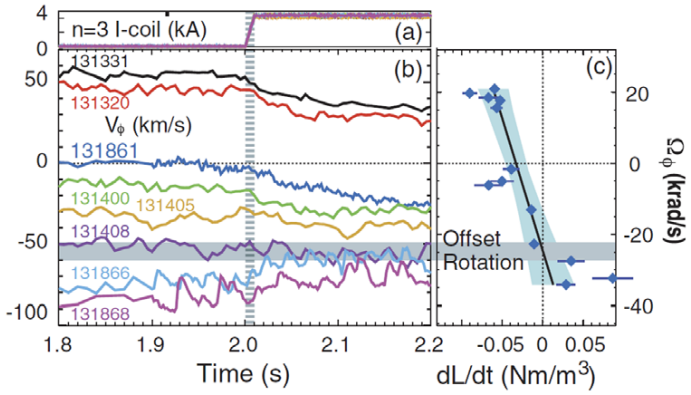

Figure 57. Experiments demonstrating the NTV offset rotation in DIII-D.

non-resonant NTV in this core region shows consistency with the measured rotation damping.

More recently, toroidal rotation damping in the core of the KSTAR device during electron cyclotron resonant heating (ECRH) [361] has been connected to non-resonant NTV caused by the excitation of an internal kink mode [362]. This result is particularly noteworthy, as toroidal rotation changes due to ECRH have been measured in many devices. However, there is no widely accepted explanation for the observed effects on the toroidal rotation profile evolution. The experiments were run with ECRH alone, and in combination with neutral beam heating. Internal kink modes appeared whenever ECRH was injected. The toroidal rotation of argon impurities was measured using an x-ray imaging crystal spectrometer, and of carbon impurities by charge exchange spectroscopy in plasmas heated by NBI. The radial extent of the internal kink extends to the sawtooth inversion radius in sawtoothing plasmas. The toroidal rotation profile was observed to decrease the magnitude in the plasma core during the period when ECRH is injected and the internal kink is correspondingly destabilized in the plasmas with (figure 58), or without NBI.

Non-resonant NTV was evaluated for these plasmas using the $1/\nu$ regime formulation (section 8.2.1). The perturbed magnetic field caused by the ECRH-induced internal kink modes was estimated from the measured plasma displacement profile in the core plasma from electron cyclotron emission. The peak normalized field perturbation $\delta B/B$ was computed to be approximately 0.005. The computed non-resonant NTV torque density profile in the core (figure 59) is shown to have a magnitude and radial dependence consistent with the observed experimental rotation damping, and computed magnitude of the injected torque from the neutral beams.

Recently, non-resonant NTV has been investigated experimentally in TCV investigating the effect on plasmas with resonant instabilities (2/1 and 3/2 tearing modes) [359]. This work examines evidence of an associated neoclassical toroidal viscous torque observed as a pronounced flattening and global braking of plasma rotation at the onset of these tearing instabilities. As in the KSTAR experiments mentioned above, the TCV plasmas also have ECRH applied. The work clearly states the presence of both resonant and non-resonant causes for the observed rotation damping. This, added to the use of ECH, for which the associated intrinsic rotation physics is not yet established, makes the modelling difficult (for example, island NTV effects, discussed in section 8.4, should be included). These results are notable in that the maturity of NTV theory and the significant number of experimental comparisons since the early investigations (section 11.2) have yielded an understanding that makes more complicated investigation involving multiple modes more tractable. Some of the general conclusions are noteworthy. It was found that within experimental uncertainty, the evolution of the toroidal rotation profile is consistent with the general effect of an NTV torque proportional to the difference between the toroidal velocity and the NTV offset rotation, which was found to be finite, evaluated in steady-state conditions. The best fits to the experimental ω_ϕ evolution were found by taking into account an offset rotation frequency in co-I_p direction, despite the usual counter-I_p rotation offset expected from neoclassical theory for ions. The presence of resonant magnetic perturbations was given as a potential reason for the change of sign of the offset rotation.

11.4. Exploration of the superbanana plateau regime

The theoretically anticipated significant increase of NTV as a tokamak plasma enters the superbanana plateau regime [223] (section 8.2.4) is a concern for future tokamak operation at reduced collisionality and at low plasma rotation (e.g. in ITER). The increase in NTV anticipated in this regime has been observed in tokamaks in the past few years. Results show that while the NTV and associated rotation damping rate of plasma rotation increases, the braking remains non-resonant, and does not lead to mode locking and consequent plasma disruption.

Experiments in DIII-D conducted at moderate $\beta_N = 1.6 - 1.7$ (below the $n = 1$ ideal MHD no-wall stability limit) have accessed the superbanana plateau regime and have demonstrated a peak in NTV at low ω_E [363, 364]. In these experiments, an $n = 3$ field configuration was applied to the plasma using the DIII-D I-coil set in odd parity (defined as the upper and lower set of coils applying $n = 3$ fields that differ in toroidal phase by 180°), and plasma rotation feedback actuated by NBI was utilized. The total NTV torque, T_{NTV}, was evaluated as a function of plasma toroidal rotation by measuring the change in NBI torque, ΔT_{NBI}, needed to sustain a given rotation when the applied $n = 3$ field was switched

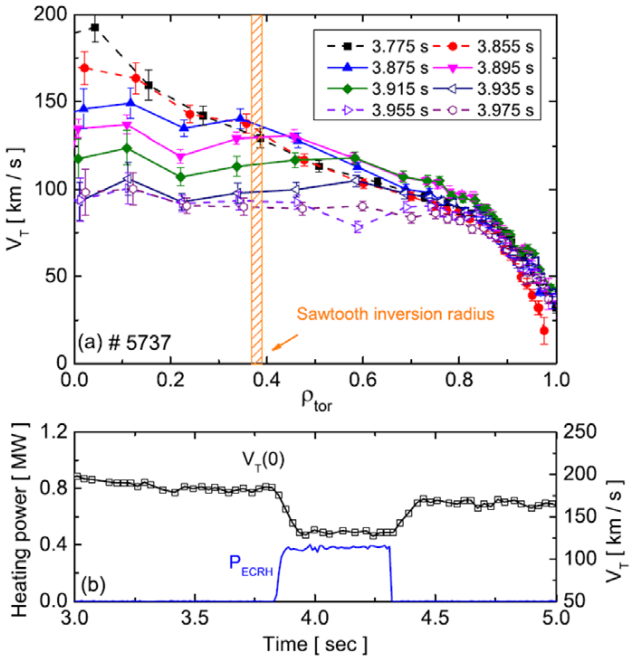

Figure 58. Toroidal rotation profile damping (top) during ECRH and NBI and associated core internal kink destabilization in KSTAR. The toroidal rotation recovers once the ECRH pulse is terminated (bottom).

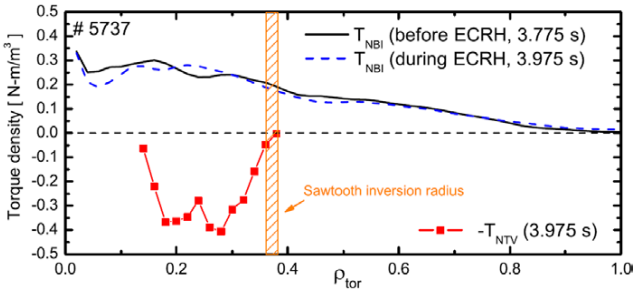

Figure 59. Torque density profile computed for non-resonant NTV in the $1/\nu$ regime (red trace with squares) for a KSTAR ECRH plasma with NBI that exhibits a saturated core kink mode. The torque density profile provided by the neutral beam is also shown before (black solid line) and during (blue dashed line) ECRH.

on (assuming $\Delta T_{\rm NBI} = -T_{\rm NTV}(\omega_\phi)$). The resulting scan in plasma rotation yielded a peak in near zero deuterium rotation speed (figure 60). The measured peak in $T_{\rm NTV}$ occurs at a toroidal rotation rate where the radial electric field is near zero as determined by radial ion force balance.

Experiments in NSTX at high $\beta_{\rm N} = 4-5$ (at, or above the $n = 1$ ideal MHD no-wall stability limit) have also entered the superbanana plateau regime [358] by varying the ratio of the ion collisionality to the $E \times B$ frequency, ω_E, a key parameter that determines the scaling of NTV with $\nu_{\rm i}$ in the collisionless regime ($\nu_{\rm i}^* < 1$) (section 8.2.4). As $|\omega_E|$ is reduced, $T_{\rm NTV}/\omega_\phi$ is expected to scale as $1/\nu_i$ when $(\nu_{\rm i}/\varepsilon)\,/\,(nq|\omega_E|) > 1$ and maximize when it falls below the ∇B drift frequency and enters the superbanana plateau regime. In these experiments, a constant $n = 3$ field configuration was applied to the plasma using the midplane control coils. Increased braking strength was observed at constant $|\delta \boldsymbol{B}|$ and $\beta_{\rm N}$ in experiments when ω_ϕ (and $|\omega_E|$) were sufficiently decreased, as expected by NTV theory (figure 61). Lithium wall preparation was used to suppress tearing modes that would have led to resonant braking, mode locking and plasma disruption, allowing the investigation of non-resonant NTV braking down to low values of ω_ϕ and $|\omega_E|$. The low levels of ω_ϕ were sustained, even with the $q = 2$ surface in the region of low rotation. It is especially notable that the stronger NTV in the superbanana plateau regime yielded a steady, low rotation state with no mode locking, and that the plasma rotation frequency (based on carbon impurity measurement) approached zero, instead of a finite offset rotation frequency.

Operation in the superbanana plateau regime was originally thought to be an issue for future tokamaks. Devices operating with low plasma rotation, and ω_E near zero may be thought to suffer MHD instabilities as the stronger NTV in this regime rapidly brings the plasma rotation to the NTV offset rotation frequency, which might be small in future devices. While this may still be an issue for future devices and requires further experimental investigation, operation of plasmas in this regime in both DIII-D and NSTX give confidence that the

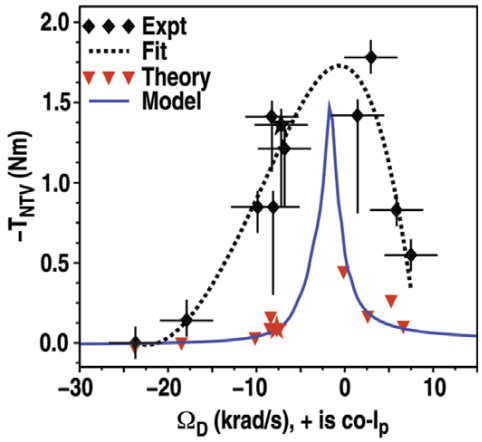

Figure 60. DIII-D experimental results demonstrating a peak near zero deuterium rotation frequency (black stars) in comparison with theory (red inverted triangles).

plasma can exist in this state. The NSTX results show that high plasma performance can be reached in the Sb-P regime, without mode locking and associated disruptions.

11.5. Applications of NTV in tokamak research

The seminal theory for NTV is now well established, with tokamak experiments in the early to mid-2000s establishing some of the core physics elements with quantitative agreement with theory. Extensive tokamak experiments have been conducted to date, further investigating the broader scope of the physical characteristics of NTV. While several aspects of the theory remain to be verified by experiment, enough research has been accomplished to date to have confidence in the use of non-resonant NTV to enable and improve high performance steady-state tokamak operation.

Non-resonant NTV is an excellent example of the positive use of 3D fields in otherwise axisymmetric tokamak devices. The non-resonant aspect is important for tokamak operation in general, as this form of NTV prevents MHD mode locking at low rotation. Several applications of non-resonant NTV logically follow directly from initial experiments that have already been conducted. NTV has been used in several experiments including NSTX, DIII-D, JET, KSTAR and MAST (section 11.3.1) to alter the toroidal plasma rotation and profile in a controlled, reproducible manner using non-resonant applied field configurations, even for plasma entering the superbanana plateau regime. Devices with unidirectional NBI, such as NSTX and KSTAR, have effectively utilized non-resonant NTV for pre-programmed, open-loop plasma rotation control in a variety of experiments in topical areas including stability and transport. A logical next-step is to use non-resonant NTV as an actuator for real-time, closed-loop rotation control. This has been proposed for NSTX-U [365] and KSTAR, utilizing non-resonant NTV, NBI, and (in KSTAR) ECRH as actuators, with a key use being the avoidance of plasma disruptions by tailoring the plasma rotation profile to avoid MHD instabilities. NTV offers significant advantages as an actuator over NBI in this role, as its variation does not substantially change the plasma stored energy, and the amount of desired change in the rotation profile can be made as precisely as the control circuit feeding the actuator coils allows. This approach to rotation control provides some challenges to the control algorithm, as a weak non-linearity exists in the non-resonant NTV torque term involving the applied field current and the plasma rotation speed. The success of using the neoclassical offset rotation to produce and sustain QH mode in DIII-D gives greater confidence for using this physics to sustain favoured modes of tokamak operation in future devices envisioned to have plasma rotation magnitude substantially lower than present tokamak devices with neutral beam heating.

NTV theory has also been investigated to potentially understand the dependence of resonant error field mode locking thresholds on plasma density in ohmically heated plasmas [366]. Further application of NTV theory to experiments investigating resonant mode locking may discover further understanding of the plasma parameter dependence on mode locking [359, 367] for more accurate extrapolation to future experiments. The reduction of error fields in present tokamaks has also been addressed using NTV theory. Since non-resonant NTV produces a global change in the plasma rotation profile, that does not lead to mode locking, the correction of non-resonant error fields in turn will generally produce increased plasma rotation in a tokamak heated by neutral beams that provide momentum input. This result was used to produce optimal error field correction of the $n = 3$ field component in NSTX, with non-resonant NTV modelling that was consistent with the reduction of the magnetic braking observed with the corrected field [368]. NTV is now similarly evaluated in several devices to minimize error fields. Most notable for future devices has been related work with the IPEC code to minimize error fields in ITER [369].

11.6. Implications for ITER and future devices

NTV research and related 3D physics effects in tokamaks have potentially positive effects for ITER and future tokamak fusion devices. The application of non-resonant NTV for plasma rotation control of MHD instabilities for disruption avoidance has been discussed above in section 11.5. Devices with significant momentum input can in principle alter the plasma rotation speed and profile from maximum rotation magnitude to near zero without mode locking for instability avoidance. In ITER, plasma rotation is expected to be low. The NTV offset rotation may be able to support an operational scenario as it has for the DIII-D QH mode. Still, operation of ITER near MHD stability limits, which may be required for ITER to achieve fusion power production goals, may require a rotation magnitude larger than that provided by the NTV offset rotation [370]. Recent transport computations for ITER utilizing the NTV offset rotation have found that this intrinsic rotation (the Kikuchi model of offset rotation [371] was utilized) can result in the formation of an internal transport barrier (ITB), located in normalized minor radius between $r/a = 0.6$–0.8 which can have a strong positive impact on the plasma performance in the device [372]. The ITB is formed in the model by the suppression of anomalous transport due to ω_E flow shear and magnetic shear. NTV theory has been essential in understanding the ITER test blanket module (TBM) error

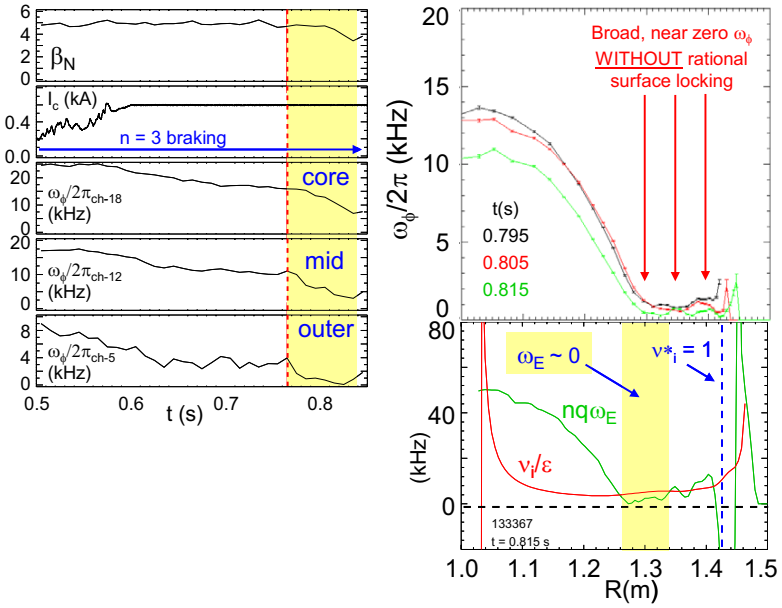

Figure 61. NSTX experimental results accessing the superbanana plateau regime, displaying increased non-resonant magnetic braking at fixed applied field and β_N at low ω_E.

field simulation experiments at DIII-D [373]. In these experiments, a toroidally localized three-coil mock-up of two magnetized ITER TBMs in one ITER equatorial port was mounted on the DIII-D device and operated producing magnetic error fields similar to those expected from the proposed ITER test blanket modules containing ferromagnetic material. The largest effect was a significant self-similar reduction in plasma toroidal rotation velocity across the entire radial profile caused by non-resonant NTV braking (figure 62). The largest non-resonant component of the NTV torque density profile causing the non-resonant braking was shown to be due to the $n = 1$ component which penetrated to the plasma core. This understanding of the cause of the magnetic braking allows computations of correction fields needed to alleviate the drag to the plasma rotation created by the TBM. These experiments give confidence that the NTV-related magnetic braking from fairly arbitrary (in this case, toroidally localized) non-axisymmetric fields can be confidently evaluated and altered. However, several key aspects of NTV theory are yet to be fully verified across experiments as already stated throughout section 11. Arguably, the largest issue is both the accurate modelling, and accurate internal diagnosis of the plasma response to applied non-axisymmetric fields, or to non-axisymmetric field perturbations created by saturated MHD instabilities. This issue is especially important in plasmas operating at high beta [354, 374], as will occur in ITER advanced scenarios, FNSF in the role of a component test facility, or DEMO.

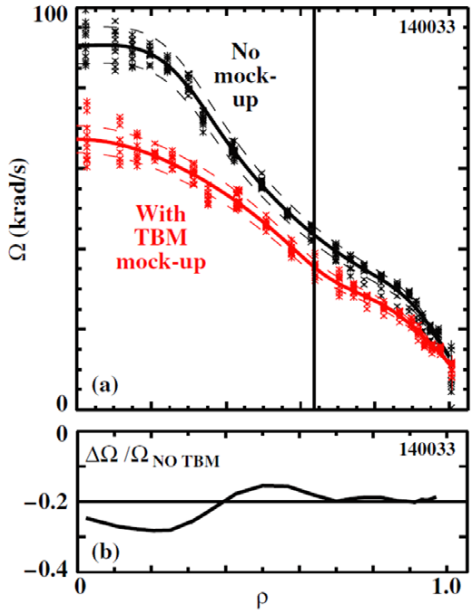

Figure 62. (*a*) Radial profiles of toroidal rotation of C+6 measured by charge recombination spectroscopy in DIII-D TBM experiments for shots without (black) and with (red) the TBM fields energized, (*b*) the normalized difference between these profiles.

12. Discussions and summary

It has been demonstrated here that the eight-moment neoclassical methodology can be applied to calculate transport fluxes for a variety of plasma conditions that are of interest to thermonuclear fusion reactors. Once the closure quantities such as plasma viscosity are calculated, all transport fluxes can be evaluated using the plasma flows determined from the momentum and heat flux equations. The approach is particularly useful for modelling transport consequences in toroidal plasmas.

12.1. Discussions

One of the common features of the theories discussed here is that there is an intrinsic steady-state plasma flow even without external momentum sources. The flow generation without external momentum sources is not as farfetched as it seems. The well-known diamagnetic flow is generated without external momentum sources. The origin of the momentum for the diamagnetic flow is the unbalanced particle momenta from neighbouring gyro-orbits. The existence of the intrinsic poloidal and toroidal flows in toroidal plasmas has been known long before experimentalists emphasized them. The steady-state plasma flows exist in practically every theory regardless of the nature of the theory. The magnitude of the flow is of the order of $v_t\rho_{pi}/L_n$ for most theories. Thus, if a flow with a magnitude of the order of $v_t\rho_{pi}/L_n$ is needed to control plasma confinement, it is not necessary to do anything externally to obtain a flow of such magnitude.

The physics understanding for the origin of the momentum for such flows has been presented in [194] using the well-known neoclassical poloidal flow generation in tokamaks as an example. The steady-state neoclassical poloidal flow is proportional to the equilibrium ion temperature gradient in large aspect ratio tokamaks [6, 7]. Without collisions or de-correlation, the equilibrium temperature gradient only contributes to the diamagnetic heat flow and not the diamagnetic mass flow because of the exact cancellation of the particle momenta from the neighbouring particle orbits resulting from the $\left(x^2 - 5/2\right)$ in the definition of the heat flow $\boldsymbol{q}$ after integrating over an equilibrium Maxwellian distribution as can be seen from equations (3.1) and (3.2). The independent variables are (p, T) here. However, when energy dependent collisions occur, the exact cancellation is destroyed, and the equilibrium temperature gradient generates a diamagnetic like fluid flow that contributes to the parallel plasma viscosity that damps the poloidal flow shown in equation (4.2.1.2). This point is further corroborated by the fact that there is no time-dependent poloidal heat flow dependence in the time-dependent viscosity given in equation (4.2.1.2) in the asymptotic limit where $\partial/\partial t$ operator dominates. Thus, the reason that there is a steady-state neoclassical poloidal flow is a result of the energy dependent collision frequency. During the poloidal flow damping process, the exact cancellation of the particle momenta from neighbouring orbits is destroyed as illustrated schematically in figure 63. Thus, the neoclassical poloidal flow is diamagnetic in nature in tokamaks.

The same physics picture is applicable to poloidal generation in other collisionality regimes, and the toroidal flow generation resulting from the neoclassical toroidal plasmas viscosity in toroidal plasmas with arbitrary symmetry property. The exact cancellation of the particle momenta from neighbouring orbits is destroyed because the de-correlation time and step size depend on energy. Similarly, the physics picture is also valid for the turbulence generated toroidal flow resulting from the residual stress in [174, 176] because the de-correlation time, and the step size depend on particle energy.

12.1.1. Summary and discussion. Both the eight-moment approach to neoclassical theory for non-axisymmetric tori, with axisymmetric tokamaks as a special case, and the experimental tests on plasma viscosity and plasma flows have been reviewed. The effects of compressibility and shock formation are not discussed in detail, however.

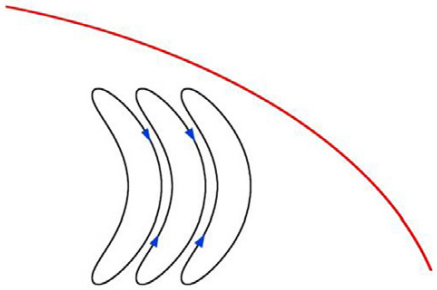

Figure 63. The origin of the momentum for flow generation without external momentum sources is illustrated here. The red line indicates the equilibrium temperature profile. The neighbouring banana orbits are shown to indicate the cancellation of the local particle momentum from neighbouring orbits.

It has been demonstrated in section 4 that the eight-moment approach unifies the transport fluxes, the physics of the momentum relaxation, and ambipolarity through the relation between plasma viscosity, or, in general, plasma stress and transport fluxes. It has been shown that after the momentum on the magnetic surface is relaxed, steady-state plasma flows emerge, and the plasmas reach an ambipolar state. The relaxation processes are dictated by the components of the viscous forces. The transport fluxes follow naturally from the flux–force relation, which relates fluxes with the components of the viscous forces in all regimes except the Pfirsch–Schlüter regime, by substituting plasma flows into viscosity. Thus, the approach illuminates the pivotal role of the momentum and heat balance equations in the transport theory. The approach is most suited for modelling the plasma rotation and transport in toroidal plasmas. The viscosity for the conventional theory for axisymmetric tokamaks has been summarized in section 6 and been implemented in the NCLASS code for self-consistent modelling of the plasma confinement. The approach is employed in the DKES code to model plasma flows and transport fluxes in stellarators. The neoclassical methodology has also been applied to the transport processes caused by the turbulent fluctuations to unify both neoclassical theory and quasilinear theory as illustrated in section 7. One of the most important conclusions is that even in turbulent toroidal plasmas, neoclassical theory provides a powerful tool to understand confinement physics quantitatively.

A systematic method of calculating the components of plasma viscosity for a variety of plasmas that are of interest to tokamak and stellarator operations has been illustrated in sections 6, 7, 8 and 9. The key is to solve the drift kinetic equation with plasma flows instead of gradients as the driving terms. Most of the theories are developed for large aspect ratio tori, except the parallel viscosity for axisymmetric tokamaks, mainly because the difficulty in having compact analytic expressions for particle trajectories and in solving the complete test particle collision operator.

Results of the effects of orbit squeezing in section 6 can be used to model ion heat transport and bootstrap current in the pedestal region of H-mode plasmas in tokamaks. The ion heat

conductivity in that region should be smaller than that in the standard theory. In the vicinity of the magnetic axis, the potato bootstrap current can be used to maintain a 100% bootstrap current equilibrium. However, there are no experimental tests on this issue at the moment.

The most important aspect of plasma viscosity perhaps is that it depends on the radial electric field and parallel flow speed non-linearly as illustrated in sections 6, 8 and 9. The non-linearity can lead to bifurcated solutions of equilibrium plasma flows. It has been tested in the electrode induced L–H transition. However, it has never been tested in naturally occurring L–H transition. To resolve the L–H transition mechanism in naturally occurring transitions, the non-linearity must be tested. Indeed, the generic consequences of different sets of non-linear equations are similar. The only way to distinguish them is to test the underlying non-linearity experimentally.

The neoclassical methodology is used to unify neoclassical theory and quasilinear theory in section 7. The most important consequence of the unification is that not all transport coefficients are equally anomalous. Thus, even in turbulent toroidal plasmas, some coefficients are still close to neoclassical predictions, e.g. bootstrap current, and plasma resistivity. The theory provides a theoretical foundation for operating tokamaks with high bootstrap current fraction. The quasilinear toroidal plasma viscosity consists of diffusion, convection and residual stress. The residual stress drives a local plasma flow; the direction of which depends on the characteristic mode frequency in fluctuations.

When toroidal symmetry is broken, the symmetry breaking induced transport fluxes in tokamaks are qualitatively similar to those in stellarators. Results in all known collisionality regimes have been presented in section 8. They can be employed to model present and future experiments when applied 3D fields are used to control plasma flows, and plasma confinement. The symmetry breaking induced energy losses for energetic alpha particles may ultimately limit the magnitude of symmetry breaking magnetic fields in thermonuclear fusion reactors [375]. The results, from the solution of the bounce averaged drift kinetic equation, have also been checked in a code that solves the drift kinetic equation using quasilinear approximation [376]. The theory for neoclassical toroidal plasma viscosity and transport fluxes are being extended for finite aspect ratio tokamaks [377].

Transport fluxes in real stellarators are rather difficult to calculate analytically in the low collisionality regimes. However, the basic collisionality scalings can be understood using results derived from a model magnetic field spectrum as illustrated in section 9. It has been known that the confinement of thermal particles can be improved by controlling the radial electric field. However, one of the crucial issues for thermonuclear fusion reactors based on the stellarator concept is the energy confinement of fusion-born alpha particles, which are not usually susceptible to the effects of the radial electric field.

In stellarator/heliotron devices, the contribution of neoclassical parallel viscosity in the toroidal direction is comparable to that in the poloidal direction. The perpendicular flow (radial electric field or space potential as a constant quantity on magnetic flux surface) and parallel flow are considered to be important rather than toroidal/poloidal flows. The parallel flow and perpendicular flow are treated separately (for example, the non-ambipolar condition gives only the perpendicular flow). The neoclassical toroidal and poloidal viscosities are treated as a projection of the neoclassical parallel viscosity in the toroidal and poloidal directions. This is in contrast to the situation in tokamaks where the toroidal and poloidal flows/viscosities are treated separately or independently. This is because there is no neoclassical toroidal viscosity without an external perturbation magnetic field because of the toroidal symmetry. Then the neoclassical toroidal viscosity experiment in tokamak is focused to the plasma response to the perturbation magnetic field, which breaks the toroidal symmetry, while the neoclassical toroidal viscosity experiment in stellarator is focused on predicting the toroidal flow in the plasma without the external toroidal torque. The toroidal viscosity in the stellarator/heliotron is larger than that in a tokamak even with a perturbation magnetic field. The experimental results from stellarators/heliotron would be good examples to test the neoclassical toroidal viscosity, because the neoclassical toroidal viscosity is usually larger than the anomalous perpendicular viscosity near the edge. This is not the case in a tokamak where the anomalous perpendicular viscosity is still more dominant in most experiments.

In helical plasmas, both toroidal and poloidal flows are affected by the damping process due to parallel viscosity. Experiments on toroidal and poloidal viscosities in CHS, Heliotron-J, HSX, Tohoku-Heliac, W-7AS and LHD demonstrated that these viscosities have reasonable agreement with that expected from neoclassical theory. The symmetric direction, where the parallel viscosity is minimum, is between the toroidal and poloidal directions. Plasma flow along the symmetric direction is observed in HSX and CHS, when a large electric field exists in the plasma and the plasma flow is mainly determined by the intrinsic flow. Because the symmetric direction is tilted from the magnetic field direction, the spontaneous toroidal flow is anti-parallel to the direction of the $E_r \times B_\theta$ drift in helical plasmas. This is in contrast to the spontaneous toroidal flow in the direction parallel to the direction of the $E_r \times B_\theta$ drift in JFT-2M tokamak plasmas. The poloidal flow inside the magnetic island was found to be zero, which indicates a flat space potential inside the magnetic island. Then the strong flow shear appears at the boundary of the magnetic island and it may contribute to the reduction of transport near the boundary of the magnetic island through turbulence suppression by $\boldsymbol{E} \times \boldsymbol{B}$ shear as observed in the TJ-II stellarator. The experiments on toroidal and poloidal flows in helical systems suggest that the theory of neoclassical viscosity can give a reasonable prediction of the flow pattern (toroidal and poloidal flows) for the plasma with a normal nesting magnetic flux surface. However, the flow patterns in the magnetic island and stochastic magnetic field region are complicated [378] and further study of neoclassical viscosity theory in plasmas with magnetic islands will be necessary in the future.

Early investigations of non-axisymmetric field effects in tokamaks [37] inspired theoretical investigations to confirm the NTV effect in experiments, with initial calculations underestimating quantitative agreement with experiment due to simplification of the computed field perturbation.

The theoretical suggestion of an expanded field spectrum [38] inspired more complete three-dimensional computations of the non-axisymmetric field and its potential amplification, which led to quantitative agreement between NTV theory and tokamak experiments [41]. Further investigations reviewed in the previous section have established additional dependences of NTV on plasma parameters including the toroidal mode spectrum of the applied non-axisymmetric field, dependence on collisionality (ion temperature in the '$1/\nu$' regime), and the manifestation of the superbanana plateau regime. The lack of hysteresis of the NTV effect as a function of plasma velocity is a favourable characteristic for its use in open or closed-loop plasma rotation feedback control systems. Additional positive applications of NTV in present and future tokamaks, including ITER have also been discussed in section 11.

A further critical area of investigation in tokamaks that specific NTV experiments can strongly support is the establishment and/or testing of physical models of plasma response. A detailed and quantitatively accurate first-principles model of the plasma response in tokamaks has not yet been established. As shown in the previous section, especially for spectra dominated by $n = 1$ fields, plasma response is typically needed to find quantitative agreement between NTV theory and experiments, while field configurations dominated by higher n elements (e.g. $n = 2$, 3) when non-resonant with strong tearing modes may not need strong amplification of the applied field to quantitatively match theory and experiment. In either case, these examples suggest that NTV theory can be used as a strong constraint for any plasma response model proposed when tested against experiments that accurately measure the NTV torque profile. This is due to the dependence of the NTV torque profile being strongly related to the applied field—by the square of the field. Therefore, any model of the field amplification by the plasma response over the vacuum field will be generally increased by the square of this amplification when compared to experiments. At present, the most accurate measurements of the peak NTV torque in tokamak experiments are nominally within a factor of two of the theory. Therefore, the maximum tolerated error in a plasma amplification model in a radial region of strong NTV in such experiments is limited to approximately the square root of this factor, or about 40%. As published plasma amplification models have shown far greater variations of the resultant amplified field—sometimes greater than an order of magnitude—the comparison of the theoretical NTV produced by these models against experiments accurately measuring the NTV radial profile can produce conclusive determination of the validity of any proposed plasma-induced field amplification model.

Acknowledgments

The authors would like to thank Dr M S Chu for carefully reading section 3. They would like to thank Dr W H Ko for charge exchange recombination spectroscopy measurements and analysis of toroidal plasma rotation in KSTAR. The work by KCS was supported by the Ministry of Science and Technology, Taiwan, under Grant No. 100-2112-M-006-004-MY3, and Foundation for the Advancement of Outstanding Scholarship, Taiwan. The work by KI was supported in part by a Grant-in-Aid for Specially-Promoted Research (No. 21224014) and a Grant-in-Aid for Scientific Research (No. 23246164) of JSPS, Japan. The work by SAS was supported by the US Department of Energy under Grant No. DE-FG02-99ER54524.

References

[1] Braginskii S.I. 1965 *Review of Plasma Physics* vol 1, ed M.A. Leontovich (New York: Consultants Bureau) p 205
[2] Galeev A.A. and Sagdeev R.Z. 1968 *Sov. Phys.—JETP* **26** 233
[3] Galeev A.A. and Sagdeev R.Z. 1979 *Review of Plasma Physics* vo1 7, ed M.A. Leontovich (New York: Consultants Bureau) p 257
[4] Galeev A.A., Sagdeev R.Z., Furth H.P. and Rosenbluth M.N. 1969 *Phys. Rev. Lett.* **22** 511
[5] Rosenbluth M.N., Hazeltine R.D. and Hiaton F.L. 1972 *Phys. Fluids* **15** 116
[6] Hinton F.L. and Hazeltine R.D. 1976 *Rev. Mod. Phys.* **48** 239
[7] Hirshman S.P. and Sigmar D.J. 1981 *Nucl. Fusion* **21** 1079
[8] Hinton F.L. and Rosenbluth M.N. 1973 *Phys. Fluids* **16** 836
[9] Hazeltine R.D. and Ware A.A. 1976 *Nucl. Fusion* **16** 538
[10] Hirshman S.P. 1976 *Phys. Fluids* **19** 155
[11] Hirshman S.P. 1978 *Nucl. Fusion* **18** 917
[12] Shaing K.C. 1986 *Phys. Fluids* **29** 2231
[13] Shaing K.C. and Hirshman S.P. 1989 *Phys. Fluids* B **1** 705
[14] Wagner F. *et al* 1982 *Phys. Rev. Lett.* **49** 1408
[15] Shaing K.C. and Crume E.C. Jr 1989 *Phys. Rev. Lett.* **63** 2369
[16] Shaing K.C., Crume E.C. Jr and Houlberg W.A. 1990 *Phys. Fluids* B **2** 1492
[17] Shaing K.C., Lee G.S., Carreras B.A., Houlberg W.A. and Crume E.C. Jr 1989 *Proc. 12th Int. Conf. on Plasma Physics and Controlled Fusion Research (Nice, France, 1988)* vol 2 (Vienna: IAEA) p 13
[18] Terry P.W. 2000 *Rev. Mod. Phys.* **72** 109
[19] Shaing K.C. 1988 *Phys. Fluids* **31** 8
[20] Itoh S.-I. and Itoh K. 1988 *Phys. Lett.* A **127** 267
[21] Shaing K.C. 1988 *Phys. Fluids* **31** 2249
[22] Ware A.A. 1970 *Phys. Rev. Lett.* **25** 916
[23] Galeev A.A. 1971 *Sov. Phys.—JETP* **32** 752
[24] Bickerton R.J., Connor J.W. and Taylor J.B. 1971 *Nature Phys. Sci.* **229** 110
[25] Hinton F.L. and Oberman C. 1969 *Nucl. Fusion* **9** 119
[26] Kadomtsev B.B. and Pogutse O.P. 1971 *Nucl. Fusion* **11** 67
[27] Nührenberg J. and Zille R. 1988 *Phys. Lett.* A **129** 113
[28] Gibson A. and Mason D.W. 1969 *Plasma Phys.* **11** 121
[29] Hazeltine R.D. 1973 *Plasma Phys.* **15** 77
[30] Hirshman S.P. and Sigmar D.J. 1976 *Phys. Fluids* **19** 1532
[31] Kovrizhnikh L.M. 1984 *Nucl. Fusion* **24** 851
[32] Ida K. *et al* 1999 *Nucl. Fusion* **39** 1849
[33] Ida K. *et al* 2003 *Phys. Rev. Lett.* **91** 085003
[34] Ida K. *et al* 2001 *Phys. Rev. Lett.* **86** 5297
[35] Yoshinuma M. *et al* 2004 *Plasma Phys. Control. Fusion* **46** 1021
[36] Ida K. *et al* 2005 *Nucl. Fusion* **45** 391
[37] La Haye R.J. *et al* 2002 *Phys. Plasmas* **9** 2051
[38] Lazzaro E. and Zanca P. 2003 *Phys. Plasmas* **10** 2399
[39] Sabbagh S.A., Bialek J.M. and Bell R.E. 2004 *Nucl. Fusion* **44** 560
[40] Sabbagh S.A. *et al* 2006 *Nucl. Fusion* **46** 635
[41] Zhu W. *et al* 2006 *Phys. Rev. Lett.* **96** 225002
[42] Hamada S. 1962 *Nucl. Fusion* **2** 23
[43] Boozer A. 1983 *Phys. Fluids* **26** 496
[44] Isaev M.Yu., Mikhailov M.I. and Shafranov V.D. 1994 *Plasma Phys. Rep.* **20** 319
[45] Pustovitov V.D. 1998 *Plasma Phys. Rep.* **24** 279

[46] Shaing K.C., Hirshman S.P. and Callen J.D. 1986 *Phys. Fluids* **29** 521
[47] Shaing K.C., Chu M.S. and Sabbagh A.A. 2010 *Nucl. Fusion* **50** 125012
[48] Grad H. and Rubin H. 1958 Theoretical and experimental aspects of controlled nuclear fusion *Proc. 2nd UN Int. Conf. on the Peaceful Uses of Atomic Energy (Geneva, Switzerland, 1958)* vo1 31, p 190
[49] Shafranov V.D. 1958 *Sov. Phys.—JETP* **8** 545
[50] Grad H. 1967 *Phys. Fluids* **10** 137
[51] Hirshman S.P. 1983 *Phys. Fluids* **26** 3553
[52] Hirshman S.P. and Van Rij W.I. 1986 *Comput. Phys. Commun.* **43** 143
[53] Shaing K.C. and Callen J.D. 1983 *Phys. Fluids* **26** 3315
[54] Coronado M. and Wobig H. 1987 *Phys. Fluids* **30** 3171
[55] Shaing K.C., Carreras B.A., Dominguez N., Lynch V.E. and Tolliver J.S. 1989 *Phys. Fluids* B **1** 1663
[56] Artsimovich L.A. 1972 *Nucl. Fusion* **12** 215
[57] Coloborod'ko V.Ya., Kolesnichenko Ya.I. and Yavorskij V.A. 1984 *Nucl. Fusion* **23** 399
[58] Kolesnichenko Ya.I., Andeson D., Lisak M. and Wilhelmsson H. 1984 *Phys. Rev. Lett.* **53** 1825
[59] Shaing K.C., Aydemir A.Y., Lin-Liu Y.R. and Miller R. 1997 *Phys. Rev. Lett.* **79** 3652
[60] Hirshman S.P. 1978 *Nucl. Fusion* **18** 917
[61] Shaing K.C. 1986 *Phys. Fluids* **29** 2231
[62] Grad H. and Hogan J. 1970 *Phys. Rev. Lett.* **24** 1337
[63] Hirshman S.P. and Jardin S.C. 1979 *Phys. Fluids* **22** 731
[64] Chew G.F., Goldberger M.L. and Low F.E. 1956 *Proc. R. Soc. Lond.* A **236** 112
[65] Shaing K.C. 1996 *Phys. Plasmas* **3** 4276
[66] Shaing K.C., Tsai T.H., Chu M.S., Sun Y. and Sabbagh S.A. 2011 *Nucl. Fusion* **51** 073043
[67] Coronado M. and Wobig H. 1986 *Phys. Fluids* **29** 527
[68] Rosenbluth M.N., Rutherford P.H., Taylor J.B., Frieman E.A. and Kovrizhnikh L.M. 1971 *Proc. Conf. on Plasma Physics and Controlled Nuclear Fusion Research* (Vienna: IAEA) vol 1, p 495
[69] Hazeltine R.D. 1974 *Phys. Fluids* **17** 961
[70] Tsang K.T. and Frieman E.A. 1976 *Phys. Fluids* **19** 747
[71] Hassam A.B. and Kulsrud R.M. 1978 *Phys. Fluids* **21** 2271
[72] Hsu C.T., Shaing K.C. and Gormley R. 1994 *Phys. Plasmas* **1** 132
[73] Hinton F.L. and Rosenbluth M.N. 1999 *Plasma Phys. Control. Fusion* **41** A653
[74] Rutherford P.H. 1970 *Phys. Fluids* **13** 482
[75] Kovrizhnikh L.M. 1969 *Sov. Phys.—JETP* **29** 475
[76] Shaing K.C. 2005 *Phys. Plasmas* **12** 052514
[77] Shaing K.C. 1992 *Phys. Fluids* B **4** 171
[78] Shaing K.C. 2005 *Phys. Plasmas* **12** 082508
[79] Shaing K.C. and Hsu C.T. 2012 *Phys. Plasmas* **19** 022502
[80] Seol J. and Shaing K.C. 2013 *Phys. Plasmas* **20** 042504
[81] Shaing K.C. and Callen J.D. 1983 *Phys. Fluids* **26** 1526
[82] Hazeltine R.D. and Ware A.A. 1978 *Plasma Phys.* **20** 673
[83] Shaing K.C. and Spong D.A. 1990 *Phys. Fluids* B **2** 1190
[84] Soel J. and Shaing K.C. 2012 *Phys. Plasmas* **19** 072512
[85] Bolton C. and Ware A.A. 1983 *Phys. Fluids* **26** 459
[86] Sauter O., Angioni C. and Lin-Liu Y.R. 1999 *Phys. Plasmas* **6** 2834
[87] Belli E.A. and Candy J. 2012 *Plasma Phys. Control. Fusion* **54** 015015
[88] Chang C.S. and Hinton F.L. 1982 *Phys. Fluids* **25** 1493
[89] Houlberg W.A., Shaing K.C., Hirshman S.P. and Zarnstorff M.C. 1997 *Phys. Plasmas* **4** 3230
[90] Stix T.H. 1972 *Plasma Phys.* **14** 367
[91] Stringer T.E. 1974 *Plasma Phys.* **16** 651
[92] Rome J.A. and Peng Y.-K.M. 1079 *Nucl. Fusion* **19** 1293
[93] Porcelli F., Stankiewicz R., Berk H.L. and Zhang Y.Z. 1992 *Phys. Fluids* B **4** 3017
[94] Shaing K.C., Hazeltine R.D. and Zarnstorff M.C. 1997 *Phys. Plasmas* **4** 771
[95] Gott Yu.V. and Yuchenko E.I. 1999 *Plasma Phys. Rep.* **25** 363
[96] Gott Yu.V. and Yuchenko E.I. 2014 *Plasma Phys. Rep.* **49** 243
[97] Lin-Liu Y.R. and Miller R.L. 1995 *Phys. Plasmas* **2** 1666
[98] Hazeltine R.D., Hinton F.L. and Rosenbluth M.N. 1973 *Phys. Fluids* **16** 1645
[99] Shaing K.C., Hsu C.T., Yokoyama M. and Wakatani M. 1995 *Phys. Plasmas* **2** 349
[100] Taguchi M. 1988 *Plasma Phys. Control. Fusion* **30** 1897
[101] Taguchi M. 2013 *Phys. Plasmas* **20** 014505
[102] Taguchi M. 2014 *Phys. Plasmas* **24** 052505
[103] Shaing K.C. 2002 *Phys. Plasmas* **9** 736
[104] Landau L.D. 1946 *J. Phys. (USSR)* **10** 25
[105] Shaing K.C., Yokoyama M., Wakatani M. and Hsu C.T. 1996 *Phys. Plasmas* **3** 965
[106] Furukawa M., Wakatani M. and Shaing K.C. 1999 *J. Plasma Fusion Res.* **75** 481
[107] Kikuchi M. and Azumi M. 1995 *Plasma Phys. Control. Fusion* **37** 1215
[108] Hirshman S.P., Shaing K.C., Van Rij W.I., Beasley C.O. Jr and Crume E.C. Jr 1986 *Phys. Fluids* **29** 2951
[109] Berk H.L. and Galeev A.A. 1967 *Phys. Fluids* **10** 441
[110] Shaing K.C. and Hazeltine R.D. 1992 *Phys. Fluids* B **4** 2547
[111] Hazeltine R.D. and Catto P.J. 1981 *Phys. Fluids* **24** 290
[112] Shaing K.C., Hsu C.T. and Hazeltine R.D. 1994 *Phys. Plasmas* **1** 3365
[113] Wang W.X., Hinton F.L. and Wong S.K. 2001 *Phys. Rev. Lett.* **87** 055002
[114] Shaing K.C. and Zarnstorff M.C. 1997 *Phys. Plasmas* **4** 3928
[115] Shaing K.C. and Lai A.L. 2013 *Phys. Plasmas* **20** 122504
[116] Shaing K.C. 2000 *Phys. Plasmas* **7** 5081
[117] Belli E.A. and Candy J. 2008 *Plasma Phys. Control. Fusion* **50** 095010
[118] Lin Z., Tang W.M. and Lee W.W. 1995 *Phys. Plasmas* **2** 2975
[119] Shaing K.C., Hazeltine R.D. and Zarnstorff M.C. 1997 *Phys. Plasmas* **4** 1375
[120] Shaing K.C., Hazeltine R.D. and Zarnstorff M.C. 1997 *Phys. Plasmas* **4** 1371
[121] Nocentini A., Tessarotto M. and Engelmann F. 1975 *Nucl. Fusion* **15** 359
[122] Wang S. 1998 *Phys. Plasmas* **5** 3319
[123] Sigmar D.J. 1973 *Nucl. Fusion* **13** 17
[124] Miller R.L., Lin-Liu Y.R., Turnbull A.D., Chan V.S., Pearlstein L.D., Sauter O. and Villard L. 1997 *Phys. Plasmas* **4** 1062
[125] Kikuchi M. and Azumi M. 2012 *Rev. Mod. Phys.* **84** 1807
[126] Shaing K.C., Houlberg W.A. and Strand P.I. 2002 *Phys. Plasmas* **9** 1654
[127] Shaing K.C. and Hazeltine R.D. 1998 *Phys. Plasmas* **5** 953
[128] Shaing K.C. 1990 *Phys. Fluids* B **2** 2847
[129] Shaing K.C. and Christenson P.J. 1993 *Phys. Fluids* B **5** 666
[130] Winsor N., Johnson J.L. and Dawson J.M. 1970 *J. Comput. Phys.* **6** 430
[131] Hazeltine R.D., Lee E.P. and Rosenbluth M.N. 1971 *Phys. Fluids* **14** 361
[132] Shaing K.C., Hazeltine R.D. and Sanuki H. 1992 *Phys. Fluids* B **4** 404
[133] Shaing K.C. and Hsu C.T. 1993 *Phys. Fluids* B **5** 3596
[134] Hinton F.L. and Wong K.L. 1985 *Phys. Fluids* **28** 3082
[135] Shaing K.C. 1993 *Phys. Fluids* B **5** 3841
[136] Shaing K.C., Hsu C.T. and Dominguez N. 1994 *Phys. Plasmas* **1** 1168
[137] Taylor R.J., Brown M.L., Fried B.D., Grote H., Liberati J.R., Morales G., Prebyl P., Darrow D. and Ono M. 1989 *Phys. Rev. Lett.* **63** 2365
[138] Okabayashi M. and Yoshikawa S. 1972 *Phys. Rev. Lett.* **29** 1725
[139] Stringer T.E. 1969 *Phys. Rev. Lett.* **22** 770
[140] Stringer T.E. 1970 *Phys. Fluids* **13** 810
[141] Stringer T.E. 2003 *Nucl. Fusion* **33** 1249
[142] Soel J. and Shaing K.C. 2012 *Phys. Plasmas* **19** 072512
[143] Rome J.A., McAlees D.G., Callen J.D. and Fowler R.H. 1976 *Nucl. Fusion* **16** 55

[144] Chankin A.V. and McCracken G.M. 1993 *Nucl. Fusion* **33** 1459
[145] Miyamoto K. 1996 *Nucl. Fusion* **36** 927
[146] Hinton F.L. and Chu M.S. 1985 *Nucl. Fusion* **25** 345
[147] deGrassie J.S., Mueller S.H. and Boedo J.A. 2012 *Nucl. Fusion* **52** 013010
[148] Stacey W.M., Sayer M.H., Floyd J.P. and Groebner R.J. 2013 *Phys. Plasmas* **20** 012509
[149] Ware A.A. 1984 *Phys. Fluids* **27** 1215
[150] Shaing K.C. 1992 *Phys. Fluids* B **4** 290
[151] Shaing K.C. 1992 *Phys. Fluids* B **4** 3310
[152] Shaing K.C. 2003 *Phys. Plasmas* **10** 1530
[153] Itoh S.I. and Itoh K. 1988 *Phys. Rev. Lett.* **60** 2276
[154] Shaing K.C. 2002 *Phys. Plasmas* **9** 1
[155] Shaing K.C. and Hsu C.T. 1995 *Phys. Plasmas* **2** 1801
[156] Lee K.C. 2006 *Phys. Plasmas* **13** 062505
[157] Aydemir A.Y. 2007 *Phys. Rev. Lett.* **98** 225002
[158] Aydemir A.Y. 2009 *Nucl. Fusion* **49** 065001
[159] Aydemir A.Y. 2012 *Nucl. Fusion* **52** 063026
[160] Taniuti T. *et al* 1992 *J. Phys. Soc. Japan* **61** 568
[161] Greene J. *et al* 1971 *Phys. Fluids* **14** 1258
[162] Vedenov A., Velikhov E. and Sagdeev R. 1962 *Nucl. Fusion* **2** 465 (Suppl.)
[163] Drummond W.E. and Pines D. 1962 *Nucl. Fusion* **2** 1049 (Suppl.)
[164] Kaufman A.N. 1972 *J. Plasma Phys.* **8** 1
[165] Dewar R.L. 1973 *Phys. Fluids* **16** 1102
[166] Tang W.M. 1978 *Nucl. Fusion* **18** 1089
[167] Hitchcock D.A., Mahajan S.M. and Hazeltine R.D. 1979 *Plasma Phys.* **21** 741
[168] Dominguez R. and Waltz R.Z. 1987 *Nucl. Fusion* **27** 65
[169] Waltz R.Z. 1982 *Phys. Fluids* **25** 1269
[170] Horton W. 1999 *Rev. Mod. Phys.* **71** 735
[171] Itoh S. 1982 *J. Phys. Soc. Japan* **51** 3345
[172] Itoh S.-I. and Itoh K. 1988 *Phys. Lett.* A **127** 267
[173] Shaing K.C. 1990 *Phys. Fluids* B **2** 764
[174] Shaing K.C. 2001 *Phys. Rev. Lett.* **86** 640
[175] Shaing K.C. 2001 *Phys. Plasmas* **8** 193
[176] Dominguez R.R. and Staebler G.M. 1993 *Phys. Fluids* B **5** 387
[177] Coppi B. 1994 *Plasma Phys. Control. Fusion* **36** B107
[178] Nagashima K., Koida Y. and Shirai H. 1994 *Nucl. Fusion* **34** 449
[179] Mattor N. and Diamond P.H. 1988 *Phys. Fluids* **31** 1180
[180] Hogan J.T. 1984 *Phys. Fluids* **27** 2308
[181] Stacey W.M. and Sigmar D.J. 1985 *Phys. Fluids* **28** 2800
[182] Connor J.W., Cowley S.C., Hastie R.J. and Pan L.R. 1987 *Plasma Phys. Control. Fusion* **29** 919
[183] Hsu C.T. and Sigmar D.J. 1990 *Plasma Phys. Control. Fusion* **32** 499
[184] Claassen H.A. and Gerhauser H. 1999 *Czech. J. Phys.* **49** 69
[185] Claassen H.A., Gerhauser H., Rogister A. and Yarim C. 2000 *Phys. Plasmas* **7** 3699
[186] Catto P.J. and Simakov A.N. 2005 *Phys. Plasmas* **12** 012501
[187] Wong S.K. and Chan V.S. 2005 *Phys. Plasmas* **12** 092513
[188] Wong S.K. and Chan V.S. 2009 *Phys. Plasmas* **16** 122507
[189] Brizard A.J. and Hahm T.S. 2007 *Rev. Mod. Phys.* **72** 421
[190] Taguchi M. 1999 *J. Plasma Phys.* **62** 269
[191] Sugama H. and Horton W. 1997 *Phys. Plasmas* **4** 405
[192] Hahm T.S., Diamond P.H., Gurcan O.D. and Rewoldt G. 2007 *Phys. Plasmas* **14** 072302
[193] Coppi B. 2002 *Nucl. Fusion* **42** 1
[194] Shaing K.C., Chu M.S., Hsu C.T., Sabbagh S.A., Seol J. and Sun Y. 2012 *Plasma Phys. Control. Fusion* **54** 124033
[195] Dupree T.H. 1972 *Phys. Fluids* **15** 334
[196] Figarella C.F., Benkadda S., Beyer P., Garbet X. and Voitsekhovitch I. 2003 *Phys. Rev. Lett.* **90** 15002
[197] Biglari H., Diamond P.H. and Terry P.W. 1990 *Phys. Fluids* B **2** 1
[198] Zhang Y.Z. and Mahajan S.M. 1992 *Phys. Fluids* B **4** 1385
[199] Hahm T.S., Beer M.A., Lin Z., Hammett G.W., Lee W.W. and Tang W.M. 1999 *Phys. Plasmas* **6** 922
[200] Zhang Y.Z., Xie T. and Mahajan S.M. 2012 *Phys. Plasmas* **19** 020701
[201] Mase A., Itakura A., Inutake M., Ishii K., Jeong J.H., Hattori K. and Miyoshi H. 1991 *Nucl. Fusion* **31** 1725
[202] Lazzaro E. *et al* 2002 *Phys. Plasmas* **9** 3906
[203] Snipes J.A., Campbell D.J., Haynes P.S., Hender T.C. Hugon M., Lomas P.J., Lopes Cardozo N.L., Nave M.F.F. and Schuller F.C. 1988 *Nucl. Fusion* **28** 1085
[204] Liu C.S. 1971 *Phys. Rev. Lett.* **27** 399
[205] Yoshikawa S. 1973 *Nucl. Fusion* **13** 433
[206] Smolyakov A.I., Hirose A., Lazzaro E., Re G.B. and Callen J.D. 1995 *Phys. Plasmas* **2** 1581
[207] Shaing K.C. 2001 *Phys. Rev. Lett.* **87** 245003
[208] Shaing K.C. 2003 *Phys. Plasmas* **10** 1443
[209] Boozer A.H. 2006 *Phys. Plasmas* **13** 044501
[210] Yushmanov P.N. 1990 *Review of Plasma Physics* vol 16 (New York: Consultants Bureau)
[211] Connor J.W. and Hastie R.J. 1973 *Nucl. Fusion* **13** 221
[212] Hastie R.J., Taylor J.B. and Haas F.A. 1967 *Ann. Phys.* **41** 302
[213] Goldston R.J., White R.B. and Boozer A.H. 1981 *Phys. Rev. Lett.* **47** 647
[214] Tsang K.T. 1977 *Nucl. Fusion* **17** 557
[215] Davidson J.N. 1975 *Nucl. Fusion* **16** 731
[216] Shaing K.C. *et al* 2008 *Phys. Plasmas* **15** 082506
[217] Callen J.D. 2011 *Nucl. Fusion* **51** 094026
[218] Shaing K.C., Sabbagh S.A. and Chu M.S. 2010 *Nucl. Fusion* **50** 025022
[219] Sun Y., Liang Y., Shaing K.C., Koslowski H.R., Wiegmann C. and Zhang T. 2010 *Phys. Rev. Lett.* **105** 145002
[220] Sun Y., Liang Y., Shaing K.C., Koslowski H.R., Wiegmann C. and Zhang T. 2011 *Nucl. Fusion* **51** 053015
[221] Shaing K.C., Seol J., Sun Y., Chu M.S. and Sabbagh S.A. 2010 *Nucl. Fusion* **50** 125008
[222] Shaing K.C., Sabbagh S.A. and Chu M.S. 2009 *Plasma Phys. Control. Fusion* **51** 035004
[223] Shaing K.C., Sabbagh S.A. and Chu M.S. 2009 *Plasma Phys. Control. Fusion* **51** 035009
[224] Shaing K.C., Sabbagh S.A. and Chu M.S. 2009 *Plasma Phys. Control. Fusion* **51** 055003
[225] Su C.H. and Oberman C. 1968 *Phys. Rev. Lett.* **20** 427
[226] Rutherford P.H. 1970 *Phys. Fluids* **13** 482
[227] Chu M.S., Rawls J.M., Wong S.K. and Hinton F.L. 1977 *Phys. Fluids* **20** 127
[228] Abramowitz M. and Stegun I.A. (ed) 1965 *Handbook of Mathematical Functions* (New York: Dove)
[229] Sun Y., Shaing K.C., Liang Y., Shen B. and Wan B. 2013 *Nucl. Fusion* **53** 073026
[230] Hastings D.E. and Shaing K.C. 1985 *Phys. Fluids* **28** 1402
[231] Shaing K.C. 1984 *Phys. Fluids* **27** 1567
[232] Ryutov D.D. and Stupakov G.V. 1987 *Reviews of Plasma Physics* (New York: Springer) pp 93–202
[233] Yavorskij V.A., Andrushchenko Zh.N., Edenstrasser J.W. and Goloborod'ko V.Ya. 1999 *Phys. Plasmas* **6** 3853
[234] Yavorskij V., Moskvitin A., Moskvitina Yu., Goloborod'ko V. and Schoepf K. 2010 *Nucl. Fusion* **50** 084022
[235] Park J.-K., Boozer A.H. and Menard J.E. 2009 *Phys. Rev. Lett.* **102** 065002
[236] Shaing K.C., Chu M.S. and Sabbagh S.A. 2009 *Plasma Phys. Control. Fusion* **51** 075015
[237] Shaing K.C. 1996 *Phys. Rev. Lett.* **76** 4364
[238] Yokoyama M., Wakatani M. and Shaing K.C. 2002 *Nucl. Fusion* **35** 153
[239] Liu Y.Q., Chu M.S., Chapman I.T. and Hender T.C. 2008 *Phys. Plasmas* **15** 112503
[240] Hu B. and Betti R. 2004 *Phys. Rev. Lett.* **93** 105002
[241] Gradshteyn I.S. and Ryzhik I.M. 1980 *Table of Integrals, Series and Products* (New York: Academic)
[242] Shaing K.C. 2002 *Phys. Plasmas* **9** 3470
[243] Rutherford P.H. 1973 *Phys. Fluids* **16** 1903
[244] Garbet X. *et al* 2010 *Phys. Plasmas* **17** 072505
[245] Shaing K.C., Tsai T.H., Chu M.S. and Sabbagh S.A. 2011 *Nucl. Fusion* **51** 043013

[246] Stroth U., Itoh K., Itoh S.I., Hartfuss H. and Laqua H. 2001 *Phys. Rev. Lett.* **86** 5910
[247] Yokoyama M. *et al* 2007 *Nucl. Fusion* **47** 1213
[248] Ida K. *et al* 2004 *Plasma Phys. Control. Fusion* **46** A45
[249] Dinklage A. *et al* 2007 *Nucl. Fusion* **47** 1265
[250] Hirsch M. *et al* 2008 *Plasma Phys. Control. Fusion* **50** 053001
[251] Tsypin V.S., Mikhailovskii A.B., Galvao R.M.O., Nascimento I.C., Tendler M., Azevedo C.A. and de Assis A.S. 1998 *Phys. Plasmas* **5** 3358
[252] Mikhailovskii A.B. and Tsypin V.S. 1984 *Sov. J. Plasma Phys.* **10** 51
[253] Hirshman S.P. 1977 *Phys. Fluids* **20** 589
[254] Shaing K.C., Crume E.C. Jr, Tolliver J.S., Hirshman S.P. and Van Rij W.J. 1989 *Phys. Fluids* B **1** 148
[255] Rodriguez-Solano Ribeiro E. and Shaing K.C. 1987 *Phys. Fluids* **30** 8
[256] Beidler C.D. and Maaßberg H. 1996 *Theory of Fusion Plasmas* (Varenna)
[257] Shaing K.C., Hirshman S.P. and Tolliver J.S. 1986 *Phys. Fluids* **29** 2548
[258] Shaing K.C., Carreras B.A., Dominguez N., Lynch V.E. and Tolliver J.S. 1989 *Phys. Fluids* B **1** 1663
[259] Watanabe K.Y., Nakajima N., Okamoto M., Nakamura Y. and Wakatani M. 1992 *Nucl. Fusion* **32** 1499
[260] Cooper W.A. 2002 *Plasma Phys. Control. Fusion* B **44** 357
[261] Ferrando I.M.S. *et al* 2004 *Fusion Sci. Technol.* **46** 44
[262] Ware A.S. *et al* 2002 *Phys. Rev. Lett.* **89** 125003
[263] Spong D.A. *et al* 2001 *Nucl. Fusion* **41** 711
[264] Zarnstorff M.C. *et al* 2001 *Plasma Phys. Control. Fusion* **43** A237
[265] Nakajima N. and Okamoto M. 1992 *J. Phys. Soc. Japan* **61** 833
[266] Watanabe K. *et al* 1995 *Nucl. Fusion* **35** 335
[267] Helander P., Geiger J. and Maaßberg H. 2011 *Phys. Plasmas* **18** 092505
[268] Boozer A.H. 1983 *Phys. Fluids* **26** 496
[269] Pytte A. and Boozer A.H. 1981 *Phys. Fluids* **24** 88
[270] Shaing K.C. 1997 *Phys. Plasmas* **4** 3341
[271] Shaing K.C. and Hokin S.A. 1983 *Phys. Fluids* **26** 2136
[272] Mynick H.E., Chu T.K. and Boozer A.H. 1982 *Phys. Rev. Lett.* **48** 322
[273] Frieman E.A. 1970 *Phys. Fluids* **13** 490
[274] Stringer T.E. 1972 *Nucl. Fusion* **12** 689
[275] Nemov V.V., Kasilov S.V., Kernbichler W. and Heyn M.F. 1999 *Phys. Plasmas* **6** 4622
[276] Hinton F.L. 2012 *Phys. Plasmas* **19** 082516
[277] Crume E.C., Shaing K.C., Hirshman S.P. and Van Rij W.I. 1988 *Phys. Fluids* **31** 11
[278] Taguchi M. 1992 *Phys. Fluids* B **4** 3638
[279] Sugama H. and Nishimura S. 2002 *Phys. Plasmas* **9** 4637
[280] Spong D.A. 2005 *Phys. Plasmas* **12** 056114
[281] Maaßberg H., Beidler C.D. and Turkin Y. 2009 *Phys. Plasmas* **16** 072504
[282] Nemov V.V., Kasilov S.V., Kernbichler W. and Heyn M.F. 1999 *Phys. Plasmas* **6** 4622
[283] Kernbichler W., Kasilov S.V., Leitold G.O., Nemov V.V. and Allmaier K. 2008 *Plasma Fusion Res.* **3** S1061
[284] Beidler C.D., Hitchon W.N.G. and Shohet J.L. 1987 *J. Comput. Phys.* **72** 220
[285] Wakasa A., Murakami S., MaaßBberg H., Beidler C.D., Nakajima N., Watanabe K., Yamada H., Okamoto M., Oikawa S. and Itagaki M. 2001 *J. Plasma Fusion Res. Ser.* **4** 408
[286] Tribaldos V. 2001 *Phys. Plasmas* **8** 1229
[287] Isaev M.Yu., Brunner S., Cooper W.A., Tran T.M., Bergmann A., Beidler C.D., Geiger J., Maaßberg H., Nührenberg J. and Schmidt M. 2006 *Fusion Sci. Technol.* **50** 440
[288] Allmaier K., Kasilov S.V., Kernbichler W. and Leitold G.O. 2008 *Phys. Plasmas* **15** 072512
[289] Beidler C.D. *et al* 2011 *Nucl. Fusion* **51** 076001
[290] Jaeger E.F., Spong D.A. and Hedrick C.L. 1978 *Phys. Rev. Lett.* **40** 866
[291] Mynick H.E. and Hitchon W.N.G. 1983 *Nucl. Fusion* **23** 1053
[292] Shaing K.C., Sabbagh S.A., Chu M.S., Becoulet M. and Cahyna P. 2008 *Phys. Plasmas* **15** 082505
[293] Ida K. *et al* 1991 *Phys. Rev. Lett.* **67** 58
[294] Ida K. *et al* 1997 *Phys. Plasmas* **4** 310
[295] Nakajima N., Okamoto M. and Fujiwara M. 1992 *J. Plasma Fusion Res.* **68** 503
[296] Watanabe K.Y. *et al* 1995 *Nucl. Fusion* **35** 335
[297] Gerhardt S.P. *et al* 2005 *Phys. Rev. Lett.* **94** 015002
[298] Gerhardt S.P. *et al* 2005 *Phys. Plasmas* **12** 056116
[299] Lee H. *et al* 2013 *Plasma Phys. Control. Fusion* **55** 035012
[300] Garofalo A.M. *et al* 2008 *Phys. Rev. Lett.* **101** 195005
[301] Kitajima S. *et al* 2006 *Nucl. Fusion* **46** 200
[302] Takahashi S. 2006 *Plasma Phys. Control. Fusion* **48** 39
[303] Rozhansky V. and Tendler M. 1992 *Phys. Fluids* B **4** 1877
[304] Itoh K. and Itoh S.-I. 1996 *Plasma Phys. Control. Fusion* **38** 1
[305] Fujisawa A. *et al* 1997 *Phys. Rev. Lett.* **79** 1054
[306] Fujisawa A. *et al* 1998 *Phys. Rev. Lett.* **81** 2256
[307] Ida K. *et al* 1994 *Phys. Plasmas* **1** 116
[308] Wagner F. 2007 *Plasma Phys. Control. Fusion* **49** B1
[309] Hirsch M. 2000 *Plasma Phys. Control. Fusion* **42** A231
[310] Sano F. *et al* 2005 *Nucl. Fusion* **45** 1557
[311] Morita S. *et al* 2007 *Nucl. Fusion* **47** 1033
[312] Morita S. *et al* 2006 *Plasma Phys. Control. Fusion* **48** A269
[313] Ida K. *et al* 2001 *Phys. Rev. Lett.* **86** 3040
[314] Briesemeister A. *et al* 2010 *Contrib. Plasma Phys.* **50** 741
[315] Yoshinuma M. *et al* 2009 *Nucl. Fusion* **49** 075036
[316] Ida K. *et al* 2002 *Plasma Phys. Control. Fusion* **44** 361
[317] Ida K. *et al* 2002 *Phys. Rev. Lett.* **88** 015002
[318] Ida K. *et al* 2004 *Nucl. Fusion* **44** 290
[319] Fujisawa A. 2004 *Phys. Rev. Lett.* **93** 165002
[320] Xia H., Shats M.G. and Punzmann H. 2006 *Phys. Rev. Lett.* **97** 255003
[321] Waelbroeck F.L. 2009 *Nucl. Fusion* **49** 104025
[322] Koide Y. *et al* 1994 *Phys. Rev. Lett.* **72** 3662
[323] Hogweij G.M.D. *et al* 1996 *Phys. Rev. Lett.* **76** 632
[324] Ida K. *et al* 2004 *Phys. Plasmas* **11** 2551
[325] Castejón F. *et al* 2004 *Nucl. Fusion* **44** 593
[326] Estrada T. *et al* 2007 *Nucl. Fusion* **47** 305
[327] Vargas V.I. *et al* 2007 *Nucl. Fusion* **47** 1367
[328] Van Milligen B.P. *et al* 1993 *Nucl. Fusion* **33** 1119
[329] Inagaki S. *et al* 2004 *Phys. Rev. Lett.* **92** 055002
[330] Evans T.E. *et al* 2008 *Nucl. Fusion* **48** 024002
[331] Gerhardt S.P. *et al* 2009 *Nucl. Fusion* **49** 032003
[332] Buttery R.J. *et al* 2008 *Phys. Plasmas* **15** 056115
[333] Berkery J.W. *et al* 2010 *Phys. Rev. Lett.* **104** 035003
[334] Sabbagh S.A. *et al* 2010 *Nucl. Fusion* **50** 025020
[335] ITER Physics Basis Editors *et al* 1999 *Nucl. Fusion* **39** 2137
[336] Peng Y.K.-M. *et al* 2005 *Plasma Phys. Control. Fusion* **47** B263
[337] Peng Y.K.-M. *et al* 2009 *Fusion Sci. Technol.* **56** 957
[338] Wilson H.R., Ahn J. and Akers R. 2004 *Nucl. Fusion* **44** 917
[339] Fitzpatrick R. 1998 *Phys. Plasmas* **5** 3325
[340] Fitzpatrick R. 1993 *Nucl. Fusion* **33** 1049
[341] Hender T. *et al* 1992 *Nucl. Fusion* **32** 2091
[342] Yokoyama M., Callen J.D. and Hegna C.C. 1996 *Nucl. Fusion* **36** 1307
[343] Stix T.H. 1962 *The Theory of Plasma Waves* (New York: McGraw-Hill) p 207
[344] Sabbagh S.A., Bell R.E. and Bell M.G. 2002 *Phys. Plasmas* **9** 2085
[345] Glasser A.H. and Chance M.S. 1997 *Bull. Am. Phys. Soc.* **42** 1960
[346] Solomon W.M. *et al* 2008 *Phys. Rev. Lett.* **101** 065004
[347] Kaye S.M.*et al* 2009 *Nucl. Fusion* **49** 045010
[348] Sun Y. *et al* 2010 *Plasma Phys. Control. Fusion* **52** 105007
[349] Liang Y. *et al* 2010 *Nucl. Fusion* **50** 025013

[350] Park Y.S. *et al* 2013 *Nucl. Fusion* **53** 083029
[351] Chapman I.T. *et al* 2011 *Nucl. Fusion* **51** 073040
[352] Sun Y. *et al* 2012 *Nucl. Fusion* **52** 083007
[353] Finken K.H. *et al* 1999 *Nucl. Fusion* **39** 637
[354] Park J.K. *et al* 2009 *Phys. Plasmas* **16** 056115
[355] Liu Y. *et al* 2010 *Phys. Plasmas* **17** 122502
[356] Garofalo A.M. *et al* 2009 *Phys. Plasmas* **16** 056119
[357] Burrell K.H. *et al* 2012 *Phys. Plasmas* **19** 056117
[358] Sabbagh S.A. *et al* 2010 *Proc. 23rd IAEA Fusion Energy Conf. on Fusion Energy (Daejeon, Korea, 2010)* (Vienna: IAEA) CD-ROM file ICC/P5-06, www-naweb.iaea.org/napc/physics/FEC/FEC2010/html/index.htm
[359] Nowak S. *et al* 2012 *J. Phys.: Conf. Ser.* **401** 012017
[360] Hua M.D. *et al* 2010 *Plasma Phys. Control. Fusion* **52** 035009
[361] Kwak J.G. *et al* 2013 *Nucl. Fusion* **53** 104005
[362] Seol J. *et al* 2012 *Phys. Rev. Lett.* **109** 195003
[363] Cole A.J. *et al* 2011 *Phys. Rev. Lett.* **106** 225002
[364] Cole A.J. *et al* 2011 *Phys. Plasmas* **18** 055711
[365] Sabbagh S.A. *et al* 2014 *Proc. 25th IAEA Fusion Energy Conf. (St. Petersburg, Russia, 2014)* (Vienna: IAEA) EX/1–4
[366] Cole A.J. *et al* 2007 *Phys. Rev. Lett.* **99** 065001
[367] Reimerdes H. *et al* 2009 *Nucl. Fusion* **49** 115001
[368] Gerhardt S.P. *et al* 2010 *Plasma Phys. Control. Fusion* **52** 104003
[369] Park J.K. *et al* 2008 *Nucl. Fusion* **48** 045006
[370] Berkery J.W. *et al* 2010 *Phys. Plasmas* **17** 082504
[371] Kikuchi M. 2011 On offset toroidal rotation in NTV *38th EPS Conf. on Plasma Physics (Strasbourg, France)* P4. 115 http://ocs.ciemat.es/EPS2011PAP/pdf/P4.115.pdf
[372] Chatthong B. and Onjun T. 2013 *Nucl. Fusion* **53** 013007
[373] Schaffer M.J. *et al* 2011 *Nucl. Fusion* **51** 103028
[374] Sabbagh S.A. *et al* 2013 *Nucl. Fusion* **53** 104007
[375] Shaing K.C. and Hsu C.T. 2014 *Nucl. Fusion* **54** 033012
[376] Kasilov S.V., Kernbichler W., Martitsch A.F., Maaßberg H. and Heyn M.F. 2014 *Phys. Plasmas* **21** 092506
[377] Shaing K.C. 2015 *J. Plasma Phys.* **81** 905810203
[378] Ida K. *et al* 2015 *Nat. Commun.* **6** 5816